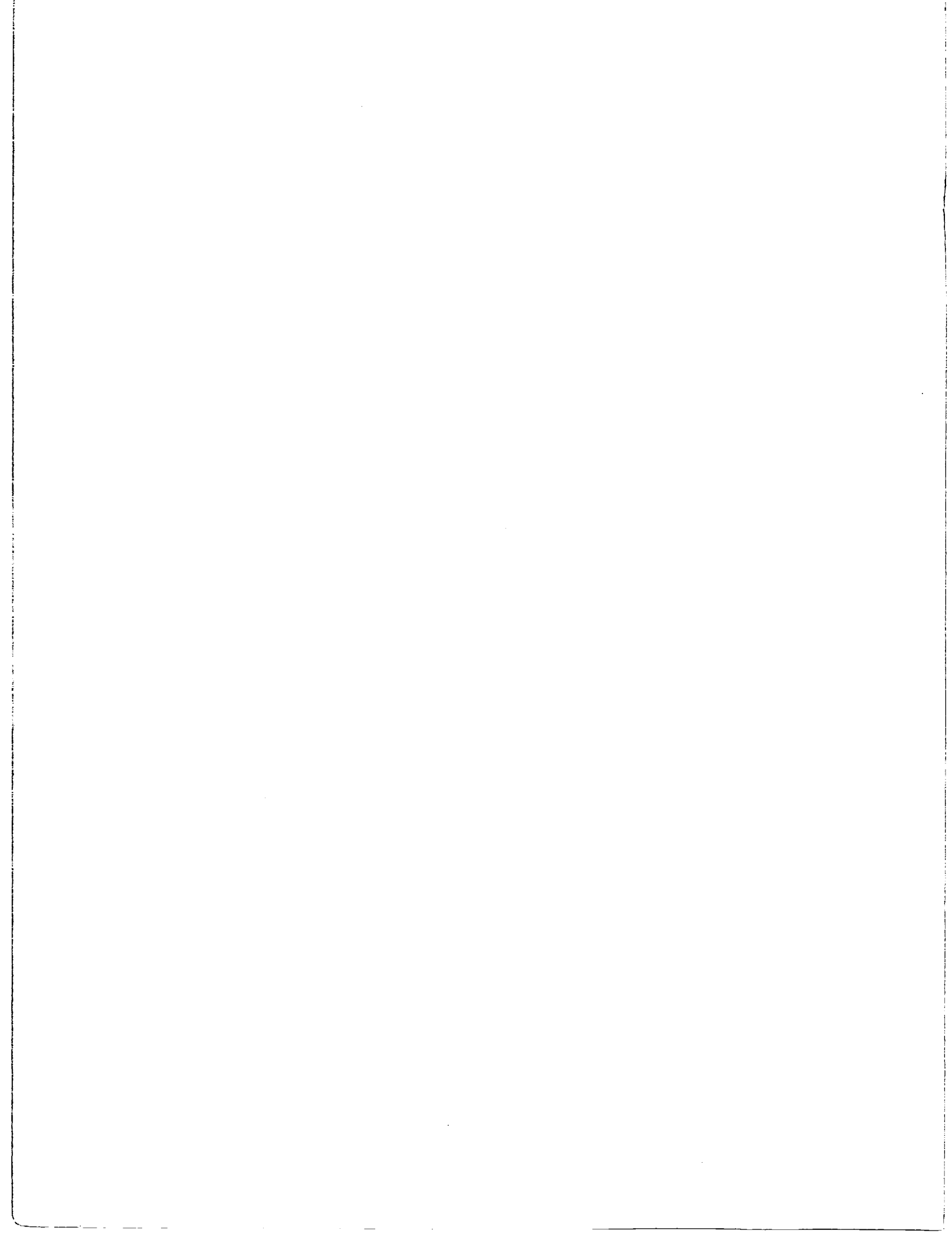NASA Technical Memorandum 82549

Space Processing Applications Rocket (SPAR) Project

SPAR IX Final Report

JANUARY 1984

NASA

NASA Technical Memorandum 82549

Space Processing Applications Rocket (SPAR) Project

SPAR IX *Final Report*

R. Poorman, *Compiler*
George C. Marshall Space Flight Center
Marshall Space Flight Center, Alabama

NASA

TABLE OF CONTENTS

CHAPTER I

SPACE PROCESSING APPLICATIONS ROCKET (SPAR) PROJECT

SPAR IX - FINAL REPORT

INTRODUCTION

The unique low-g environment of space affords an opportunity for exploring and developing techniques for processing a variety of materials without the constraining gravitational influences as evidenced with the processing of liquid phase materials or melts on Earth. The Materials Processing in Space (MPS) program is directed toward the stimulation and development of the associated science and technology required to pursue these investigations. This NASA activity is undertaken in cooperation with the scientific community and includes follow-on studies of specific areas of scientific research emphasizing those selected investigations of materials and processes which best demonstrate potential benefit from the enhanced sensitivity of the controlled processing in a low-g environment. Examples of interest in the program are the reduction and/or elimination of adverse thermal effects such as convection, sedimentation of heavy particles, buoyancy rise and positioning aspects of bubbles in liquids or melts, and the stratification effects of particulates of variable densities in solution. These and similar studies are considered to be the means to expand the limiting frontier in the development of new materials and processes which

are envisioned ultimately to be of benefit to mankind. As complementary to the research and technological nature of the investigations, the evolving emphasis is being directed, with the advent of the Shuttle and increased payload potential, toward the development of self-sustaining programs yielding direct product benefit.

The initial precursory zero-g demonstrations and investigations associated with this family of scientific experiments were proposed and developed for the Apollo flights beginning in the late 1960's and continued with Skylab and Apollo-Soyuz flights through the mid-1970's. During the period between the close of that era and the orbital space flights on the Space Shuttle in the 1980's, the Space Processing Applications Rocket (SPAR) project has provided the only viable flight opportunity for low-g scientific investigations for experimenters and is serving in a precursory role for planned and approved Shuttle investigations.

The SPAR project is part of the MPS program of the Office of Space Science and Applications (OSSA), which is responsible for directing research into the scientific efforts of materials processing in the unique environment of space. This effort involves participation and interaction from various disciplines of the scientific community, government-supported laboratories, universities, and industrial organizations, in addition to foreign particpation.

The Black Brant VC (BBVC) sounding rocket series, which is currently the carrier vehicle for the scientific payloads, with a Nike-boosted configuration available for heavier payloads, provides the opportunity to process materials in a low-g environment for periods up to five minutes in duration during a sub-orbital flight.

The rocket flights, which are conducted at the White Sands Missile Range (WSMR), afford experimenters and apparatus developers a flight opportunity for a proof-of-concept verification and/or refinement of equipment operation and procedures prior to the longer duration, more sophisticated Shuttle flights.

This SPAR flight, which was ninth in a planned series of rocket flights, occurred on January 20, 1981 and carried four experiments. The investigations for the experiments comprising the payload manifest were managed and coordinated by the MPS Projects Office of the Marshall Space Flight Center (MSFC). Three such experiments were proposed and devised by industrial firms and one by a government-supported laboratory.

Previous experiments flown on the SPAR flights include the measurement of liquid mixing due to spacecraft motion and the dispersion of normally immiscible materials in the area of fluid dynamics. Solidification experiments involving the gravitational effects on dendritic growth, epitaxial growth, and solidification of eutectic materials with widely differing densities have flown previously, in addition to solidification studies of interactions between second-phase particles and an advancing crystal-liquid interface and gravity-induced convection on cast microstructures. In the area of multiphase particle interaction, various

experients were conducted on the migration and coalescence of bubbles and particles, closed-cell metal foam, and dispersion strengthening of composites.

The SPAR project has been increasingly active in supporting research in the promising area of containerless processing with previous flights, including experiments on cast beryllium and the processing of amorphous ferro-magnetic materials in an electromagnetic field, and control of liquid droplets by an acoustic field in the furtherance of state-of-the-art of acoustic containerless processing technology.

The SPAR flights have, through an evolutionary program, addressed experiments of increasing complexity and refinement and have afforded additional flight opportunities consistent with the maturity of each investigation. The payloads selected for this flight manifest were based on the advanced state-of-preparedness of their ground-based research activity.

The following experiments are included in this SPAR IX report: a) Directional Solidification of Magnetic Composites" (Experiment No. 76-22/2), describing the ground-based research, including experiments leading to selection of the flight sample composition; b) Directional Solidification of Immiscible Al-Indium Alloys (Experiments Nos. 76-51/1 and 76-51/2), dealing with the analysis of mechanisms in structural formation of aluminum-indium alloys; c) Comparative Alloy Solidification (Experiment No. 76-36/1), continuing studies of segration and casting phenomena is metal alloys. A report on "Foam Copper", (Experiment No. 77-9) is not included since processing temperatures were not achieved in the General Purpose·Rocket Furnace (GPRF) during flight. (This experiment was reflown on the SPAR X flight.)

The post-flight results and analyses of each experiment flown on SPAR IX as prepared by the respective flight investigators, in addition to an engineering report on the performance of the SPAR IX Science Payload, are contained in separate sections of this technical memorandum. With the successful completion of this flight and subsequent data analysis, much useful data and information were accumulated for directing and developing experimental techniques and investigations toward an expanding, beneficial program of materials processing in the Shuttle era.

NASA

National Aeronautics and
Space Administration

George C. Marshall Space Flight Center
Marshall Space Flight Center, Alabama 35812

SPACE PROCESSING APPLICATIONS ROCKET PROJECT

SPAR IX

ENGINEERING REPORT

DECEMBER 1981

SCIENCE AND ENGINEERING
OFFICE OF THE ASSOCIATE DIRECTOR FOR ENGINEERING

TABLE OF CONTENTS

LIST OF FIGURES

SPAR IX POST-FLIGHT ENGINEERING REPORT

1.0   SUMMARY

The SPAR IX Nike-Black Brant VC rocket lifted off the launch pad at WSMR on Tuesday, January 20, 1981, at 1705:00:00 G.M.T. (5:05 p.m., MDT). The launch was successful and the payload was recovered intact.

Payload power was applied to all experiments as planned, and all experiments operated within the predicted near zero gravity. All MSFC flight support requirements to each experiment were met as indicated by the reduced flight data. Power to the payload experiments was programmed to be removed at T+728 seconds, but this could not be verified due to loss of telemetry signal, LOS, at T+722 seconds.

2.0   SPAR IX (R-17) PAYLOAD CONFIGURATION

The SPAR IX (R-17) science payload consisted of four materials experiments, the Experiment Support Module (ESM), and the Abbreviated Measurement Module (AMM). The SPAR IX experiments are:

76-22/2	Directional Solidification of Magnetic Composites
76-36/2	Comparative Alloy Solidification
76-51/1 & 2	Directional Solidification of Immiscible Aluminum-Indium Alloys
77-9	Foam Copper Experiment

The orientation of the experiments within the SPAR IX rocket vehicle is shown in Figure 1.
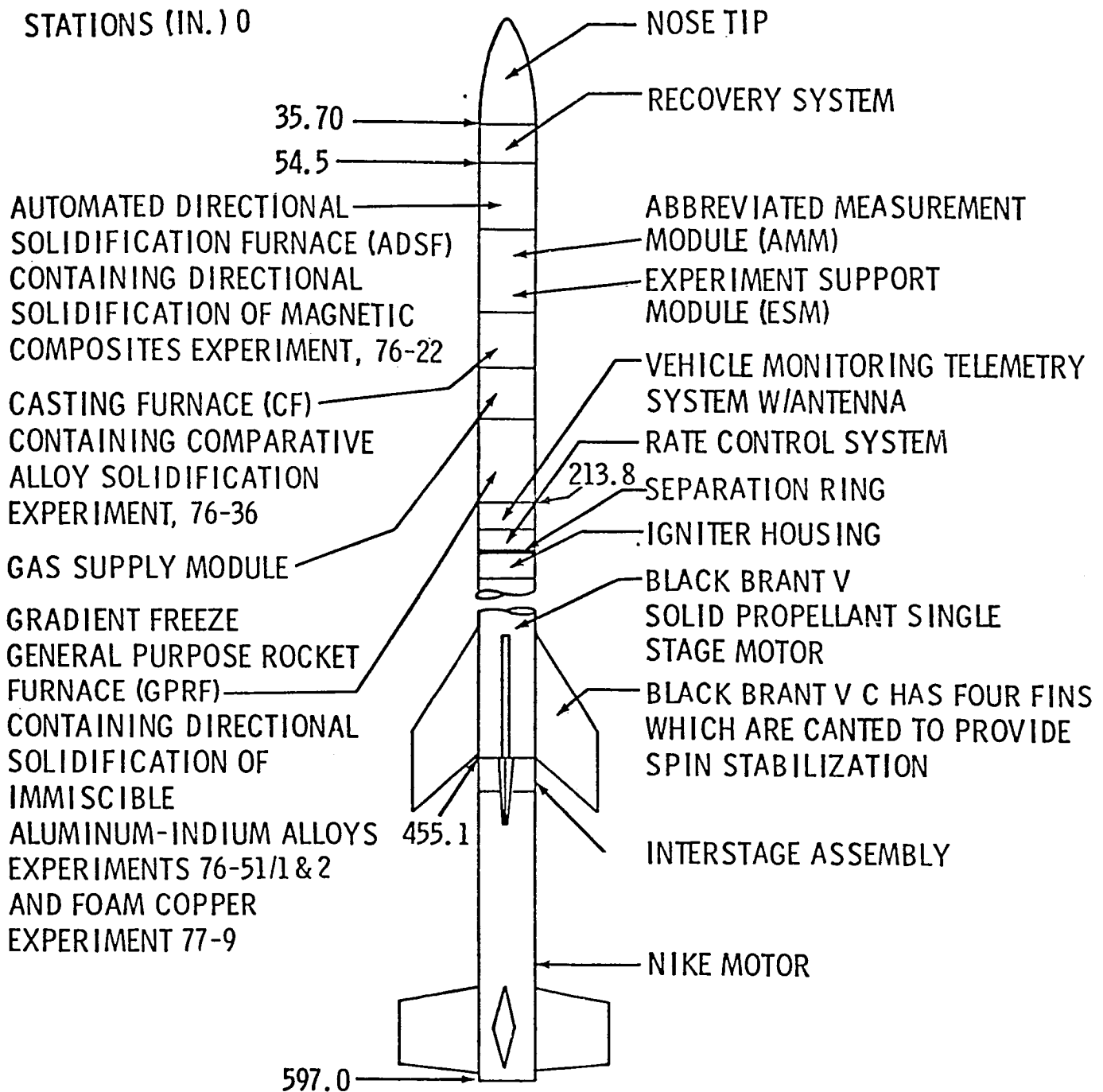
3.0   ROCKET PERFORMANCE

3.1   Flight Sequence

The SPAR IX flight profile is shown in Figure 2. The predicted and actual sequence of events are shown as a function of flight time.

3.2   Low Gravity

The predicted low-g (10^{-4} or less) time was based upon an all-up payload weight of 1046 pounds. Actual all-up weight measured at WSMR was 1095 pounds. The science payload furnished by MSFC weighed 736 pounds.

The measurement module low-g accelerometer measurements indicated that the low-g period on the X-axis began at T+82, and ended at T+383 seconds. The entry and exit times for the Y and Z axes are ques-

STATIONS (IN.) 0

35.70

54.5

AUTOMATED DIRECTIONAL
SOLIDIFICATION FURNACE (ADSF)
CONTAINING DIRECTIONAL
SOLIDIFICATION OF MAGNETIC
COMPOSITES EXPERIMENT, 76-22

CASTING FURNACE (CF)
CONTAINING COMPARATIVE
ALLOY SOLIDIFICATION
EXPERIMENT, 76-36

GAS SUPPLY MODULE

GRADIENT FREEZE
GENERAL PURPOSE ROCKET
FURNACE (GPRF)
CONTAINING DIRECTIONAL
SOLIDIFICATION OF
IMMISCIBLE
ALUMINUM-INDIUM ALLOYS
EXPERIMENTS 76-51/1 & 2
AND FOAM COPPER
EXPERIMENT 77-9

455.1

597.0

NOSE TIP

RECOVERY SYSTEM

ABBREVIATED MEASUREMENT
MODULE (AMM)

EXPERIMENT SUPPORT
MODULE (ESM)

VEHICLE MONITORING TELEMETRY
SYSTEM W/ANTENNA

RATE CONTROL SYSTEM

213.8 SEPARATION RING

IGNITER HOUSING

BLACK BRANT V
SOLID PROPELLANT SINGLE
STAGE MOTOR

BLACK BRANT V C HAS FOUR FINS
WHICH ARE CANTED TO PROVIDE
SPIN STABILIZATION

INTERSTAGE ASSEMBLY

NIKE MOTOR

SPAR IX LAUNCH VEHICLE AND R-19 PAYLOAD CONFIGURATION
FIGURE I

II-2

SPAR PROJECT
NIKE BLACK BRANT VC ROCKET 27.017
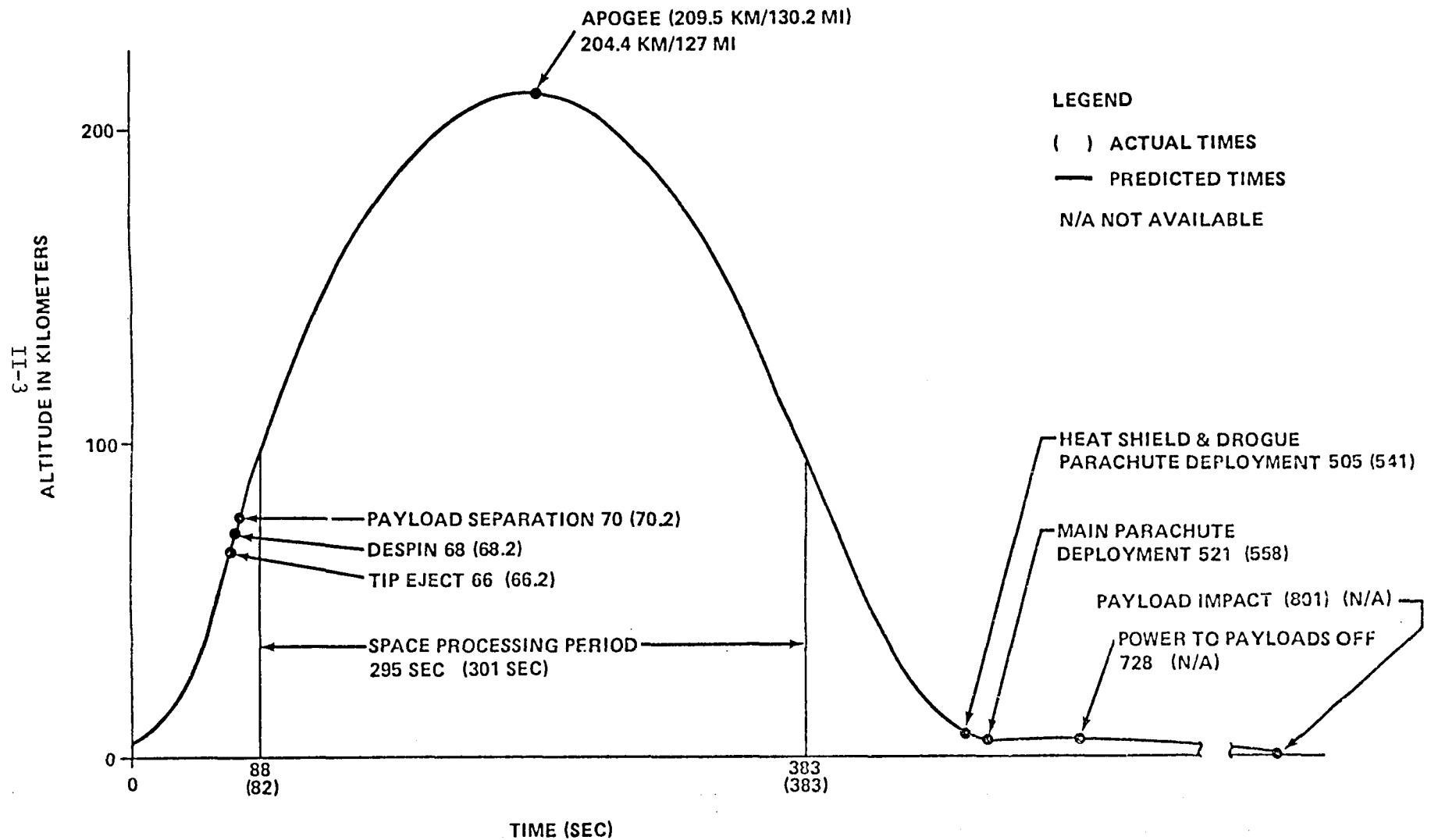FLIGHT PROFILE AND EVENTS/CONDITIONS

APOGEE (209.5 KM/130.2 MI)
204.4 KM/127 MI

LEGEND

( ) ACTUAL TIMES

— PREDICTED TIMES

N/A NOT AVAILABLE

ALTITUDE IN KILOMETERS

200 —

100 —

0

II-3

PAYLOAD SEPARATION 70 (70.2)
DESPIN 68 (68.2)
TIP EJECT 66 (66.2)

SPACE PROCESSING PERIOD
295 SEC (301 SEC)

HEAT SHIELD & DROGUE
PARACHUTE DEPLOYMENT 505 (541)

MAIN PARACHUTE
DEPLOYMENT 521 (558)

PAYLOAD IMPACT (801) (N/A)

POWER TO PAYLOADS OFF
728 (N/A)

88
(82)

0

383
(383)

TIME (SEC)

FIGURE 2. FLIGHT PROFILE AND EVENTS

tionable, due to erratic wiper action on the accelerometer pickoffs (see paragraph 6.1). Consequently, the X-axis entry and exit times should be used in determining the SPAR IX low-g time. This data yields a low-g period of 301 seconds. The minimum low-g period required by experiments was 292 seconds.

4.0   PAYLOAD SUPPORT

4.1   Payload Sequence of Events

All experiments required preheat power prior to launch that was supplied by ground power. At T-0, a lift-off signal was given which activated a timer within each experiment for control of events during the flight. The events are shown in Figure 3.

The actual timelines were well within the acceptable limits of each experiment. The planned power removal to experiments at T+728 seconds could not be verified due to the Loss of Telemetry Signal (LOS) coverage at T+722 seconds.

4.2   Payload Power

Transfer of electrical power from ground support equipment to the flight battery was accomplished at T minus 3 minutes. The science payload battery, located in the Experiment Service Module, supplied power to all experiments. Battery voltage measurement (M01-SM) indicates that the battery voltage was 33 volts at lift-off and jumped to 33.5 Vdc at T+280 seconds, corresponding to the GPRF Module 1 power cut-off. Here it remained essentially constant until LOS at T+722 seconds. The battery current measurement (M39-SM) indicates that the current was about 48 amperes at lift-off, which is 5 amperes higher than had been calculated from battery load profiles. The data is very noisy in the early part of the flight, but the current appears to have dropped to about 25 amps at T+50 seconds. At T+122 seconds, it increased to 30 amps as the 76-22 motors were activated. This was predicted to be 35 amps, thereby agreeing favorably. At T+280 seconds, the current dropped to 12 amps, whereas 16 amps had been predicted due to the GPRF Module 1 power cut-off at this point, where it remained essentially constant until LOS at T+722 seconds. Overall, the telemetry data indicates about 4 amperes less than the predicted current profile (Figure 4). The actual voltage profile agreed favorably with that which had been predicted.

A 1.5-second data dropout occurred on all telemetry channels at T+188 seconds. This dropout had occurred in previous testing at both GSFC and WSMR. Post-flight analysis of the voltage regulator powering
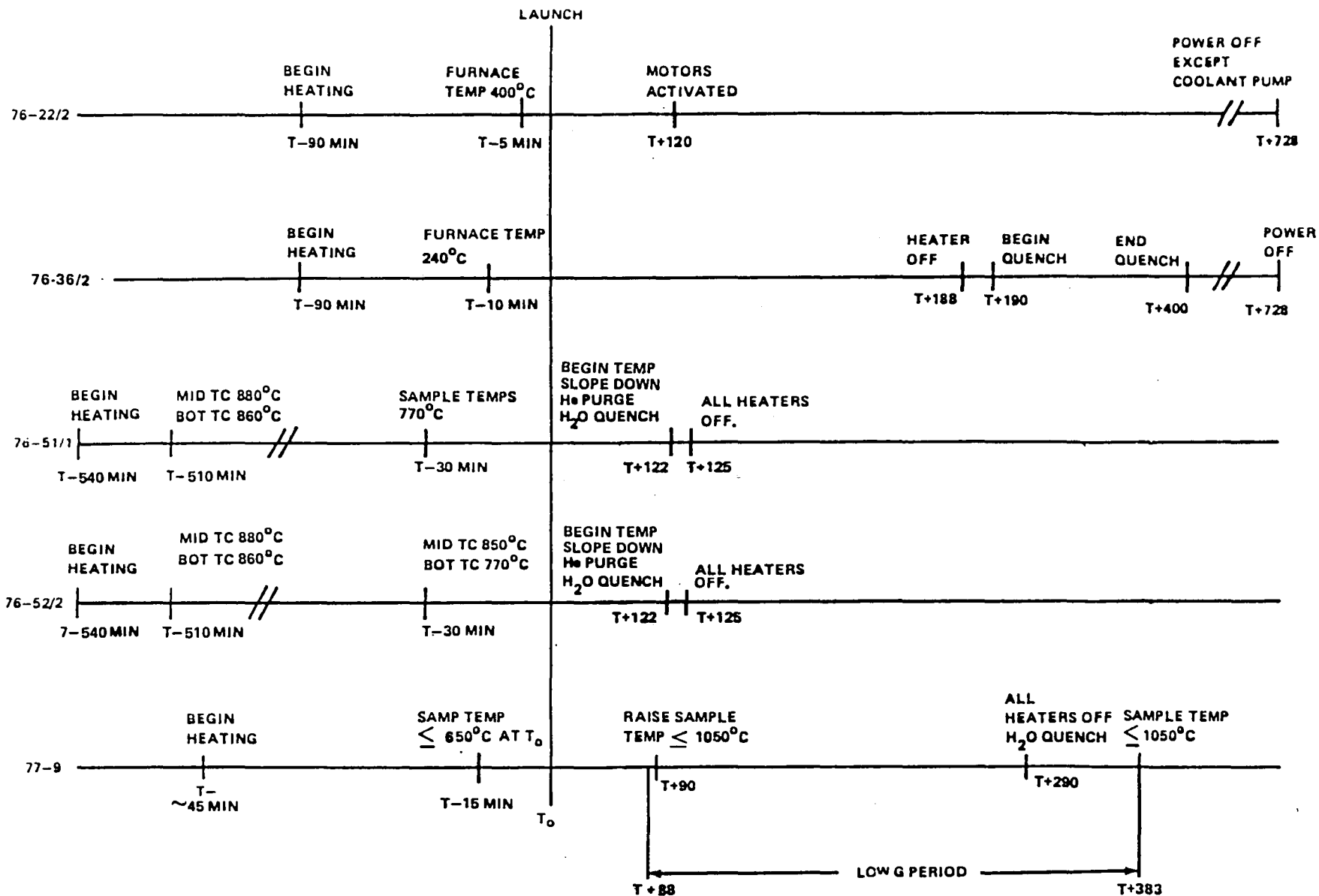
FIGURE 3 SPAR IX (R-17) EXPERIMENT TIMELINE

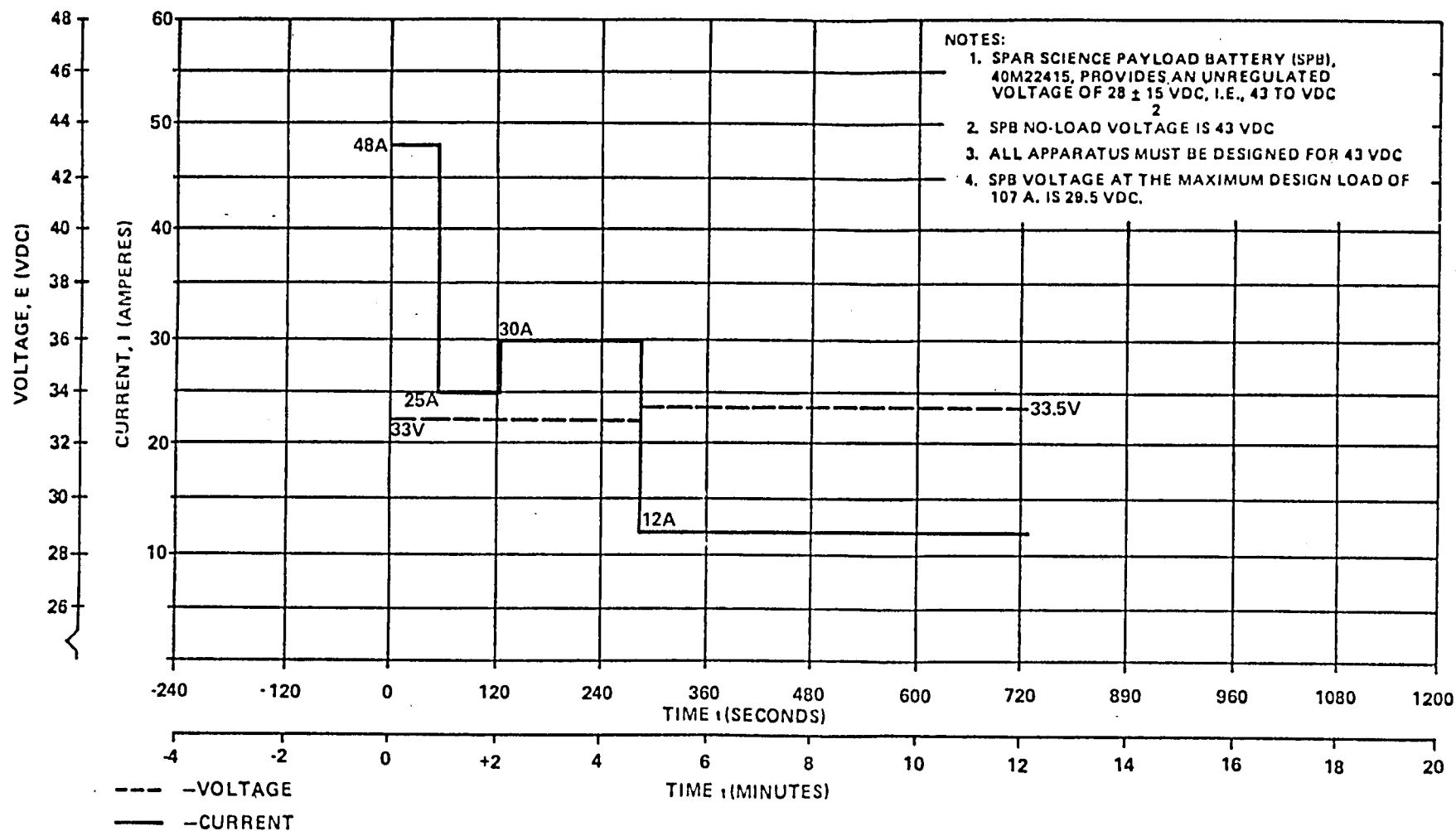# SPAR IX
VOLTAGE AND CURRENT PROFILES

NOTES:
1. SPAR SCIENCE PAYLOAD BATTERY (SPB), 40M22415, PROVIDES AN UNREGULATED VOLTAGE OF 28 ± 15 VDC, I.E., 43 TO VDC
2
2. SPB NO-LOAD VOLTAGE IS 43 VDC
3. ALL APPARATUS MUST BE DESIGNED FOR 43 VDC
4. SPB VOLTAGE AT THE MAXIMUM DESIGN LOAD OF 107 A. IS 29.5 VDC.

--- —VOLTAGE
——— —CURRENT

FIG. 4

9-II

the telemetry system discovered a thermally sensitive solder joint which was apparently heating sufficiently to interrupt power momentarily for 1.5 seconds.

4.3   Gradient Freeze General Purpose Rocket Furnace (GPRF)

The GPRF consists of 3 individual gradient heater modules, each containing an experiment cartridge. Heater Module 1 contained the Foam Copper Experiment, 77-9, Module 2 contained the Directional Solidification of Immiscible Aluminum-Indium Alloys, Experiment 76-51/1, and Module 3 contained Experiment 76-51/2. Modules 2 and 3 were preheated for 33 hours prior to launch, due to a 24-hour launch delay, and Module 1 for about 1 hour pre-launch, in accordance with the requirements levied by the two Principal Investigators.

The Module 1 Cold Temperature (C150-RF) indicates that the temperature was 670°C at lift-off and increased to 1070°C at T+62 seconds. Here it remained until T+123 seconds, when the heat-up was programmed to level off (see Figure 5) and decreased steadily to 950°C at T+283 seconds, when heating was ended. From this point, it continued to decrease, reaching 500°C at T+383 seconds, the end of the low-g period, and 300°C at T+722 seconds, which was LOS.

The Module 1 Hot Temperature (C151-RF) was 515°C at lift-off, increased to 750°C at T+123 seconds, and decreased steadily, reaching 215°C at low-g end and 240°C at LOS. It should be noted that the Module 1 hot heater winding was burned open in AST testing at MSFC and was not functional, subsequently, which accounts for the low temperatures in comparison with C150-RF, above.

The Module 1 Medium Temperature (C152-RF) was 670°C at lift-off, increased to 1070°C at T+123, decreased to 890°C at T+283 seconds, and continued decreasing to reach 500°C at low-g end and 275°C at LOS.

The 77-9 experiment sample in Module 1 failed to reach processing temperature (1150°C) because the internal potentiometer settings that determine the temperature profile were never verified, due to the concern of over-stressing the heater windings by extra testing. The settings were found to be correct for 1070°C in post-flight examination.

Power to the Module 1 heaters was removed at T+300 seconds, as programmed (K095-SM).

Experiment 77-9 (in Module 1) had no sample temperature measurements.

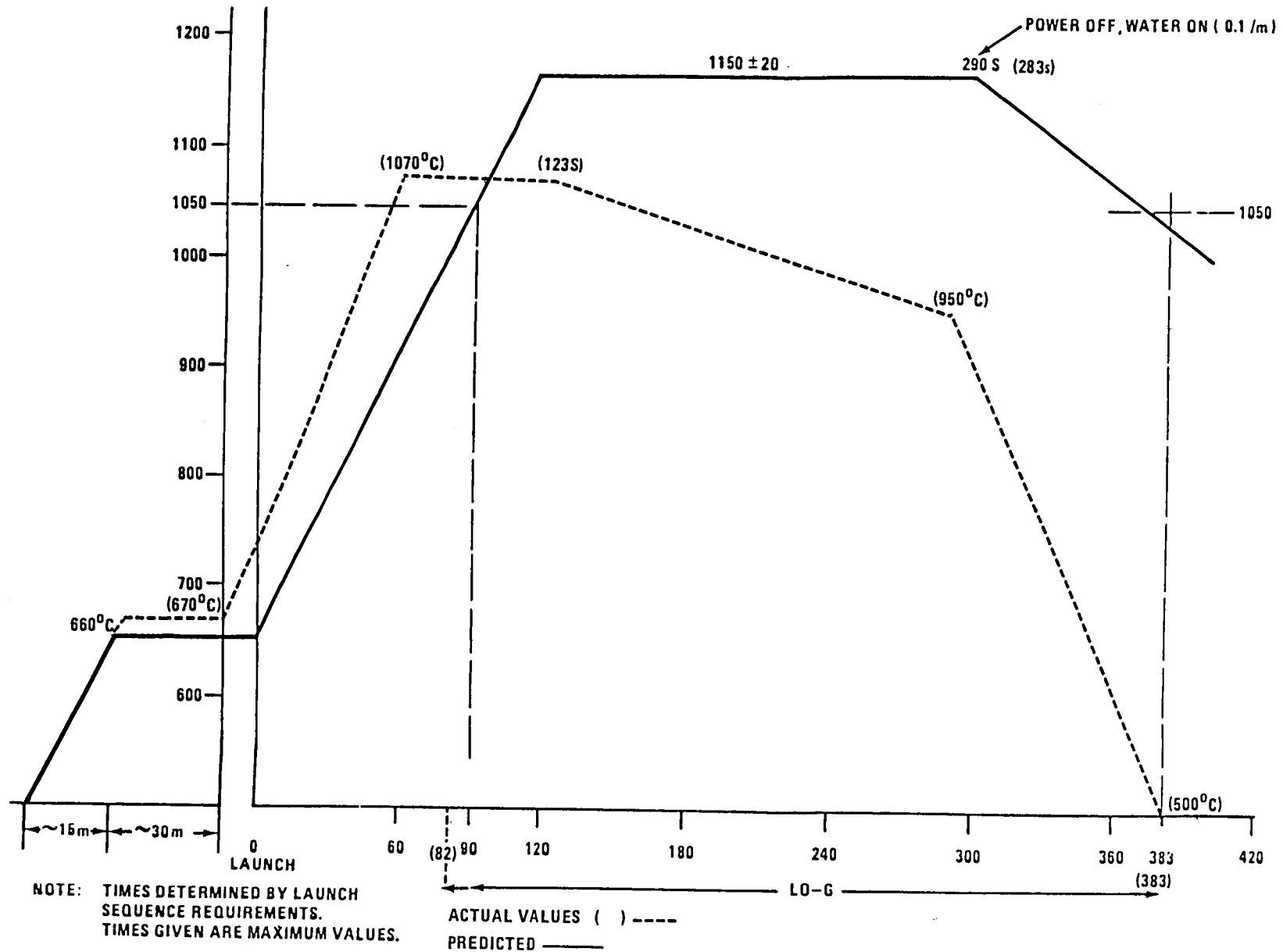FOAM COPPER EXPERIMENT, 77-9, TEMP VS. TIME
(CONTROL THERMOCOUPLE)

FIGURE 5

The Module 2 Cold Temperature (C153-RF) was 860°C at lift-off and rose to 880°C at T+123 seconds, when quench was initiated. From this point, it decreased steadily, reaching 105°C at low-g end and then rose slightly to reach 150°C at LOS.

The Module 2 Hot Temperature (C154-RF) was 650°C at lift-off, and rose to 700°C at quench initiation. From this point, it decreased steadily, reaching 80°C at low-g end, and then rose slightly to reach 130°C at LOS.

The Module 2 Medium Temperature (C155-RF) was 770°C at lift-off, and rose to 840°C at quench start. From this point, it decreased steadily, reaching 125°C at low-g end and then rose slightly to reach 160°C at LOS.

Experiment 76-51/1 (in Module 2) had 2 sample thermocouples on its experiment cartridge. The Mid-Sample Temperature (C011-51) was 770°C at lift-off and rose to 800°C at quench initiation before cooling to 450°C at low-g end and finally reached 240°C at LOS. The Bottom Sample Temperature (C012-51) was 770°C at lift-off and fell to 700°C at T+17 seconds, rose to 760°C at T+32 seconds, where it remained until quench initiation. From this point, it began cooling and reached 320°C at low-g end and 200°C at LOS. These temperatures are shown in Figure 6.

Power to the Module 2 heaters was removed at T+125 seconds, as programmed (K099-SM).

The Module 3 Cold Temperature (C156-RF) was 920°C at lift-off and dropped to 860°C at quench start at T+123. From this point, it decreased steadily, reaching 100°C at low-g end and then rose slightly to reach 120°C at LOS.

The Module 3 Hot Temperature (C157-RF) was 720°C at lift-off and rose to 780°C at quench initiation. From this point, it decreased steadily, reaching 120°C at low-g end and then rose slightly to reach 140°C at LOS.

The Module 3 Medium Temperature (C158-RF) was 860°C at lift-off and rose to 960°C at quench initiation. From this point, it decreased rapidly to reach 40°C at low-g end and increased to 115°C at LOS.

Power to the Module 3 heaters was removed at T+125 seconds, as programmed (K102-SM and K103-SM).

DIRECTIONAL SOLIDIFICATION OF IMMISCIBLE AI-IN ALLOYS
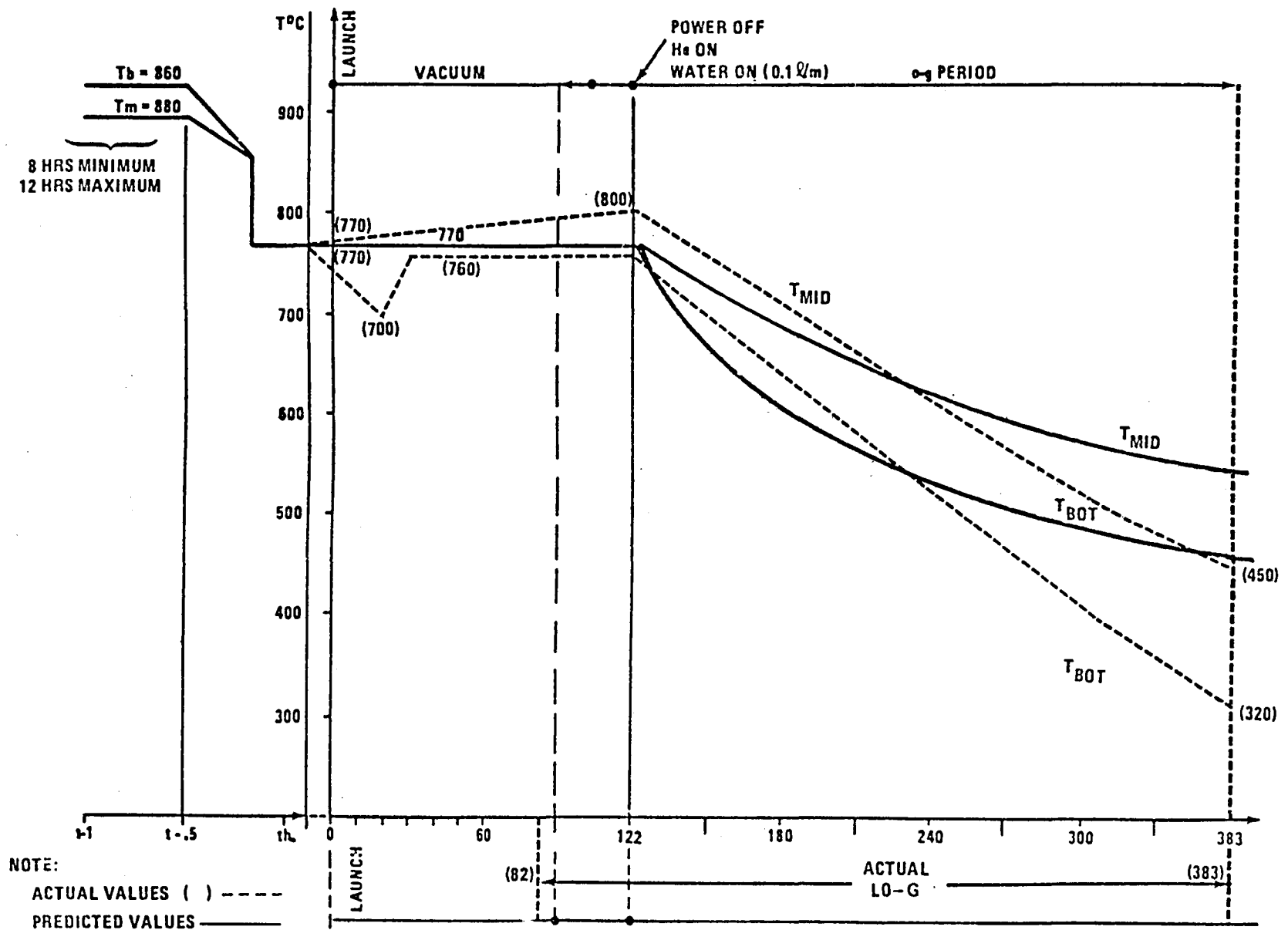## EXPERIMENT 76 51/1

FIGURE 6

Experiment 76-51/2 (in Module 3) had 2 sample thermocouples on its experiment cartridge. The Mid-Sample Temperature (C013-51) was 850°C at lift-off and rose to 890°C at water quench initiation at T+123 seconds. From this point, it decreased steadily to reach 400°C at low-g end and 190°C at LOS. The Bottom Sample Temperature (C014-51) was 750°C at lift-off and fell to 720°C at water quench start. From this point, it rose slightly to 740°C for 4 seconds and then decreased to 210°C at T+190 seconds, where it rose to 300°C at T+245 seconds and remained for 45 seconds. Finally, it decreased to reach 220°C at low-g end and 150°C at LOS. These temperatures are shown in Figure 7.

The Helium Sphere Pressure (D002-RF) was 2050 psia at lift-off and decreased steadily from quench start at T+123 seconds to reach 50 psia at T+440 seconds, where it remained until LOS at T+722 seconds. This performance was nominal.

The GPRF Water Bladder pressurizing gas storage tank Pressure (D011-RF) was 1850 psia at lift-off and decreased from quench start to reach 1500 psia minimum at T+194 seconds, before increasing to 1600 psia at LOS. From this measurement, it is obvious that the water quench bladder was pressurized for at least 71 seconds, from T+123 to T+194; hence, some water quench was obtained. Of the 4.0 liters of water originally contained in the water quench system, 2.8 liters were recovered at MSFC during post-flight examination. Since no water flowed to the Module 1 heat extractor intentionally, the average water flow rate to Modules 2 and 3 was approximately 1.0 liter/min. This rate is slightly high, since the metering valves were adjusted for flow rates of 0.1 liters/min. and 0.73 liters/min. to Modules 2 and 3, respectively, giving a total flow of 0.83 liters/min.

Overall, the GPRF performed satisfactorily. Modules 2 and 3 achieved the desired temperature profile in spite of the failure of the water quench system. As mentioned previously, the 77-9 experiment sample in Module 1 failed to reach processing temperature (1150°C) because the internal potentiometer settings that determine the temperature profile were never verified, due to the concern of over-stressing the heater windings by extra testing. The settings were found to be correct for 1070°C in post-flight examination. Hence, the GPRF performed exactly as it was programmed, but the potentiometer settings were in error. Even though the Hot Module 1 heater winding had failed in All Systems Testing (AST), it appears that there was still enough heating capability from the two good windings to achieve the desired temperature profile.

The failure of the water quench system is thought to have been caused by the shorting to ground of the gas supply solenoid (Figure 8), causing it to close and stop gas flow and allowing pressure to drop on the water supply bladder. This, in turn, caused the water flow to the module heat exchangers to slow and finally cease altogether. This failure mode also accounts for the fact that 1600 psia was found in the gas bottle, even though the gas depletion valve had supposedly been opened at T+600 sec.

DIRECTIONAL SOLIDIFICATION OF IMMISCIBLE
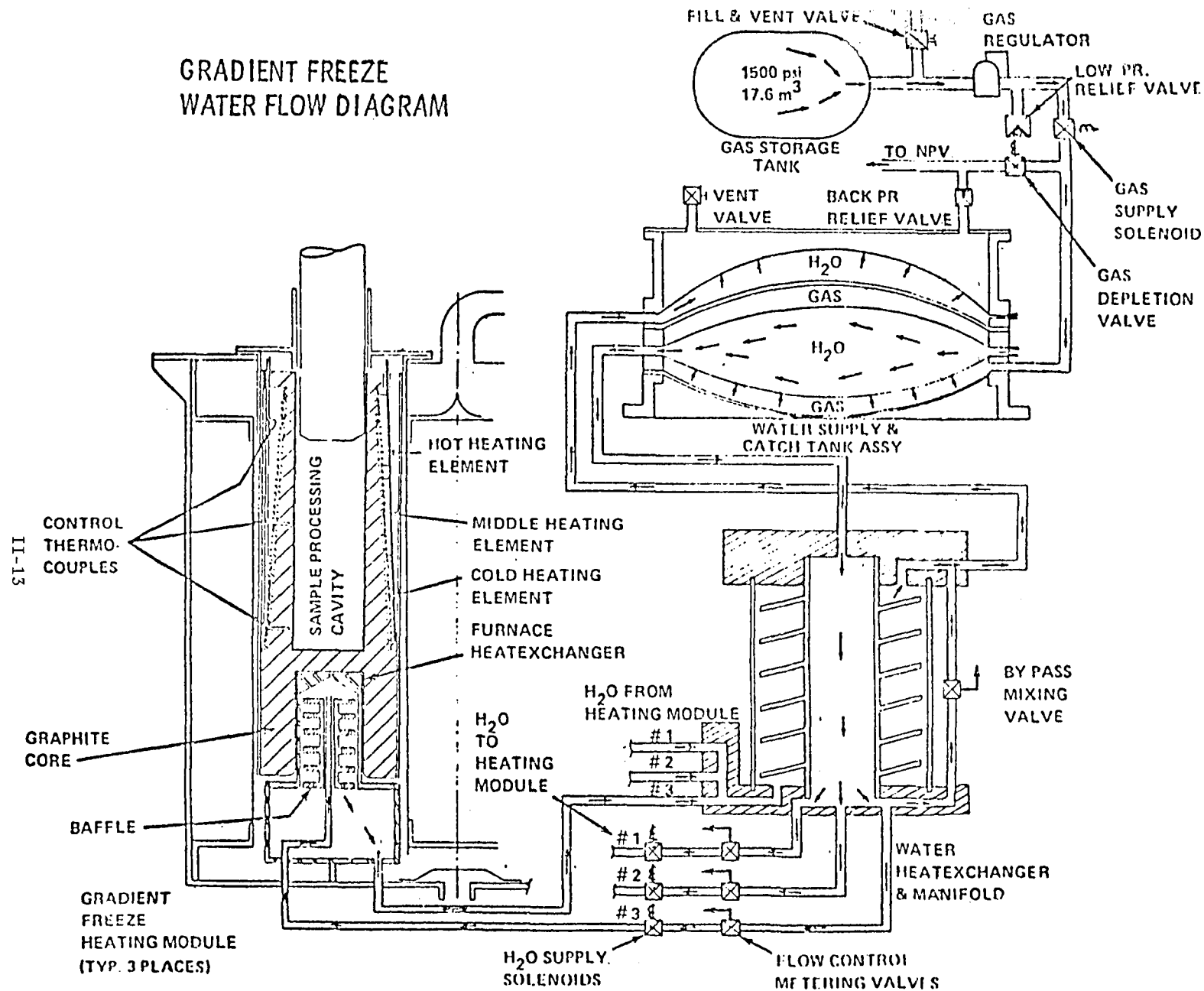# AL-IN ALLOYS EXPERIMENT 76-51/2

FIGURE 7

NOTE:
ACTUAL VALUES ( ) — — — —
PREDICTED VALUES ————

II-12
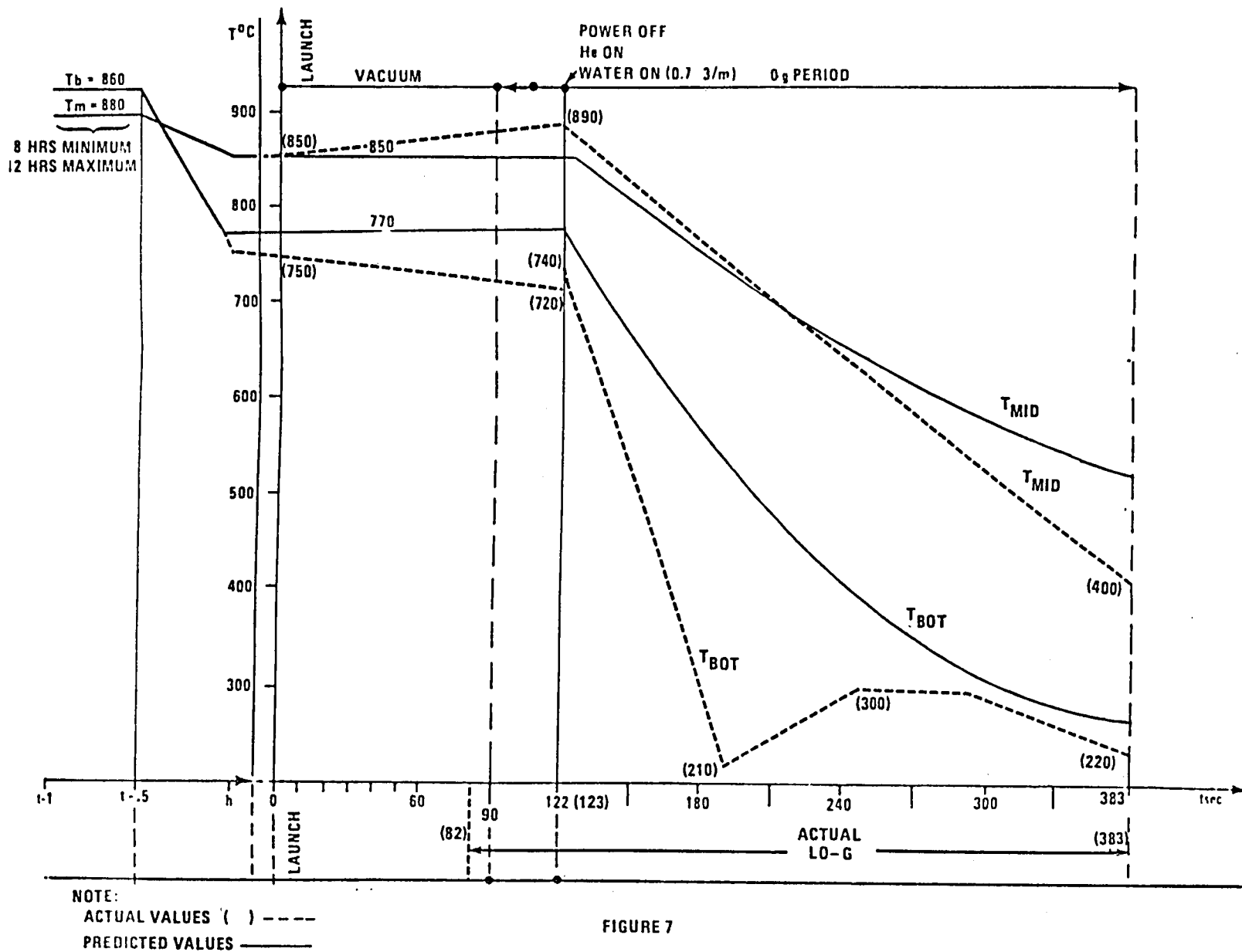
GRADIENT FREEZE
WATER FLOW DIAGRAM

FILL & VENT VALVE

GAS REGULATOR

1500 psi
17.6 m^3

GAS STORAGE TANK

TO NPV

LOW PR. RELIEF VALVE

GAS SUPPLY SOLENOID

GAS DEPLETION VALVE

VENT VALVE

BACK PR RELIEF VALVE

H_2O

GAS

H_2O

GAS

WATER SUPPLY & CATCH TANK ASSY

HOT HEATING ELEMENT

MIDDLE HEATING ELEMENT

COLD HEATING ELEMENT

FURNACE HEATEXCHANGER

SAMPLE PROCESSING CAVITY

CONTROL THERMO-COUPLES

GRAPHITE CORE

BAFFLE

GRADIENT FREEZE HEATING MODULE (TYP. 3 PLACES)

H_2O TO HEATING MODULE

H_2O FROM HEATING MODULE

#1
#2
#3

BY PASS MIXING VALVE

WATER HEATEXCHANGER & MANIFOLD

#1
#2
#3

H_2O SUPPLY SOLENOIDS

FLOW CONTROL METERING VALVES

II-13

Figure 8

This valve is not monitored by telemetry and its activation cannot be verified, although in ground testing at WSMR prior to launch, the valve opening was verified by listening. An examination of Figure 8 shows that it is possible to open the depletion valve and have no gas flow, due to the failure of the gas supply valve. Furthermore, a burned solenoid control wire was found in post-flight examination, due to the lacing of the wire to the non-propulsive vent (NPV) lines, which heated during gas dump. This problem had first been discovered during testing at GSFC and it was thought all wires had been rerouted and replaced. This one wire had been laced far up on the NPV line and, therefore, escaped detection.

The exact time of the water quench system failure cannot be determined because the bladder continued to drive water to the heat exchangers until the gas pressure on the bladder was equal to the pressure of the water it was trying to displace. However, since the minimum water bladder pressure occurred at T+194 seconds, the valve failure occurred earlier.

5.0 SCIENCE PAYLOAD INSTRUMENTATION

5.1 Low-G Accelerations

The SPAR IX low-g data was very noisy on the Y and Z axes, due to erratic wiper action on the accelerometer pickoffs, and consequently, only the X-axis data is of sufficient quality for any type of analytical work. The Y and Z-axis accelerometers were of a new type which had not been previously flown on SPAR and which, unfortunately, proved to be unsatisfactory in the SPAR application. Since the SPAR IX flight, these accelerometers have been replaced with the conventional type which had previously been used on SPAR with satisfactory results.

The X-axis Linear Acceleration Measurement (A002-MM) indicates that low-g entry was at about T+82 seconds and exit at about T+383 seconds, with the g levels during this period ranging from -0.10 to 0.17 x 10^{-4}g. Spikes in the +X (downrange North) direction occurred at T+102, 126, 171, and 232 seconds, and spikes in the -X direction occurred at T+127, 137, 186, 226, and 233 seconds. There is little correlation between these spikes and programmed payload events (Figure 3), but those occurring at T+126 and 127 may be attributed to the GPRF helium flow from the non-propulsive vents.

Attempts were made to reduce the Y and Z-axis data by using a smoothing technique whereby 8 data points, representing 8 seconds of data, were averaged and 1 data point formatted for every 8 second increment. Obviously, any data gained by such attempts is not truly representative of the flight situation and for this reason, no analyses of the Y and Z axes were made.

5.2   Pressures

Ambient pressure in the AMM (D01-MM) was 13.0 psia at lift-off, and 0.6 psia ($\sim$ 30 torr) at T+39 seconds. The SPL ambient pressure measuring device (D06-MM) was also located in the AMM, and was capable of monitoring from 30 to 10^{-4} torr in six ranges. It indicated that the ambient pressure continued to decrease until a minimum of 1.5 torr was reached at approximately T+403 seconds. From this point, the pressure rose rapidly to 30 torr at T+435 seconds and increased rapidly to reach 1.4 psia at T+434 seconds when the heat shield and drogue chute were deployed. From this point, the pressure increased steadily until it reached 12.1 psia when telemetry contact was lost at T+722 seconds.

5.3   Vibration and Shock

The X, Y, and Z vibration measurement data were not evaluated, since the vibration environment on SPAR has been well characterized from previous flight data.

Eight impact-o-graphs, capable of measuring shock levels from 150 to 750 G's, were mounted on the forward side of the GSFC Telemetry Module Extension (Figure 11). The impact-o-graph results are tabulated in Table I. The shock level experienced on impact was less than 150 G's, but the exact level cannot be determined.
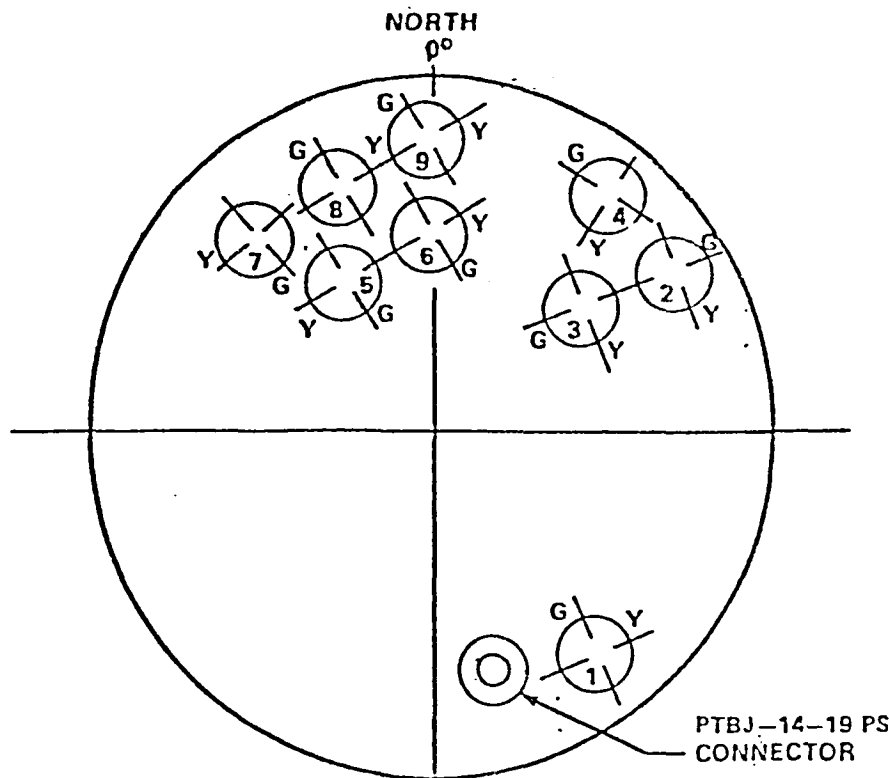
FIGURE 9 LOCATION OF THE IMPACT–O–GRAPHS ON THE FORWARD SIDE OF GSFC'S SPAR RATE CONTROL SYSTEM EXTENSION

IMPACT–O–GRAPH		SPRINGS AND BALLS FOUND UNSET AFTER LANDING		REMARKS
NO	Gs ± 5G	G (GREEN) AXIS	Y(YELLOW) AXIS	
1	750	NO	NO	
2	150	NO	NO	
3	700	NO	NO	
4				NO IMPACT–O–GRAPH WAS FLOWN IN THIS POSITION DUE TO CLEARANCE PROBLEM
5	200	NO	NO	
6	300	NO	NO	
7	600	NO	NO	
8	400	NO	NO	
9	500	NO	NO	

TABLE I LOCATION, NOMINAL G - LEVELS AND THE RESULTS ON SPAR IX

6.0 PAYLOAD RECOVERY

Due to the late-in-the-day launch time, the payload was not recovered until early the next day.

The payload landing/recovery site was located approximately 60 miles due North of the launch site in a sandy flat. The payload landed on its aft end and appeared to have gently tilted over in a Northeasterly direction coming to rest on a low dune. There was no visible external damage to the payload.

Upon arrival of the recovery team at the payload landing area, the electrical safing box was used to ensure the payload was de-energized. The parachute was disconnected from the payload and rolled-up. The payload was separated into two sections to minimize the hazard of lifting the heavy payload by hand. The separation plane was between the General Purpose Rocket Furnace and the Comparative Alloy Solidification Furnace (Experiment 76-36/2). The electrical cables bridging this interface were cut as planned, using cable cutters. The cargo helicopter was then positioned near the payload and the two sections and the parachute were loaded aboard the cargo helicopter, secured, and transported to the VAB without incident.

7.0   CONCLUSION

In conclusion, the flight data and post-flight analysis shows the launch, flight, and recovery of SPAR IX to have been successful.

Grumman Research and Development Center
Report RE-642

SPAR IX TECHNICAL REPORT FOR
EXPERIMENT 76-22 - DIRECTIONAL
SOLIDIFICATION OF MAGNETIC
COMPOSITES

by

Ron G. Pirich

Research and Development Center
Grumman Aerospace Corporation
Bethpage, New York 11714

Post-Flight Technical Report on Contract NAS8-32219

for

George C. Marshall Space Flight Center
National Aeronautics and Space Administration
Marshall Space Flight Center, Alabama   35812

June 1982

ABSTRACT

The role of gravity on Bridgman-Stockbarger directional solidification of eutectic Bi/MnBi has been studied in reduced gravity $(10^{-4}g_e)$ during the SPAR IX flight experiment and contrasted with an earlier SPAR VI flight experiment and normal gravity (one-g_e) investigations. The directional solidification of eutectic Bi/MnBi results in a low volume fraction, faceted/non-faceted aligned rod eutectic whose MnBi rod size, interrod spacing, thermal and magnetic properties are sensitive functions of solidification processing conditions.

Four samples were solidified during the 280-s, low gravity interval of the SPAR IX flight experiment at a growth velocity of 50 cm/h. This furnace velocity is near the maximum growth rate at which a planar furnace isotherm may be maintained. The morphology of the flight samples showed striking differences compared with identically processed normal gravity samples. As was observed during the SPAR VI experiment conducted at a lower solidification velocity of 30 cm/h, the MnBi rod diameter and interrod spacing distributions were significantly smaller, approximately 50%, for the low gravity samples. Accompanying the smaller MnBi rod diameters, the smallest ever achieved in the Mn-Bi system, was an increase in permanent magnet properties. For example, the intrinsic coercivity reached greater than 97% of the theoretical maximum, the largest ever observed in the Mn-Bi system. Also, in-situ thermal measurements during solidification showed a statistically significant lower solidification temperature in low gravity compared with one gravity with an increased interfacial undercooling of about 5.5°C. In addition, a lower volume fraction of dispersed MnBi, on the order of 8% was indicated for most of the low gravity interval of solidification. This suggests a change in the equilibrium diagram in the vicinity of the eutectic composition which is in qualitative agreement with the increased undercooling noted during low gravity solidification. Gravitationally induced convection in one-gravity is suggested to explain the morphological differences between one and low gravity solidification. As a result of this convection, an adjustment between interrod spacing, interfacial undercooling and effective interface velocity in the context of a Jackson-Hunt like model for eutectic growth is proposed.

CONTENTS

ILLUSTRATIONS

TABLES

INTRODUCTION

Considerable effort has focused on controlled directional solidification of binary eutectics in which the microstructure was related to conditions of solidification, for example growth rate and imposed thermal gradient (Ref. 1-5). More recently, convection that occurs when the fluid density depends on temperature and solute concentration has been investigated (Ref. 6 and 7). To assess the role of solidification conditions and gravitationally induced convective transport on the crystal growth of eutectic binary alloys, we have investigated the directional solidification of eutectic Bi/MnBi in a low gravity, $10^{-4}g_e$, environment and compared these results with previous low gravity (Ref. 8) and normal gravity, one-g_e, investigations.

The Bi/MnBi eutectic was chosen because its microstructure, when grown by Bridgman-Stockbarger directional solidification, results in an aligned ensemble of faceted rods of highly magnetic MnBi dispersed in a non-faceted Bi terminal solid solution. The morphological, thermal and magnetic properties have been shown (Ref. 9) to be affected by solidification variables and solidification orientation with respect to the direction of gravity in one-g_e (Ref. 10). For example, at lower growth velocities, V < 5 cm/h, deviation from the constant λ^2V = behavior expected for a Jackson-Hunt type model has been observed. In addition, a previous low gravity experiment (Ref. 8) conducted on SPAR flight VI at a moderately high growth velocity of V = 30 cm/h demonstrated that a reduction of gravity resulted in statistically smaller interrod spacings and rod diameters as well as a lower volume fraction of dispersed MnBi.

Unfortunately, nearly all eutectic growth models have neglected convection in the fluid and assumed a completely diffusion controlled solidification process. These models also assume nearly equiatomic volume fractions which make their application to a low volume fraction eutectic like Bi/MnBi somewhat uncertain.

In view of the lack of a theoretical model which adequately includes gravitationally induced convection and both low and one gravity experimental evidence in which significant gravity related effects have been observed, further low and one gravity studies were conducted. The objectives of this investigation included:

(1) Determining the effect of a reduction in gravity for eutectic samples grown at the highest solidification velocity possible while maintaining a planar furnace isotherm. The growth velocity selected, 50 cm/h, allowed comparison with the previous SPAR VI results. This high velocity also permitted most of each sample to be grown during the low gravity time interval of solidification thus making efficient use of the short duration, SPAR flight time.

(2) Determining at one-g_e, in the low growth velocity regime of ~ 3 cm/h, the nature of significant dependences of morphology, magnetic and thermal properties on gravity direction during solidification as well as a deviation from the constant $\lambda^2 V$ behavior anticipated from diffusion controlled growth.

EXPERIMENTAL PROCEDURE

SAMPLE PREPARATION & DIRECTIONAL SOLIDIFICATION PROCESSING

Eutectic Bi/MnBi ingots were prepared from commmercially pure Mn(99.9 w/o) and high purity Bi (99.999 w/o) using induction melting. Bulk composition and uniformity were determined using differential scanning calorimetry and chemical spectrophotometric absorbance. The eutectic composition was found to be 0.72 ± 0.03 w/o Mn (Ref. 11) resulting in a MnBi volume fraction of 3.18 ± 0.09%. Portions of these starting ingots were encapsulated in evacuated 0.4-cm inner diameter quartz ampoules and further instrumented with 0.004 cm bead diameter chromel-alumel thermocouples as described elsewhere (Ref. 7). The one-g_e experiments used one in-situ thermocouple located midway down the length of each 5-cm long sample. The one-g_e flight comparison and low gravity flight samples, four in each experiment, had two ampoules instrumented with two thermocouples each and two with four thermocouples.

Directional solidification processing was performed using the Bridgman-Stockbarger technique in furnace assemblies built by General Electric (Ref. 12). A single furnace assembly was used for the one-g_e investigations while an apparatus consisting of four symmetrically mounted furnace assemblies was used for the one-g_e flight comparison and low gravity flight experiments. The flight apparatus will be referred to as the ADSS, Automatic Directional Solidification System. For the ADSS, furnace assemblies mounted in opposition moved in unison and in the opposite direction with respect to the other furnace pair so that the total apparatus momentum was zero. The apparatus also underwent ground base vibration evaluation so as to monitor the level of external force produced by furnace movement at the location of each ampoule. These levels were found to be less than 10^{-5} g_e over a frequency range of 10 to 100 Hz.

The furnace assemblies produced a well controlled, unidirectional thermal gradient near the equilibrium solidification temperature of 265°C over the range of thermal gradients, G_L = 20 to 150°C/cm, and furnace velocities, V = 0.3 to 50 cm/h, investigated. The flight comparison and low gravity flight experiments were conducted at a nominal thermal gradient of G_L = 100°C/cm and furnace velocity, V = 50 cm/h.

Each cylindrical furnace assembly consisted of a nichrome heated hot zone, adiabatic or insulating zone in which solidification occurred and a fluid cooled copper cold zone. The furnace assembly translated along the stationary, cylindrical quartz sample ampoule. The temperature of the furnace hot zone and cold zone, furnace velocity as well as in-situ thermocouple temperatures were monitored during the solidification processing as described elsewhere (Ref. 10).

NORMAL GRAVITY (ONE-g_e) & FLIGHT ($10^{-4}g_e$) EXPERIMENTS

Four preflight experiments were conducted in the ADSS apparatus at the Marshall Space Flight Center in accordance with the SPAR IX flight timeline. One of these tests, the Pre-Installation Acceptance Test (or PIAT), was conducted with the ADSS unit separated from the other flight experiments, in ambient atmosphere and temperature, and in a vertical growth geometry with two furnace assemblies moving up (heater on top) and two moving down (heater on bottom). The purpose of the PIAT was to ensure that unidirectional solidification occurred at the SPAR IX growth conditions and to establish baseline criteria for the flight experiment. In the other three preflight experiments, two of which were unsuccessful due to apparatus malfunction (Ref. 13), the entire flight apparatus was placed in a sealed cannister filled with dry N_2 gas and run in conjunction with the other flight experiments. All conditions were identical with the flight experiment except for the presence of the vertical gravity vector. These tests, referred to as All-Systems-Tests, provided one-g_e samples to be used for direct comparison with the SPAR IX flight samples.

The SPAR IX flight experiment began with initiation of furnace heating 90 min before launch. At 5 min before launch, each in-situ thermocouple temperature was monitored and compared against the baseline criteria established following the PIAT test. After launch, directional solidification commenced 15 s after $10^{-4}g_e$ had been obtained and continued through the low gravity time interval of 280 s in which more than 80% of the sample was grown. Solidification terminated 580 s after launch and after the entire length of each eutectic sample had been solidified with 3.7 cm directionally solidified in low gravity.

Each SPAR IX comparison and flight sample was partitioned, as shown in Fig. 1, at four equally spaced fraction solidified locations by means of a
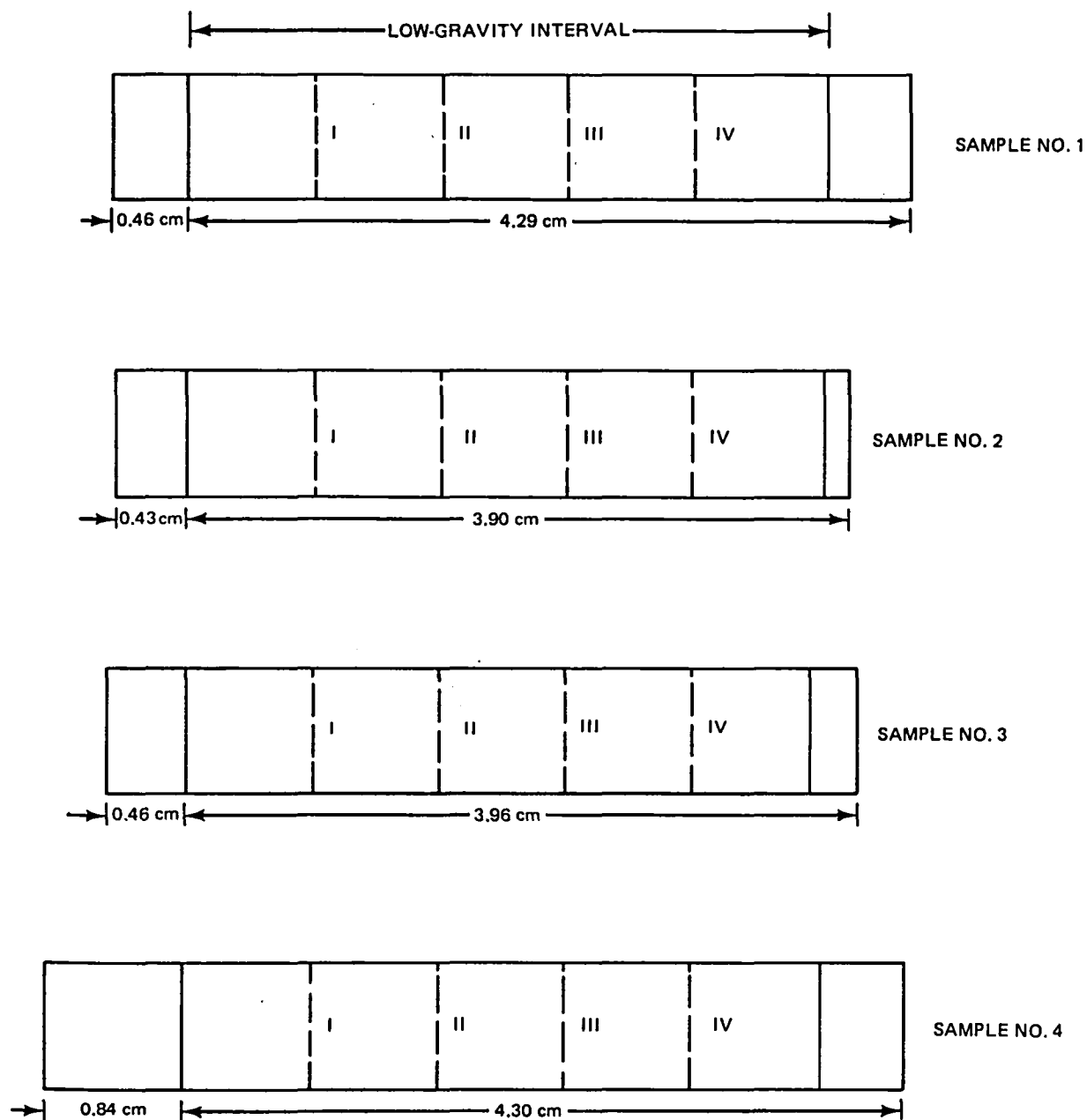
Fig. 1 Schematic Representation of Sample Partitioning of Low-g, Flight Samples. Quantitative Metallographic Data was Collected at Transverse Regions I Through IV.

1161-001(T)

diamond impregnated string saw. The string saw was used to avoid unnecessary stress during the sectioning process. Comparison between flight and ground base samples was made at the same fraction solidified location or fraction solidified interval for samples grown in the identical furnace assembly so as not to skew the results systematically.

In a separate series of normal gravity experiments, eutectic samples were grown up (heater on top) and down (heater on bottom) with respect to the gravity vector at furnace velocities of V = 0.5 and 0.3 cm/h in a thermal gradient of G_L = 100°C/cm. Samples were also grown at V = 3 cm/h with furnace hot zone temperatures of 450°C, corresponding to G_L = 100°C/cm, and 550°C corresponding to G_L = 150°C/cm. Each sample was instrumented with one in-situ thermocouple located half-way down the length of each sample and was directionally solidified in the single furnace assembly described earlier.

MORPHOLOGICAL, THERMAL & MAGNETIC PROPERTY ANALYSIS

Sample morphology, e.g., MnBi rod cross-sectional area and volume fraction, was determined from fifteen optical micrographs taken transverse to the solidification direction. Each surface was mechanically polished and lightly etched with a 10% solution of acetic acid in water. Several micrographs parallel to the solidification direction were also analyzed. Quantitative metallographic analysis was performed using a computer-aided Leitz particle analysis system. Mean rod diameters, <d>, and interrod spacings, <λ>, were determined by fitting the measured rod diameter and interrod spacing distributions with a Poisson distribution function and minimizing x^2, as is shown in Fig. 2 for a SPAR IX flight sample. The Poisson type distribution was selected as the most representative after careful evaluation of other common types of distributions such as Gaussian and Lorentzian. The Poisson curve fit to the observed distributions is quite good except at the lower rod or interrod sizes regardless of mean rod or interrod size. Even with this systematic deviation, the resulting x^2 were typically < 0.5.

In-situ thermal measurements as a function of elapsed solidification time were also investigated. For the SPAR IX experiment, temperature was measured once every second for each thermocouple. These measurements were transmitted via telemetry and recorded both in digital and analog format. The subsequent analog voltages were converted to temperature by assuming a quadratic
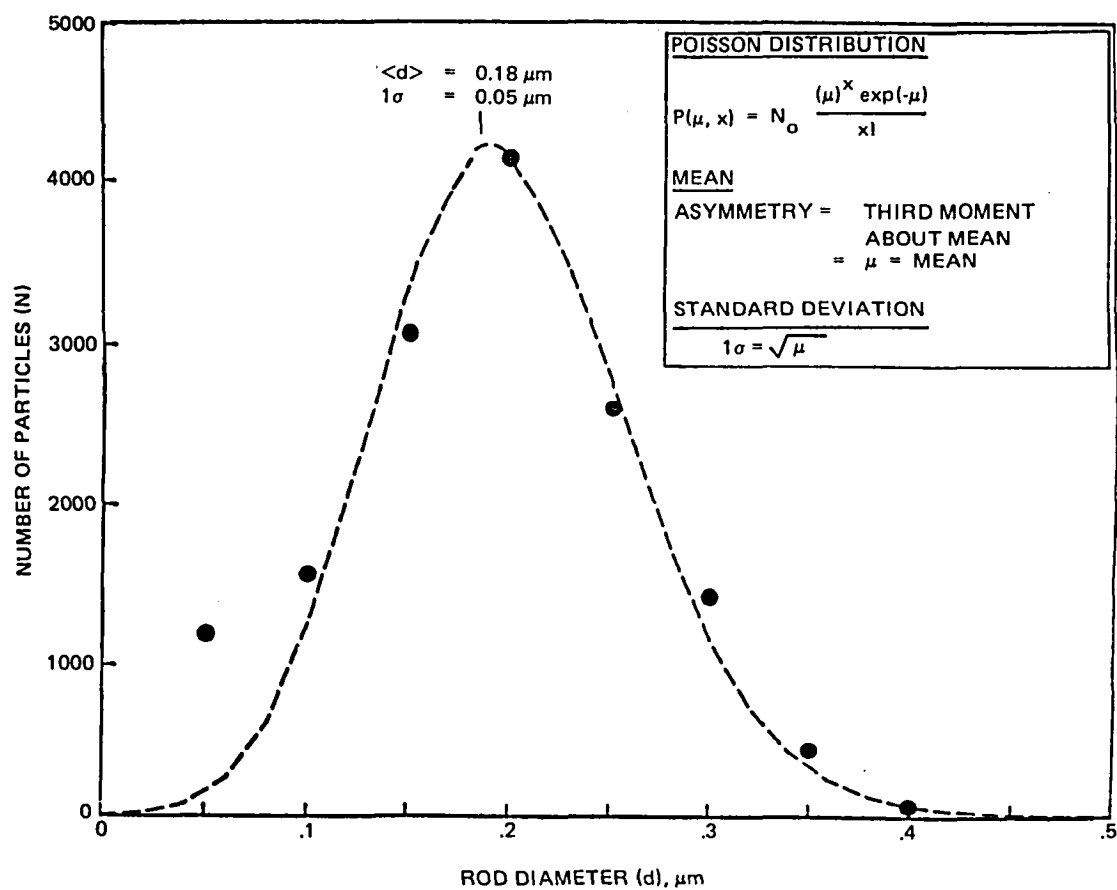
III-6

Fig. 2 Representative Poisson Curve Fit to Rod Diameter Distribution Obtained from all Transverse Regions Measured for Low-gravity Sample Grown in Furnace Assembly No. 1.

relationship between voltage and temperature. Due to a lack of point-to-point grounding in the ADSS apparatus, resolution of the in-situ thermocouple measurements was limited to ± 0.07 mV (± 1.9°C). For the remaining normal gravity experiments, in-situ thermocouple measurements were monitored using a Digital MINC II minicomputer system with a temperature resolution of ± 0.3°C.

Magnetic properties were determined from magnetization measurements of cylindrically shaped samples. Magnetization was measured parallel and perpendicular to the solidification direction at 290 and 77K in applied fields up to 280 kOe at the Francis Bitter National Magnet Laboratory using a low frequency vibrating sample magnetometer. A high frequency vibrating sample magnetometer was used at Grumman to measure magnetization as a function of angle with respect to the solidification direction. Applied·fields up to 17 kOe were used over a temperature range from 290K to the eutectic melting temperature of 538K. It was anticipated that because the equilibrium MnBi phase is ferromagnetic below 628K (Ref. 14 and 15), the magnetic properties could be used to measure the effect of solidification processing on MnBi rod size and alignment. For example, the resistance to demagnetization or intrinsic coercivity, $_mH_c$, of ferromagnetic materials controlled by crystal anisotropy should increase with decreasing particle size and approach the theoretical maximum (Ref. 16) when each particle contains only one magnetic domain (single domain behavior). It was observed, however, that directionally solidified Bi/MnBi with comparable morphologies differed dramatically in magnetic properties depending on solidification processing and heat treatment after solidification (Ref. 17 to 19). Another magnetic phase was identified as the origin of these differences. This new magnetic phase, termed the high coercivity or HC phase because of its unusually large intrinsic coercivity at cryogenic temperatures, was found to coexist with the equilibrium ferromagnetic phase in a magnetically additive form. With the applied magnetic field parallel to the solidification direction (easy axis of magnetization of the ferromagnetic, equilibrium phase), the hysteresis curves containing both magnetic phases were distinct and separate so that separation of each phase was straightforward (Ref. 17). Since the magnetization could be measured reproducibly to better than ±1% (±10^{-3}emu), the uncertainty in determining the amount of each magnetic phase and hence the volume fraction of MnBi varied from ±0.3% for 100% of the equilibrium phase to ±1.0% for a 30/70% combination of equilibrium/HC phases at the eutectic Bi/MnBi composition.

RESULTS

LOW GRAVITY EXPERIMENT - GENERAL OBSERVATIONS

On January 19, 1981 SPAR IX was successfully flown from White Sands Missle Range and the payload was recovered on the following day. The ampoules were removed at White Sands, returned to MSFC on January 22 and hand delivered to Grumman on February 19.

The Bi/MnBi eutectic samples in all ampoules were completely intact with their in-situ thermocouples still functioning properly. As is shown in Fig. 3, each ampoule had been fractured near the top lock-nut washer but the fractures were located sufficiently far away from the Bi/MnBi samples so that the samples were not affected. The fractures most probably occurred as a result of the buckling of the ADSS support baseplate at impact and after all samples had been completely solidified. Reinforcement of the baseplate structure is urged to prevent this problem in future SPAR flights.

Several photographs of the ampoules and removed samples, Fig. 4, were taken. In addition, x-ray radiographs of each ampoule before sample removal were made and revealed no unusual porosity or leakby of the melted eutectic samples as is shown in Fig. 5.

Evaluation of the furnace temperature and velocity data as well as in-situ thermocouple telemetry data showed a better resolution than was obtained during the earlier SPAR VI experiment. The telemetry results showed that all furnace velocities, within statistical limits of resolution, were the same during the flight experiment compared with the last of the All-Systems-Test-experiments. The furnace velocities varied from 48.1 ± 0.7 cm/h for furnace assemblies Nos. 2 and 4 to 49.3 ± 0.7 cm/h for furnace assemblies Nos. 1 and 3. For example, a comparison between the flight and comparison one-g_e furnace velocities for furnace assembly No. 1 during the period corresponding to low-g solidification is shown in Fig. 6.

The furnace thermocouples showed that a higher furnace hot zone temperature was attained during the low gravity flight experiment compared with the normal gravity All-Systems-Test experiment. For example, in furnace assembly No. 1, the furnace hot zone temperature was T_F = 464 ± 3°C in low gravity compared with T_F = 452 ± 3°C in normal gravity as seen in Table 1.
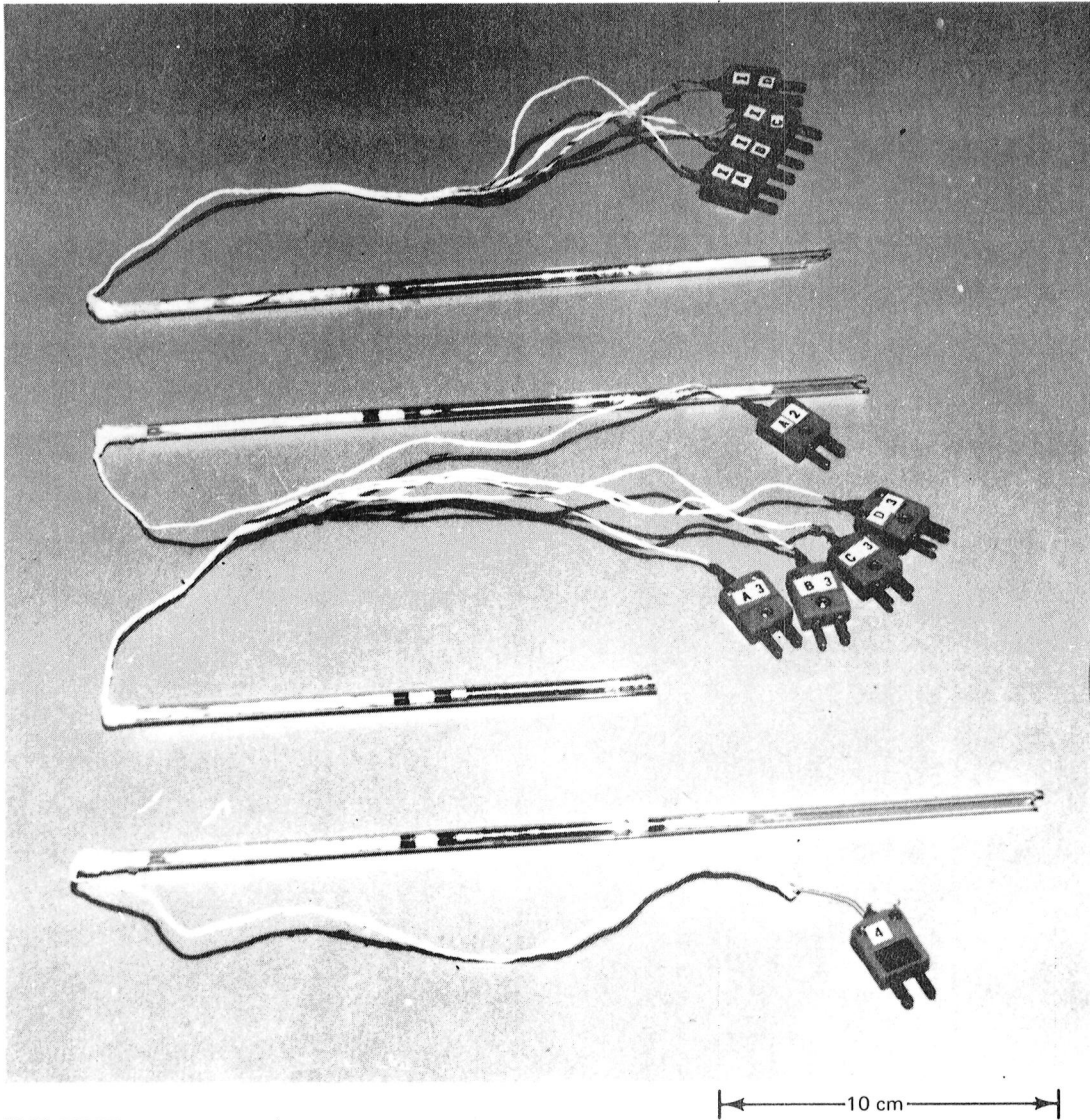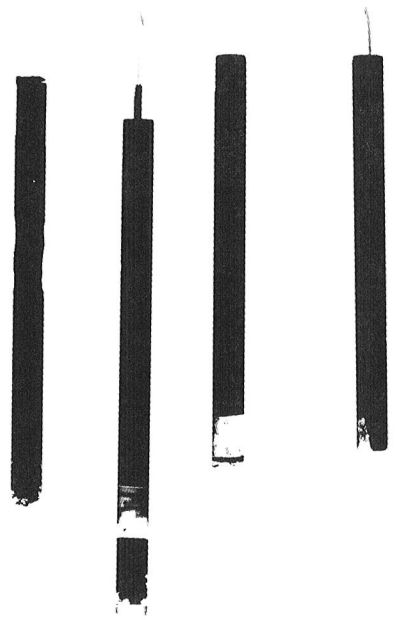
1161-003(T)

Fig. 3 SPAR IX Flight Ampoules as Received After the Low-Gravity Flight Experiment.
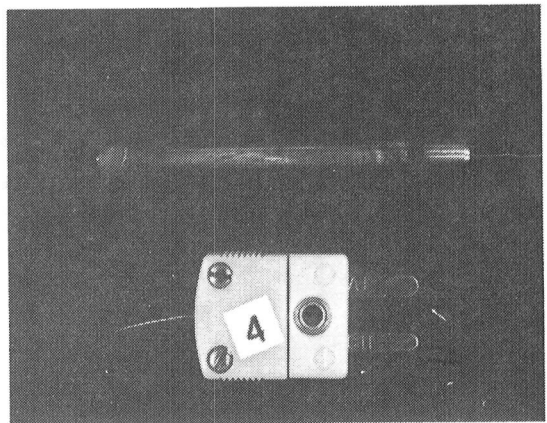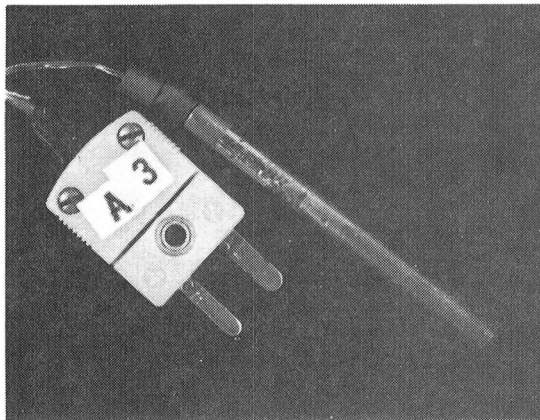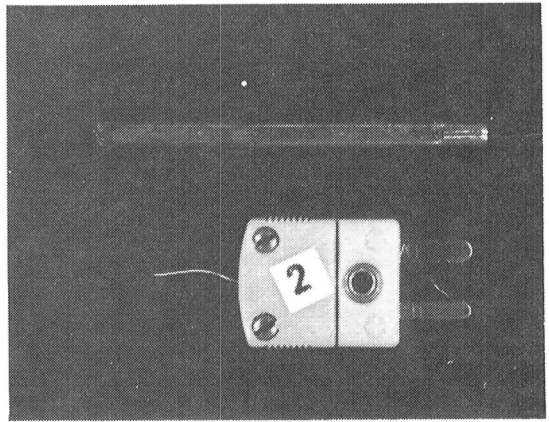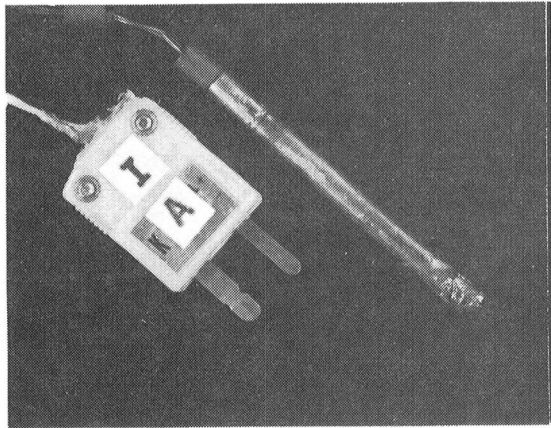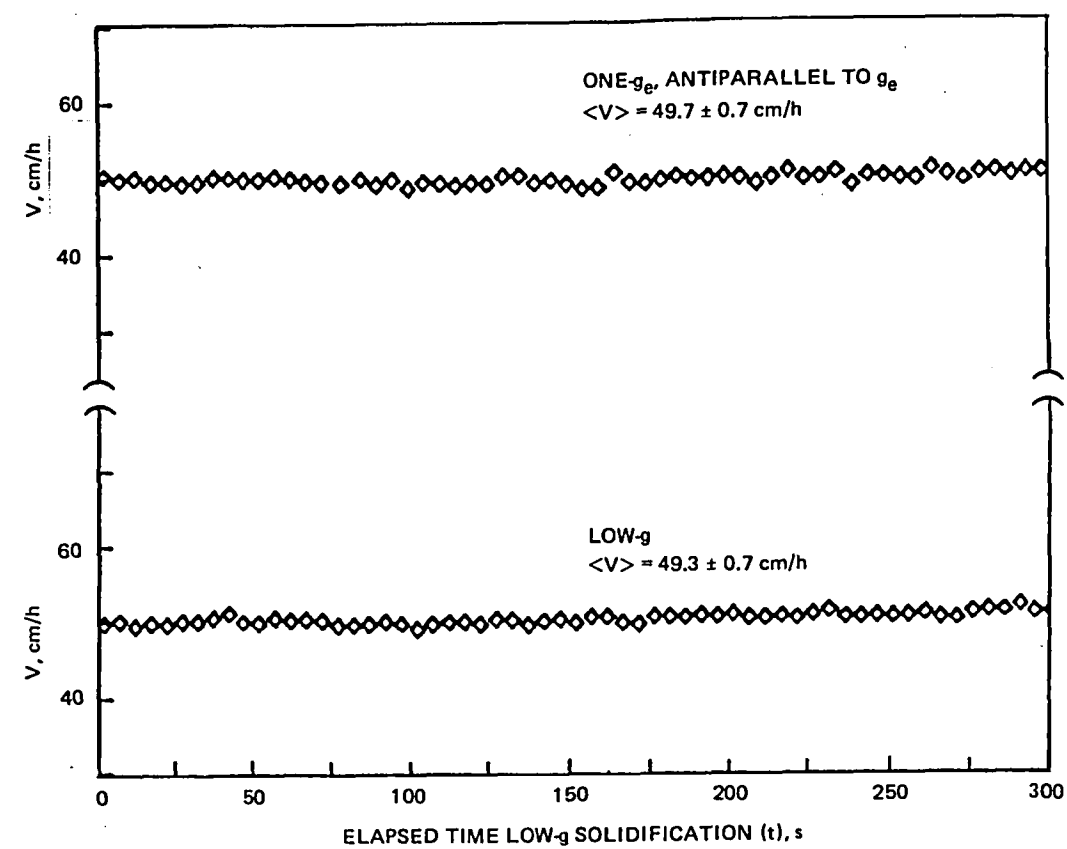
1161-004(T)

Fig. 4 Photographs of Flight Samples After Removal From Ampoules.

NO. 4   NO. 3   NO. 2   NO. 1

1161-005(T)

**Fig. 5 X-Ray Radiographs of Flight Samples Before
Removal from Ampoules.**

ONE-g_e, ANTIPARALLEL TO g_e
$<V> = 49.7 \pm 0.7$ cm/h

LOW-g
$<V> = 49.3 \pm 0.7$ cm/h

1161-006(T)

Fig. 6 Comparison of Furnace Velocities, for Furnace Assembly No. 1, Between the All-Systems-Test and Flight Experiment During the Time Interval Corresponding to Low-gravity Solidification.

| Experimental Measurement	All-Systems Test (One-g$_e$) Furnace Assembly No.				SPAR Flight (10^{-4} g) Furnace Assembly No.			
	1	2	3	4	1	2	3	4
Bulk starting composition, (w/o Mn)	0.72 ± 0.03	0.72 ± 0.03	0.71 ± 0.03	0.72 ± 0.03	0.72 ± 0.03	0.72 ± 0.03	0.73 b 0.03	0.71 ± 0.03
Furnace assembly velocity, x 10^{-3} cm/s	13.8 ± 0.3	13.4 ± 0.3	13.7 ± 0.3	13.5 ± 0.3	13.8 ± 0.3	13.5 ± 0.3	13.6 ± 0.3	13.4 ± 0.3
Furnace hot zone temperature, °C	452 ± 3	460 ± ·3	455 ± 3	453 ± 3	464 ± 3	472 ± 3	467 ± 3	465 ± 3
Furnace quench block temperature, °C	48 ± 1	47 ± 1	48 ± 1	48 ± 1	48 ± 1	48 ± 1	49 ± 1	47 ± 1
Solidification temperature, °C								
— Thermocouple No. A	265.3 ± 1.9	---	265.1 ± 1.8	---	259.7 ± 1.9	---	260.1 ± 2.0	---
— Thermocouple No. B	265.1 ± 1.8	265.2 ± 1.9	265.1 ± 1.9	265.3 ± 1.9	259.5 ± 1.8	258.8 ± 1.9	259.9 ± 1.9	260.5 ± 2.0
— Thermocouple No. C	265.5 ± 2.0	---	265.4 ± 2.1	---	259.9 ± 1.9	---	257.8 ± 1	---
— Thermocouple No. D	---	---	---	---	259.6 ± 1.9	---	261.0	---
Thermal gradient at interface/liquid, °C/cm								
— Thermocouple No. A	96.8 ± 2.9	---	97.6 ± 2.9	---	101.4 ± 3.0	---	101.9 ± 3.0	---
— Thermocouple No. B	97.0 ± 3.1	99.2 ± 2.9	99.0 ± 3.1	98.3 ± 2.9	102.1 ± 2.9	104.4 ± 3.1	102.6 ± 2.9	102.8 ± 2.8
— Thermocouple No. C	96.1 ± 2.7	---	98.1 ± 2.7	---	100.6 ± 2.7	---	103.1 ± 3.0	---
— Thermocouple No. D	---	---	---	---	102.4 ± 2.9	---	102.4 ± 2.7	---
Thermal gradient at interface/solid, °C/cm								
— Thermocouple No. A	161.5 ± 14.0	---	162.6 ± 13.5	---	180.3 ± 15.6	---	181.2 ± 15.5	---
— Thermocouple No. B	165.0 ± 13.1	164.4 ± 12.8	161.2 ± 14.2	166.0 ± 14.0	179.8 ± 15.0	186.1 ± 16.0	183.6 ± 15.7	182.8 ± 15.3
— Thermocouple No. C	168.1 ± 14.1	---	164.0 ± 13.6	---	177.7 ± 14.8	---	179.7 ± 15.2	---
— Thermocouple No. D	---	---	---	---	182.1 ± 15.4	---	180.2 ± 15.6	---
Mean MnBi interrod spacing (λ), μm								
— Region I	0.87 ± 0.15	0.92 ± 0.16	0.89 ± 0.15	0.91 ± 0.16	0.49 ± 0.09	0.47 ± 0.08	0.52 ± 0.10	0.47 ± 0.08
— Region II	0.92 ± 0.16	0.89 ± 0.15	0.91 ± 0.16	0.93 ± 0.16	0.46 ± 0.08	0.49 ± 0.08	0.47 ± 0.08	0.49 ± 0.09
— Region III	0.90 ± 0.16	0.86 ± 0.15	0.90 ± 0.16	0.89 ± 0.15	0.47 ± 0.08	0.51 ± 0.09	0.46 ± 0.08	0.46 ± 0.08
— Region IV	0.91 ± 0.16	0.93 ± 0.17	0.92 ± 0.17	0.89 ± 0.17	0.50 ± 0.09	0.46 ± 0.08	0.49 ± 0.09	0.50 ± 0.09
Mean MnBi rod diameter (D), μm								
— Region I	0.34 ± 0.09	0.32 ± 0.08	0.33 ± 0.08	0.31 ± 0.07	0.18 ± 0.05	0.19 ± 0.05	0.17 ± 0.15	0.20 ± 0.06
— Region II	0.31 ± 0.07	0.34 ± 0.08	0.31 ± 0.07	0.34 ± 0.09	0.20 ± 0.06	0.17 ± 0.05	0.21 ± 0.06	0.18 ± 0.05
— Region III	0.33 ± 0.08	0.31 ± 0.08	0.35 ± 0.09	0.32 ± 0.08	0.17 ± 0.05	0.18 ± 0.05	0.18 ± 0.05	0.17 ± 0.05
— Region IV	0.33 ± 0.08	0.33 ± 0.08	0.32 ± 0.08	0.32 ± 0.08	0.17 ± 0.05	0.20 ± 0.05	0.17 ± 0.05	0.17 ± 0.05
Global volume percent HC MnBi phase normalized to v/o MnBi, %	99.2 ± 1.0	99.4 ± 0.9	99.0 ± 1.1	99.1 ± 0.9	99.3 ± 0.9	99.4 ± 1.1	99.6 ± 0.8	99.2 ± 1.0
Global volume percent MnBi from magnetic property measurements, %	3.16 ± .10	3.18 ± .10	3.17 ± .10	3.17 ± .10	2.94 ± .10	2.91 ± .10	2.89 ± .10	2.94 ± .10
Resistance to demagnetization (intrinsic coercivity) for annealed, equilibrium MnBi magnetic phase, kOe	32.0 ± 0.5	31.5 ± 0.5	---	---	34.1 ± 0.5	34.0 ± 0.5	---	---

1161-021(T)

Table 1. Comparison of Thermal, Morphological & Magnetic Properties for Samples Grown During All-Systems-Test (One-g$_e$) & SPAR IX Flight (Low-g) Experiments. Comparison is Normalized to Low-g Time Interval Regions of Solidification.

Similar low gravity effects have been observed in other SPAR experiments (Ref. 20) and are believed to result from an absence of gravitationally driven convection as a heat transfer mechanism within the N_2 gas filled annular region between the nichrome wire furnace hot zone and ampoule. The absence of gravitationally assisted heat transfer out of this annular region gives rise to a higher furnace hot zone and thus a higher sample temperature. This results in a steeper thermal gradient in the liquid at the liquid-solid interface in low gravity compared with normal gravity (see Fig. 7). In fact, statistically higher thermal gradients were observed during low gravity and are presented in the next section of this report.

FLIGHT & NORMAL GRAVITY PROPERTY COMPARISON

Morphology

As was observed during the SPAR VI experiment, quantitative morphological measurements of MnBi rod diameter and interrod spacing distributions on all four eutectic samples directionally solidified during the low gravity time interval of the SPAR IX flight showed statistically significant differences with respect to the same fraction solidified regions for eutectic samples grown under identical furnace velocity conditions, in the same furnace assembly at normal gravity conditions. This behavior is illustrated at different regions for samples grown in furnace assembly No. 1 in Fig. 8 and at the same fraction solidified region for all four samples in Fig. 9. Specific data for all the samples are given in Table 1. A comparison of the mid low-gravity interval of solidification regions for both the SPAR VI and SPAR IX flight and one-g_e comparison experiments is illustrated in Fig. 10. Both the mean MnBi rod diameters and interrod spacings have smaller values for the low gravity compared with normal gravity solidified samples. The average for all SPAR IX samples, including all four transverse sections measured, showed the mean MnBi rod diameters and interrod spacings to be $\langle d \rangle$ = 0.18 ± 0.05 μm and $\langle \lambda \rangle$ = 0.48 ± 0.09 μm respectively for samples grown under low gravity conditions compared with $\langle d \rangle$ = 0.33 ± 0.08 μm and $\langle \lambda \rangle$ = 0.90 ± 0.16 μm for samples grown in normal gravity. The metallographically measured MnBi volume fraction of all low gravity flight samples, as determined from quantitative particle size analysis, was 2.92 ± 0.26% and was statistically equivalent to the normal gravity comparison samples value of 3.17 ± 0.41 %, even though less local inhomogeniety was noted in the low gravity solidified material.
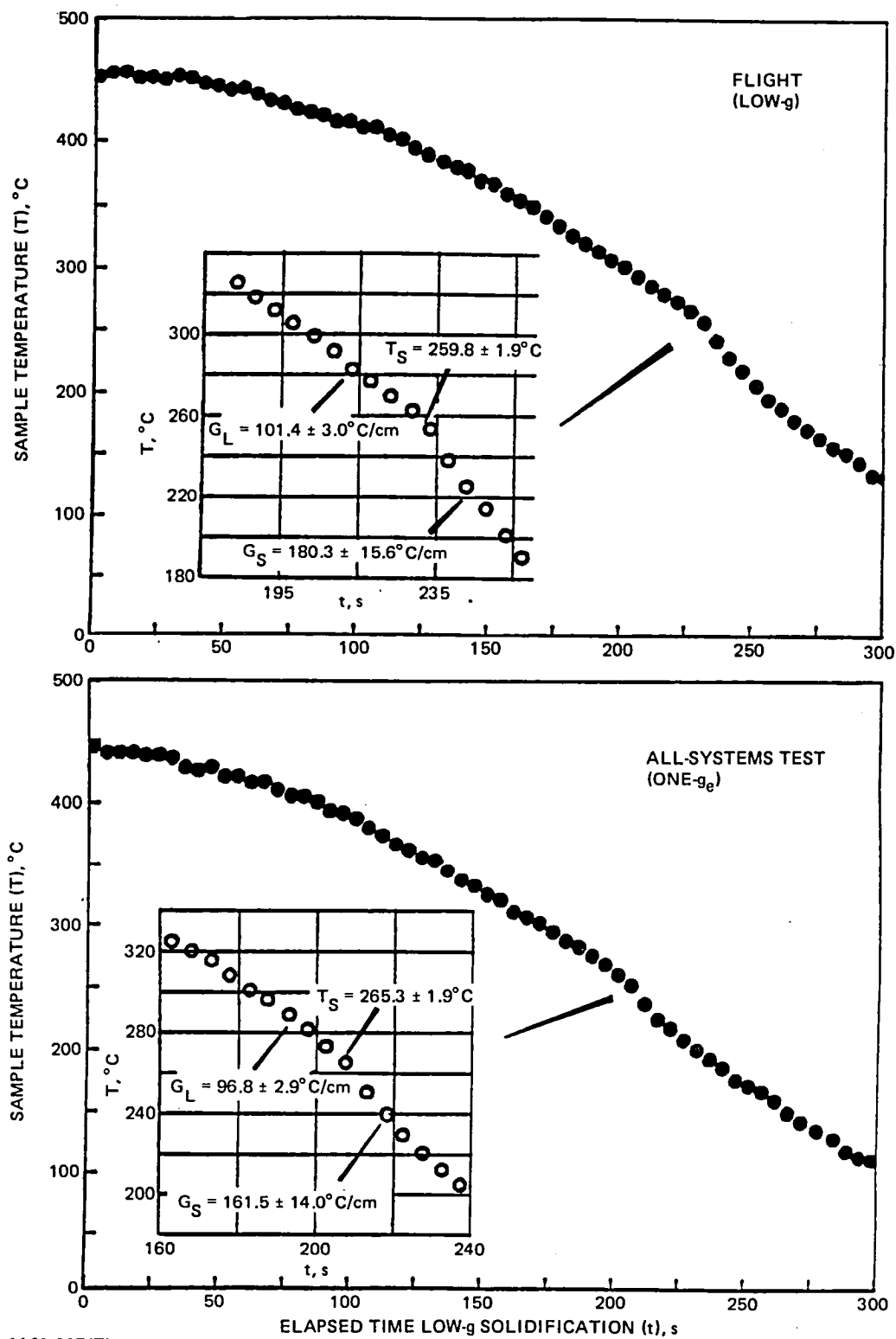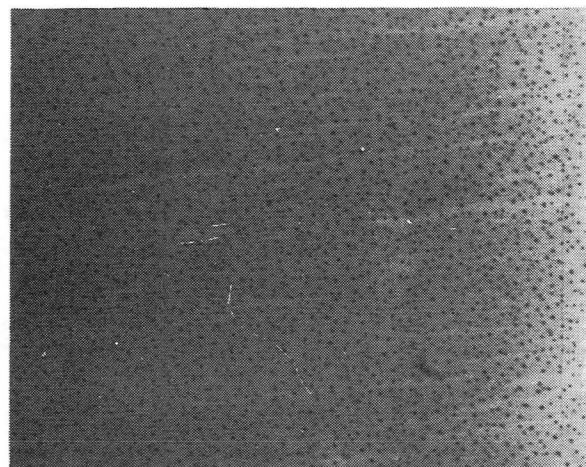
Fig. 7 Comparison of All-Systems-Test and Flight Sample Thermal Profiles Near the Solidification
Temperature for Samples Solidified in Furnace Assembly No. 1.

1161-007(T)

III-16

LOW-g

|←— 15 μm —→| |←— 15 μm —→| |←— 15 μm —→| |←— 15 μm —→|

ONE-g_e

REGION I   REGION II   REGION III   REGION IV
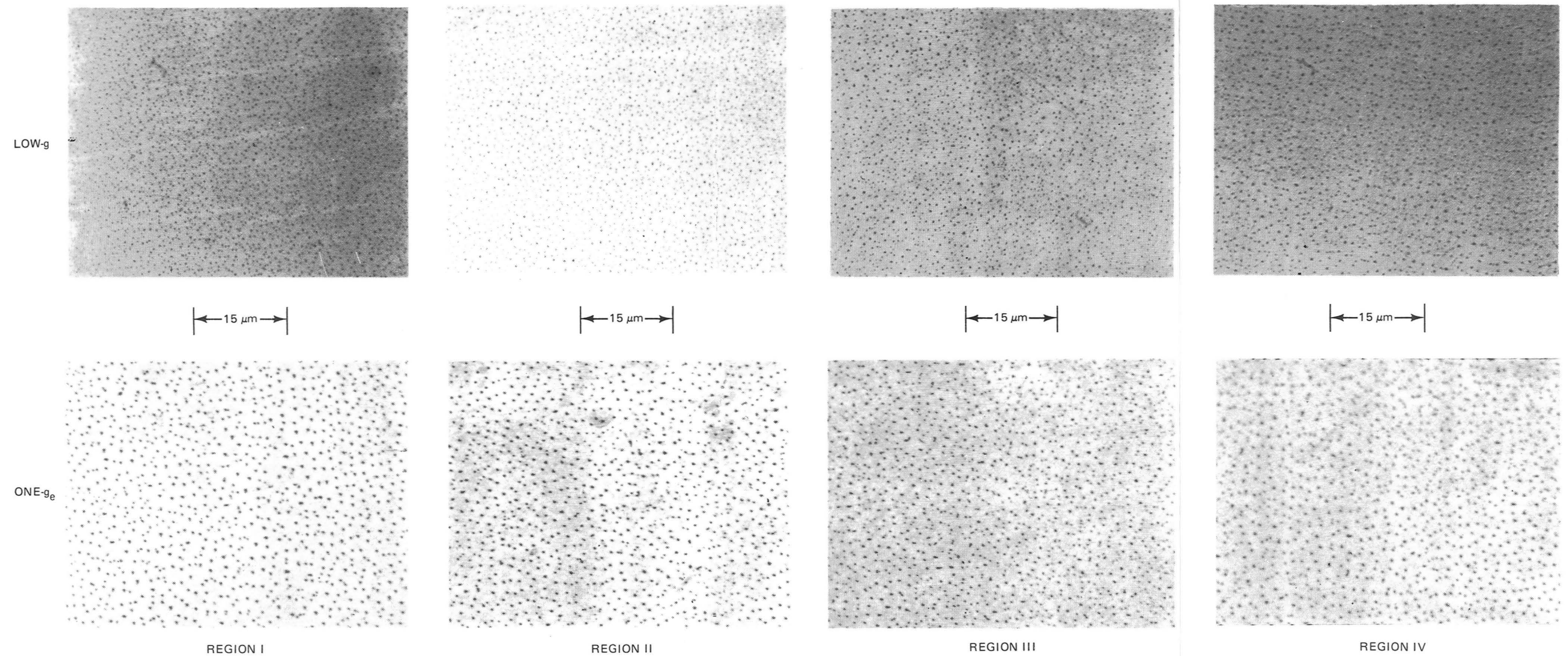
1161-008(T)

Fig. 8 Comparison of Flight and All-Systems-Test Micro-structures Transverse to Solidification Direction for Samples Processed in Furnace Assembly No. 1 as a Function of Fraction Solidified, i.e., Regions I Through IV.

LOW-g

ONE-g$_e$

|←— 15 μm —→| |←— 15 μm —→| |←— 15 μm —→| |←— 15 μm —→|
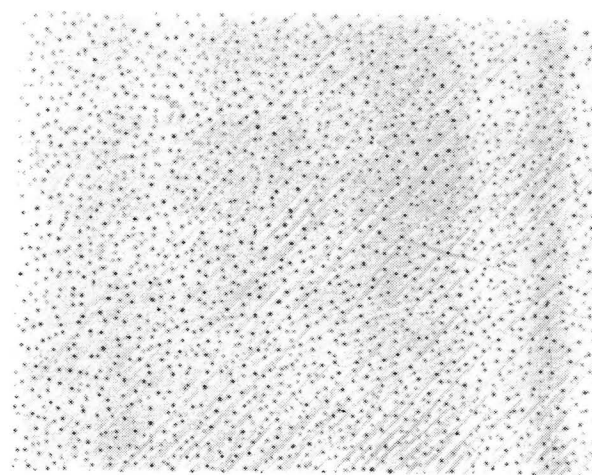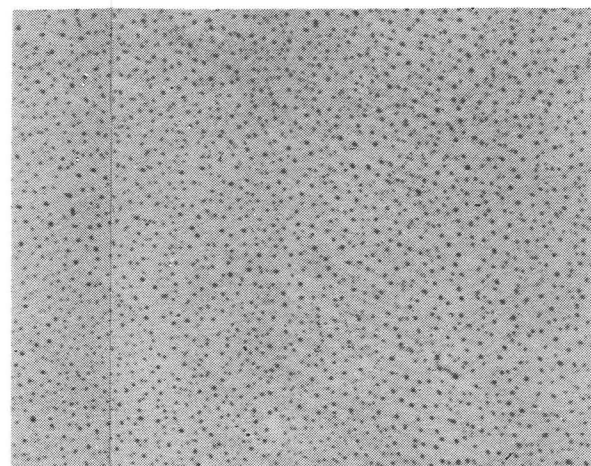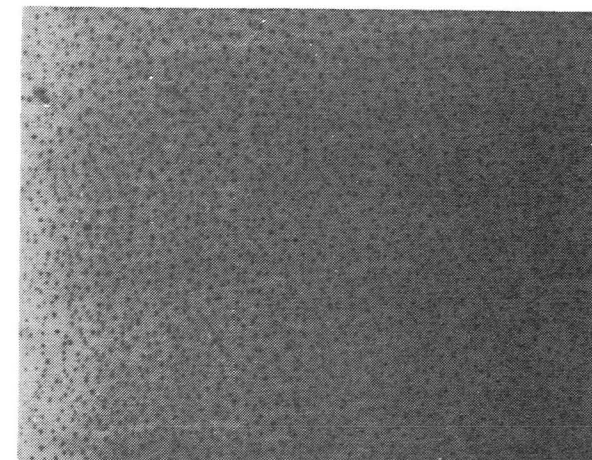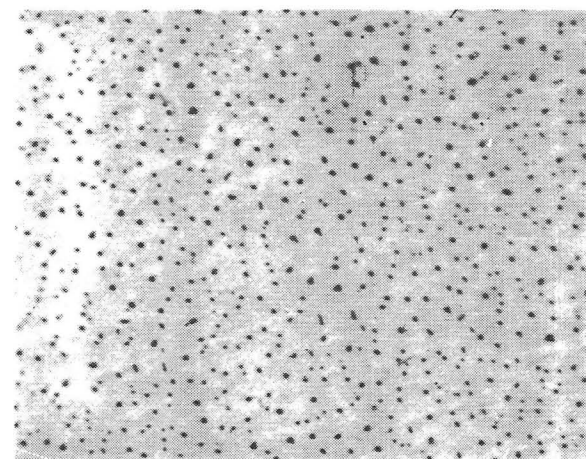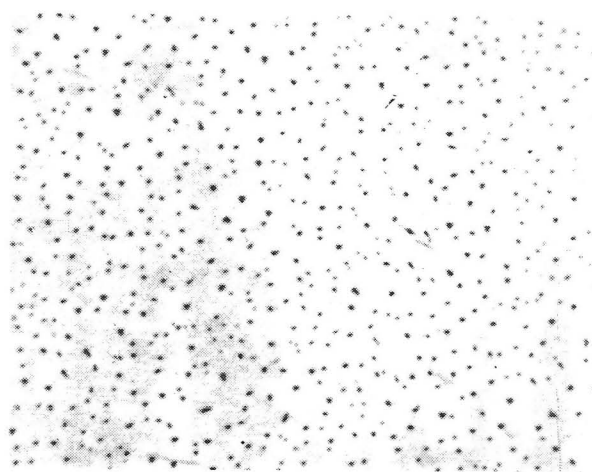
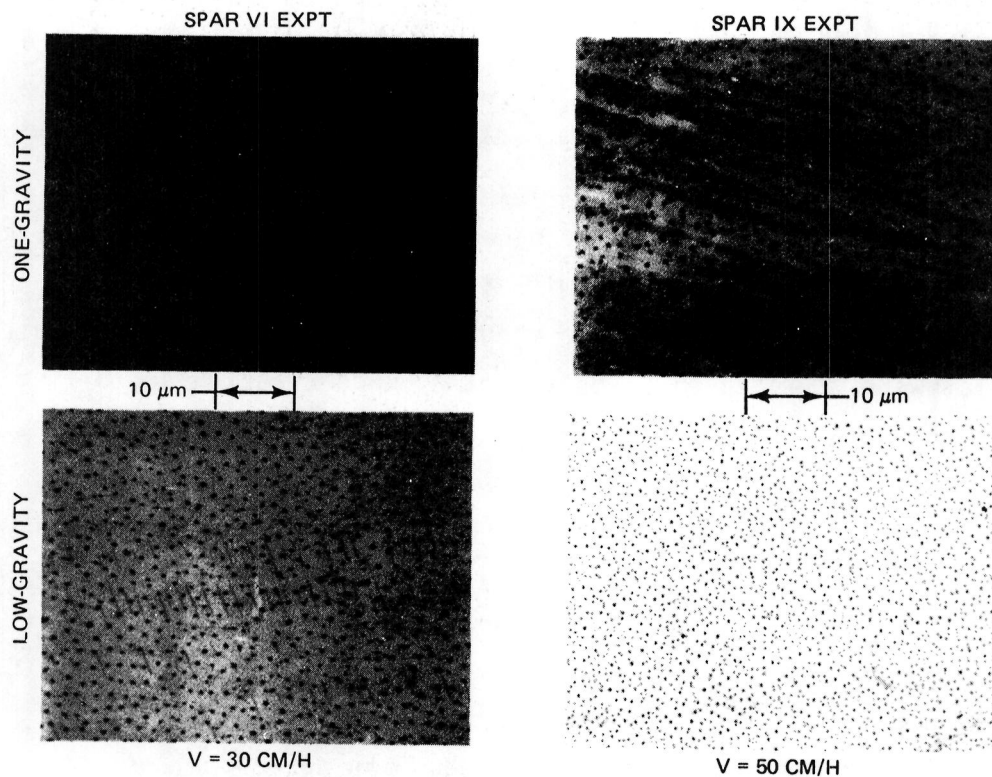SAMPLE NO. 1   SAMPLE NO. 2   SAMPLE NO. 3   SAMPLE NO. 4
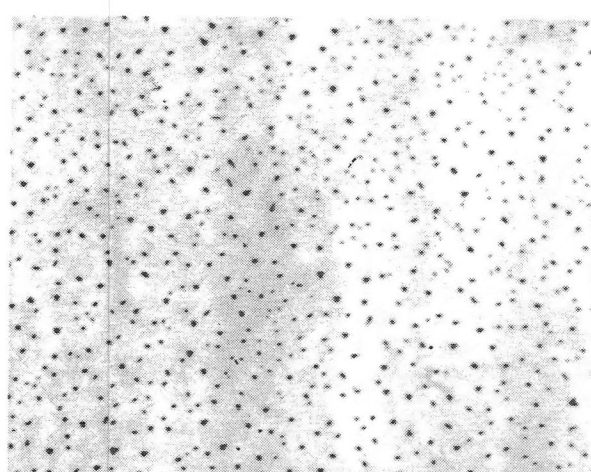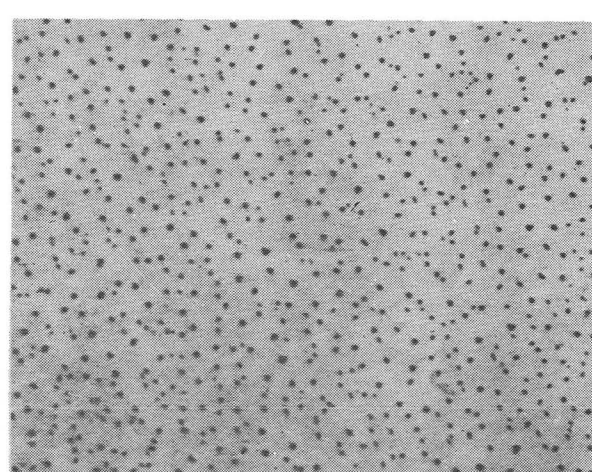
1161-009(T)

Fig. 9 Comparison of Flight and All-Systems-Test Microstructures Transverse to Solidification Direction at Same Fraction Solidified Location (Region I).
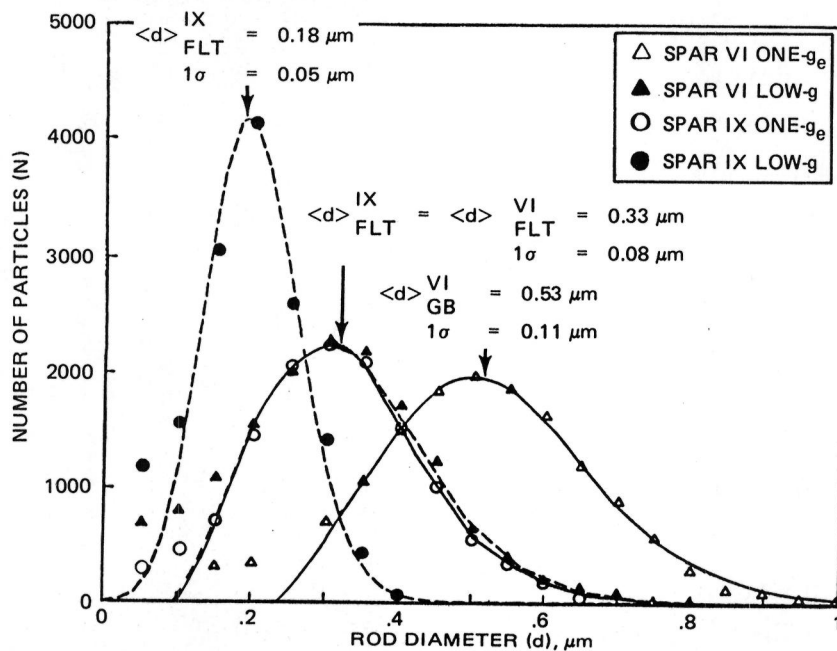
Fig. 10 **Microstructural and Quantitative Particle Size Analysis of the Mid Low-Gravity Interval of Solidification Regions for Both the SPAR VI and SPAR IX Flight and One-g_e All-Systems-Test Experiments for Samples Grown in Furnace Assembly No. 1.**

1161-010(T)

Thermal Properties

Comparison of thermal data through the solidification temperature was limited to one measurement per sample in furnace assemblies No. 2 and 4 respectively since each of these samples was instrumented with only one thermocouple per ampoule. In furnace assemblies No. 1 and 3, four temperature versus elapsed time intervals in the vicinity of the solidification temperature were recorded at equally spaced fraction solidified locations since each ampoule was instrumented with four thermocouples as described earlier. The temperature profiles of each sample instrumented with multiple thermocouples were statistically equivalent at each fraction solidified location as shown in Table 1 for both low and normal gravity conditions. However, in low gravity, the average solidification temperature was T_s = 259.8 ± 1.9°C compared with T_s = 265.3 ± 1.9°C obtained during normal gravity as shown in Fig. 7 for furnace assembly No. 1. This behavior was also observed in all other samples as well and is shown in Table 1. The lower solidification temperature observed in low gravity represents an increased interfacial undercooling of ΔT = 5.5 ± 2.7°C. Such an undercooling was suggested following the SPAR VI experiment but was not experimentally observed within statistical limits of resolution during that lower growth velocity experiment. In addition, as was noted earlier, because of a lack of gravity driven convection in the gas filled annular region between furnace heating elements and sample hot zone, a higher sample hot zone temperature which led to a higher thermal gradient was observed during low gravity compared with normal gravity processing and is illustrated in Fig. 7 and Table 1.

Magnetic Properties

The magnetic properties, magnetization as a function of applied field and temperature, of both the low gravity and normal gravity comparison samples were very similar in that both were dominated by the HC or high coercivity phase for samples measured in the as solidified and non-heat treated state. The magnetization data, as shown in Fig. 11 and Table 1, for samples grown in furnace assembly No. 1 show that both the low and normal gravity samples contain greater than 99 v/o HC phase. This behavior is shown in Fig. 11 by the strong paramagnetic behavior and lack of hysteresis at room temperature and the large coercive strength at 77K. Also shown in Fig. 11 is a higher magnetization in one-g_e compared with low-g per unit volume
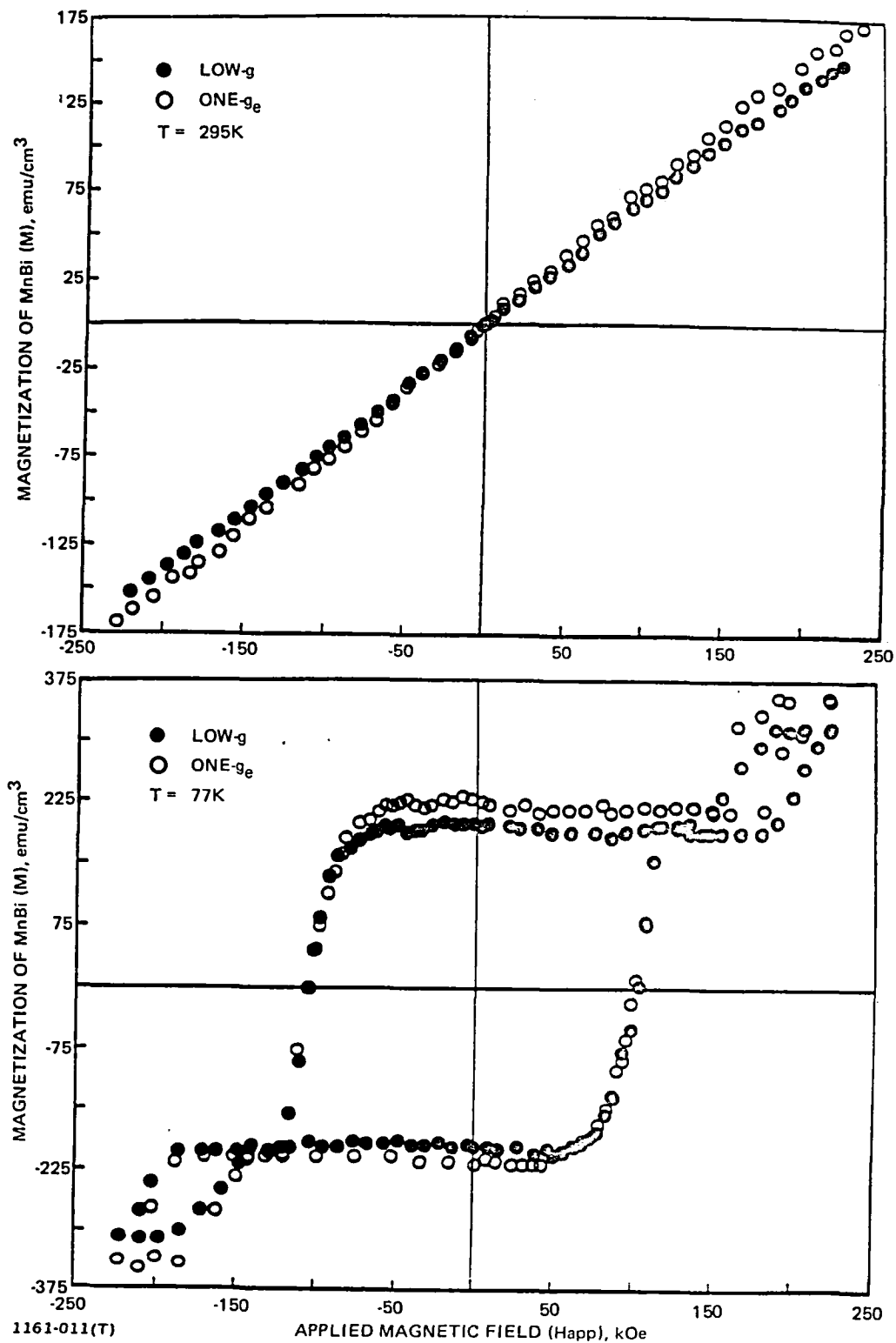
Fig. 11 Room (T = 295K) and Liquid Nitrogen (T = 77K) Temperature Hysteresis Curves for Both Flight and One-g_e Samples Grown in Furnace Assembly No. 1 and Partitioned at Region II. The Higher Magnetization Observed in One-g_e Indicates that a Lower Volume Fraction of MnBi is Formed in Low-Gravity.

normalized only to the MnBi phase. This behavior indicates that a lower volume fraction of MnBi forms in low-g. Selected low and normal gravity pieces, two each from samples grown in furnace assemblies No. 1 and 2, were isothermally heat treated and their room temperature hysteresis measured after each anneal cycle. Identical fraction solidified segments, corresponding to the middle of the low gravity interval of solidification, regions II and III (see Fig. 1), were heat treated together in the same apparatus and allowed to cool slowly, i.e., over several minutes, from the anneal temperature of 250°C. The first observation is that the v/o of dispersed MnBi, determined by deconvoluting the total magnetization into HC and equilibrium phase components and normalizing to the equivalent v/o of MnBi (Ref. 17), remained unchanged from the as solidified state, as shown in Fig. 12. This was supported by selected optical micrographs which revealed an absence of coarsening as seen in Fig. 13. The intrinsic coercivity and magnetic moment of all samples increased as a function of heat treatment as the HC phase transformed to the equilibrium MnBi ferromagnetic phase (Ref. 17). However, as is shown in Fig. 14, the intrinsic coercivity of the low gravity segments is consistently larger at any given percent transformed and reaches on the average 34 ± 0.5 kOe for a complete HC to equilibrium magnetic phase transformation compared to 32 ± 0.5 kOe for the normal gravity processed segments and 27.5 ± 0.5 kOe for the one-g_e SPAR VI samples. The 34 kOe is the largest intrinsic coercivity observed in the Mn-Bi system and the largest reported for any ferromagnetic material except for certain rare earth-cobalt systems. Also, the higher intrinsic coercivity obtained in the low gravity samples is consistent with the smaller mean rod diameters observed in the morphology studies (Ref. 16).

In addition, the magnetization of each low gravity and comparison normal gravity sample was measured as a function of fraction solidified and the resultant v/o of dispersed MnBi determined. Very uniform Mn concentration, corresponding to the nominal eutectic composition (Ref. 11), was observed over the entire fraction solidified intervals measured for all normal gravity processed samples. However, as shown in Fig. 15, a statistically significant lower volume fraction was observed for most of the low gravity interval of solidification, rising above the nominal eutectic composition near the termination of low gravity. This behavior is similar to that observed during the previous SPAR VI experiment (Ref. 8).
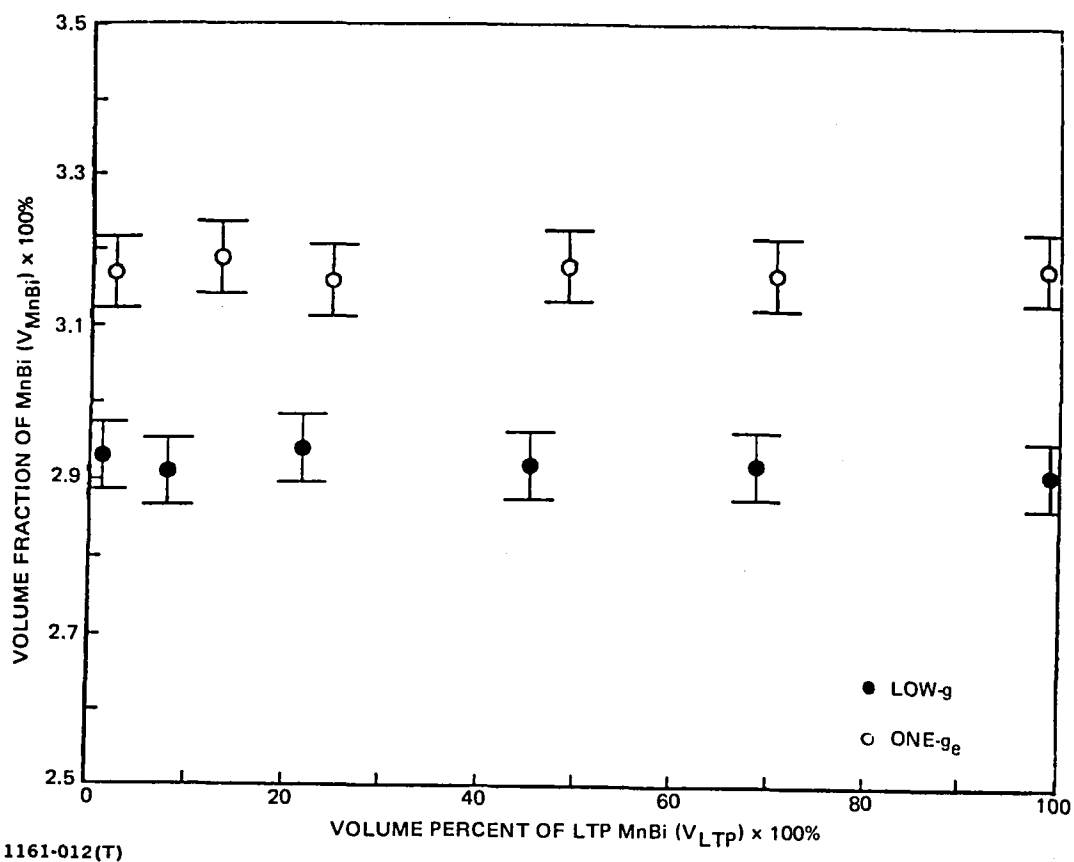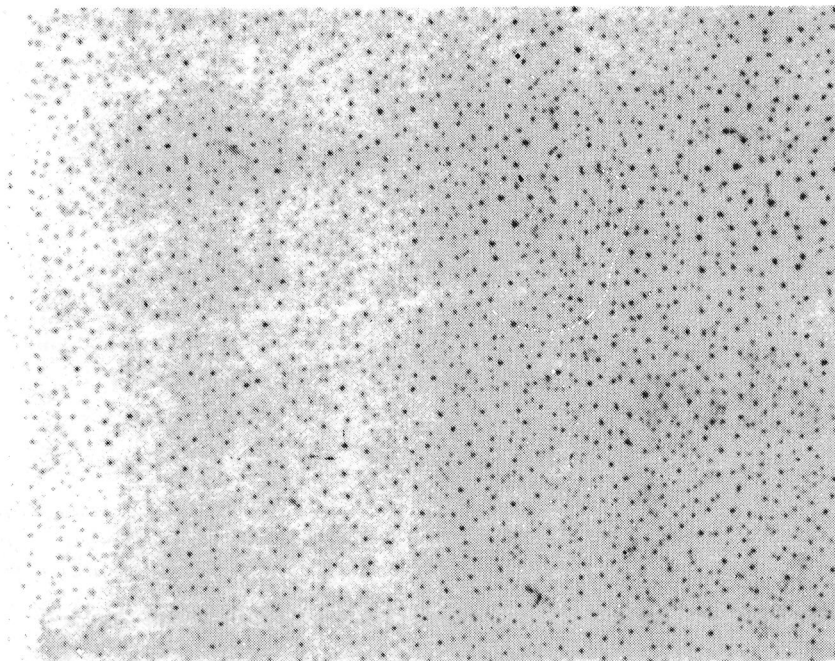
1161-012(T)

Fig. 12 Volume Fraction of Dispersed MnBi as a Function of Percent Ferromagnetic Equilibrium
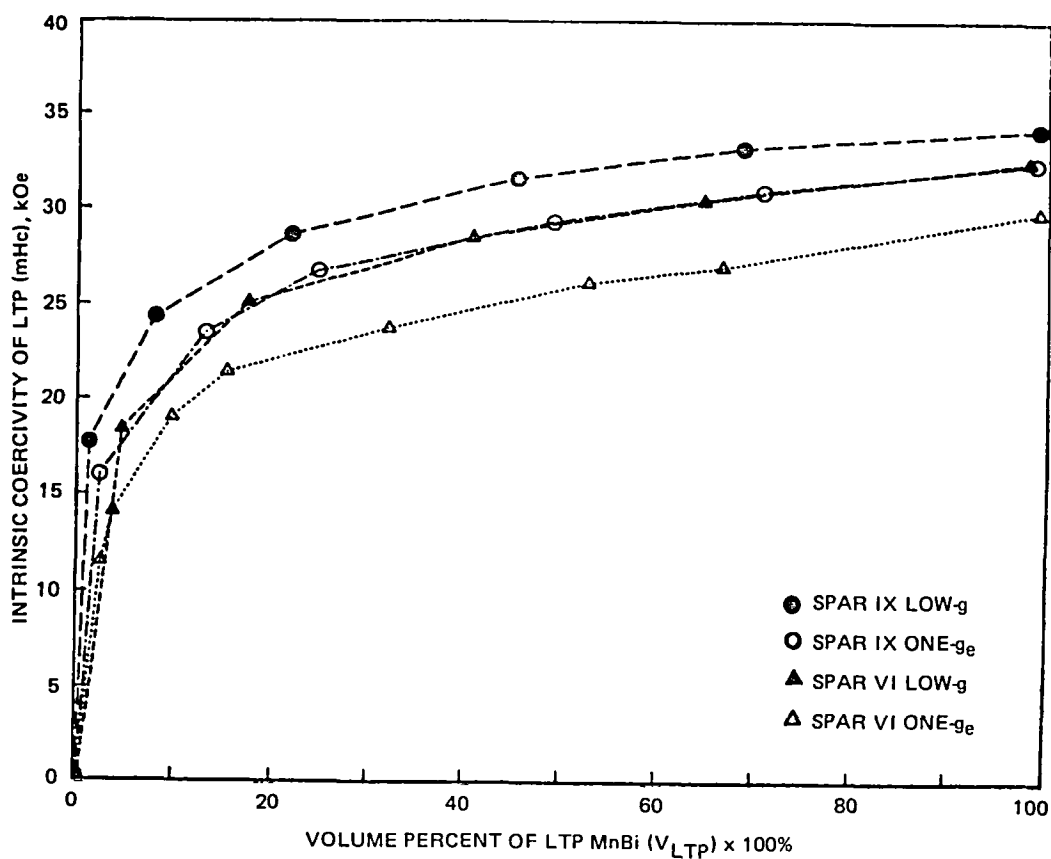(LTP) MnBi Phase Transformed During Heat Treatment Anneal at 250°C.
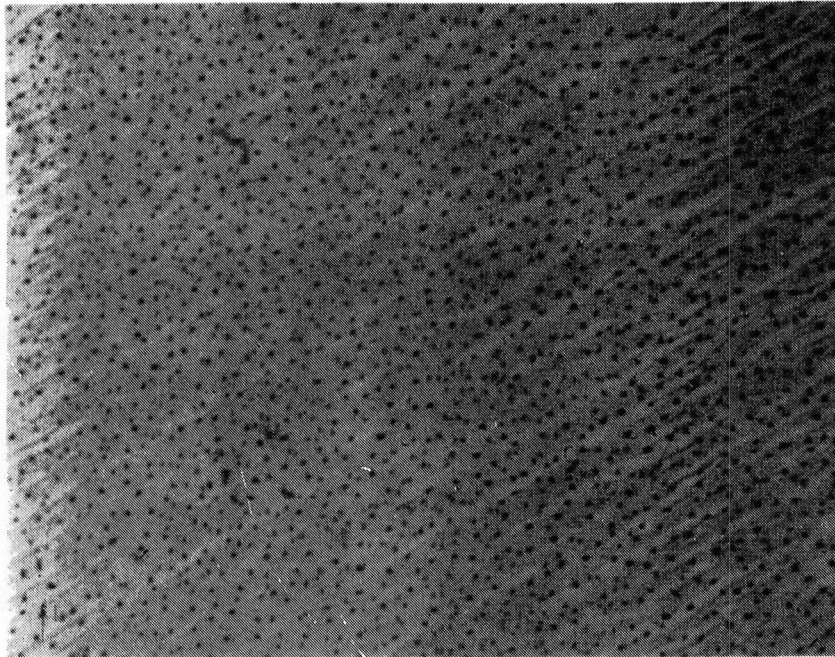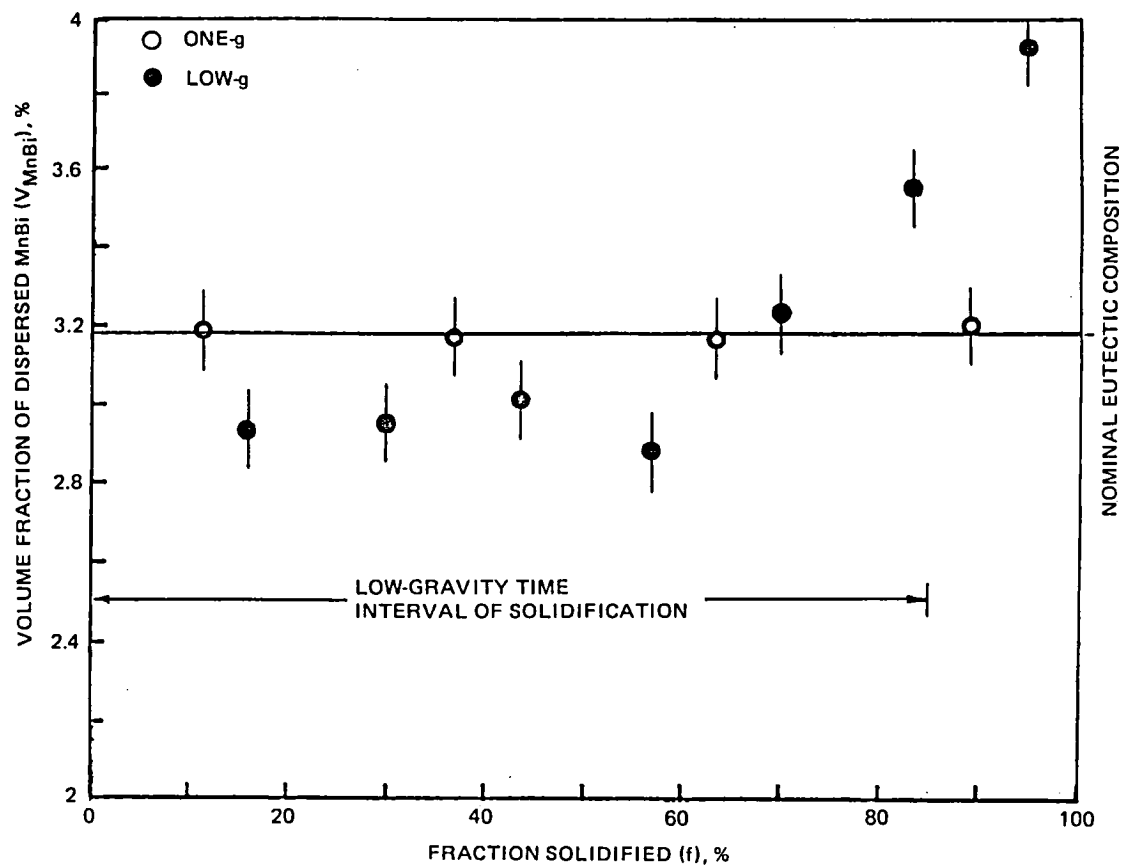
AS-GROWN

|◄——— 15 μm ———►|

HEAT-TREATED

1161-013(T)

Fig. 13 Comparison of Flight, Low-g Morphology for Sample No. 2, Region II in the As-grown State and After Heat-treatment at 250°C for 24 h.

1161-014(T)

Fig. 14 Effect of Isothermal Heat-treat Anneal on Intrinsic Coercivity of SPAR IX and SPAR VI Low and One-gravity Samples. Higher Intrinsic Coercivity at any Given Percent Transformed, Ferromagnetic LTP MnBi Component for the Flight Samples Suggests Smaller Rod Diameter Distribution for Samples Solidified in Low-gravity.

**Fig. 15** Comparison of Volume Fraction of MnBi as a Function of Sample Length (Fraction) Solidified for Flight and All-Systems-Test Samples Grown in Furnace Assembly No. 1. Lower Volume Fraction for Low-g Compared With One-g_e Solidification and Increase Near End of Low-gravity Time Suggests Bi Rich, Off-eutectic Solidification in Low-g. Note that Total Bulk Composition of Both Samples is the Same.

1161-015(T)

III-26

NORMAL GRAVITY OBSERVATIONS

We have observed, in previous normal gravity studies, a deviation from the constant $\lambda^2 V$ behavior anticipated for regular eutectics (Ref. 21). Accompanying this deviation was a change in rod cross-section morphology. As shown in Fig. 16, the rod cross-sections were degenerate faceted and irregular for V < 3 cm/h and more circular-like and regular for higher growth velocities, V > 5 cm/h. Also, increasing inhomogeniety occurred with decreasing solidification velocity, i.e., the percent standard deviation, $\sigma_\lambda/\langle\lambda\rangle$, increased from 15% at V = 50 cm/h to 30% at V = 0.5 cm/h as seen in Fig. 17.

Noting this unanticipated behavior in the the low solidification velocity regime, even lower growth velocities were investigated. At solidification velocities, V = 0.3 cm/h, a breakdown in cooperative growth was observed, as shown in Fig. 18, for growth antiparallel to the gravity vector. Even though the furnace isotherms remained linear, an apparent morphological instability was encountered which resulted in non-aligned, irregularly dispersed MnBi fibers. It has been suggested (Ref. 22) that at low growth velocities, a long wavelength convective-like instability may occur for solute concentrations which exceed some critical value determined from the boundary conditions at the liquid-solid interface. This type of instability is different from the familiar morphological instability associated with constitutional supercooling criteria which is found at much shorter instability wavelengths. Unfortunately, the application of such a model to eutectic growth has not yet been attempted, but this model may offer a possible qualitative description of the decoupling behavior we have observed.

Additionally, in view of the thermal instability model postulated to explain the SPAR VI results (Ref. 8), i.e., gravitationally induced thermal fluctuations which results in unsteady interface motion and larger rod diameters and interrod spacings in normal gravity, the thermal stability as a function of interface curvature was studied. For a linear furnace isotherm in which the furnace hot zone temperature was maintained less than 500°C, no apparent thermal instability was observed within the low frequency range of our experimental technique, i.e., temperature measurements every four seconds. For furnace hot zone temperatures $T_F > 550°C$, the solidification interface may have been displaced a sufficient distance towards the furnace
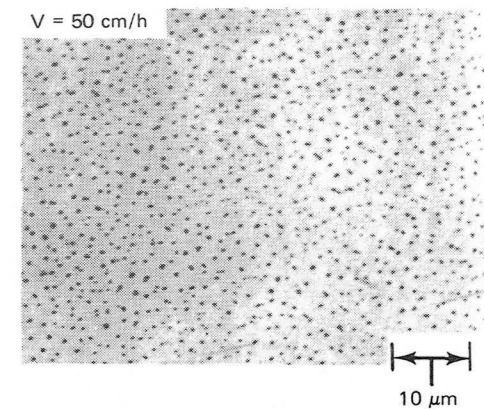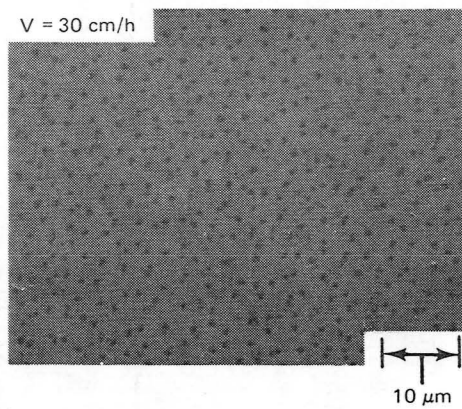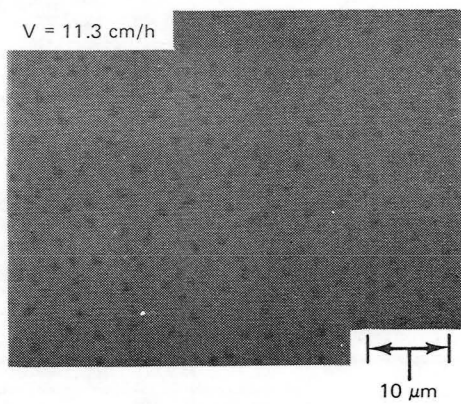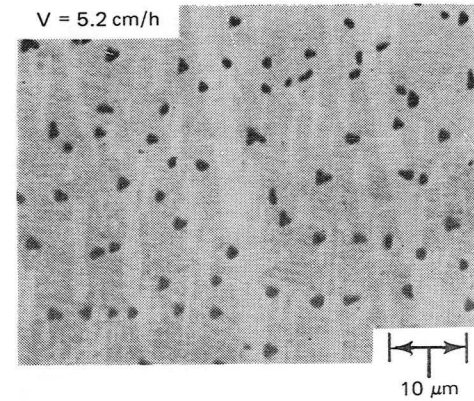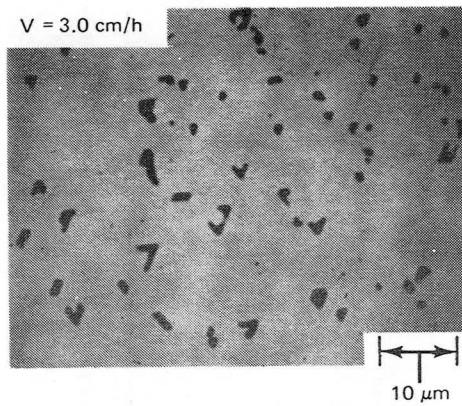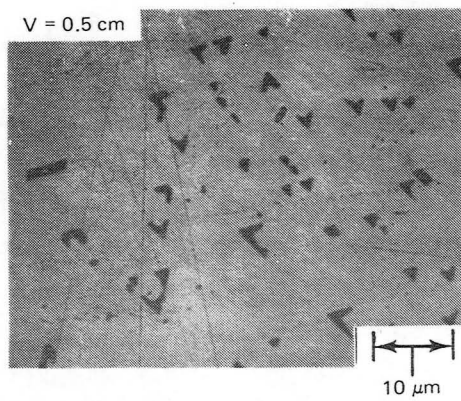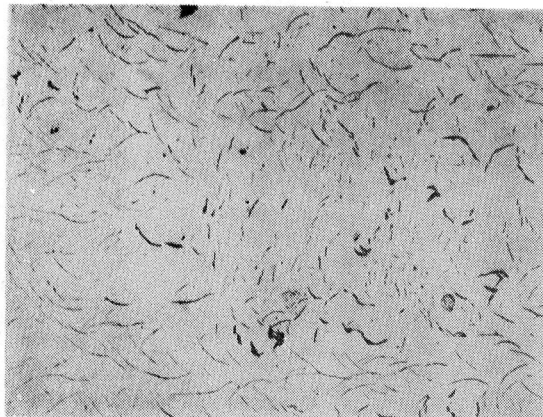
1161-016(T)

Fig. 16 Effect of Solidification Velocity on Dispersed MnBi Rod Size and Shape Transverse to Solidification Direction in One-g_e.
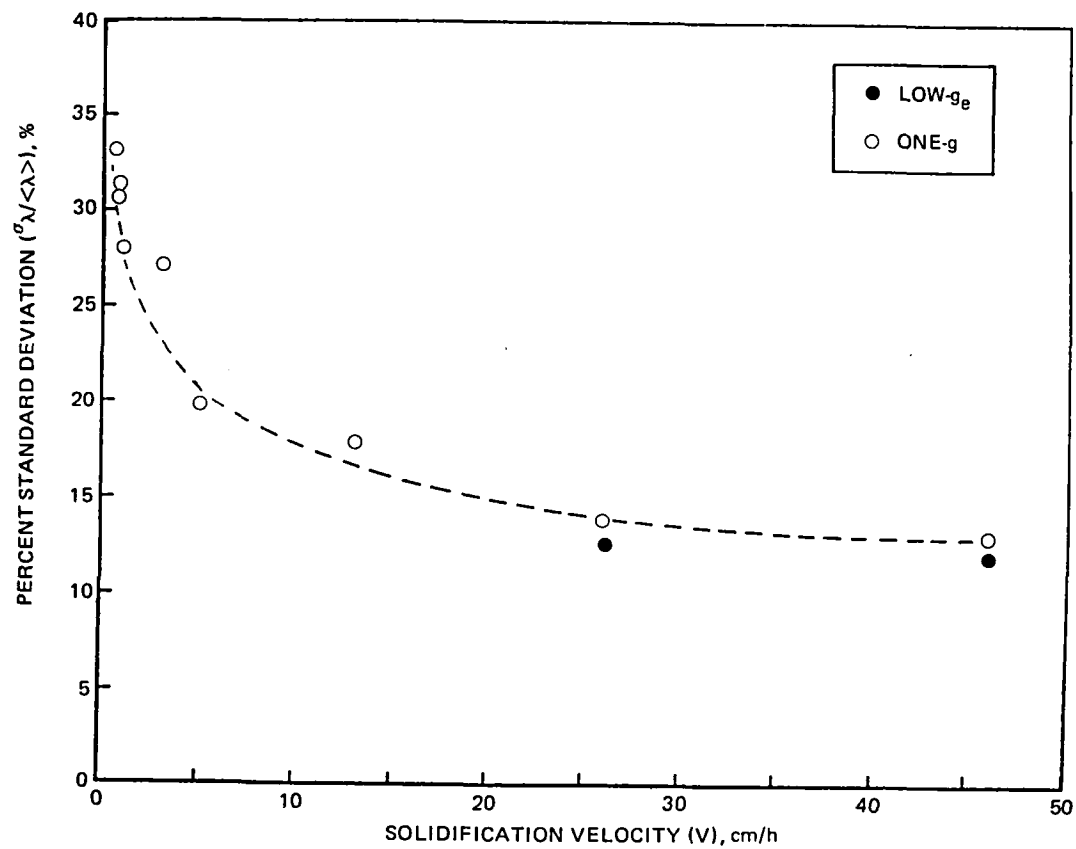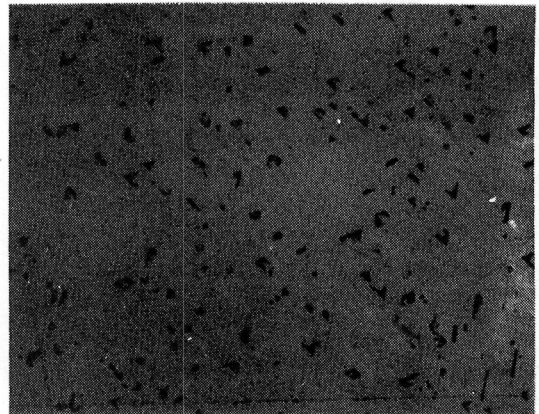
1161-017(T)

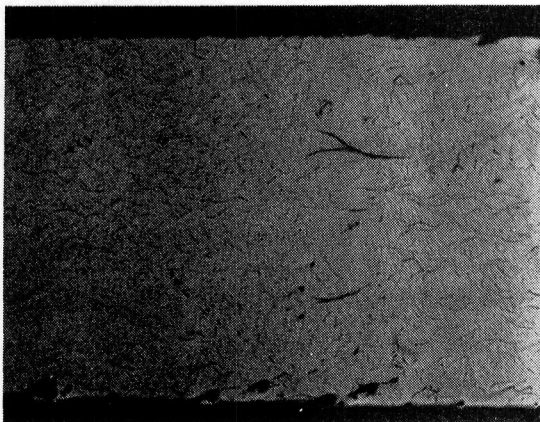Fig. 17 Percent Standard Deviation of Mean MnBi Rod Diameter as a Function of Solidification (Furnace Growth) Velocity as Determined from Quantitative Particle Size Analysis.
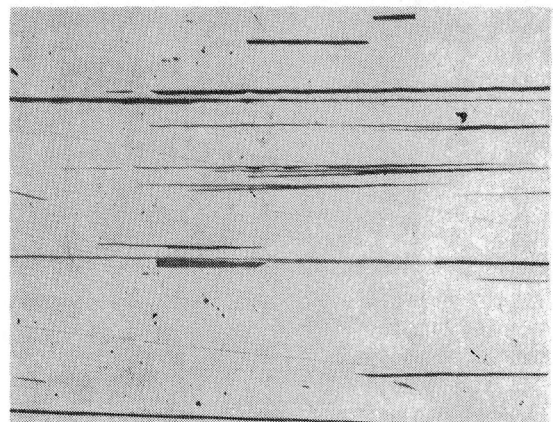
500 μm |→←→|

50 μm |→←→|

1000 μm |→←→|

100 μm |→←→|

V = 0.3 cm/h

V = 0.5 cm/h

1161-018(T)

Fig. 18 Morphological Instability Observed at $V < 0.5$ cm/h in One-g_e for Growth Antiparallel to g_e at the Eutectic Composition.

cold zone (Ref. 23) so that, presumably, interface curvature occurred. No interface demarkation experiments have yet been performed to verify this assumption. The resulting microstructures reveal, Fig. 19, a banding-like structure both transverse and longitudinal to the solidification direction with the longitudinal bands exhibiting appreciable curvature. In addition to the microstructural banding, statistically significant thermal fluctuations were observed. As an example, in Fig. 20, the measured deviations from the mean liquid temperature near the liquid-solid interface showed a slowly varying periodicity for a eutectic sample grown antiparallel at V= 3 cm/h and a furnace hot zone temperature of T_F = 550°C. The magnitude of the deviations was δT = 2.8 ± 0.4°C with a major frequency f = 1.0 ± 0.2 x 10^{-2} Hz. This is contrasted, in Fig. 20, with a sample grown under identical conditions but a reduced hot zone temperature of T_F = 450°C where no statistically significant temperature or microstructural deviations were observed. It is still unclear whether the thermal instabilities and associated microstructural inhomogeniety is a result of liquid-solid interface curvature which might lead to convective flow or whether other gravity related phenomena caused the observed curved and banded microstructure and associated thermal fluctuations.
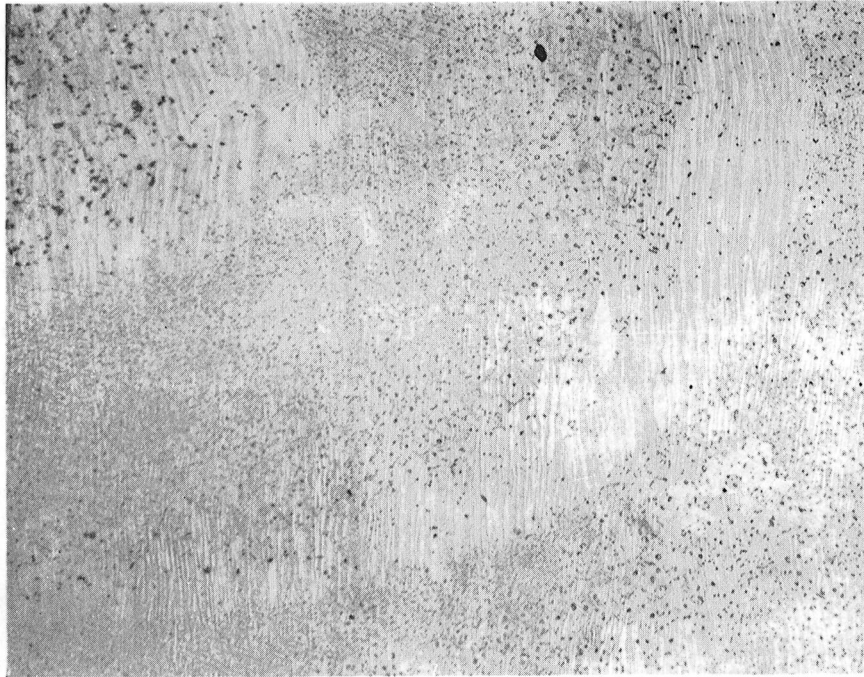
(a) TRANSVERSE

|← 250 μm →|
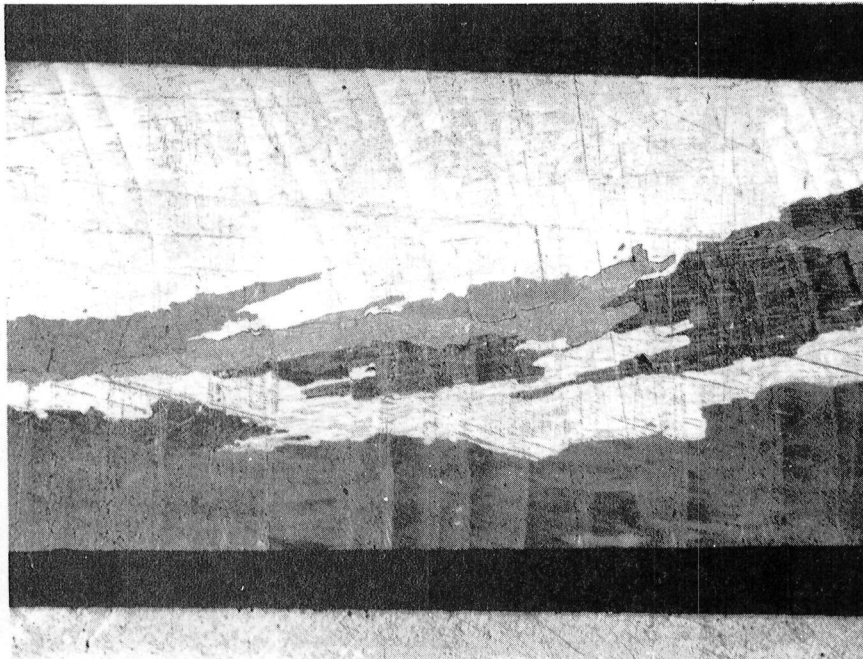
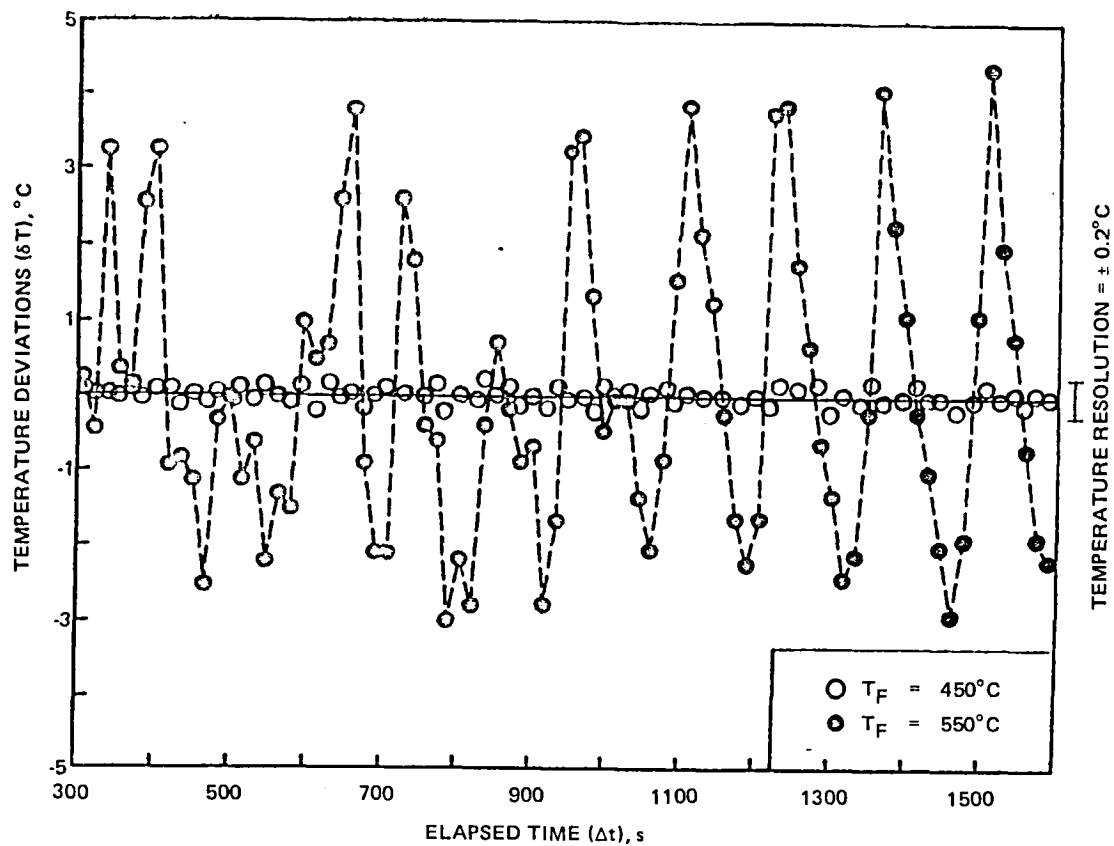(b) LONGITUDINAL

|← 1500 μm →|

1161-019(T)

Fig. 19 Banded-like Morphology Observed at V = 3 cm/h for Furnace Hot Zone Temperatures T_F = 550°C Both (a) Transverse and (b) Longitudinal to the Solidification Direction.

Fig. 20 Thermal Fluctuations Noted in Furnace Hot Zone Region from In-situ Thermocouple Measurements as Furnace Temperature is Raised from T_F = 450 to $550°C$.

1161-020(T)

DISCUSSION

SPAR IX vs SPAR VI

Both the SPAR IX and previous SPAR VI low gravity experiments were performed in the high solidification velocity regime, V = 50 cm/h for SPAR IX and V = 30 cm/h for SPAR VI; in the same thermal environment, G_L = 100°C/cm; and involved the nominal eutectic composition of Bi/MnBi. Both experiments exhibited directional solidification with cooperative growth and were conducted in identical sister apparatus; the ADSS-E2 unit for SPAR VI and the ADSS-E1 unit for SPAR IX. The ampoule and eutectic sample geometries were identical.

The similarity in results between the two experiments are:

o   Statistically significant reductions in mean MnBi rod diameters and interrod spacings for samples directionally solidified in low gravity with respect to normal gravity. For SPAR VI, the global (average of all samples) mean interrod spacings and rod diameters were reduced from $\langle\lambda\rangle$ = 1.54 ± 0.19 µm and $\langle d\rangle$ = 0.53 ± 0.11 µm in normal gravity to $\langle\lambda\rangle$ = 1.00 ± 0.17 µm and $\langle d\rangle$ = 0.33 ± 0.08 µm in low gravity. For SPAR IX, the global mean interrod spacings and mean rod diameters changed from $\langle\lambda\rangle$ = 0.90 ± 0.16 µm and $\langle d\rangle$ = 0.33 ± 0.08 µm in normal gravity to $\langle\lambda\rangle$ = 0.48 ± 0.09 µm and $\langle d\rangle$ = 0.18 ± 0.05 µm in low gravity.

o   An increase in resistance to demagnetization or intrinsic coercivity of the low gravity compared with normal gravity samples accompanying the change in mean rod diameters between low and normal gravity processing. For a fully transformed, HC to equilibrium, ferromagnetic MnBi phase segment, the observed global mean increase in intrinsic coercivity for SPAR VI between normal and low gravity was m_Hc ≈ 27.5 ± 0.5 kOe to 32.0 ± 0.5 kOe while for SPAR IX the change measured was from 32.0 ± 0.5 kOe to 34.0 ± 0.5 kOe. This increase would be anticipated from the smaller rod diameters noted in the low gravity material. The intrinsic coercivity of materials like the ferromagnetic, MnBi phase is controlled by their magnetocrystalline anisotropy which increases with decreasing

particle size. The intrinsic coercivity should approach the theoretical maximum, 35 kOe, for elongated single domain MnBi particles (Ref. 16 and 24), when the particle contains only one magnetic domain. It is therefore reasonable to assume that near single domain behavior has been achieved in the SPAR IX low gravity material.

o   That the low gravity samples contained a statistically lower amount of the MnBi phase than normal gravity processed samples. For the SPAR VI flight experiment, the MnBi volume fraction was found to be uniform with 7 ± 3 % less MnBi than similarly processed, normal gravity samples. Approximately 45% of the total sample length was solidified during low gravity. For the SPAR IX flight experiment, 85% of the total sample length was solidified during low gravity with about 70% of the low gravity length exhibiting 8 ± 3 % less MnBi than the normal gravity comparison samples. In addition, a volume fraction increase was observed in the remaining 30% of low gravity sample length which approached the volume fraction expected for the nominal eutectic composition. This behavior is similar to that expected for Bi-rich, off-eutectic solidification (Ref. 25).

It should be noted that the microstructures and magnetic properties achieved in low gravity during SPAR VI were duplicated under normal gravity conditions at a higher solidification velocity, i.e., the SPAR IX conditions, since d, λ and magnetic properties are proportional to $V^{-1/2}$ in this growth velocity range. For the growth velocity used during SPAR IX, however, the ability of the apparatus to remove heat in a unidirectional manner is near its limit. Experiments conducted at $V = 60$ cm/h have indicated the onset of interface curvature and therefore nonaligned growth (Ref. 9). This occurs presumably because the temperature at which solidification occurs is no longer within the adiabatic zone of the furnace. Heat transfer is thus no longer one dimensional. It is therefore impossible to achieve the MnBi rod eutectic morphologies and corresponding magnetic properties that were obtained during the SPAR IX low gravity experiment in a normal gravity environment using the ADSS furnace assembly.

EUTECTIC SOLIDIFICATION MODELING & CANDIDATE MECHANISMS

Growth models for the steady state have been shown to describe well the behavior of directionally solidified, regular doubly non-faceted eutectics (Ref. 1 to 4). However, less progress has been obtained for the faceted-nonfaceted or double-faceted regular and irregular cases (Ref. 5), and almost no effort has focused on the effects of convection. In Table 2, we show the evolution of theoretical attempts to treat the problem of coupled growth of eutectics.

Jackson and Hunt (Ref. 2) were the first workers to provide a coherent model which qualitatively explained many experimental observations. Their approach assumed negligible, microscopic phase curvature, i.e., an approximate planar, isothermal liquid-solid interface. They also assumed that the concentration at the interface essentially equals the eutectic composition which makes the application of their model to eutectics of widely different phase fraction, like Bi/MnBi, somewhat uncertain. More importantly, their calculations did not take into account any convective interactions i.e., they assumed no-mixing and only diffusion in the liquid.

Verhoeven and Homer (Ref. 22) performed a similar analysis except they assumed, in analogy with a Burton-Prim-Slichter type analysis (Ref. 26), no convection within a finite stagnant film, δ, extending from the solid-liquid interface into the liquid and complete mixing or convection outside of this film. Their expressions are identical to those of Jackson-Hunt except for the introduction of terms involving trigonometric functions of δ/λ. When $\delta/\lambda \ll 1$, convection becomes an important influence although this case is rarely observed experimentally. For $\delta/\lambda > 1$, their expressions are essentially equal to the non-convective case of the Jackson-Hunt formulation. The $\delta/\lambda > 1$ case was observed during all of our normal and low gravity processing.

Sato and Sayama (Ref. 27) attempted to study the effect of non planarity of the solid-liquid interface on solute redistribution and hence interrod spacing and interfacial undercooling. They also assumed a convectionless fluid but included only those parts of the interface which were isothermal with one another, i.e., any part of the interface which might be depressed or non-isothermal was ignored. The same functional relationships between λ, V and T as appeared in the Jackson-Hunt model were found except the values of the proportionality constants were up to 50% larger than in the Jackson-Hunt formulation. The larger proportionality constants result in larger λ and ΔT.

Table 2 Evolution of Solidification Models Proposed to Describe Cooperative, Eutectic Growth

Model	Assumptions	Composition Variables	Interrod Dependence	Undercooling Dependence
Jackson-Hunt (1966; Ref. 2)	• Stagnant liquid • No interface phase curvature • One parameter model	$V, \lambda, D_L, S_\alpha, S_\beta, C_E, C_o$	$\lambda = f(V, S_\alpha, K^{J\text{-}H})$	$\Delta T = f(\lambda, V, K^{J\text{-}H})$
Verhoeven-Homer (1970; Ref. 22)	• Stagnant film, completely mixed fluid • No interface phase curvature • One parameter model	$V, \lambda, D_L, S_\alpha, S_\beta, C_E, C_o, \delta$	$\lambda = f(V, S_\alpha, K^{J\text{-}H}, \delta)$	$\Delta T = f(\lambda, V, K^{J\text{-}H})$
Sato-Sayama (1974; Ref. 27)	• Stagnant liquid • Partially planar interface/unconstrained • Unconstrained, two parameter model	$V, \lambda, DL, S_\alpha, C_E, C_o, W$	$\lambda = f(V, S_\alpha, K^{S\text{-}S}, W)$ where $K^{S\text{-}S} \sim 2 K^{J\text{-}H}$	$\Delta T = f(\lambda, V, K^{S\text{-}S})$
Fisher-Kurz (1980; Ref. 5)	• Stagnant liquid • Partially planar interface/constrained by temperature field • Constrained, two parameter model	$V, \lambda, C_L, S_\alpha, C_E, C_o, W, G$	$\lambda = f(V, S_\alpha, K^{F\text{-}K}, W, G)$ where $K^{F\text{-}K} \sim 5 K^{J\text{-}H}$	$\Delta T = f(\lambda, V, K^{F\text{-}K})$
Quenisset-Naslain (1981; Ref. 28)	• Convective fluid flow parallel to liquid-solid interface • Planar, isothermal interface • Constrained, one parameter model	$V, \lambda, S_\alpha, C_E, C_o, U$	$\lambda = f(V, S_\alpha, K^{J\text{-}H}, U)$	$\Delta T = f(\lambda, V, K^{J\text{-}H})$

Key: V = Solidification velocity
λ = Interrod spacing
D_L = Liquid diffusivity
S_α = Half-width of minor phase
S_β = Half-width of major phase
C_E = Eutectic composition
C_o = Bulk liquid composition

δ = Stagnant film width
W = Isothermal part of interface
G = Imposed thermal gradient
U = Convective fluid flow velocity
ΔT = Interfacial undercooling
K = Proportionality constant, implicit function of alloy system

1161-022(T)

Fisher and Kurz (Ref. 5) extended the Sato-Sayama approach in that the geometries of the depressed and undepressed parts of the interface were fixed because they were related via surface tension effects. This gave rise to a dependence of λ and ΔT on the thermal gradient as well as solidification velocity. Unfortunately, their model also did not take into account any influence of convection on the growth mechanism.

Recently, Quenisset and Naslain (Ref. 28) have developed a theoretical approach to treat the problem of natural, gravitationally induced fluid flow parallel to the solidification interface of directionally solidified eutectics. They assumed that the liquid boundary layer in contact with the solidification interface, previously referred to as δ, is not a simple stagnant film but includes mass transfer caused by convective fluid flow. They demonstrated that such convective flow reduced the characteristic diffusional length, $\Lambda/2$, which occurs in all previously discussed growth models. This leads to a new characteristic mass transfer length that is directly proportional to the convective fluid velocity, U. This model, at least qualitatively, demonstrates the same behavior of λ and ΔT as we observed experimentally between one and low gravity processing of eutectic Bi/MnBi. As the degree of convection increases, i.e., as the magnitude of the fluid flow velocity gets larger, Quenisset and Naslain's model predicts an increase in λ and decrease in ΔT. Therefore, in the presence of, for example, natural gravitationally induced convective fluid flow, it would be anticipated that λ would be larger and ΔT smaller than in the absence of such flow.

One effect of an increase in undercooling would be to alter the phase-composition relationships in the vicinity of the eutectic. The limit of solid solubility would be increased as would the eutectic composition (Ref. 8 and 11). Since Bi/MnBi is a rather low volume fraction eutectic with asymmetrical liquidus slopes near the eutectic composition (Ref. 11), a decrease would be anticipated in both weight fraction MnBi, assuming the stoichiometry of MnBi remains at 50 a/o, as well as volume fraction of dispersed MnBi, i.e., Bi rich off-eutectic growth. In fact, such a decrease in MnBi volume fraction and off-eutectic like macrosegregation was observed in our low-gravity solidified samples.

It has also been observed that thermal convection can cause temperature fluctuations in the liquid when the temperature gradient exceeds a critical

value that depends on intrinsic properties of the particular system being solidified. When these temperature fluctuations reach the liquid-solid interface, they may induce nonsteady-state interface motion. One result of unsteady interface motion, for growth of a rod eutectic, might be to decrease the mean interface growth velocity assuming that insufficient time was available for the rod spacing to adjust to an increasing growth velocity during the period of fluctuation by, for example, a branching-type mechanism. Since MnBi, the rod component in eutectic Bi/MnBi, grows in a faceted manner, MnBi rod termination may proceed readily but MnBi rod branching or nucleation could only proceed with difficulty (Ref. 29). A fluctuating growth velocity in one-g_e would then cause d and λ to be larger than would be anticipated for the growth velocity equaling the furnace velocity. If gravity is responsible for the thermal fluctuations, then the fluctuations would decrease as one moved from one to low-gravity resulting in an initial, unsteady-state fluctuating growth velocity in one-g_e that approached the steady-state, average furnace velocity in low-g. A change in growth velocity could result in a simultaneous decrease in λ and increase in ΔT (Ref. 8) and also lead to the phenomena we observed experimentally.

The effects of gravity on Bridgman-Stockbarger directional solidification of eutectic Bi/MnBi has been studied in reduced gravity aboard the SPAR IX flight experiment and contrasted with an earlier SPAR VI flight experiment and normal gravity investigations. Significant differences between normal and low-gravity processing observed during the earlier SPAR VI experiment conducted at V = 30 cm/h were also observed during the present SPAR IX experiment performed at V = 50 cm/h. The differences included:

o   Smaller mean MnBi rod diameters and interrod spacings approximately 50% smaller, for low-gravity compared with normal gravity samples. Accompanying the smaller MnBi morphology was an increase in permanent magnet properties which approached the theoretical maximum.

o   Larger interfacial undercooling, i.e., a lower solidification temperature, of about 5°C for low-gravity compared with normal gravity samples.

o   Lower volume fraction, about 8% less, of the MnBi phase in low-gravity compared with normal gravity processing for about 70% of low-gravity processed sample length. For the remaining length solidified during low-g, an increase in volume fraction similar to that anticipated for a Bi rich, off-eutectic composition was noted. Uniform composition was observed for normal gravity processed samples.

Candidate mechanisms involving gravity induced convective fluid flow and/or thermal fluctuations are proposed to explain the differences in solidification temperature and MnBi morphology between normal and low-gravity processing. The increase in magnetic properties and off-eutectic-like segregation observed for the low-gravity samples are a natural consequence of the smaller MnBi rod diameter distribution and increased interfacial undercooling, respectively.

Also, normal gravity experiments have demonstrated an apparent morphological instability encountered at low growth velocites which resulted in a breakdown of cooperative growth. Long wavelength convective instabilities are suggested as a possible explanation.

Future experiments, both in low and normal gravity, are proposed to better characterize the unusual and potentially useful eutectic growth phenomena observed. These include low-gravity experiments at intermediate growth velocities between V = 30 and 3 cm/h for the eutectic composition; a low-gravity, low growth velocity experiment, V < 0.5 cm/h, to determine the origin of the morphological instability discovered during processing in one-g_e; a low-gravity experiment at high growth velocities, V > 10 cm/h, for off-eutectic compositions to determine if the phenomena observed for the eutectic composition also occurs for potentially useful off-eutectic growth; and investigating the utility of applied magnetic fields in one-g_e to verify proposed candidate mechanisms and control gravity induced instabilities.

ACKNOWLEDGMENTS

REFERENCES

1. W.A. Tiller, "Liquid Metals and Solidification," American Society for Metals, Cleveland, Ohio, P 276, 1958.

2. K.A. Jackson and J.D. Hunt, "Lamellar and Rod Eutectic Growth," Trans AIME, Vol 236, p 1129, 1966.

3. F.R. Mollard and M.C. Flemings, "Growth of Composites from the Melt-Part I," Trans AIME, Vol 239, p 1526, 1967.

4. M. Tassa and J.D. Hunt, "The Measurement of Aluminum-Copper Dendrite Tip and Eutectic Interace Temperatures and Their Use for Predicting the Extent of the Eutectic Range," J Crys Growth, Vol 34, p 38, 1976.

5. D.J. Fisher and W. Kurz, " A Theory of Branching Limited Growth of Irregular Eutectics," Acta Metallurgica, Vol 28, p 777, 1980.

6. W.J. Boettinger, F.S. Biancaniello and S.R. Coriell, "Solutal Convection Induced Macrosegregation and the Dendrite to Composite Transition in Off-Eutectic Alloys," Met. Trans A, Vol 12A, p 321, 1981.

7. R.G. Pirich, D.J. Larson and G. Busch, "Studies of Plane-Front Solidification and Magnetic Properties of Bi/MnBi," AIAA J, Vol 19, p 589, 1981.

8. R.G. Pirich and D.J. Larson, "Directional Solidification of Magnetic Composites," Grumman R&D Center Report RE-602, 1980.

9. R.G. Pirich, D.J. Larson, W.R. Wilcox and T.W. Fu, "Orbital Processing of Magnetic Composites," Grumman R&D Center Report RE-712, 1980.

10. R.G. Pirich and D.J. Larson, "The Influence of Gravity on Directional Solidification of Eutectic and Off-Eutectic MnBi Alloys," Annual TMS-AIME Mtg. Louisville, KY (1981).

11. R.G. Pirich, G.Busch, W. Poit and D.J. Larson, "The Bi-MnBi Eutectic Region of the Bi-Mn Phase Diagram," Met. Trans A, Vol 11A, p 193, 1980.

12. General Electric Company, Space Sciences Laboratory, "Operating Manual for Automated Directional Solidification System," prepared for NASA under contract NAS8-31536, 1978.

13. R.G. Pirich, "Directional Solidification to Magnetic Composites," Monthly Progress Report No. 50 prepared for NASA under contract NAS8-32219, 1981.

14. C. Guilland, "Ferromagnetics of Binary Alloys of Mn," Ph.D. Thesis, Strasbourg, France, p 1, 1943.

15. T. Chen, "Contribution to the Equilibrium Phase Diagram of the Mn-Bi System near MnBi," J Appl Phys, Vol 45, p 2358, 1974.

16. C. Kittel and J.K. Galt "Ferromagnetic Domain Theory," Solid State Physics (Academic Press), Vol 3, p 439, 1956.

17. R.G. Pirich and D.J. Larson, "Magnetic and Metallurgical Properties of Directionally Solidified Bi/MnBi Composites: The Effects of Annealing," J Appl Phys, Vol 50, p 2425, 1979.

18. R.G. Pirich, D.J. Larson and G. Busch, "The Role of Processing Parameters on the Magnetic Properties of Directionally Solidified Bi/MnBi Composites," IEEE Trans Mag, Vol MAG-15, p 1754, 1979.

19. R.G. Pirich, "Characterization of Effects of Plane-Front Solidification and Heat Treatment on Magnetic Properties of Bi/MnBi Composites," IEEE Trans Mag, Vol MAG-16, p 1065, 1980.

20. J.M. Papazian and T. Kattamis, "Effect of Reduced Gravity on the Solidification Microstructures of $NH_4Cl:H_2O$ Alloys," Met. Trans A, Vol 11A, p 483, 1980.

21. R.G. Pirich and D.J. Larson, "Characterization of Gravitationally Induced Convection on Solidification of the Bismuth-Manganese Eutectic," Invited Paper, 5th International Conf on Vapor Growth and Epitaxy/5th American Conf on Crystal Growth, Coronado, CA, 1981.

22. R.F. Sekerka and S.R. Coriell, "Coupled Convective and Morphological Stability," Invited Paper, 5th International Conf on Vapor Growth and Epitaxy/5th American Conf on Crystal Growth, Coronado, CA, 1981.

23. T.W. Fu and W.R. Wilcox, "Influence of Insulation on Stability of Interface Shape and Position in the Vertical Bridgman-Stockbarger Technique," J Crys Growth, Vol 48, p 416, 1980.

24. T. Chen and W. Stutius, "The Phase Transformation and Physical Properties of the MnBi and $Mn_{1.08}Bi$ Compounds," IEEE Trans Mag, Vol MAG-10, p 581, 1974.

25. J.D. Verhoeven and R.H. Homer, "The Growth of Off-Eutectic Composites from Stirred Melts," Met. Trans, Vol 1, p 3437, 1970.

26. J.A. Burton, R.C. Prim and W.P. Slichter, "Distribution of Solute in Crystals Grown from the Melt Part I. Theoretical," J Chem Phys, Vol 21, p 1987, 1953.

27. T. Sato and Y. Sayama, "Completely and Partially Cooperative Growth of Eutectics," J Crys Growth, Vol 22, p 259, 1974.

28. J.M. Quenisset and R. Naslain, "Effect of Forced Convection on Eutectic Growth," J Crys Growth, Vol 54, p 465, 1981.

29. M. Nair et al, "Response of MnBi-Bi Eutectic To Freezing Rate Changes," 5th International Conf of Vapor Growth and Epitaxy/5th American Conf on Crystal Growth, Coronado, CA, 1981.

FINAL POST-FLIGHT REPORT

on

SPAR IX PAYLOAD R-17
EXPERIMENTS NOS. 76-51/1 AND 76-51/2

DIRECTIONAL SOLIDIFICATION OF IMMISCIBLE
ALUMINIUM-INDIUM ALLOYS

to

NATIONAL AERONAUTICS AND SPACE ADMINISTRATION
George C. Marshall Space Flight Center
(Alabama)

November, 1981

Principal Investigator :

C. Potard

Commissariat à l'Energie Atomique
Centre d'Etudes Nucléaires de Grenoble
Laboratoire d'Etude de la Solidification
85 X
38041 Grenoble Cedex
France

ABSTRACT

Four samples of immiscible aluminium-indium alloy having monotectic and hypermonotectic compositions were solidified under microgravity conditions during the flight of the NASA SPAR IX space probe on 21st January 1981.

The experimental conditions were based on monitoring the capillary behaviour of the two-phase liquid alloy and on directed solidification.

With this purpose in mind, the desired specific wetting of the crucible material by the aluminium rich phase was obtained by the use of silicon carbide walls and by maintaining a high degree of purity of the materials present.

Graphite was used to promote the thermal exchanges required to obtain the non-zero thermal gradients in the alloy studied.

X-ray radiography was used to highlight the dispersed structure of the primary indium phase. Considerable segregation of the primary indium phase was found on the walls of the free volume for two of the samples and in the shrinkage hole for the other two samples. This macrosegregation depends on the solidification direction and is a result of the thrust of the interface on the globules.

The thermal conditions effectively obtained in the experiment were analysed by a two-dimensional numerical analysis. The parameters of the solidification process were thus able to be determined.

The dispersion observed in the alloys was statistically analysed as a function of the local thermal conditions prevailing in the samples.

The majority populations change in relation to the solidification speed and to the curvature of the interface.

No conclusions could be drawn as regards the effect of the thermal gradients in the liquid phase on the globule concentration and their distribution.

These experiments also clearly indicated the potential of using spatial environments to obtain dispersed structures from immiscible liquid state alloys.

This result also derives from the close monitoring of the capillarity phenomena and from the high degree of chemical homogeneity of the initial alloys.

LIST OF FIGURES

Figure 9.   X-ray picture of the monotectic sample 76-51/1-Upper.
              Considerable indium phase segregation can be seen.
              The sample was solidified from the free volume zone
              (light coloured) towards the bottom of the crucible.

Figure 10.   X-ray picture of the 32 w % sample 76-51/1-Bottom
              The free volume is scattered with the indium phase.
              Primary indium globules of varying size are identifia-
              ble in the bulk of the sample.

Figure 11.   X-ray picture of the 32 w % hypermonotectic sample
              (76-51/2-Bottom).
              The primary indium globules have a more uniform disper-
              sion in the bulk. Zones next to the crucible side
              walls are free of globules.

Figure 12.   X-ray picture of the 32 w % hypermonotectic sample
              (76-51/2-Upper).
              Solidification from the free volume zone towards the
              bottom of the crucible has led to segregation of the
              primary indium phase in the shrinkage hole.

Figure 13.   Section through the four flight samples showing the
              location of the various component phases.
              a/ 76-51/1-Upper ; b/76-51/1-Bottom ; c/ 76-51/2-Upper
              d/ 76-51/2-Bottom.

Figure 14.   Scanning electron microscopy (a) and microanalysis
              of the free volume surface (b). These consist of fields
              of indium and aluminium.
              No trace of alumina was detected.

Figure 15.   Structure of the monotectic matrix. Intergranular
              and intragranular globules are present.

Figure 16.   Primary indium phase globules in the matrix.

Figure 17.   Scanning electron microscopy after selective etching
              of the monotectic alloy.
              Accumulations of indium phase in various forms can
              be seen.

LIST OF TABLES

SPAR IX EXPERIMENTS 76-51/1 AND 76-51/2

DIRECTIONAL SOLIDIFICATION OF IMMISCIBLE ALUMINIUM-INDIUM ALLOYS

C. Potard

INTRODUCTION

Four samples of the immiscible aluminium-indium system having monotectic and hypermonotectic composition were solidified under microgravity during the SPAR IX flight of January 20th 1981.

This report presents the most advanced stage of the analysis of the results obtained, namely a description of the observations made on the samples returned and a correlation between the results obtained and the experimental conditions. A comparison is also made with the ground base test results.

Generally speaking, a comparative investigation method was adopted here in order to avoid having to consider at this stage unknown phenomena which occur in a similar manner in the various samples.

This approach will indicate the main fundamental problems that must be theoretically and experimentally investigated in the near future.

SUMMARY OF OBJECTIVES AND DESIRED EXPERIMENTAL CONDITIONS

The general objective of the research program is to obtain regular dispersed solid structures of hypermonotectic composition using weightlessness. Within this objective, the analysis of the mechanisms involved in the structure formation constitutes the first task of the research program.

IV-1

CAVITY ACCESS INSULATION PLUG

TYPICAL CONTROL THERMOCOUPLE

MULTIFOIL INSULATION

MID. TC

INCONEL 600 SUPPORT TUBE

EXPERIMENT CARTRIDGE

BOT. TC

COOLING GAS PASSAGE

HOT HEATING ELEMENT

TYPICAL HEATING ELEMENT LEAD OUT WIRE

MIDDLE HEATING ELEMENT

COLD HEATING ELEMENT

THERMAL INSERT

LIQUID COOLED HEAT EXCHANGER

ISO. – GRAD. HEATING MODULE
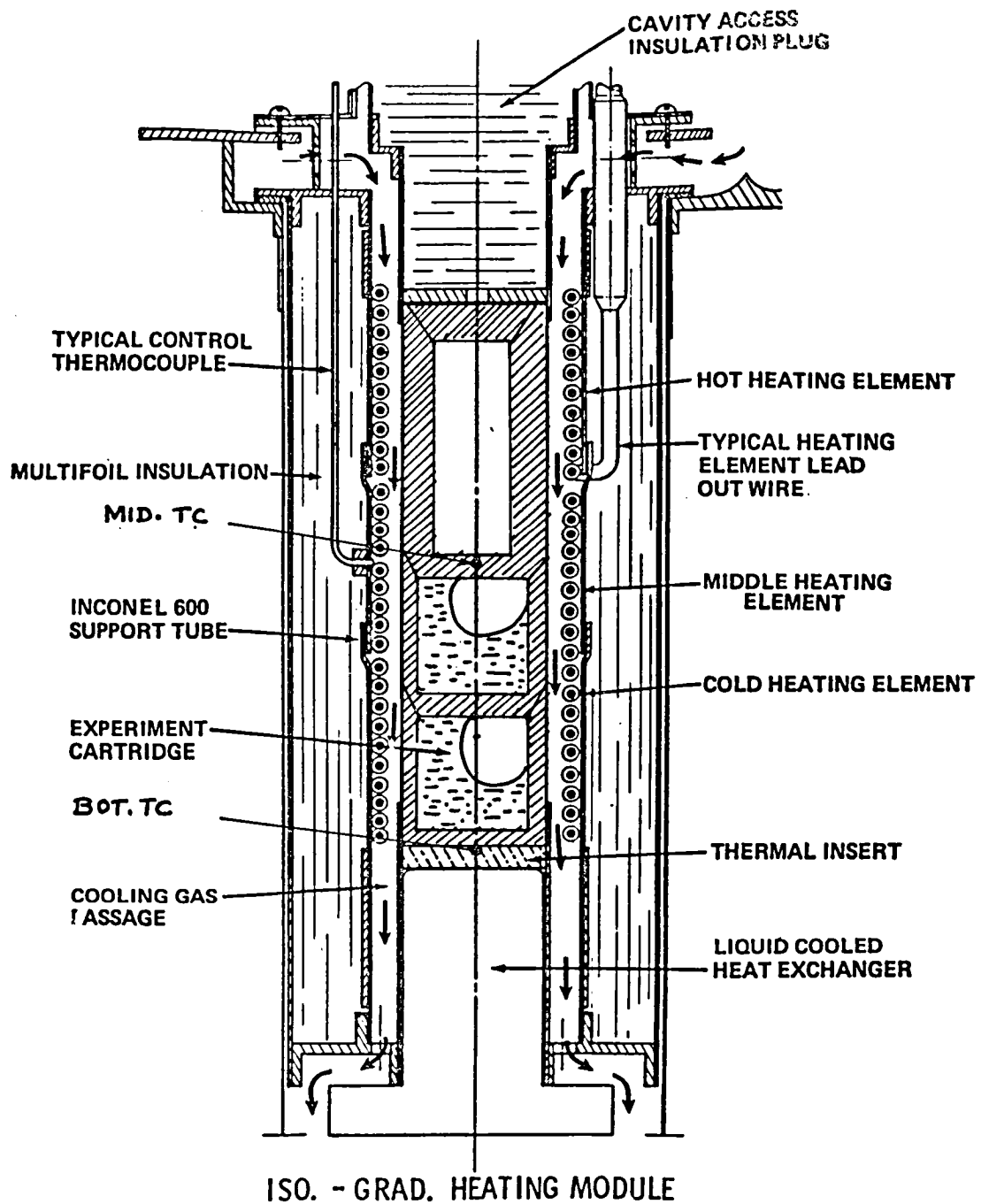
Figure 1.   Diagram of the NASA–GPRF type directed solidification furnace.

The conditions chosen for this purpose were based on:

- the control of capillary interactions between the existing phases,

- the purity of the media,

- well-defined initial stages and heat treatment processes.

These conditions and their expected consequences on the behaviour of the alloys and the experimental method have been well described in earlier works [1][2]. Only a short summary will be presented here:

The homogeneous Al-In liquid alloy held at 900°C in a Silicon Carbide crucible is progressively cooled until solidification during the microgravity period of the rocket flight. By this process, a dispersion of indium-rich liquid phase (indium phase) should be created within an aluminium-rich liquid matrix. A controlled solidification stage is the method chosen to keep the dispersion in the solid state. The General Purpose Rocket Furnace build by NASA/MSFC was used in gradient solidification mode. A schematic view is shown in figure 1.

Two cartridges each containing two samples were processed under different conditions:

- the cartridge 76-51/1-FLT "Low G" was treated under directed heat flow with a low thermal gradient, and,

- the cartridge 76-51/2-FLT "High G" sustained directed heat flow with a higher thermal gradient.

The two superposed samples are called 'Bottom' and 'Upper' by reference to the Bottom of the cartridge. Two thermocouples located on the lid of the upper crucible (Mid.TC) and on the bottom of the cartridges (Bot-TC) measured the temperatures applied to the samples.

TABLE 1. Flight cartridges : Initial characteristics of samples.

Cartridge		76-51/1 - FLT "Low G" (October 1978)		
Samples	Mass g	X_{In} at. (W.%)	Volume fraction of "In" %	Crucible volume cm^3
Bottom	7.60591	.100 (32.08)	$\simeq 9.15$	2.824
Upper	4.90803	0.0429 (16.0)	0	2.77
Cartridge		76-51/2 - FLT "High G" (April 1980)		
Bottom	5.88145	.100 (32.08)	$\simeq 9.15$	2.807
Upper	5.7823	.100 (32.09)	$\simeq 9.15$	2.232

Densities at 850°C are $\simeq 2.98$ g.cm^{-3} (hypermonotectic) and $\simeq 2.53$ g.cm^{-3} (monotectic).

Because of the non-regular shape of the crucible cavities, total filling was not possible. Consequently, large free volumes were unavoidable. This drawback may lead to perturbations of the thermal field and of liquid dynamics.

Table 2 presents the experimental conditions achieved during the SPAR campaign.

TABLE 2.   Spar IX experimental conditions.

		Annealing		Initial Cond.		Acc. flight	Stabilization	Cooling		
		Temp. °C	t h	Temp. °C	t mm	Launch	Temp. °C	Mean cooling rate °C.sec⁻¹	End 0-g temp. °C	Mid.T – Bot.T at solidification
		$t - t_0 - 34\,h \Longrightarrow$		$t_0 - 1\,h \Longrightarrow$		$t_0 = 0 \Longrightarrow$	$t = 92'' \longrightarrow$	$t = 124'' \Longrightarrow$		$t = 384'' \Longrightarrow$
76-51/1	Bottom	838 / 770	8 / 25	775	60'	765	720	1.80	330	≈ 100°C
76-51/1	Upper	900 / 772	8 / 25	780	60'	785	810	1.50	460	≈ 100°C
76-51/2	Bottom	856 / 770	8 / 25	773	60'	750	760	2.03 maxi:6.8	250	
76-51/2	Upper	900 / 810	8 / 25	853	60'	870	890	2.10	405	

Temperatures are read on Mid.TC and Bot.TC

. 0-g period ≃ 292 seconds (4'52")

. Mean acceleration (Z axis) ≃ $1.2 \; 10^{-4}$g

In order to achieve complete homogeneity, the alloys were maintained at 900°C during 34 hours. Then the temperatures were ajusted in a precooling stage to 770°C for the 'Low G' cartridge and 850-770°C for the 'High G' cartridge before launch. The microgravity period lasted 292 seconds (4'52") and the mean acceleration on Z axis was 1.2 10^{-4}g.

The required cooling process of the two cartridges as stated in our experiment proposal had to be directionally oriented. In the present case, the use of strong cold helium flows reduced the directionality of the heat flows inside the sample. The thermal analysis was consequently inaccurate, especially the records of the beginning and end of solidification, these being the basis on which the temperature fields are computed.

O-g cartridge 76-51/1 - FLT 'Low Gradient'.

Figure 2 presents the cooling curves of the 76-51/1 cartridge as recorded by telemetry of the middle thermocouple (Mid.TC) and bottom thermocouple (Bot.TC) (fig.1). The mean cooling rates are 1.50°C.s^{-1} for the Mid.TC and 1.80°C.s^{-1} for Bot.TC.

The beginning and end of solidification of the two samples are located on Mid.TC at t = 234 s and T = 636°C, and at t = 305 s and T = 567°C. Time originates at launch (see table 3). However, it is not possible to discriminate between the occurrence of these events for each sample.

The temperature difference between the two arrests can be immediately interpreted to estimate a mean solidification rate of about 3.7 10^{-2}cm.s^{-1}. The temperatures given by the thermocouples at the end of O-g are 460°C and 330°C.

The actual temperatures of the samples at this instant can be estimated from this analysis: close to 230°C for the bottom sample and to 370°C for the upper sample. These temperatures are

Figure 2.   76-51/1-FLT :

Variations in Mid-TC and Bot-TC temperatures recorded by telemetry.
The beginning and end of solidification are identified by breaks in the
slope on the two curves.

well below the monotectic point. A finer computation of the tempe-
rature field was made using thermocouple data and a finite-element
calculation method. Details of the computation are presented further
on.

O-g cartridge 76-51/2 'High Gradient'.

Figure 3 presents the cooling curve for the 76-51/2 cart-
ridge. During the first 70 s, a considerable difference is establish-
ed between the mid-temperature and the bottom temperature.
difference reaches a maximum of 550°C. This condition was precisely
what was needed for the purposes of the experiment.

Unfortunately, the water flow was interrupted 50 s after
the beginning of the cooling process (t = 174 s) which greatly
disturbed the process. The solidification stage was approximately
identified, beginning at t = 230 s (T = 650°C) and ending at
t = 291 s (T = 563°C). The mean cooling rate read on the mid.TC
is $2.10°C.s^{-1}$ ($126°C.mn^{-1}$). A rough estimate of the solidification
rate given by the two identified arrests indicates $4.36 \ 10^{-2} cm.s^{-1}$
($2.6 \ cm.mn^{-1}$).

The actual temperatures of the sample at the end of micro-
gravity period can be estimated of about 400°C and 210°C, these
values being low enough to expect complete solidification of the
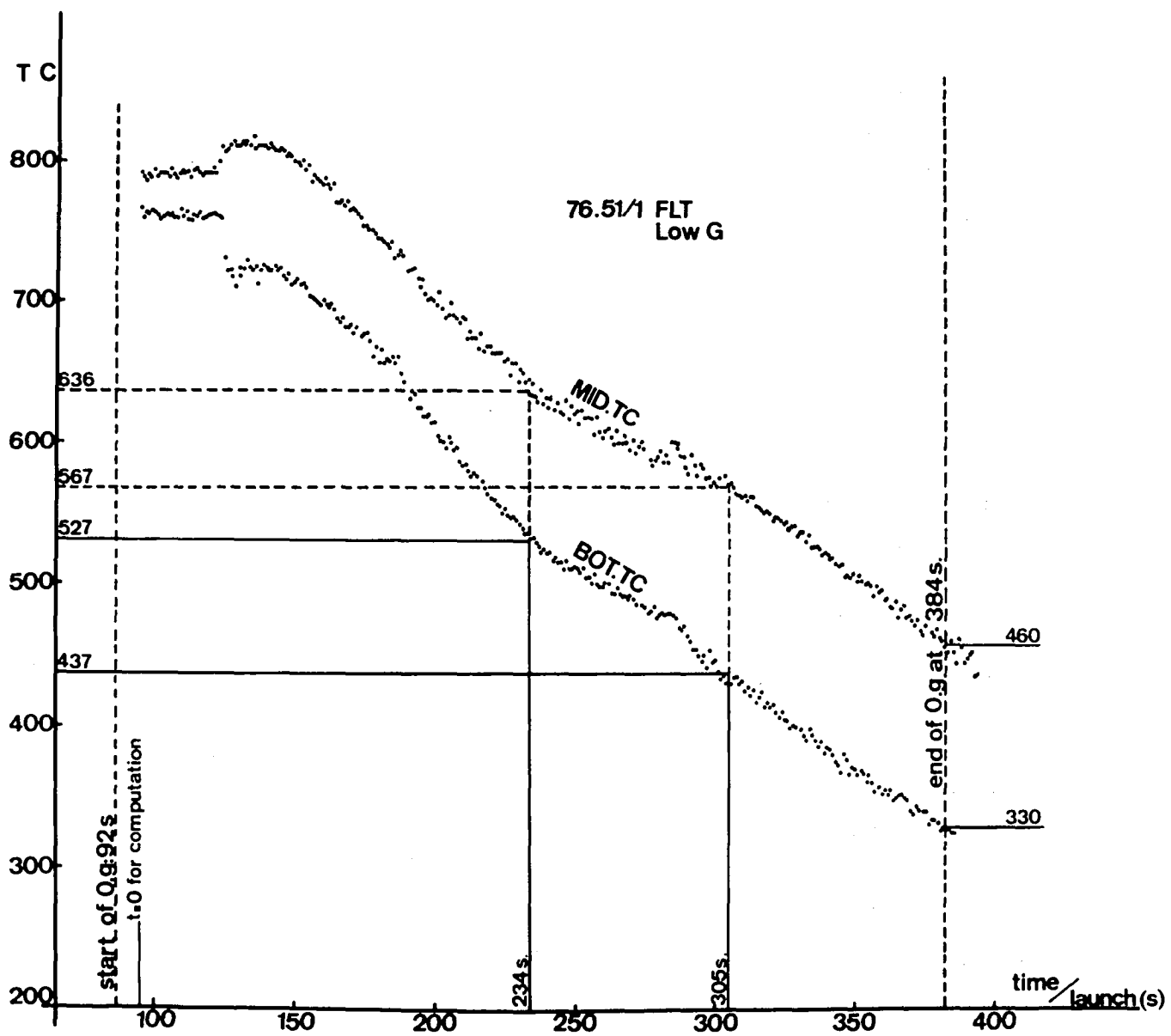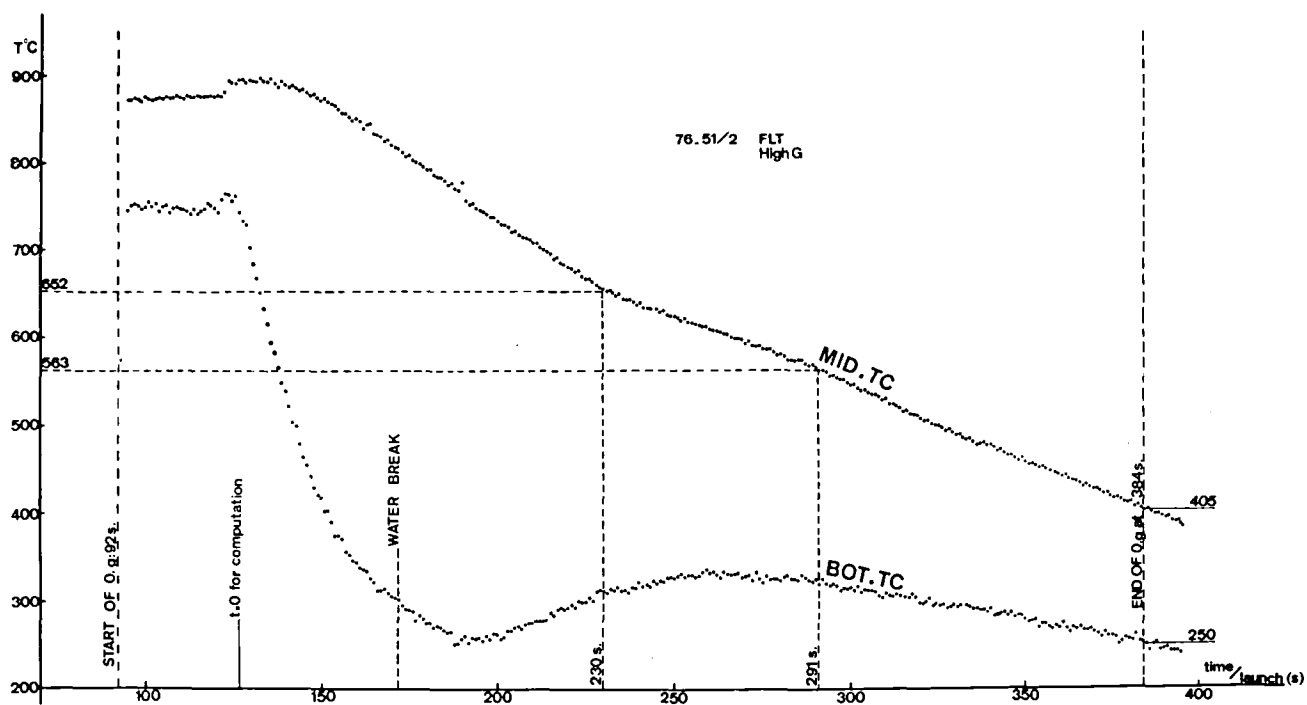monotectic matrix before the reentry perturbations.

Figure 3. 76-51/2-FLT :

Variations in Mid-TC and Bot-TC temperatures recorded by telemetry.
The beginning and end of solidification are identified only
on the Mid-TC curve.
The interruption in the water-cooling process led to considerable
disturbance.

Table 3 presents the characteristics of the cartridges and the thermal conditions used for the ground-base tests.

TABLE 3.   '1-g' sample characteristics and heat treatments.

Cartridge		76-51/1 – GBT "Low G" (November 1978)					
Samples	Total mass g and X_{In} w%	Annealing T °C	Annealing t h	Initial temp. °C	Mean cooling rate °C.sec^{-1}	End of 0-g temp. °C	Mid.T–Bot.T at solidification
Bottom	6.54937 32.08 %	900	12	770	2.01	235	≈ 200°C
Upper	5.46659 16 %	900	12	770	1.38	430	

Cartridge		76-51/2 – GBT "High G" (October 1978)					
Bottom	7.1011 32.08 %	900	12	750	1.84 (maxi:9.2)	283	≈ 450°C
Upper	7.79022 32.08 %	900	12	850	1.55	470	

The annealing stage took place at 900°C as required. The cooling stage was conducted with exactly the same parameter values as for the flight. In particular, the test of 76-51/2-GBT was conducted with the unvolontary interruption of water flow observed during the flight. The temperature measured at the end of the 0-g period indicated that the monotectic matrix has solidified.

RADIOGRAPHIC EXAMINATION OF THE SAMPLES. FIRST OBSERVATIONS

1-g GBT - Cartridges.

X-ray views of the two GBT-cartridges are shown on figures 4 and 5. The wetting behaviour of the alloys is evidenced on these pictures for the four samples. SiC crucible walls are well-wetted by the Al-rich liquid phase ($\theta_{Al} < 90°$)*. The free volume shapes depend on the filling ratio of the crucible cavities.

Longitudinal cutting of the hypermonotectic sample (fig.6 and fig.7 a-b) together with the X-ray views evidence the complete separation, coalescence and settling of the indium-rich immiscible phase for the hypermonotectic composition alloys of .10 at. of indium, except for the 76-51/1-GBT-Bottom sample for which two globules coexist.

The indium phase lies on the bottom of the crucibles in a non-wetting configuration as expected ($\theta_{In} > 90°$)*. The monotectic composition sample is not homogeneous: as shown by X-rays, a large proportion of the sample volume situated in the lower part of the cavity appears more diffuse showing higher indium content. No globules can be identified within this volume.

Flight cartridges.

The flight cartridges were examined by γ-ray radiography (fig. 8). The integrity of the crucible assembly is evidenced. The containments of the wetting liquids are perfect. On this radiograph the alloys appear in light and dark greys. The free volumes in white are situated in the upper zones and anchored on the inner surfaces of the lids.

---

* θ : contact angle on SiC.
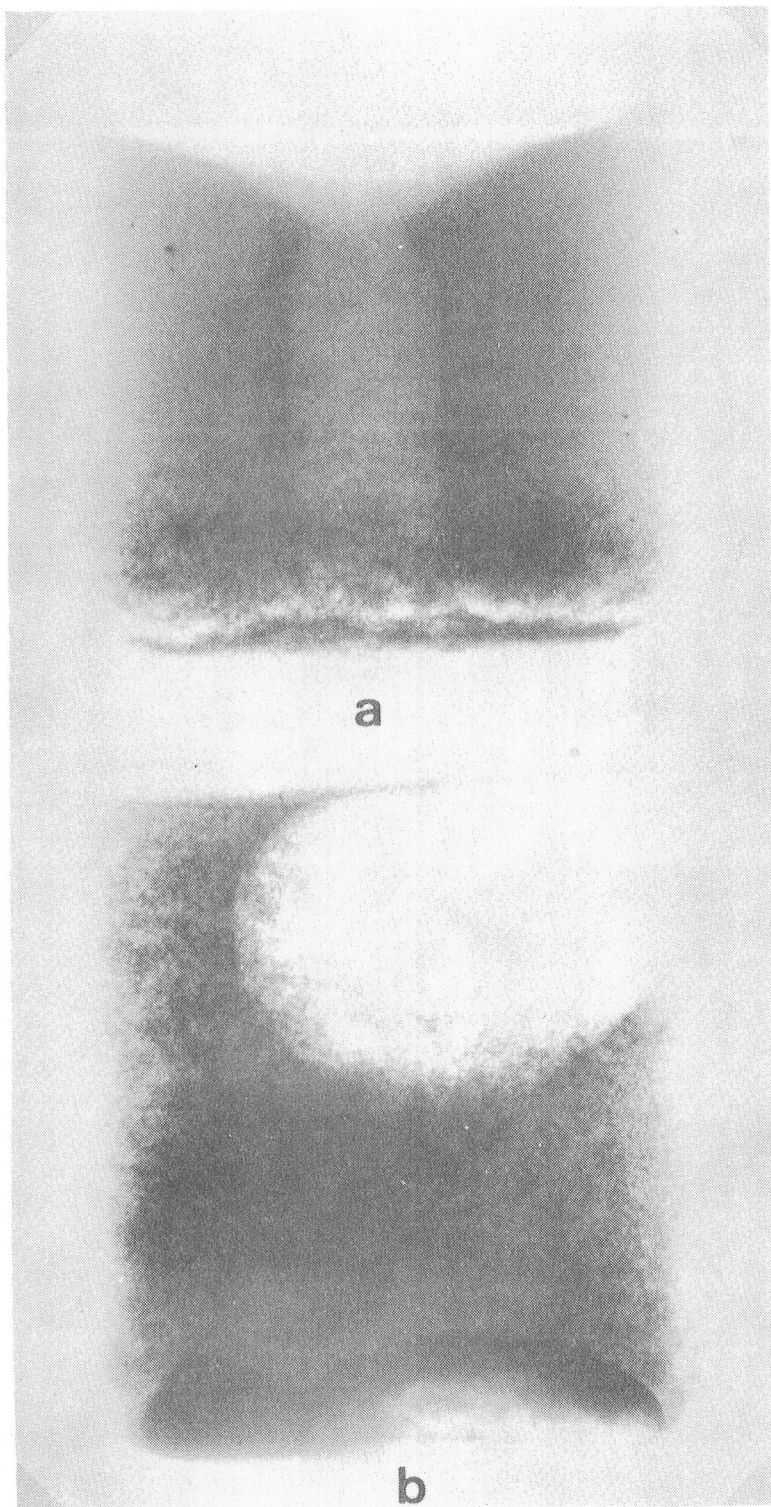
Figure 4 a-b. X-ray picture of the cartridge 76-51/1-GBT.

The 32 w % alloy has classical phase separation characteristics.
The monotectic alloy is heterogeneous but does not present any separation.
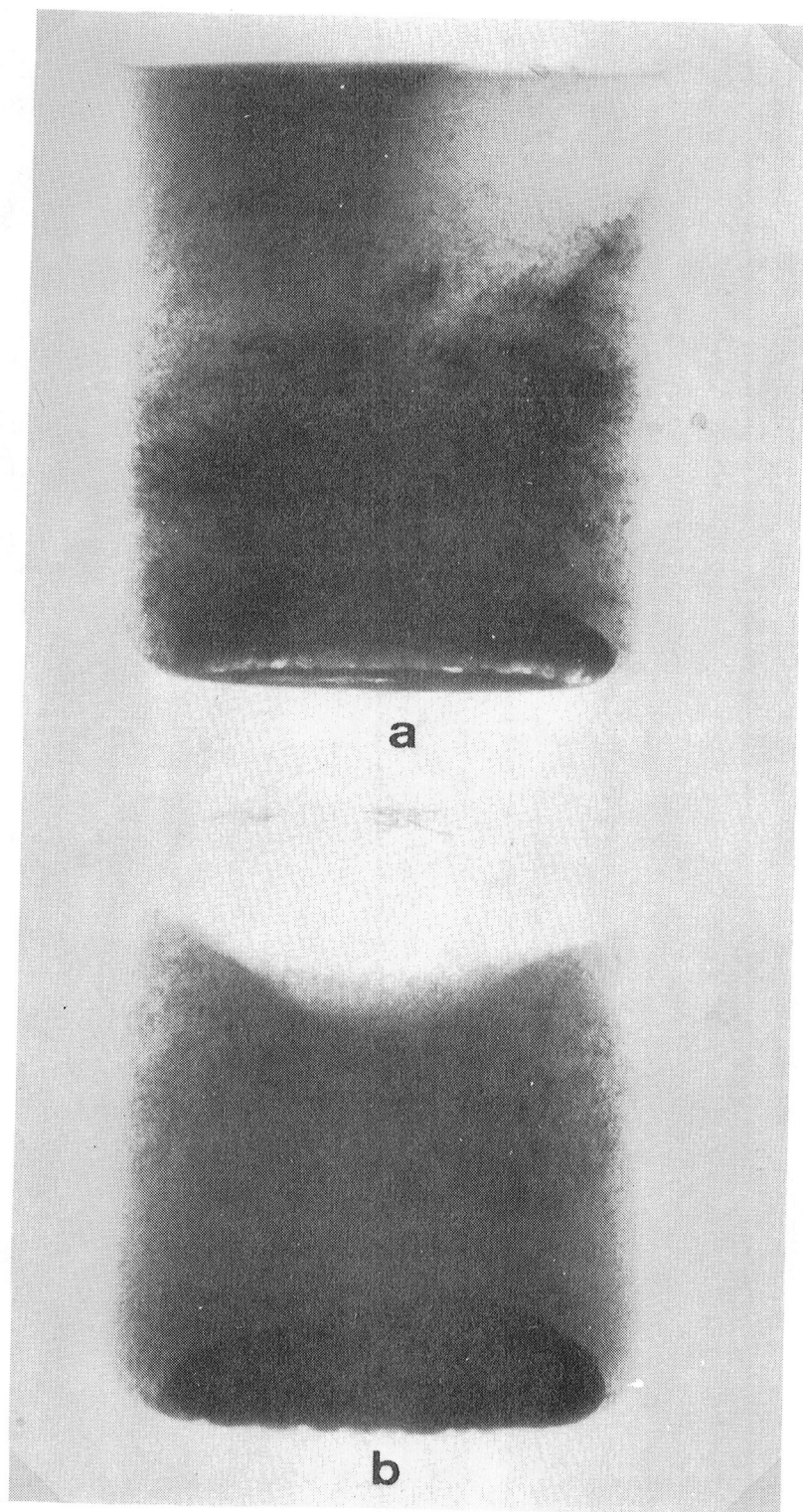
Figure 5 a-b. X-ray picture of the cartridge 76-51/2-GBT.
The phase separation is clearly apparent.
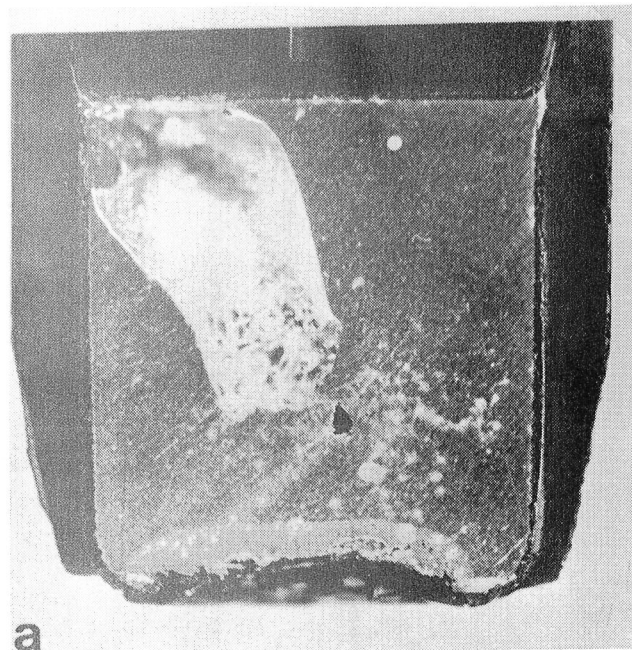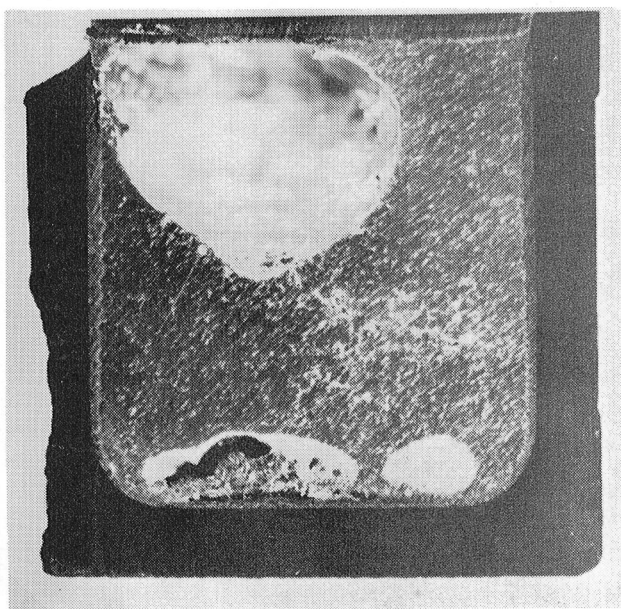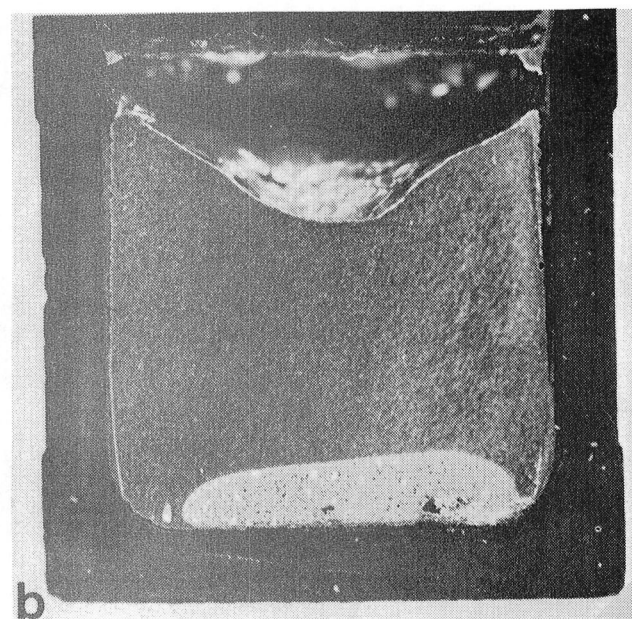
Figure 6   Figure 7 a-b

Figure 6 : Section through the sample 76-51/1-GBT-Bottom.
           The indium phase globules remain separated from the walls of the
           crucible by a film of aluminium. The shrinkage hole in the upper
           crucible is located at the bottom of the crucible.

Figure 7 : Section through the sample 76-51/1-GBT.
a-b
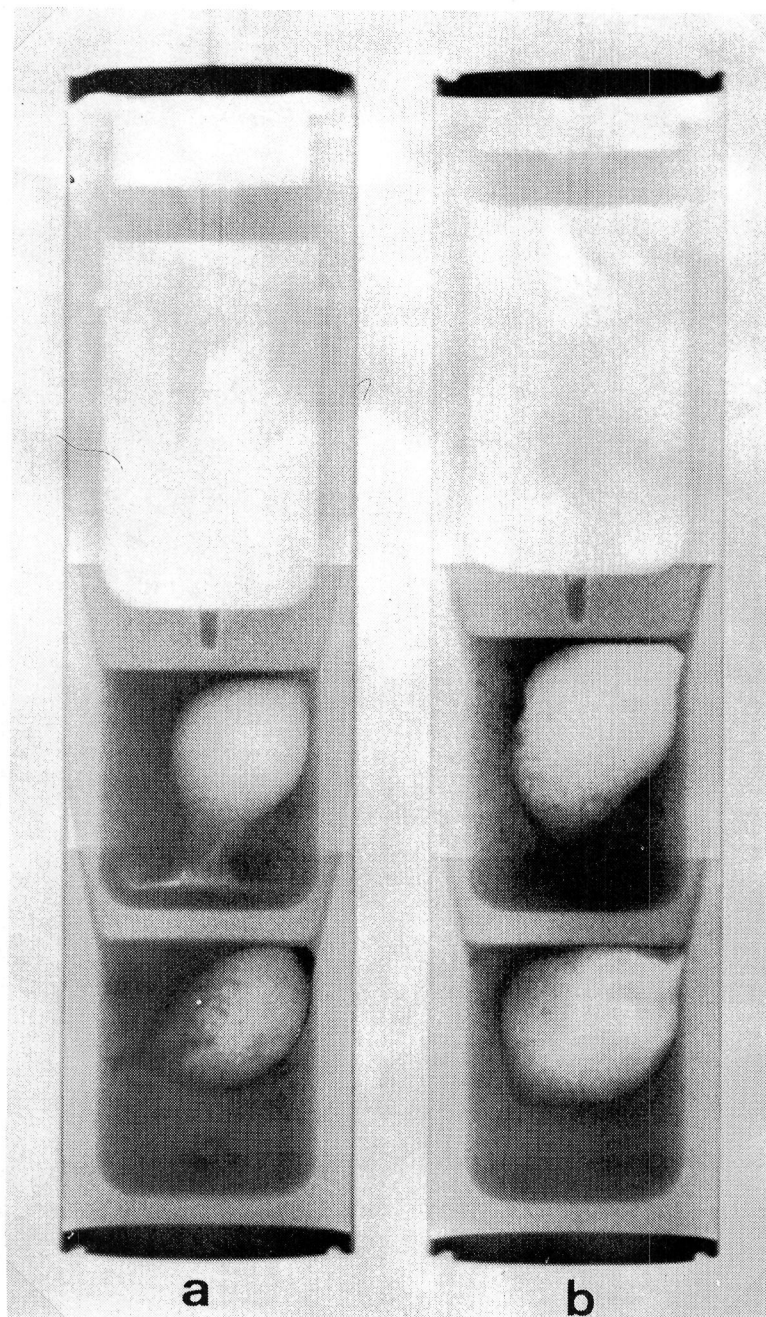
Figure 8. Gamma ray picture of the flight cartridges.

The integrity of the structure is clearly apparent.
There is total tightness as regards the wetting liquid.
The free volumes appear in the form of light-coloured spherical cavities.

<u>76-51/1 - FLT - Upper sample.</u> Figure 9 presents the X-ray view of the monotectic composition alloy. A rather uniform granular structure (considering the cylindrical symmetry) in the alloy volume is revealed (indium phase is dark). Areas less rich in black phase can be seen at the crucible bottom. This alloy is in fact hypomonotectic in composition according to Predel [3] (16 at.% instead of 18.3 at.%) so that the first stage of the solidification process should lead to the exact monotectic composition by segregation. In fact, spherical shapes of noticeable dimensions relative to the continuous background were observed and can be identified as primary phase. A shrinkage hole filled with excess indium phase is present in the crucible bottom zone.

<u>76-51/1-FLT-Bottom sample (fig. 10).</u> The granular continuum corresponding to the monotectic matrix is observed. Primary indium-rich globules of different sizes are identifiable, although their distribution is not uniform. This point will be studied further on. The crucible wall zones are free from globules, especially at the bottom of the crucible. There is no indium phase adhering to the crucible wall, and consequently no spreading of this phase: the SiC acted as a nucleating inhibitor for the primary indium phase.

The globules accumulate about 1 mm above the bottom indicating a localized migrating effect. Partial accumulation and spreading of this indium-rich phase can be observed on the free volume surface (more evidenced on a transverse cutting). By stereographic observation, areas with different curvatures are evidenced when covered by indium phase, giving a lobed spherical shape of the free volume.

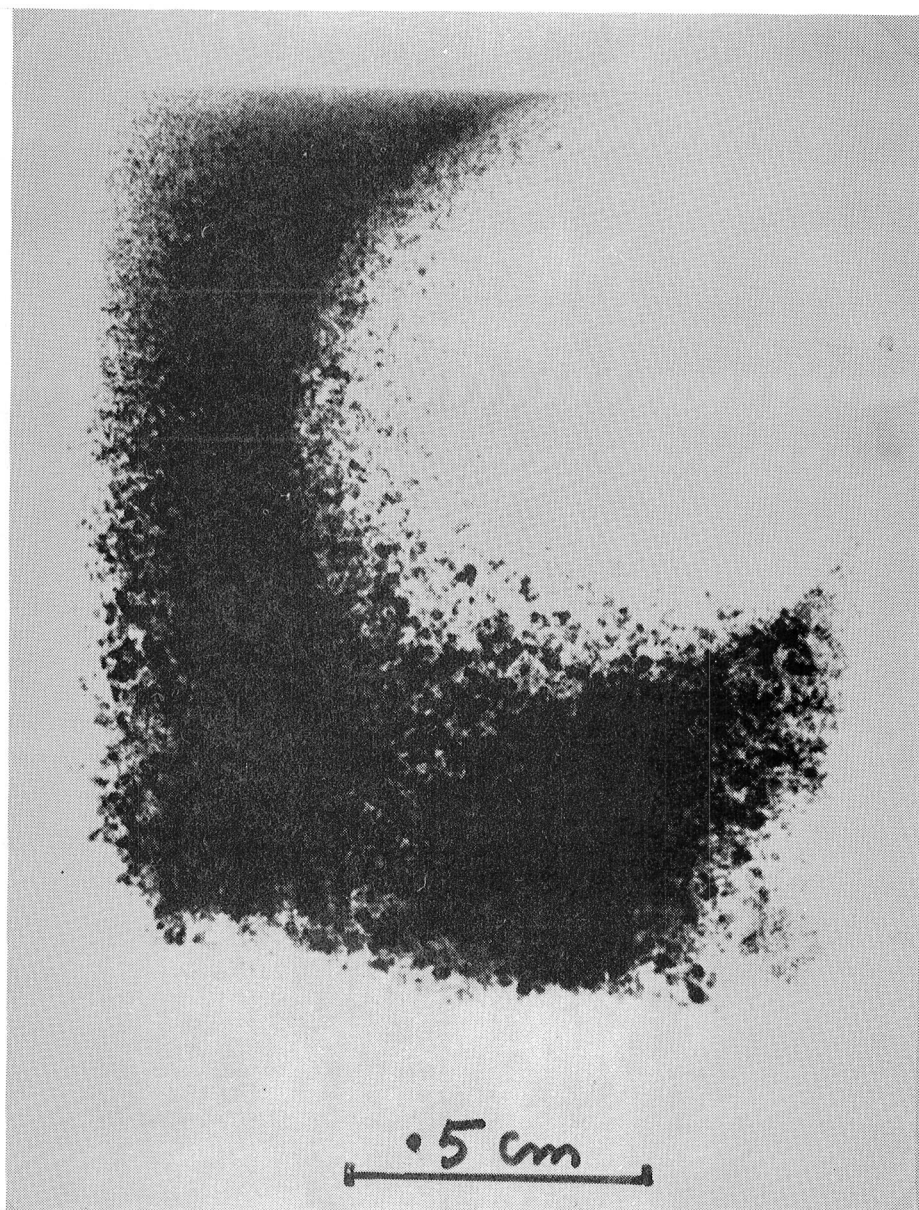Figure 9. X-ray picture of the monotectic sample 76-51/1-Upper.

Considerable indium phase segregation can be seen. The sample was
solidified from the free volume zone (light coloured) towards the
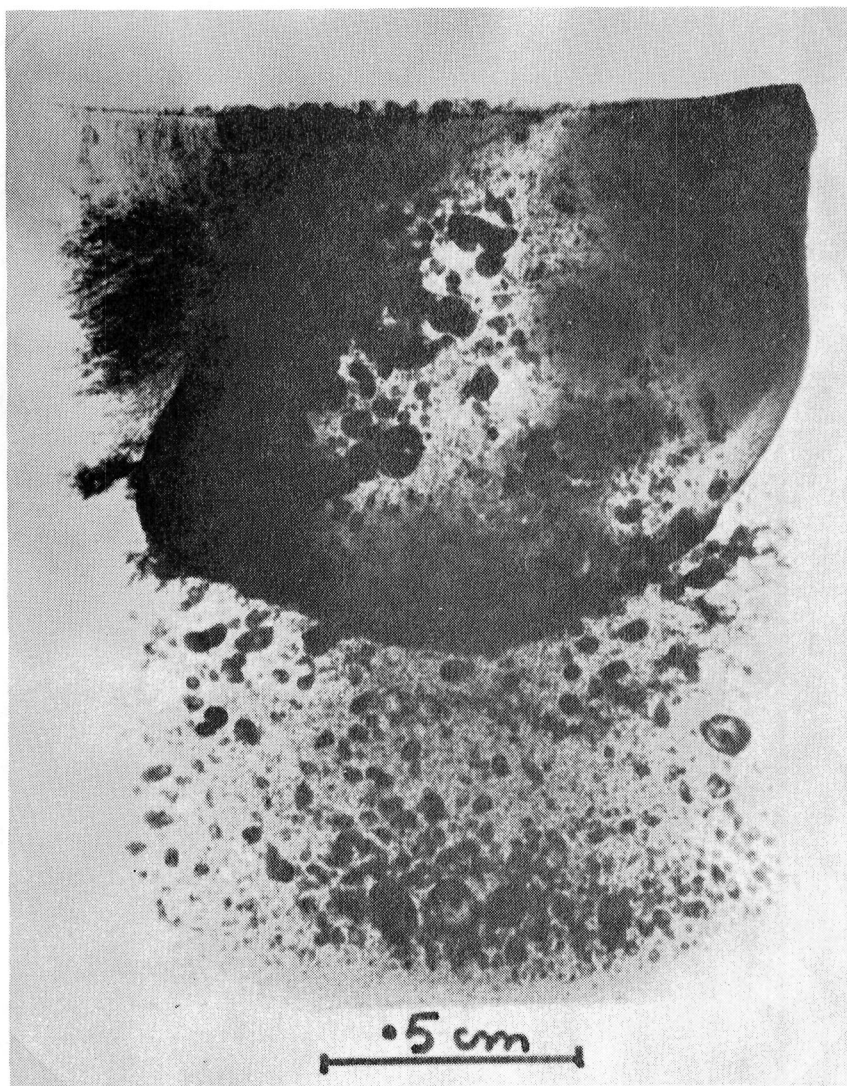bottom of the crucible.

Figure 10. X-ray picture of the 32 w % sample 76-51/1-Bottom.

The free volume is scattered with the indium phase. Primary indium globules of varying size are identifiable in the bulk of the sample.

<u>76-51/2-FLT-Bottom sample (fig. 11)</u>. The same general observations concerning the distribution of the primary indium phase as for the preceding sample can be made. The globules are less coalesced and their diameters are more similar. Their distribution is more uniform inside the matrix. The bottom zone is free from globules over a distance of about 2.2 mm. Total absence of adhesion or spreading of the indium phase is evidenced. The free volume is partially covered by indium.

<u>76-51/2-FLT-Upper sample (fig. 12)</u>. Again, similar observations concerning the primary phase can be made. A deep shrinkage hole filled with indium phase is seen in the crucible bottom zone. A much smaller part of the free volume is covered by indium lenses than in the bottom samples.

This segregation feature is similar to the 76-51/1-upper sample. As will be shown later, these two samples have been subjected to comparable thermal fields.

MICROGRAPHIC OBSERVATIONS

Free volumes and macrosegration.

The sample were cut on a diameter axial plane. Figure 13 presents the cutting of the four samples. The free surfaces were chemically analysed just after cutting in order to reduce oxidizing reactions. The free surfaces are composed of areas of indium phase distributed on the aluminium phase surface (fig. 14). No trace of alumina was detected by this analysis method. This point is of great importance for nucleation and spreading control of the indium phase.

The cuttings show thick layers of indium phase over the entire surface of the free volumes of the two bottom samples.
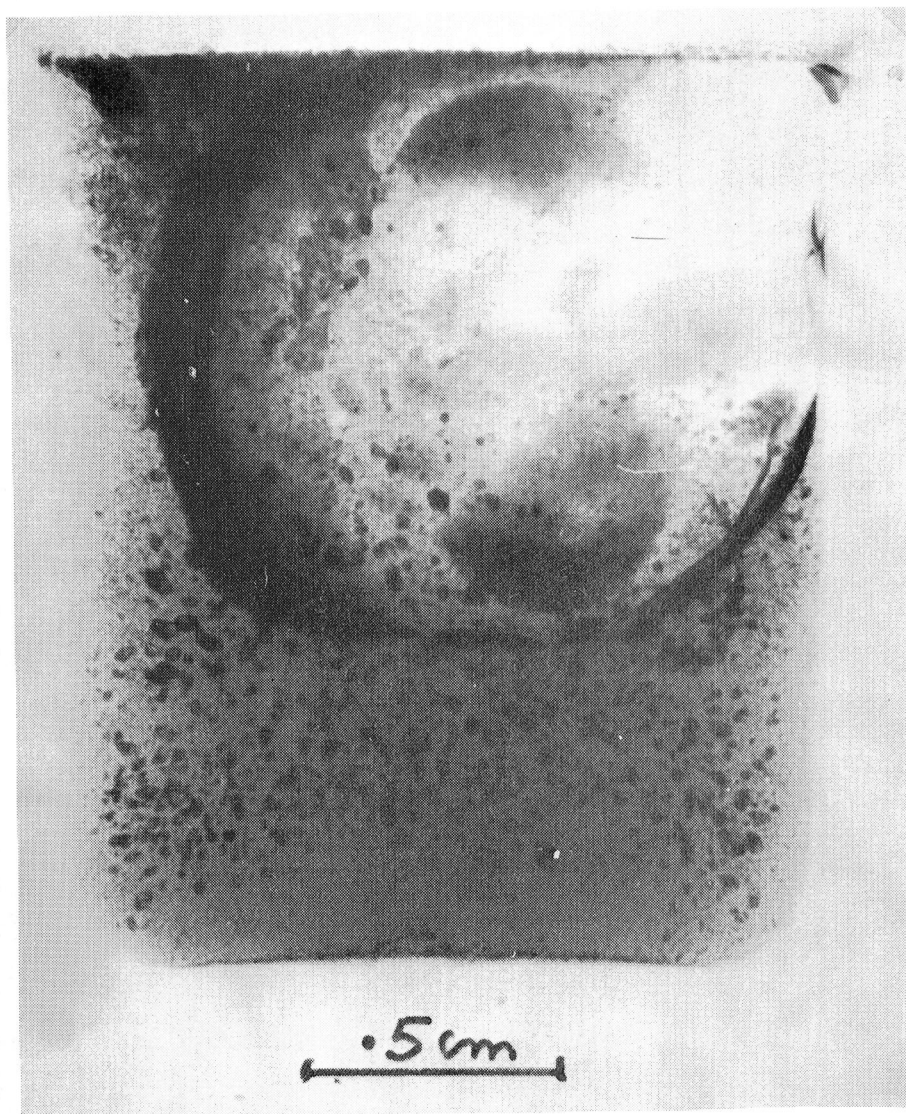
IV-19

Figure 11. X-ray picture of the 32 w % hypermonotectic sample
(76-51/2-Bottom)

The primary indium globules have a more uniform dispersion in the bulk.
Zones next to the crucible side walls are free of globules.

Figure 12. X-ray picture of the 32 w % hypermonotectic sample
(76-51/2-Upper).

Solidification from the free volume zone towards the bottom of the crucible
has led to segregation of the primary indium phase in the shrinkage hole.

Figure 13. Section through the four flight samples showing the location
of the various component phases.

a/ 76-51/1-Upper ; b/ 76-51/1-Bottom ; c/ 76-51/2-Upper
d/ 76-51/2-Bottom.

a

b

Figure 14. Scanning electron microscopy (a) and microanalysis of the free volume surface (b).

These consist of fields of indium and aluminium. No trace of alumina was detected.

IV-23

On the contrary, the two upper samples have only localized indium accumulations inside the shrinkage holes.

Chemical analyses were made on the free globule zone near the crucible walls. Indium concentration values of less than 200 ppm were found.

Microstructures of monotectic matrix (fig. 15).

The matrices are polycrystalline and have an irregular structure. The grain size varies from place to place between 70μ and 200μ.

The monotectic indium phase is present in the grain boundaries and inside the grain, although the shape and size are different : globular for the intragranular indium, about 10μ in diameters, and undefined shape for the intergranular indium, ranging between 5μ and 50μ in size.This is seen on figure 16 and on scanning pictures (fig. 17).

Uniform distribution can be observed on a macroscale over the whole cutting surface of each sample, with the exception of the crucible-alloy interfaces (fig. 18-19-20-21). This is also evidenced after strong chemical etching (fig. 18) which reveals particles and segregations due to solidification.

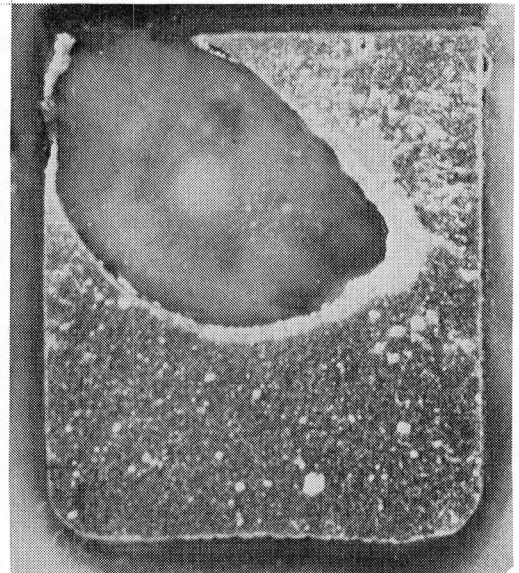In the monotectic composition sample relatively large globules are also identifiable especially in the crucible bottom zone. They are similar to the primary precipitate observed in the richer samples. Chemical analysis of the globule free zone of this sample shown a 11.6 w % indium content. This observation indicates that the monotectic composition according to Predel[3] may not be exact.
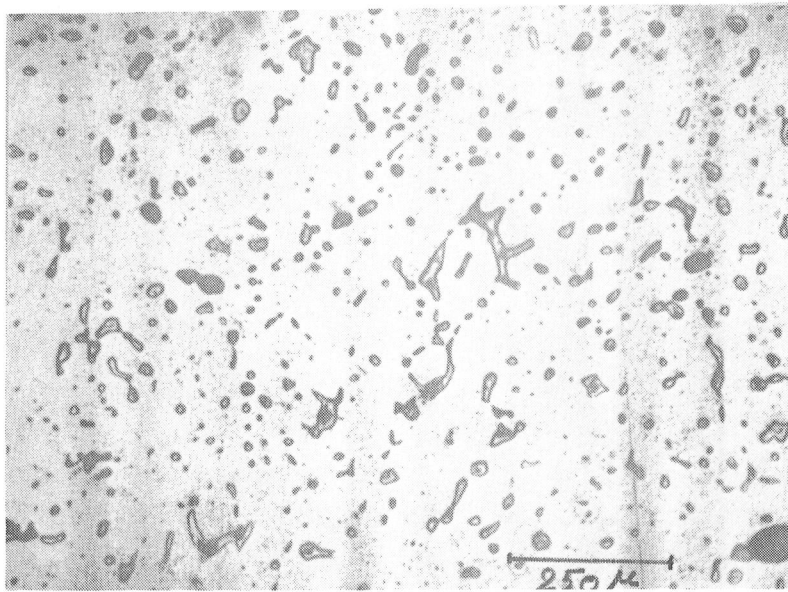
Figure 15. Structure of the monotectic matrix.
Intergranular and intragranular globules are present.
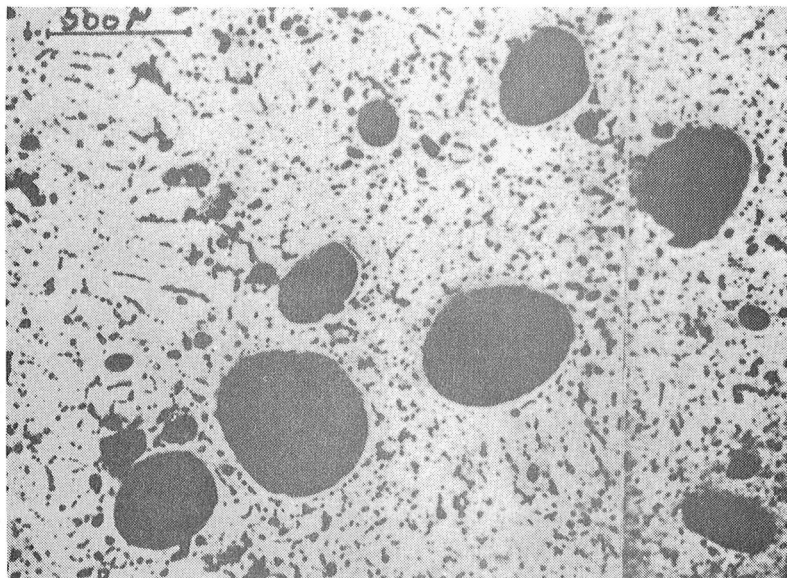
Figure 16. Primary indium phase globules in the matrix.
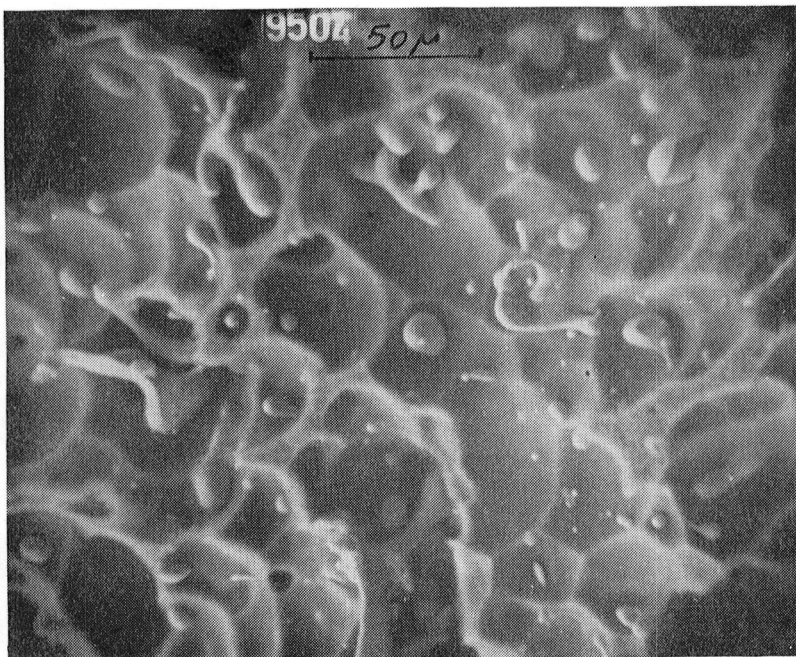
Figure 17. Scanning electron microscopy after selective etching
of the monotectic alloy.

Accumulations of indium phase in various forms can be seen.
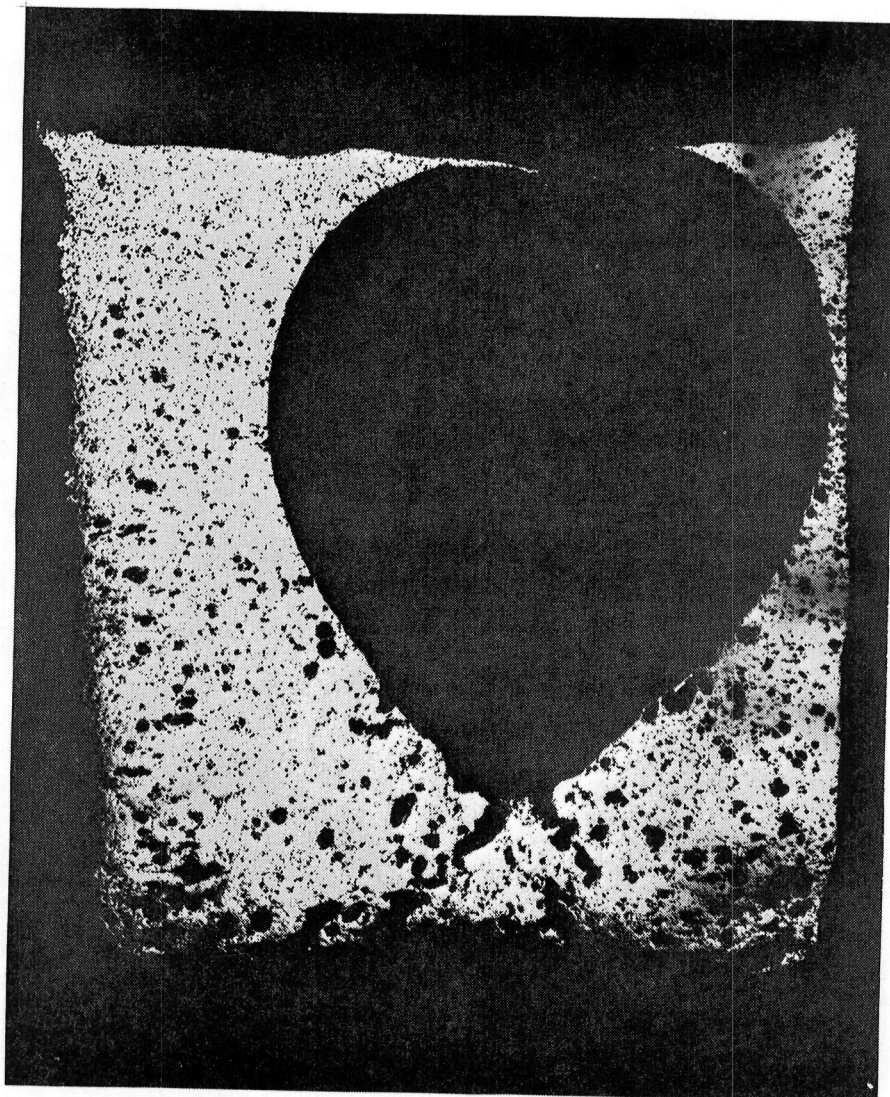
Figure 18. Section through and etching of the sample 76-51/1-Upper
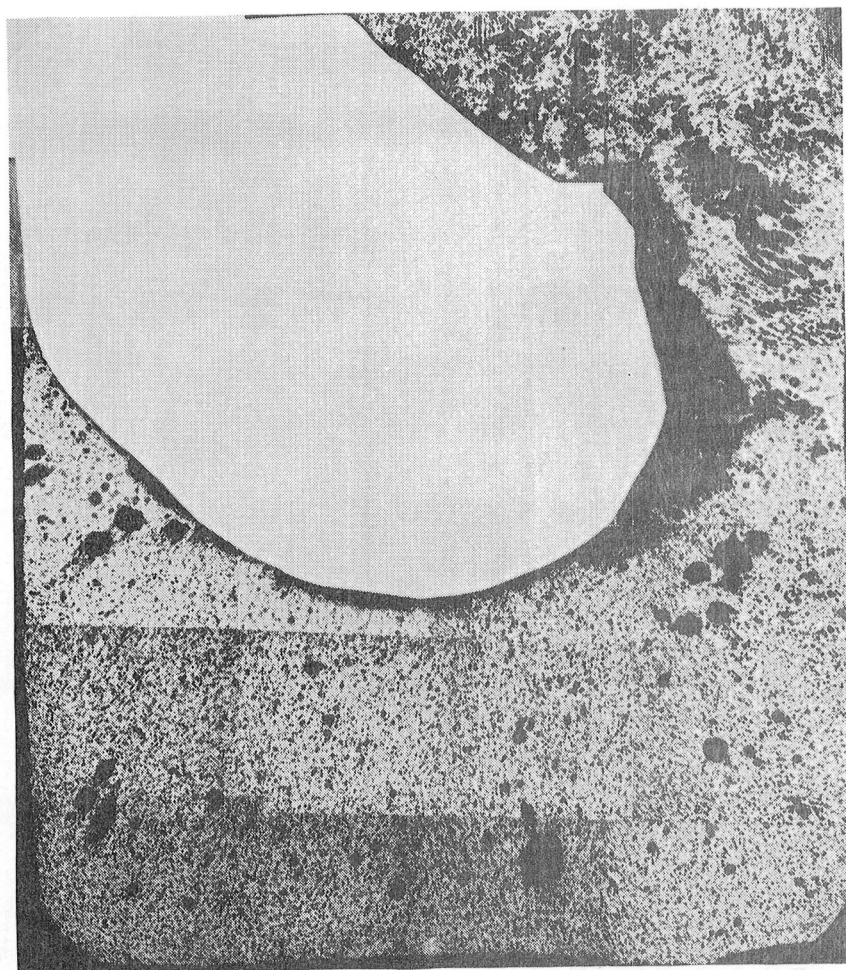
Figure 19. Section through and etching of the sample 76-51/1-Bottom.

Figure 20. Section through and etching of the sample 76-51/2-Upper.
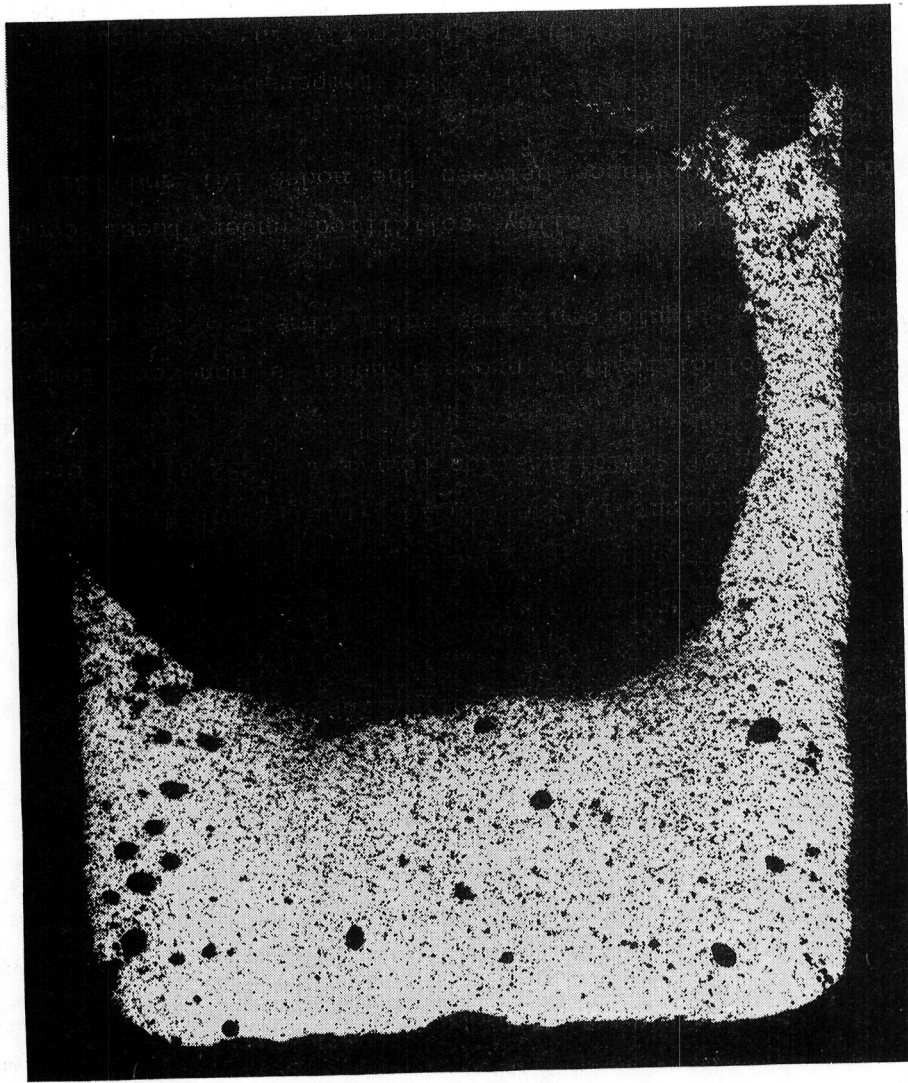
Figure 21. Section through and etching of the sample 76-51/2-Bottom.

Primary phase.

The primary indium phase is dispersed and has a spherical shape in the bulk. The intercepted globules have a unique homogeneous structure. No aluminium-rich dendrites were observed. The reverse solubility of aluminium led to the formation of an epitaxial layer deposited at the interphase limit (fig. 16). This feature is characteristic of diffusion-controlled growth of this layer. The main result of these experiments lies in the preservation of a certain degree of dispersion of the indium primary phase. This result is radically different from those already obtained under microgravity conditions on the same system and compositions (Gelles [5] ; Ahlborn [6]).

The following section will establish the characteristics of this dispersion.

ANALYSIS OF THE STRUCTURE FORMATION

Thermal field analysis.

The analysis of the structure formation is based on knowledge of the thermal field and its variation inside the samples. The thermal field prevailing in the samples was calculated by means of a code which takes into account the two-dimensional geometrical phase changes [4]. The triangular finite elements method was used.

The grid network established to simulate the SPAR cartridge contains 147 nodes which form 240 triangles (fig. 22 and 23).

The following domains are represented :
- ½ sample of the 'Upper' alloy,
- ½ sample of the 'Bottom' alloy,
- ½ of the graphite container surrounding the two samples,
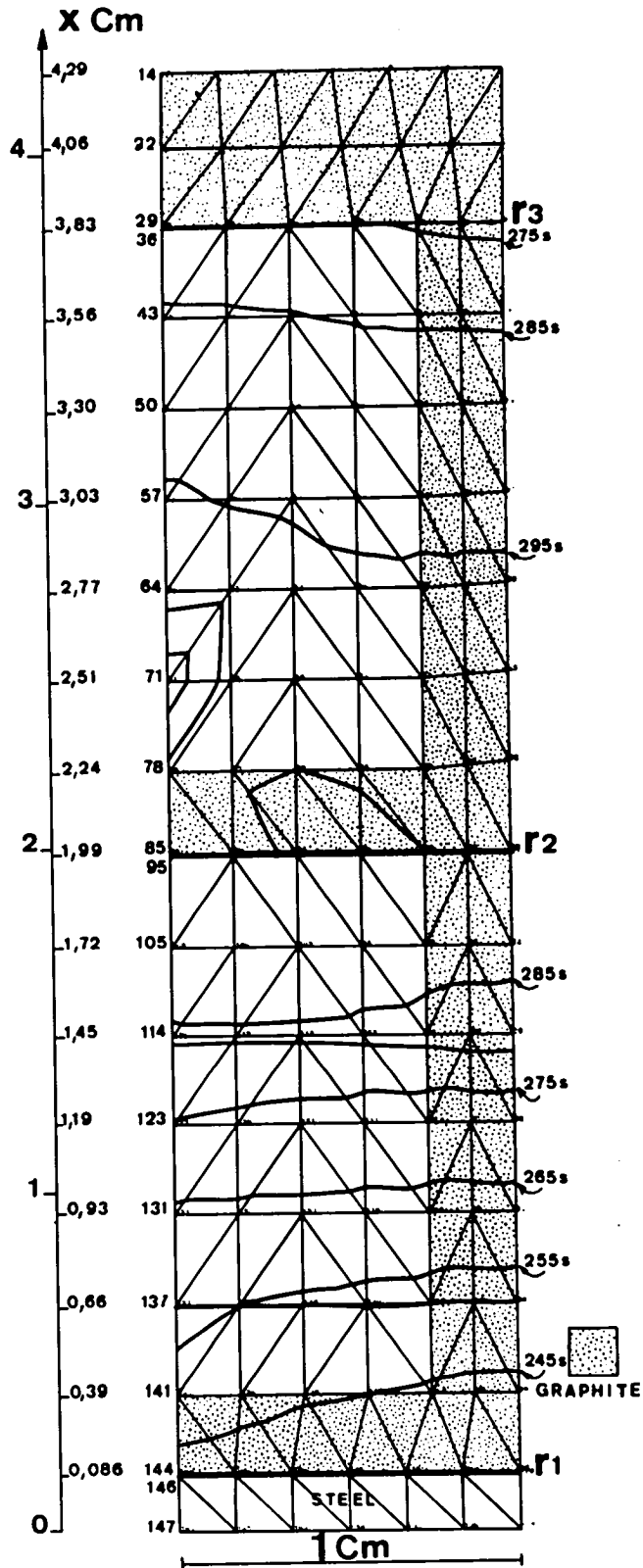
Figure 22. Grid network and position of the 635°C isotherm at different times for the sample 76–51/1–FLT.
Note that this isotherm does not correspond to the 640°C solidification isotherm retained in the present iteration.

IV-32
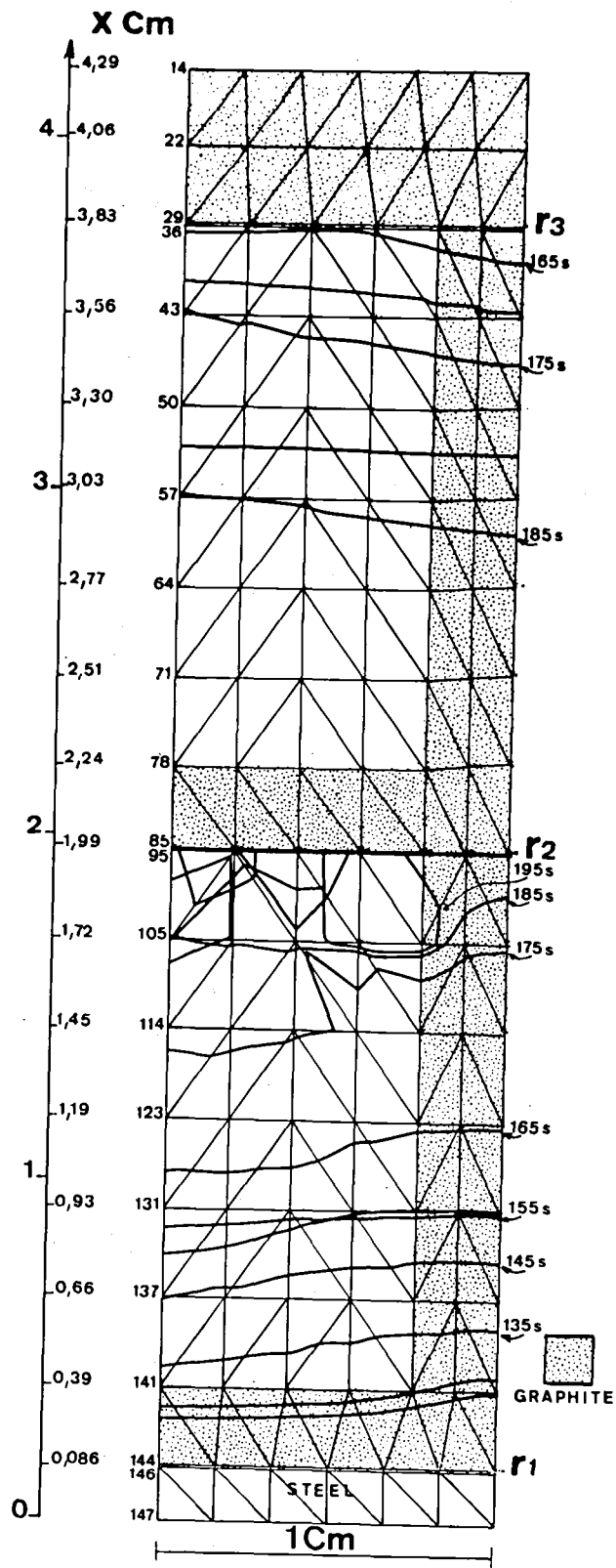
Figure 23.   Grid network and position of the 635°C isotherm at different
times for the sample 76-51/2-FLT.
Note that this isotherm does not correspond to the 645°C solidification
isotherm retained in the present iteration.

- the bottom steel plate,

- three undefined heating resistances r_1, r_2 and r_3 corresponding to the mechanical links between different parts of the structure.

Boundary conditions.

The boundary conditions are as follows : on the upper and bottom planes of the device, the temperatures recorded experimentally during the flight are imposed, and on the lateral surface of the cartridge the heat flux is assumed to be zero.

To facilitate the calculation, different time origins for each cartridge had to be adopted. These correspond to the effective start of the cooling processes which occur at different instants.

For the cartridge 76-51/1-FLT, t_{origin} = 145 s (measured with respect to lift-off time t_o).

For the cartridge 76-51/2-FLT, t_{origin} = 125 s (with respect to t_o).

Calculation conditions.

Steady conditions are calculated first of all in relation to the upper temperature level. The thermal profile thus obtained serves as a basis for calculations under unsteady conditions.

The heating resistance r_1 is then adjusted so that the calculated start of solidification coincides with the start of solidification recorded experimentally. The heating resistances r_2 and r_3 are then adjusted in order to make the calculated end of solidification.

Finally, the process is repeated from the beginning with the resistances r_1, r_2 and r_3 as determined previously and the final adjustments, if any, are made.

	T °C	Thermal conductivity CGS	Specific heat CGS	Density CGS	Latent heat of fusion CGS
ALLOY	0 634 635 (Tf) 1000	1.88×10^7 1.88×10^7 0.836×10^7 0.846×10^7	9.25×10^6 9.25×10^6 8.16×10^6 8.16×10^6	2.978 g/mm^3	1.35×10^7
GRAPHITE		8.37×10^6	1.26×10^7	1.85	
STEEL		1.2×10^6	4.18×10^6	8	

TABLE 4.   Values of parameters considered in the thermal calculation.

Results.

The thermal conductivity values of the various materials are listed in table 4. Figure 24 presents the initial temperature distribution in the steady state before the start of solidification.

a/ 'Low gradient' cartridge (76-51/1-FLT) :

Assuming the following values characterizing the <u>start of solidification</u> (fig. 2) :

On Mid.TC	t = 234 s	T = 636°C
On Bot.TC	t = 234 s	T = 527°C

and the <u>end of solidification</u> (fig. 2) :

On Mid.TC	t = 305 s	T = 567°C
On Bot.TC	t = 305 s	T = 347°C

it was possible to simulate the cartridge behaviour with the following values for the heating resistances :

$$r_1 = 7.69 \text{ cm}^2. \text{ (°K)} . \text{ W}^{-1}$$

$$r_2 = r_3 = 4 \text{ cm}^2. \text{ (°K)} . \text{ W}^{-1}$$

Figure 25 presents the temperature distributions along the axis of the cartridge at different times. The curve at t = 232 s represents the temperature distribution in the 'Upper and Bottom' samples still completely in liquid phase at the moment solidification begins. The temperature gradient in the liquid is at its maximum value and reaches 12.7°C.cm^{-1} on the cold front. The average value of the temperature gradient is 10.2°C.cm^{-1} over a distance of 1.06 cm. The various positions of the solidification interfaces are identified by a break in the curves when the temperature reaches 640°C — calculated solidification level — due to the difference in thermal conductivity between the solid ans liquid phases of the alloy.

IV-36
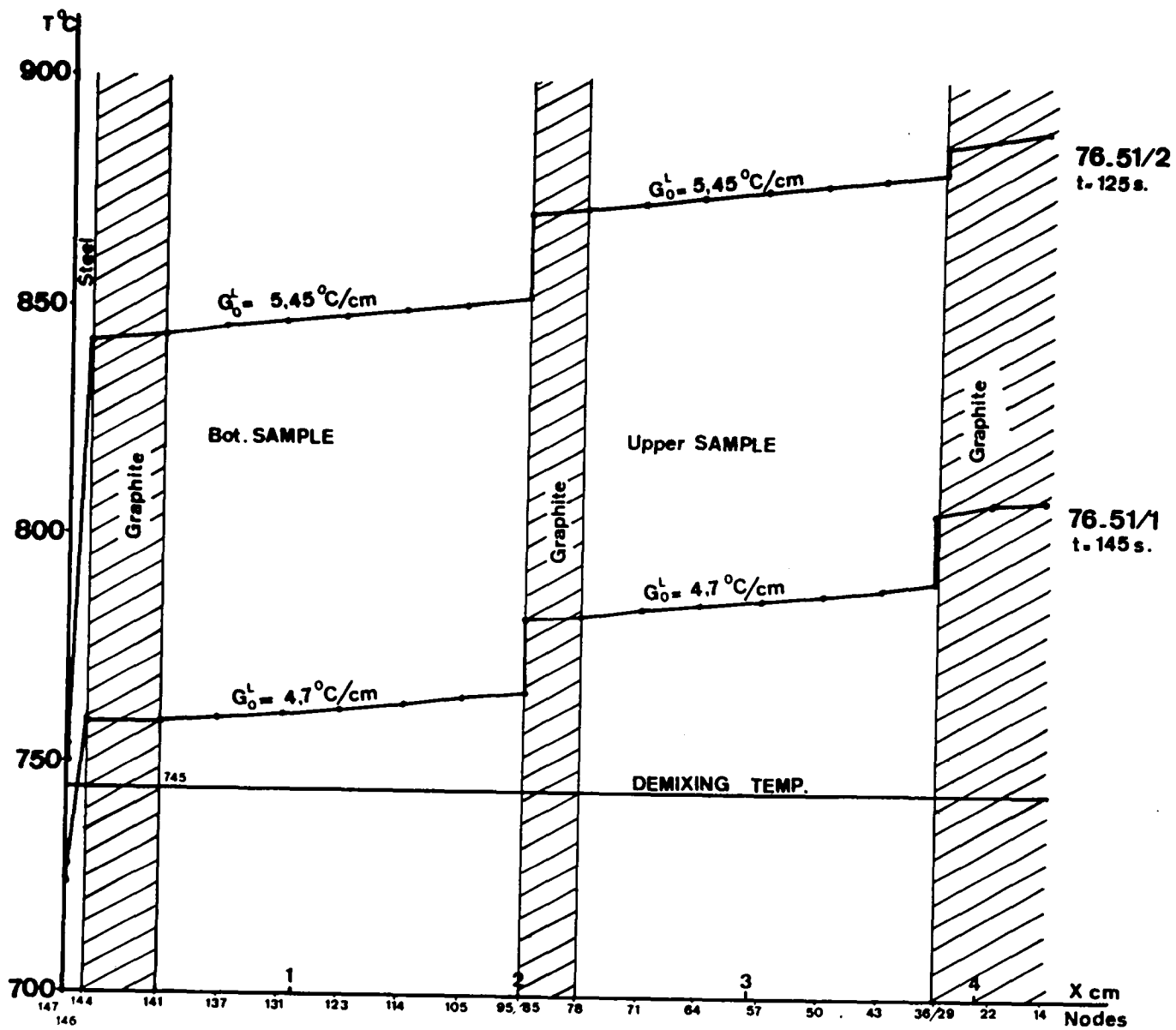
Figure 24.   Initial steady state temperature distribution.
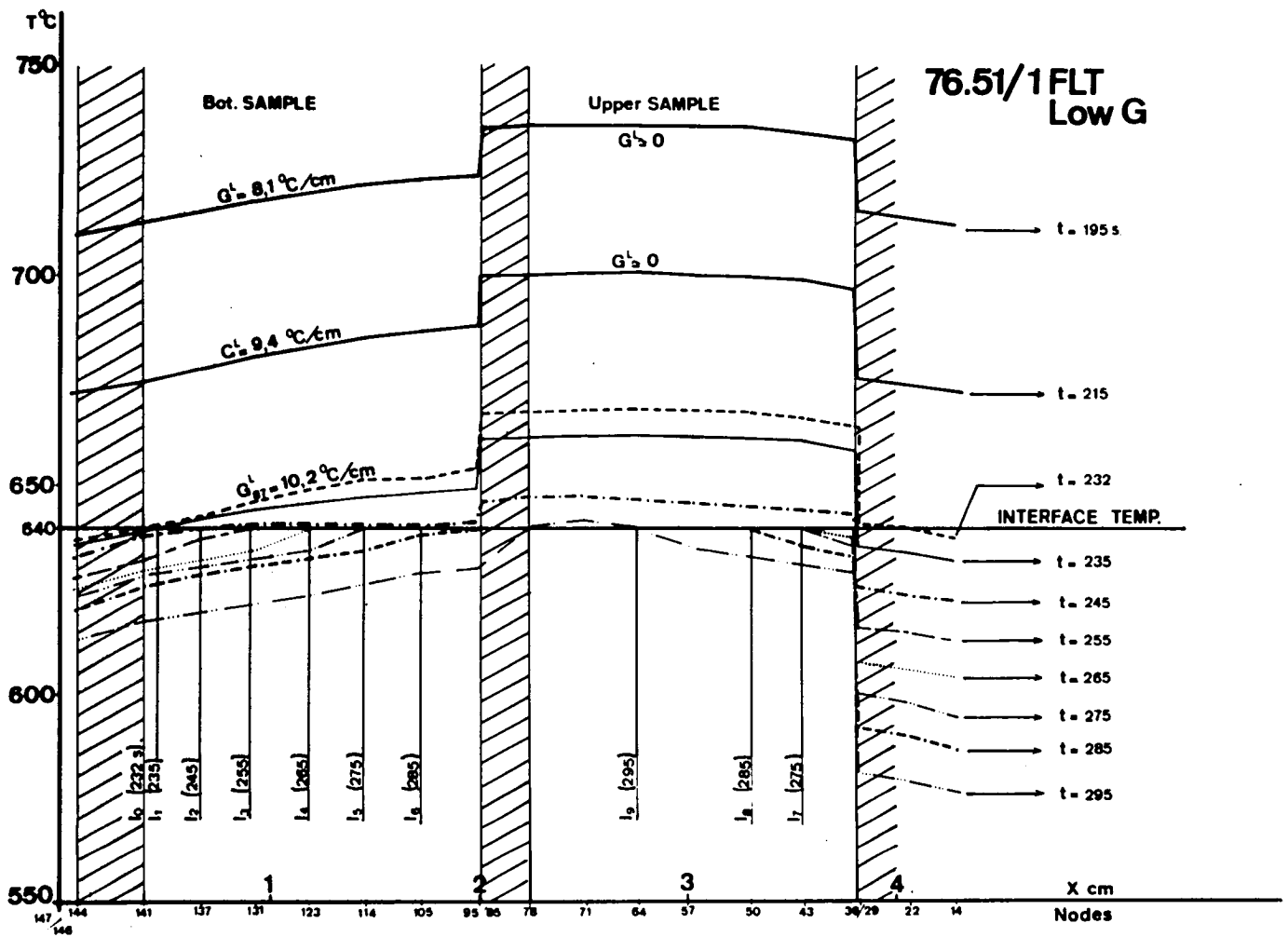
Figure 25. Temperature distribution calculated along the axis of the cartridge 76-51/1 at different times during the flight.

Bottom crucible.

Figure 26 presents the solid/liquid interface as a function of time for this sample.

In this sample, the solidification front advances from the bottom of the crucible towards the free volume with a zero axial thermal gradient in the liquid. This is not exactly the case at the beginning of solidification (curve t = 232 s), as previously mentioned.

The solidification process under a non-zero temperature gradient in the liquid continues until time t = 245 s, i.e., for 13 seconds (table 5).

The length of alloy solidified under these conditions is thus 0.5 cm (distance between the nodes 141 and 131) in the bottom crucible.

Beyond this distance, the temperature gradient in the liquid is zero. This result is perfectly in accordance with the adiabatic type of solidification expected in which the free volume acts as a thermal insulator.

Average solidification front speeds were estimated for the bottom sample (table 5). The graph obtained is plotted on figure 27.

The upper sample solidifies in a zero liquid temperature gradient and in the opposite direction to the bottom sample, i.e., from the free volume zone towards the bottom of the crucible.

Indeed, the end of solidification occurs isotropically on the bottom and sides of the crucible. The average speed is estimated to be 4.1×10^{-2} cm.s^{-1}. This result is in close agreement with observations on the upper sample. The existence of a shrinkage hole at the contact with the bottom of the crucible indicates that the solidification process ended in this zone.
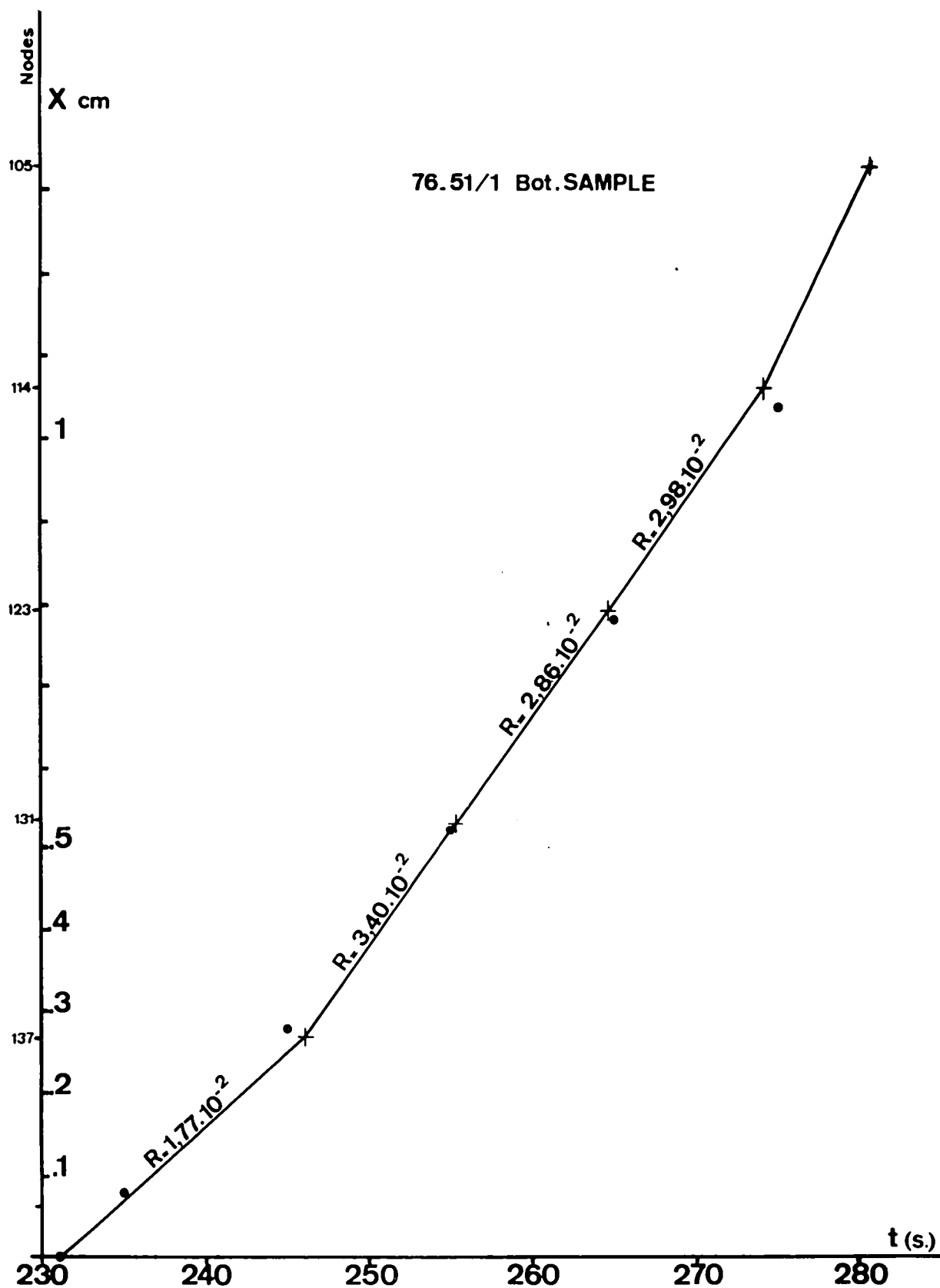
Figure 26.   Position of the solidification interface in relation to time in
the sample 76-51/1-Bottom.

IV-40

t s	Position of interface nodes	Distance above bottom of crucible cm	G^L °C.cm^{-1}	Average speed R cm.s^{-1}	Remarks
145			4.7		
195			8.1		
215			9.4		
232	(141) Start of solidif.		12.7		
235	I_1 :	0.07		1.77 x 10^{-2}	$\dfrac{G^L}{R} \simeq 415$
245	I_2 :	0.27			
247	(137) :	0.266	2.0		
255	I_3 :	0.520		3.40 x 10^{-2}	0
	(131) :	0.538	0	2.86 x 10^{-2}	0
264	(123) :	0.795	0		
265	I_4 :	0.780		2.98 x 10^{-2}	0
273	(114) :	1.063	0		
275	I_5 :	1.050		R not significant in the V.L. zone	0
281	(105) :	1.329	0		

TABLE 5. Values of solidification parameters of the sample 76-51/1-bottom in relation to time.
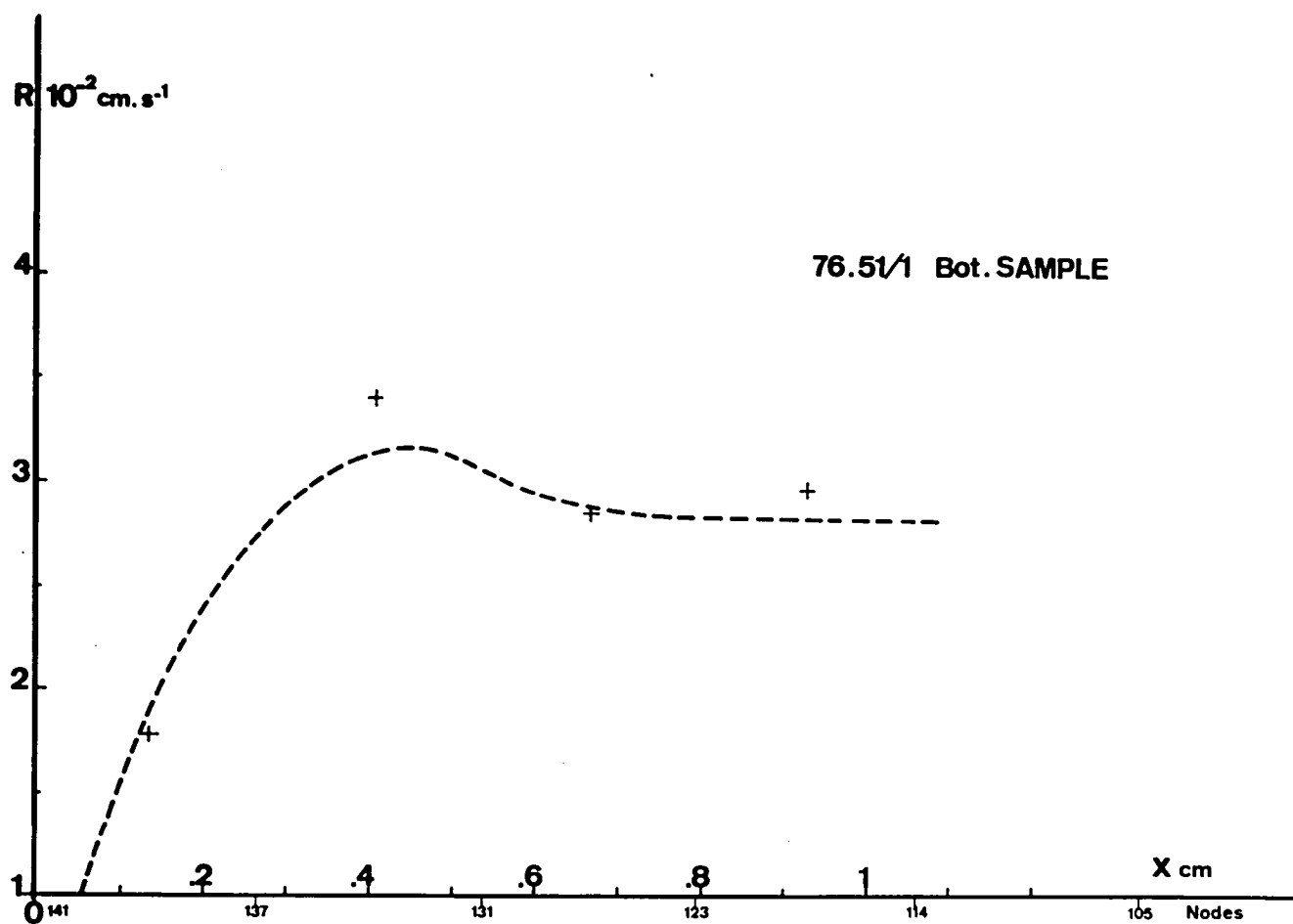
Figure 27. Solidification speed as a function of distance
(sample 76-51/1-Bottom).

b/ 'High gradient' cartridge (76-51/2-FLT) :

The solidification starting and end times were more difficult to determine because of the considerable thermal disturbance already mentioned (fig. 3).

Start of solidification :

On Mid.TC	t = 230 s	T = 650°C
On Bot.TC	not determined	not determined

End of solidification :

On Mid.TC.	t = 291 s	T = 563°C
On Bot.TC	not determined	not determined

Cartridge behaviour was simulated by making r_1 variable between 19.6 and 16.7 cm^2.(°K).W^{-1}, r_2 = 4 cm^2.(°K).W^{-1} and r_3 = 1.43 cm^2.(°K).W^{-1}.

The uncertainty in this case is greater as a result of the unaccuracy of the transformation points. Figure 28 gives the shape of the temperature distributions in the cartridge between t = 195 s and t = 275 s.

The solidification plateau given by the numerical adjustment is at T = 645°C or 10°C above the actual fusion temperature, and starts at t = 210, i.e., 20 s earlier than the actual time.

In this case as well, the 'bottom' and 'upper' samples solidifiy in opposite directions. Figure 29 presents the positions of the interface as a function of time for the 'bottom' sample. The thermal gradients in the liquid rapidly reduce to zero after solidification of a few millimetres of the alloy.
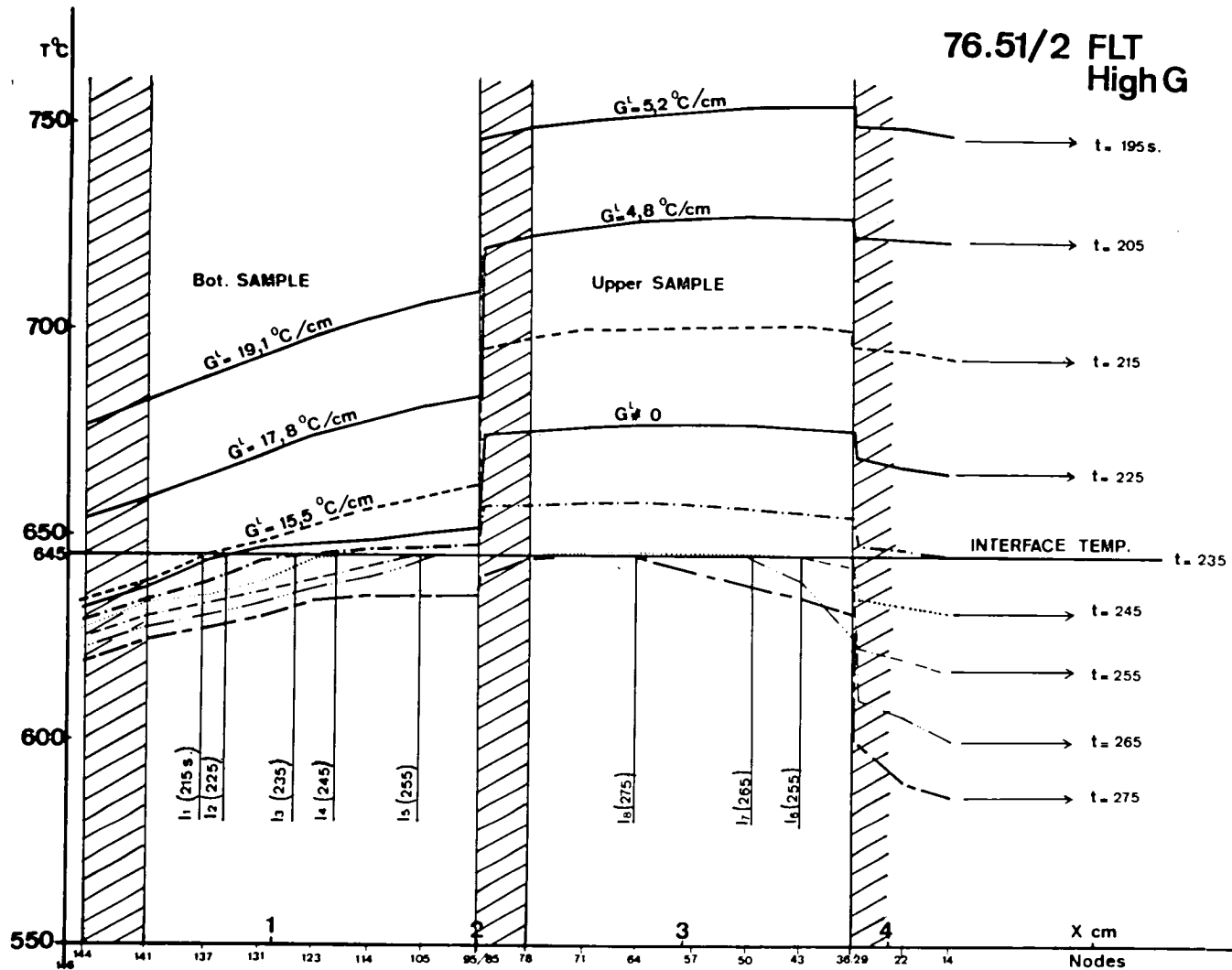
Figure 28. Calculated temperature distribution along the axis
of the cartridge 76-51/2 at different times during the flight.
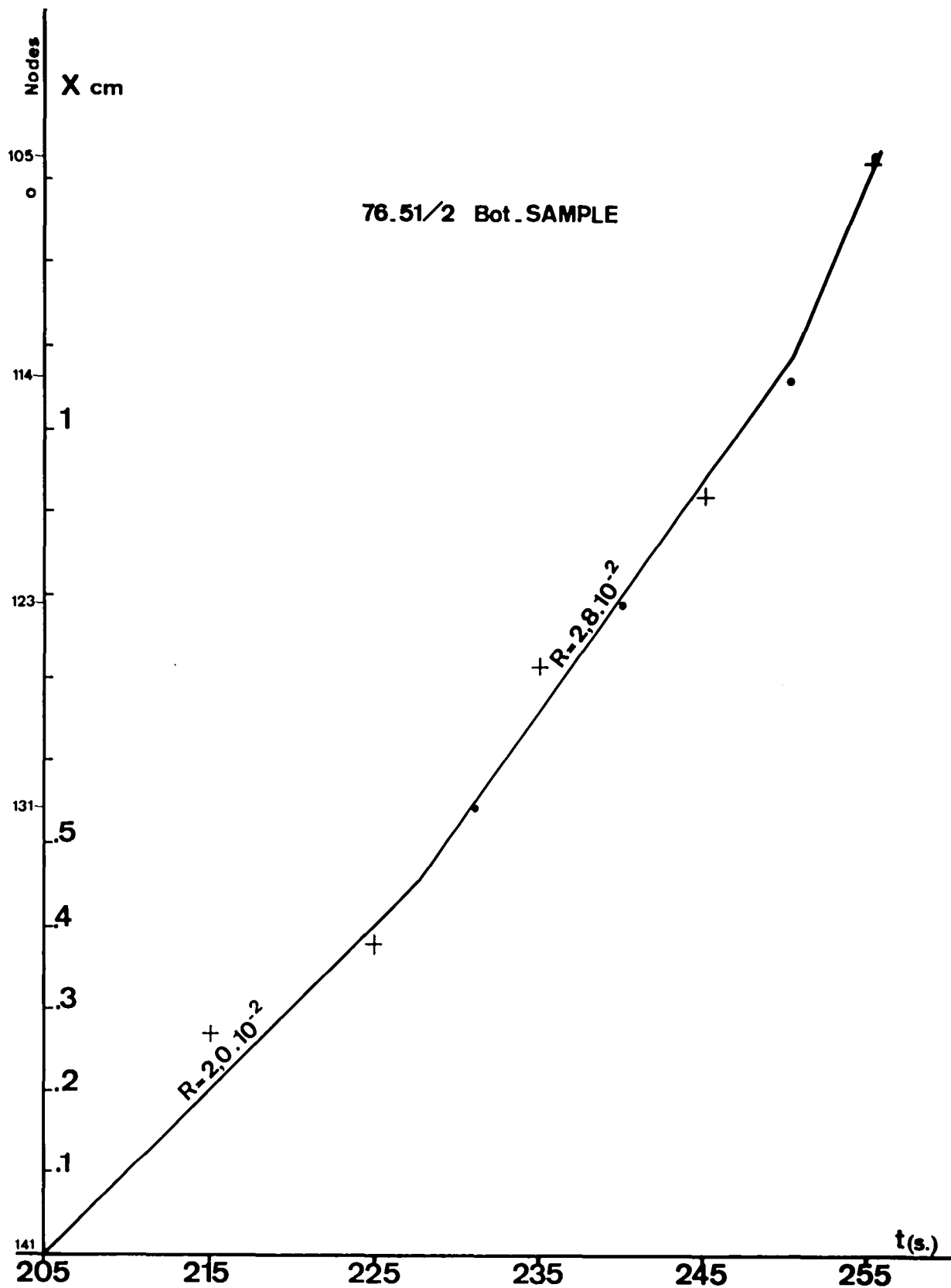
Figure 29.   Position of the solidification interface as a function of time
(sample 76-51/2-Bottom)

IV-45

For example, for t = 225 s, the solidified length is about 0.40 cm with G^L at the interface equal to $4°C.cm^{-1}$ (profile t = 225 s, fig. 26).

Beyond this time, the gradient at the interface is zero. Table 6 presents the values of G^L recorded at different times and the average solidification speed of the 'bottom' sample.

It can be seem that relatively high thermal gradients were obtained in the liquid before solidification as a result of the considerable directional cooling achieved at the start of the experiment. However, these gradients in the sample could have been much higher if the temperature drops caused by the presence of large free volumes – simulated by the heating resistances r_2 and r_3 – and the mechanical junctions – resistance r_1 – were minimized.

The thermal calculation presented in this chapter includes imperfectly defined boundary conditions which reduce the accuracy of the results. The hypothesis of zero flux on the side walls of the cartridge is a rough approximation since the cooling effect induced by the helium flux is essentially radial.

With this hypothesis, it was not possible to calculate the radial gradient in the sample, although this can be obtained by determining the curvature of the solidification isotherms.

The results presented here are therefore only strictly valid along the cartridge centre-line for which radial gradients are zero. An important fact resulting from this study is the determination of the solidification direction which reverses for the 'Upper' sample. Taking into account macrosegregations observed, it seems certain that the solidification interface by globule repulsion is responsible for this accumulation. The thermal field has only a minor effect on the formation of this structure.

t s	INTERFACE Position (on graph or node)	Distance above bottom of crucible cm	Speed cm.s^{-1}	G^L °C.cm^{-1}	$\frac{G}{R}$ °C.cm^{-2}s
145				5.5	
195				19.1	
205	(141)	0		17.8	Start of solidific.
210				16.6	$\simeq$830
215	I_1	0.20	$R=2 \times 10^{-2}$	15.5	$\simeq$775
225	I_2	0.40		$\simeq$3.8	$\simeq$190
227,5		0.45		~0	0
231	(131)	0.54		0	0
235	I_3	0.66		0	0
240	(123)	0.80	$R=2.8 \times 10^{-2}$	0	0
245	I_4	0.94		0	0
250	(114)	1.06		0	0
255	(105)	1.34		0	End of solidification

TABLE 6. Values of solidification parameters of the sample 76-51/2-bottom in relation to time.

ANALYSIS OF PRIMARY INDIUM PHASE DISPERSION

Aim.

The aim of the analysis presented is to link the primary indium globule dispersion structure in the solid state to the conditions achieved during liquid phase cooling and then during directed solidification.

The initial phenomenon of germination and growth of dispersion could be ignored at this analysis stage in view of the comparative mode adopted for this study. It should not be forgotten that the samples have the same composition - except one monotectic reference sample - and are subjected to the same initial dispersion formation conditions.

The analysis is based on the determination of spatial and diameter size distributions of the primary indium phase and on the calculation of the thermal fields presented in the previous chapter.

Method of analysis.

Since the statistical analysis should cover the maximum number of globules, the metallographic section examination, which intercepts only a limited number of globules, had to be abandoned in favour of X-ray analysis of samples taken as a whole. X-rays have the advantage of giving a direct indication of the volume of globules that the metallographic examination could only give by the use of statistical models.

The significant difference in absorption power between indium and aluminium for the radiation used (MoK_α ; μ_{In} = 31.8 ; μ_{Al} = 5.30) is, in addition, a very favourable factor for obtaining good contrast for identifying the globules.

However, considerable energy was required in order to maintain sufficient transparency of the indium and thus discriminate the superposed globules (E = 140 kV - 5 mA).

This high energy promotes aluminium scattering and leads to a loss of definition of the pictures. In addition, the fine structure of the monotectic alloy creates a continuous background on which only a certain number of globules appear. Figure 30 shows the X-ray viewing set-up.

The X-ray pictures were photographed and enlarged by a factor of 7.4. Morphological counting and identification were carried out on these transparent enlargements using gauges of 0.3, 0.5, 1.0, 1.5, 2.0, 2.5, 3.0, 3.5 and 4.0 mm diameter, thereby representing true sizes of 40, 67, 135, 200, 270, 340, 400, 470 and 540 microns. Population categories based on these diameters were thus identified. The first gauge of 40μ corresponds to the lowest limit of globule discernability.

This radiographical method was refined by the use of stereographic viewing thanks to which it was possible to clear up numerous uncertainties concerning the morphology of indium accumulations. These accumulations were thus able to be resolved into globules with a high degree of credibility.

Distribution.

Under these conditions, the spatial distribution of the globules observed in the four half samples was plotted. Figures 31 to 34 are the results of the X-ray transcriptions from which the distributions presented in tables 7 to 10 were obtained.
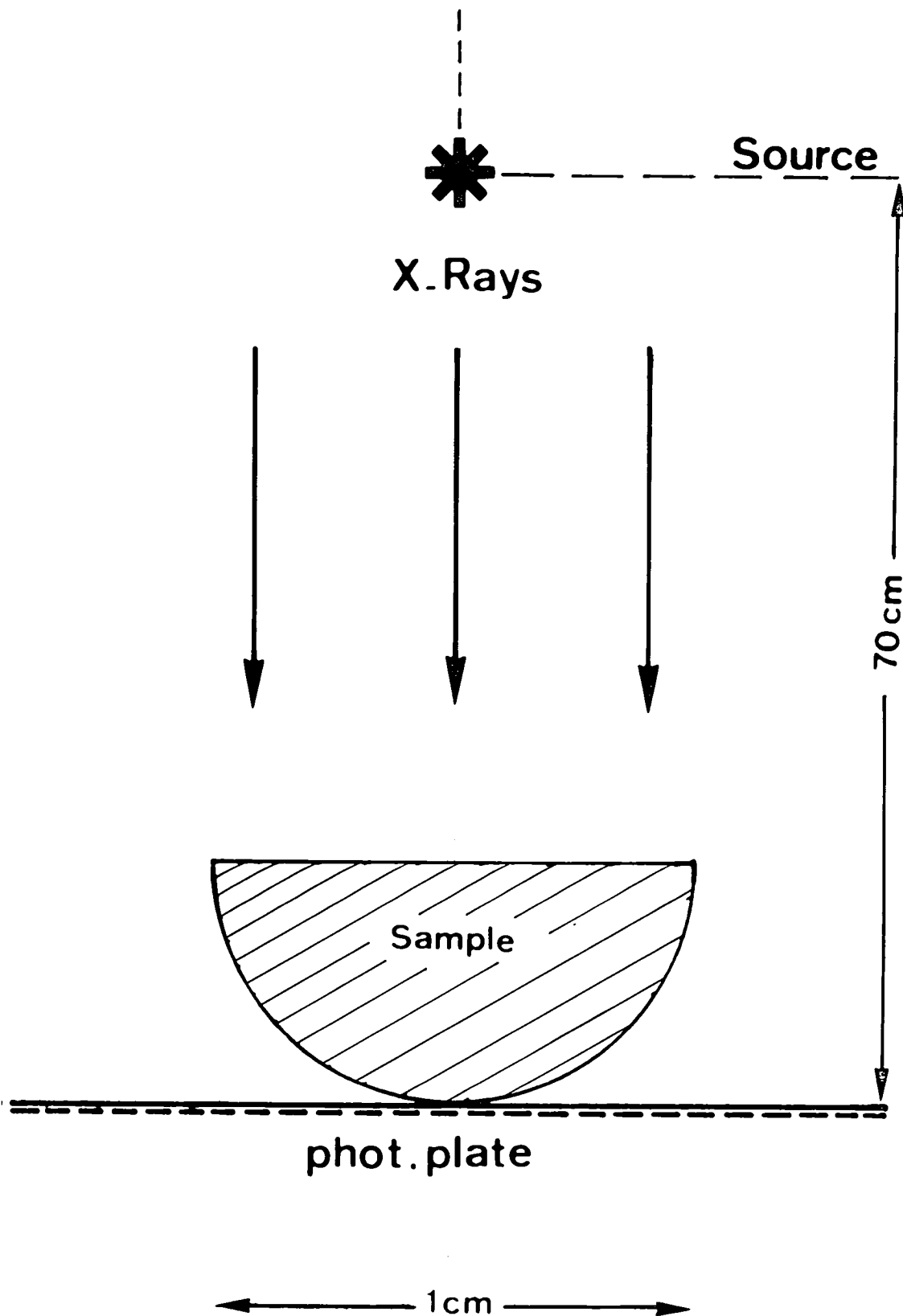
Figure 30. Diagram of the X-ray examination method.
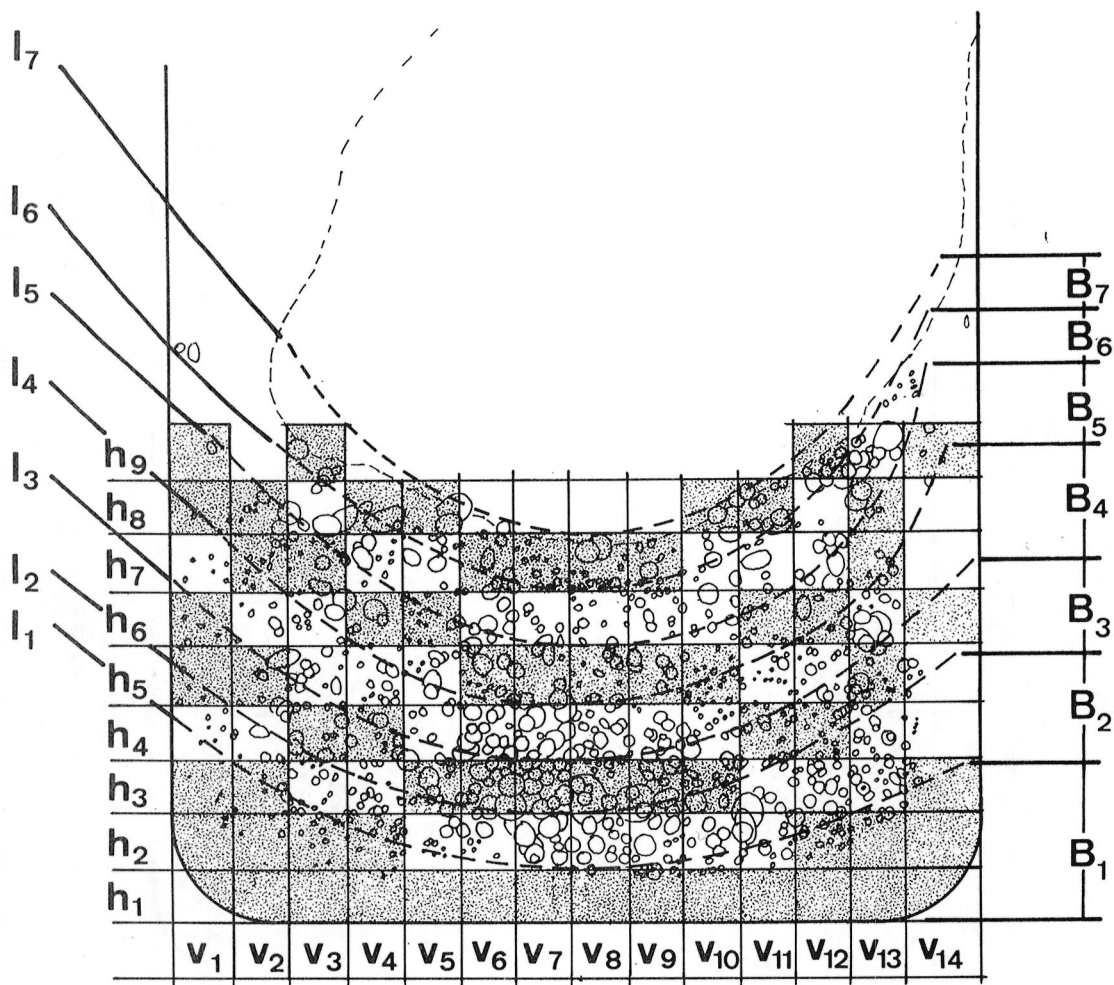
76.51/1 Bot.

Figure 31.   Chart of indium phase spatial distribution in the sample
76-51/1-Bottom.
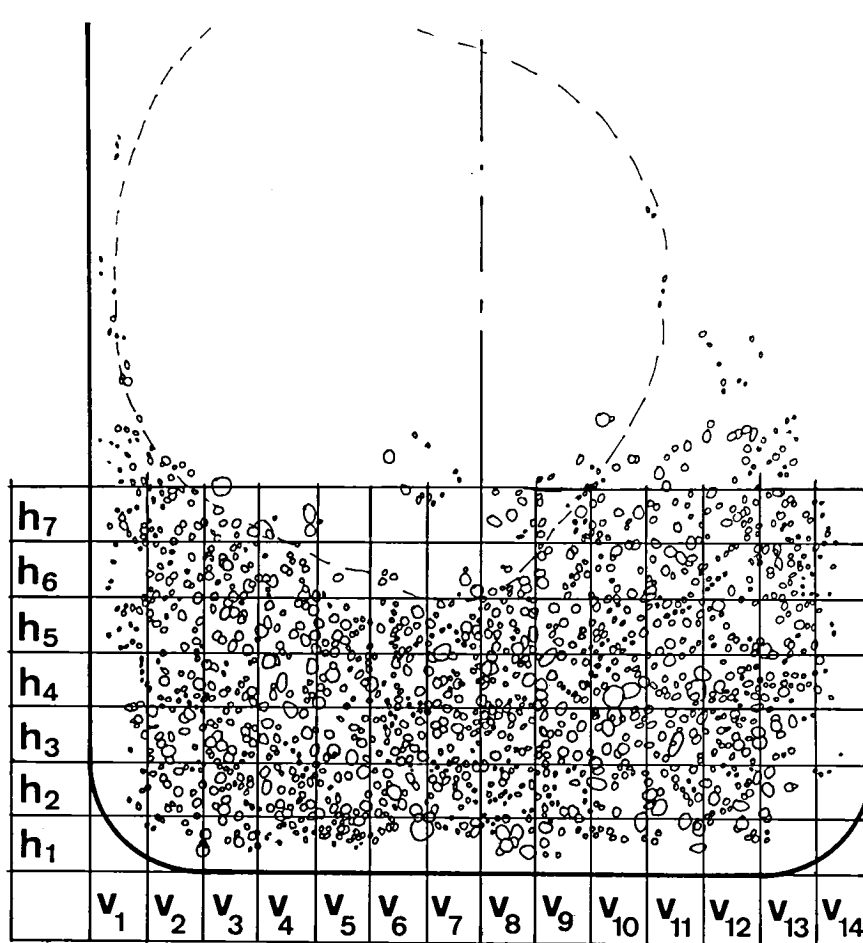
76.51/1 Up.

Figure 32. Chart of indium phase spatial distribution in the sample 76-51/1-Upper.

76.51/2 Bot.

Figure 33.   Chart of indium phase spatial distribution in the sample
76-51/2-Bottom.

76.51/2 Up.

Figure 34. Chart of indium phase spatial distribution in the sample 76-51/2-Upper.

Table 7. Matrix with rows H_1–H_9 and columns V_1–V_{14}. Each cell contains a 3×3 array of values (hatched cells are shaded; "0" indicates a single zero). The central legend gives MICRONS scale values.

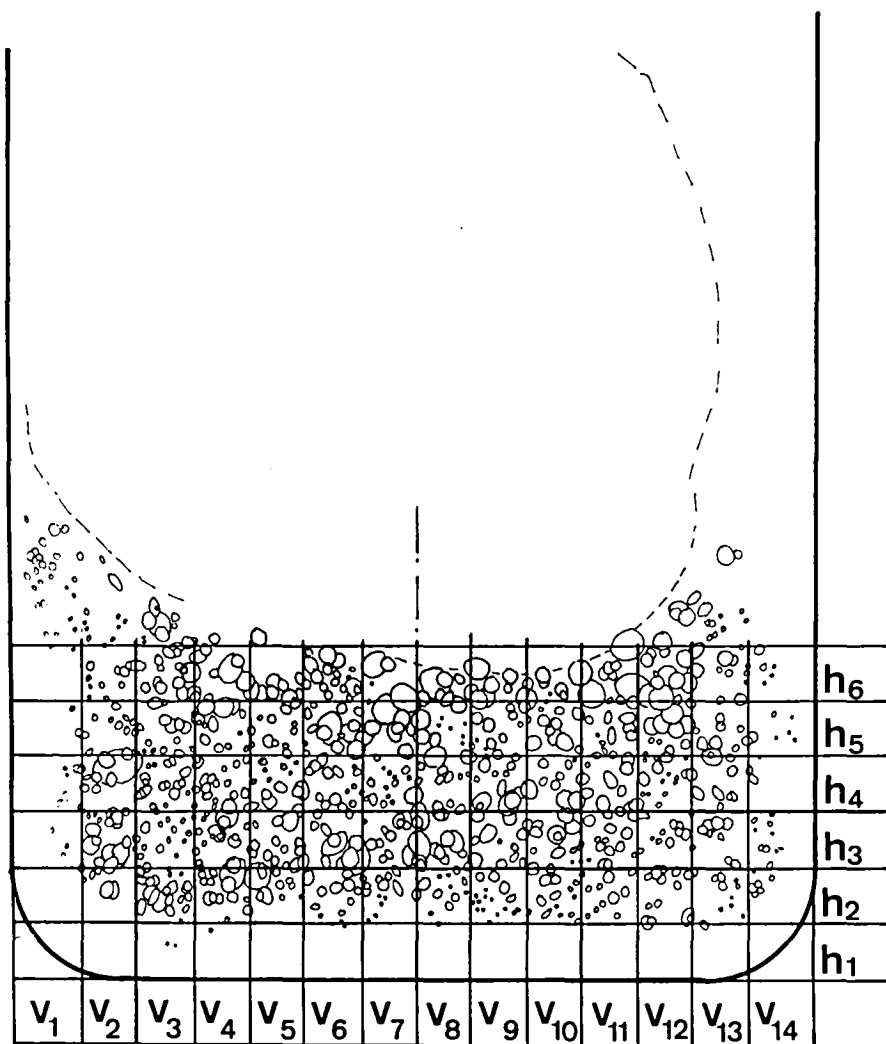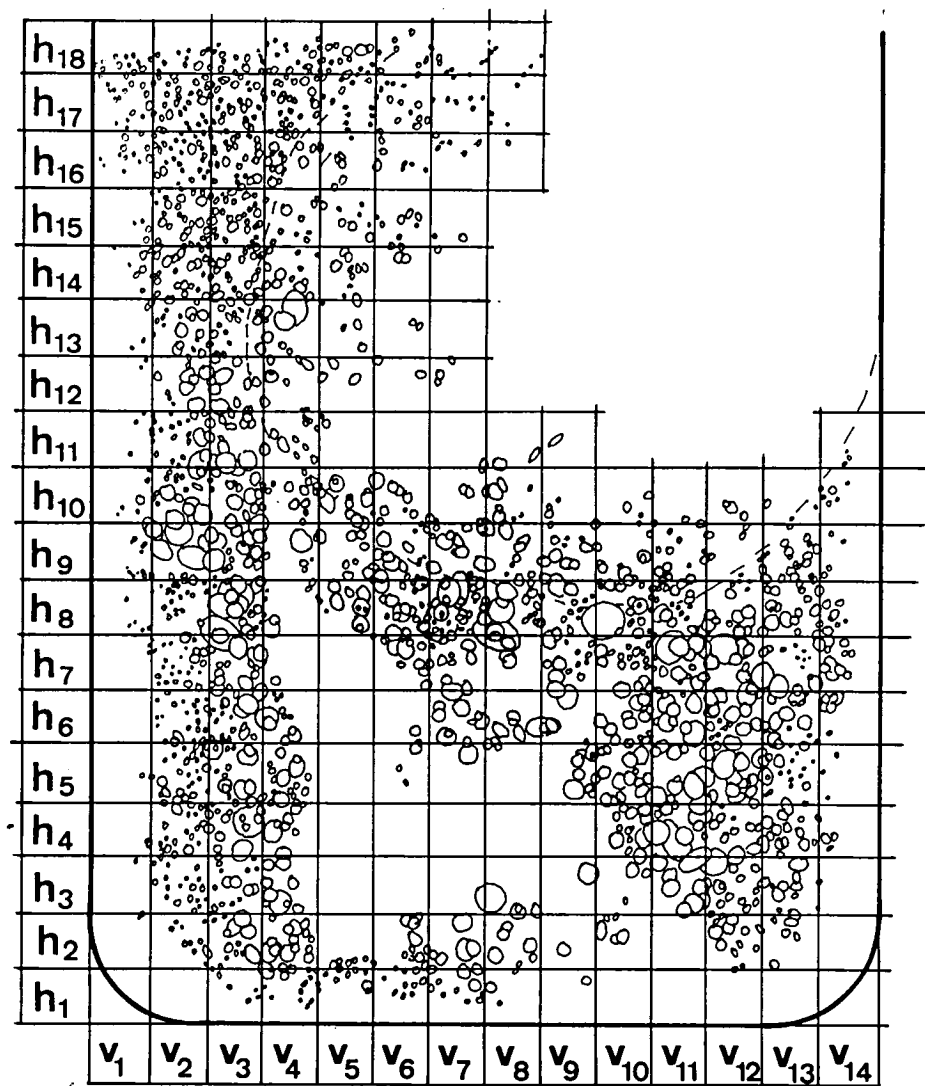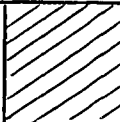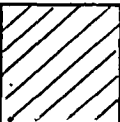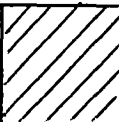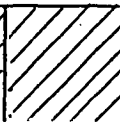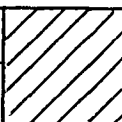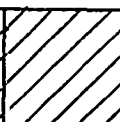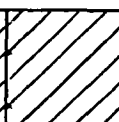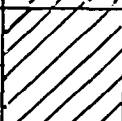|	V_1	V_2	V_3	V_4	V_5	V_6	V_7	V_8	V_9	V_{10}	V_{11}	V_{12}	V_{13}	V_{14}
H_9	- - - / 1 - - / - - -	▨	- - 1 / 1 1 1 / - - -	▨	▨	▨	MICRONS / 40 67 135		▨	▨	▨	- 2 1 / 1 - - / - - -	- - 4 / 4 1 - / - - -	- 2 - / 2 - - / - - 1
H_8	1 2 - / - - - / - - -	3 - 1 / 1 1 - / - - -	- - - / 2 - - / 2 - -	- - 1 / 1 - - / 1 - 1	- - 1 / - - - / - - -	- - 1 / 1 - - / 1 - 1	200 270 340 / 400 470 540		▨	- - - / - 1 - / - - -	- 1 - / 4 3 - / 1 - -	- 2 - / 1 1 - / - - -	- 1 2 / - 2 1 / 1 - -	- - 1 / - - - / - - -
H_7	1 5 - / - - - / - - -	- 9 2 / - - - / - - -	- 7 - / 1 1 - / - - -	2 5 1 / - 1 1 / - - -	- 3 1 / - 2 - / - - -	1 1 - / 2 2 - / - - -	4 3 4 / 1 - - / - - -	3 7 - / 1 - - / 2 - -	1 5 2 / - 1 - / 2 - -	1 2 1 / 1 2 - / - - -	- 2 1 / 1 - - / - 1 -	- 1 2 / 3 1 1 / - - -	- 2 2 / 3 - - / - - -	0
H_6	- 2 2 / - - - / - - -	- 2 2 / 2 - - / - - - 1	- 3 2 / 2 1 1 / 1 - -	- 1 2 / 1 - - / 1 - -	3 7 1 / 1 - - / - - -	- - - / 5 1 - / - - -	- 3 3 / 1 - - / - - -	1 4 1 / 2 - - / - - -	- 11 2 / 2 - - / - - -	- 2 3 / - 1 - / - - -	- 6 - / 4 - - / - - -	- 2 2 / - 1 - / - - -	2 1 3 / 2 2 - / 1 1 -	- - 1 / - - - / - - -
H_5	- 3 2 / - - - / - - -	- 2 1 / 1 - - / - - -	- 3 6 / 2 - - / - 1 -	- 5 4 / 3 - - / - - -	3 1 3 / 2 1 - / - - -	2 3 2 / 2 2 - / - - -	- 1 - / 1 3 - / - - -	4 3 2 / 2 - - / - - -	- - - / 2 2 - / - - -	12 4 2 / - - - / - - -	8 3 - / 3 - - / - - -	3 6 1 / 3 - - / - - -	4 1 7 / 1 2 - / - - -	2 1 1 / 1 - - / - - -
H_4	3 3 1 / - - - / - - -	- 1 - / 1 3 - / - - -	- 2 3 / 1 3 - / - - -	- 5 1 / 3 1 - / - - -	- 1 3 / 1 - - / - - -	- 1 1 / 6 2 1 / - - -	- 1 1 / 1 5 2 / 1 - -	- - 6 / 4 3 - / - - -	2 2 3 / 5 - - / - - -	5 1 3 / 3 1 - / - - -	4 3 1 / 3 - - / - - -	7 4 1 / 1 - - / - - -	- 4 5 / 3 1 - / - - -	4 1 1 / - - - / - - -
H_3	5 - - / - - - / - - -	- 4 3 / 1 - - / - - -	4 7 - / 3 1 - / - - -	- 1 10 / - - - / 1 - -	- 1 5 / 2 - 1 / 1 - -	- - 1 / 7 - 2 / - - -	- - - / 7 3 - / 1 - -	- 4 4 / 2 3 - / - - -	- - 1 / 3 2 - / 2 - -	- 5 6 / - 1 1 / - - -	- 5 1 / 3 - - / - - -	- 6 5 / 4 1 - / - - -	4 5 6 / 2 - - / - - -	- 1 5 / - - - / - - -
H_2	- - 2 / - - - / - - -	- 3 1 / - - - / - - -	2 9 2 / - - - / - - -	3 9 1 / - - - / - - -	4 3 - / 3 - - / - - -	3 2 - / 2 1 - / 1 - 1	- - 3 / 1 2 3 / 1 - -	- 1 2 / 3 3 - / - - -	1 1 3 / 4 2 - / 1 - -	2 2 - / 4 1 - / - - -	- 4 3 / 2 1 - / - 1 1	- 5 4 / 2 2 - / - - -	1 5 - / 1 - - / - - -	0
H_1	0	0	0	2 - - / - - - / - - -	0	0	0	1 - 1 / - - - / - - -	4 3 - / - 1 - / - - -	2 2 - / - - - / - - -	1 - - / - - - / - - -	0	0	0

TABLE 7.   76-51/1-Bottom

IV-55

MICRONS

	40	67	135
	200	270	340
	400	470	540

	V1	V2	V3	V4	V5	V6	V7	V8	V9	V10	V11	V12	V13	V14
H6	2 5 0 - - - - - -	3 10 4 - - - - - -	5 12 3 2 - - - - -	2 9 3 1 - - - - -	1 - 1 - - - - - -	- 1 2 - - - - - -	1 1 - 1 - - - - -	1 5 4 - - - - - -	2 7 5 1 - - - - -	1 5 5 - - - - - -	2 8 6 5 - - - - -	3 8 2 - - - - - -	10 14 5 - - - - - -	2 4 1 - - - - - -
H5	5 12 - - - - - - -	3 7 6 1 - - - - -	3 - 8 1 - - - - -	- 5 6 2 - - - - -	2 9 5 1 - - - - -	2 13 4 1 - - - - -	3 10 5 1 - - - - -	2 9 9 2 - - - - -	1 6 5 - - - - - -	4 15 7 - - - - - -	5 10 5 - - - - - -	2 10 2 1 - - - - -	4 7 3 - - - - - -	3 - 1 - - - - - -
H4	4 1 - - - - - - -	8 9 2 1 - - - - -	2 10 8 - - - - - -	- 8 2 3 - - - - -	- 13 5 2 - - - - -	5 9 4 1 - - - - -	2 7 10 - 1 - - - -	1 10 8 2 - 6 - - -	1 8 5 3 1 - - - -	5 6 2 - 1 1 - - -	- 7 6 2 1 - - - -	2 10 7 1 1 - - - -	1 13 4 2 - - - - -	1 2 2 - - - - - -
H3	1 4 2 - - - - - -	5 5 6 3 - - - - -	1 13 5 4 - - - - -	3 6 3 2 1 - - - -	1 4 4 3 - - - - -	5 13 7 - - - - - -	2 14 4 1 - - - - -	2 10 9 - - - - - -	- 8 6 2 - - - - -	2 9 4 1 2 - - - -	- 5 9 - 1 - - - -	- 15 4 2 - - - - -	4 3 2 3 - - - - -	1 - - - - - - - -
H2	- 4 - - - - - - -	5 6 4 - - - - - -	4 11 3 2 - - - - -	6 8 7 1 - - - - -	3 7 5 2 - - - - -	1 6 6 1 1 - - - -	7 10 7 - - - - - -	10 9 3 - - - - - -	10 7 1 1 - - - - -	- 8 2 1 1 - - - -	4 5 6 1 1 - - - -	6 11 3 3 - - - - -	- 1 2 2 - - - - -	1 2 - - - - - - -
H1	0	4 3 - 2 - - - - -	1 4 4 - - - - - -	8 4 3 1 - - - - -	8 8 3 - - - - - -	- 6 1 - - - - - -	2 3 3 1 - - 1 - -	4 3 3 4 - - - - -	- 6 2 1 - - - - -	- 7 - - 1 - - - -	- 2 1 3 - - - - -	- 5 - 1 - - - - -	- 2 1 - - - - - -	0

TABLE 8.   76-51/1-Upper

IV-56

IV-57

	V₁	V₂	V₃	V₄	V₅	V₆	V₇	V₈	V₉	V₁₀	V₁₁	V₁₂	V₁₃	V₁₄
H_9							MICRONS 40 67 135							
H_8							200 270 340 400 470 540							
H_7														
H_6	- 2 - - - - - - -	3 6 1 1 - - - - -	- 3 3 6 - - - - -	- - 3 4 1 - 1 - -	- - 1 4 3 - - - -	- 5 7 2 3 - - - -	1 - - 1 - - 1 - -	- - 2 - 1 - - - 1	- - 1 1 3 - 1 - -	1 - 2 2 1 - - - -	- - 4 - - - 2 - 1	- 1 3 2 4 - - - -	- 3 2 - 4 - - - -	3 3 1 - - - - - -
H_5	- 1 1 - - - - - -	- 6 4 - - - - - -	2 6 2 5 - - - - -	- 5 3 3 1 1 - - -	- 6 3 3 1 - - - -	- 1 6 3 2 - - 1 -	1 - 1 1 4 - - 1 1	6 - - 3 3 - - - -	3 1 4 3 2 - - - -	1 2 2 4 3 - - - -	1 3 3 5 - - - - -	- 3 4 - 4 1 2 - -	- 3 4 3 - - - - -	4 1 2 - - - - - -
H_4	1 3 2 - - - - - -	- 1 2 3 1 - - - -	4 3 7 3 - - - - -	3 5 7 1 1 - - - -	2 3 3 4 - - - - -	2 3 6 3 1 - - - -	2 4 3 - 1 - - - -	- 4 6 - 2 1 - - -	1 5 3 2 2 - - - -	1 2 3 - 2 - - - -	- 1 4 4 3 - - - -	5 5 1 4 - - - - -	- 3 2 3 1 - - - -	1 1 1 - - - - - -
H_3	1 2 - - - - - - -	4 1 4 4 4 - - - -	5 7 2 1 - - - - -	4 3 2 4 - 1 - - -	- 2 9 1 1 - - - -	- 2 3 3 2 - 1 - -	1 6 2 2 1 - - - -	- - 3 6 2 - 2 - -	- 3 4 3 1 1 - - -	2 2 2 4 3 - - - -	1 3 7 3 - - - - -	2 6 3 - - - - - -	- 4 3 3 - - - - -	6 3 1 - - - - - -
H_2	0	- 3 - 1 2 - - - -	4 4 9 4 1 - - - -	3 5 3 - 2 - - 1 -	1 3 5 2 1 - - 1 -	3 3 3 3 - - - - -	5 4 2 2 - - - - -	4 3 4 2 - - - - -	11 2 4 - - - - - -	3 5 5 2 - - - - -	1 6 2 2 - - - - -	- 5 5 2 - - - - -	4 3 3 - - - - - -	1 3 2 - - - - - -
H_1	0	0	2 - -	- 1 -	0	1 - -	0	- 1 -	0	0	0	- - - 1 - -	- - 1	0

TABLE 9.   76-51/2-Bottom

	V$_1$	V$_2$	V$_3$	V$_4$	V$_5$	V$_6$	V$_7$	V$_8$	V$_9$	V$_{10}$	V$_{11}$	V$_{12}$	V$_{13}$	V$_{14}$
H$_9$	9 2 - 1 - - - - -	- 3 - 1 3 - 1 1 -	2 4 2 7 1 2 - - -	1 1 1 - - - 1 - -	- 2 4 4 - - - - -	5 4 3 4 2 - - - -	▨	▨	▨	▨	▨	▨	5 5 9 - - - - - -	1 3 - - - - - - -
H$_8$	3 2 - - - - - - -	14 6 2 - - - - - -	1 4 2 4 2 - - - 1	4 2 1 - 1 - - - -	- 4 2 2 3 - - - -	1 5 5 3 2 - - - -	6 6 4 3 1 - 2 - -	1 3 4 3 - 1 1 - -	2 5 4 2 1 - - - -	6 3 7 2 1 - - - -	3 2 1 5 1 - - - -	1 5 5 3 1 - - - -	1 5 4 3 2 - - - -	2 2 5 - - - - - -
H$_7$	- 2 - - - - - - -	14 7 4 - - - - - -	- 3 5 1 4 1 - - -	- - - 1 1 - - - -	▨	- 3 4 1 3 - - - -	- 4 3 3 - - - - -	- - - 4 - - - - -	3 4 2 2 2 - - - -	- 8 4 4 - - - - -	- 5 1 2 2 1 - - 1	- - 2 4 2 - - 1 -	5 3 2 - - - 1 - -	- 3 2 3 1 2 - - -
H$_6$	▨	11 8 - - - - - - -	5 6 3 2 2 1 - - -	3 4 - 2 - - 1 - -	▨	- 1 - 1 - - - - -	- - 3 3 2 1 - - -	- - 2 2 2 - - - -	- 1 1 1 1 1 1 - -	- 2 2 7 2 - - - -	1 2 1 3 3 - 1 - -	- 4 2 7 1 1 - - -	2 4 1 3 3 1 - - -	- 1 3 2 - - - - -
H$_5$	- 1 - - - - - - -	6 9 6 1 - - - - -	3 3 2 3 1 2 - - -	- 7 4 1 2 - - - -	▨	2 - - 1 - - - - -	- - 1 - 1 - - - -	- 1 1 - - - - - -	- 1 3 2 1 1 - - -	- 1 4 8 2 - - - -	- 1 1 3 2 1 1 - -	- - 4 2 3 2 2 - -	6 7 3 3 2 - - - -	1 2 - - - - - - -
H$_4$	- - 1 - - - - - -	6 7 3 2 - - - - -	- 5 7 1 - - - - 1	- 3 4 2 1 1 - - -	▨	MICRONS 40 | 67 | 135		▨	▨	1 3 3 3 2 - - - -	- 1 3 1 1 1 - 1 -	- 1 6 1 - 1 - - -	- 2 7 4 1 - - - -	1 2 1 - - - - - -
H$_3$	1 - - - - - - - -	19 9 - - - - - - -	4 6 1 4 - 1 - - -	- 1 2 5 2 1 - - -	▨	200 | 270 | 340 400 | 470 | 540		- 1 - - 1 - - - -	▨	- 1 1 1 1 1 - - -	- - - 2 2 1 - 1 1	- 4 6 2 2 - - 1 -	- 2 1 4 1 - - - -	1 1 - - -
H$_2$	1 1 - - - - - - -	4 4 - - - - - - -	3 4 3 - 4 - - - -	- 4 6 1 2 1 - - -	- 4 1 - - - - - -	- 4 3 3 - - - - -	- - 1 1 1 2 - - -	- 1 1 4 2 - - - -	- - - 1 - - - - -	- 2 1 2 - - - - -	▨	- 8 1 3 1 - - - -	- 3 2 2 - - - - -	▨
H$_1$	▨	▨	2 4 - - - - - - -	7 4 3 - 1 - - - -	4 5 - 1 - - - - -	3 6 1 - - - - - -	2 5 1 3 - - - - -	- 2 - 1 - - - - -	- - 1 - - - - - -	▨	▨	- - 1 - - - - - -	▨	

TABLE 10.   76-51/2-Upper

Critical assessment of the method.

It is obvious that a total count cannot be made and that a certain number of globules do not appear in the observation either because their size is smaller than the smallest observable size or because the contrast is lost in the continuous background. The micrographic study of the samples shows that below 40 μ diameter (minimum gauge size adopted), the indium phase most probably belongs to the monotectic phase which in any case is to be excluded from the analysis.

The loss of definition of the globules in the continuous background is an essential factor for the determination of globule concentration but has little effect on the representation of a population by sampling.

General distribution.

The size distribution histograms were determined for the whole of each sample. Normal distribution curves were added to the histograms. Figure 35 shows the histogram for the sample 76-51/1-Bottom and concerns 784 globules.

A population maximum is observed for the 67μ diameter (0.5 gauge) with 32.5% of the total population. A levelling off of the right-hand branch is visible for 200 μ (1.5 gauge).

Figure 36 shows the histogram obtained for the sample 76-51/2-Bottom and concerns a total of 764 globules. The population maximum is found for the 135 μ diameter (1 mm gauge) with 28.3% of the total population.

Figure 37 shows the histogram for the sample 76-51/2-Upper and concerns a total of 1514 globules. The maximum observed is for the 67μ diameter (0.5 gauge) with 48.2% of the total population.
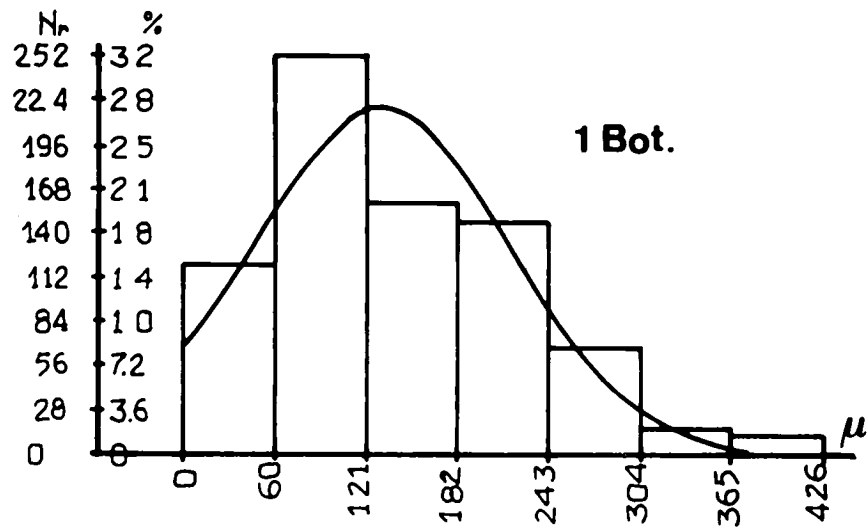
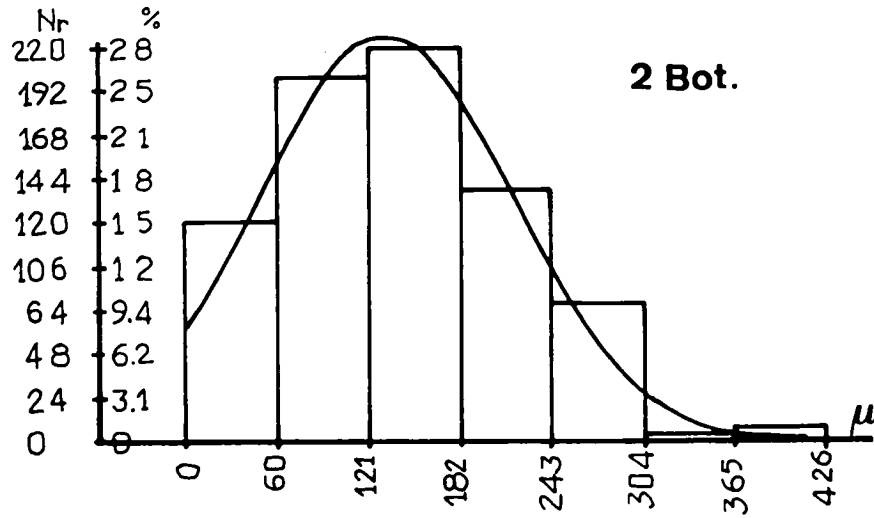Figure 35. Distribution histogram for the sample 76-51/1-Bottom.

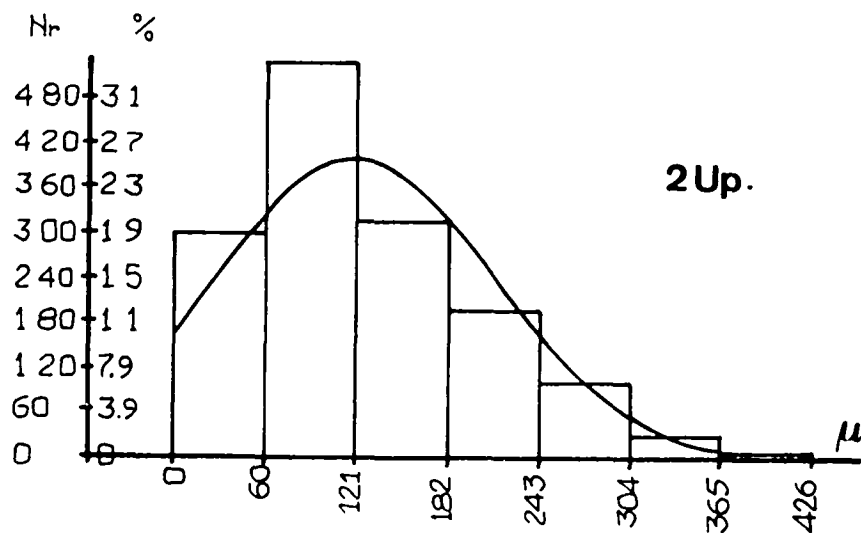Figure 36. Distribution histogram for the sample 76-51/2-Bottom.

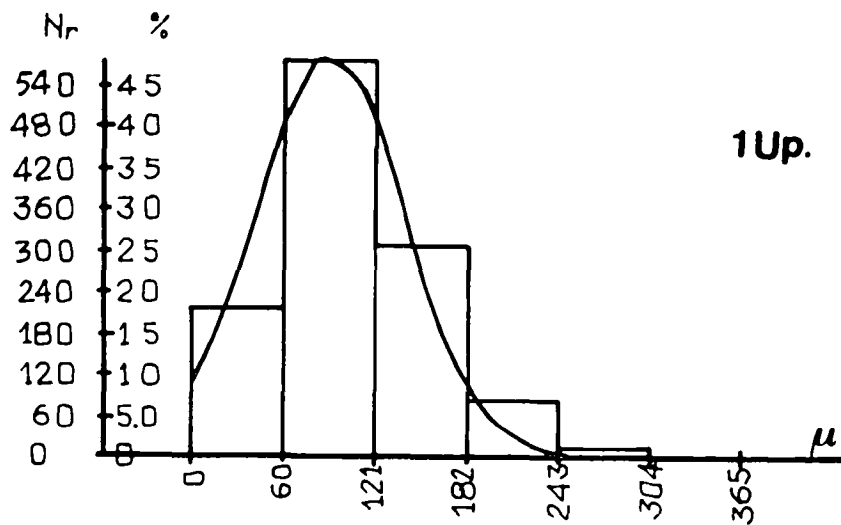Figure 37. Distribution histogram for the sample 76-51/2-Upper.

Figure 38. Distribution histogram for the sample 76-51/1-Upper.

The sample of theoretically monotectic composition was found to contain primary indium phase globules distributed over the crucible bottom zone. The part of the sample close to the free volume solidifying first does not contain any globules of gaugeable dimension. This zone of the sample has a composition similar to the monotectic alloy composition assumed and the absence of globule identification gives added weight to the choice of $40\,\mu$ gauge as the minimum identification value for primary phase globules.

The monotectic structure therefore has little effect in the determination of populations. The crucible bottom zone was analysed and the distribution concerning 1196 identifications is presented on the histogram in figure 38.

A large majority of $67\,\mu$ diameter globules (0.5 mm gauge) is evident on this figure with 48.2% of presence. A number of trend indications can be deduced from a comparison of these general distribution histograms if allowance is made for the different heat treatment processes to which the samples were subjected.

Samples 76-51/1-Bottom and 76-51/2-Bottom must be compared since they have the same chemical composition but subjected to similar heat treatments. The shift in small diameter towards the $135\,\mu$ gauge size is evidenced in the 2-bottom sample which was subjected to a greater thermal gradient. The lateral branches of the distribution histograms are comparable.

If it is assumed that the solidification conditions are similar for both samples, the only notable difference lies in the thermal gradients established in the liquid. Enlargement of the size of most populous category of globules would seem to be linked to the increase in gradient.

The 'Upper' samples, which were subject to solidification in the reverse direction and with the same low gradient presents the same peak at $67\,\mu$.

Larger globules are more numerous in the 32 w %[*] sample (76-51/2-Upper). This would seem to indicate that growth in globule size is related to the initial concentration of the samples.

STATISTICAL ANALYSIS IN RELATION TO SOLIDIFICATION CONDITIONS

The overall approach described above is not sufficient for determining the relationships that exist between the dispersion structure and local solidification conditions. It has been seen that the main factor governing the final structure was the part played by the solidification interface : strong repulsion of the primary indium phase leading to considerable accumulations of indium at the end of solidification.

It therefore became necessary to look for relationships between local globule distributions and the solidification front characteristics leading up to these distributions.

These characteristics are the mean propagation speed of the solidification front, the average thermal gradient prevailing in the adjacent liquid and the general curvature of the interface.

Such an analysis is based on the assumption that the globules are initially uniformly distributed in the hypermonotectic liquid, that the local globule distributions determined by X-ray examination are representative of the entire sample and on the thermal analysis presented in the previous chapter.

---

[*]
Note : The exact chemical composition of the sample zones considered is not known because considerable segregation took place during treatment.

IV-63

The first assumption is acceptable in view of the well-established and common initial conditions for the samples. A difference could, however, arise in the event of a non-zero thermal gradient applied to the sample 76-51/2-Bottom before its solidification and which would lead to different globule distributions in the two bottom samples. The problem of population representativeness through local samplings must be assessed before studying the change in population as a function of the position and shape of the solidification interface.

The globule spatial distribution charts highlight the masking effect of the continuous background. This effect is particularly noticeable when the number of globules counted does not vary with the thickness of the solid phase passed through by the X-rays (see chart 76-51/1-Bottom, lines V7 to V10).

Radiographic sampling thus concerns variable and non-determined volumes of solid material. It would therefore seem difficult to calculate the local globule concentrations by this method. These local concentrations can nevertheless be estimated by relating the absorption intensity of the continuous background measured by densitometer to the average size of the sampled globules at the location selected. This estimation method was not used here and is not presented.

This problem could be solved at a later date by a three-dimensional examination of the X-ray tomography type.

In the study of purely size distributions, the fact that samples were taken from a limited volume is rather an advantage given the anisotropic nature of the structure studied. Thus, the method of taking the X-ray pictures (fig. 30) concerns mainly the planar section of the sample on which the studies areas are delineated. A semi-quantitative approach to changes in size distribution is proposed here, using the previously established distribution charts.

Change in size distribution during solidification.

The principle of the examination consists in counting the populations between two known positions of the solidification front (figs. 31 and 33) and identified by the thermal calculation.

The globules observed are those which were formed from the two-phase liquid as the solidification front advanced between these two positions.

The thermal calculation gives the average values of the front propagation speed and the thermal gradients in the liquid phase.

The specific chemical etching process reveals the shape of the solidification isotherm (fig. 18) in each position, represented on figures 31 and 33. A 1 mm grid network is used to delineate the areas concerned (areas alternately grey and light in contrast on fig. 31).

Sample 76-51/1-Bottom.

Figure 39 presents the population histograms measured between seven positions of the solidification interface of the sample 76-51/1-Bottom (strips B1 to B7, fig. 31).

The normal distribution layers are superimposed on the graphs, thereby showing the distribution differences observed with respect to the ideal situation. The deviation calculation has not been considered here. The initial distribution is close to the Gaussian distribution (B 1) with a half peak length to height ratio = 0.46.

The isotherms 1 to 4 indicate a progressive shift of the greatest diameters, increasing from 67μ (47.2%) to an accumulation of diameters around 135 and 200μ (49.3%).
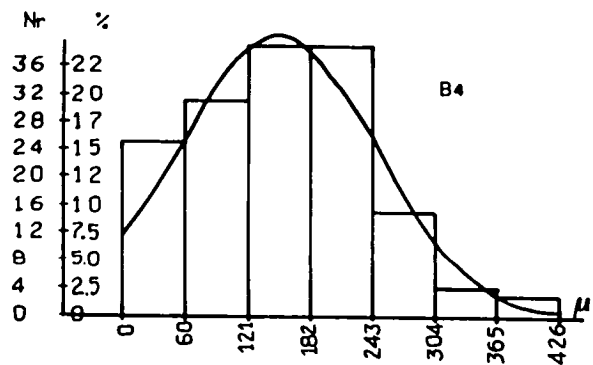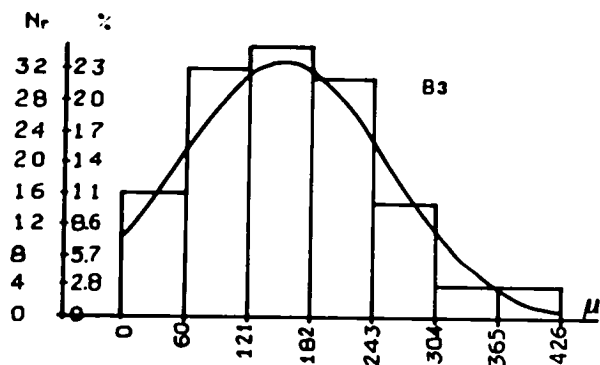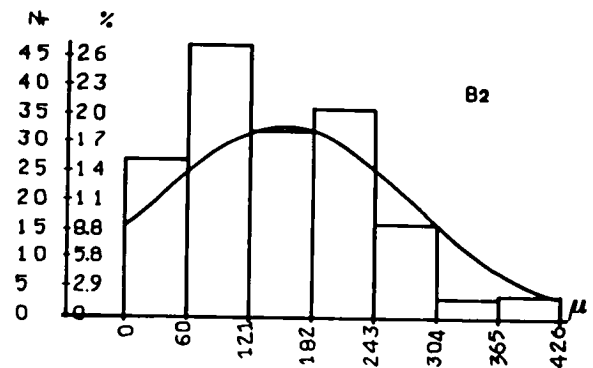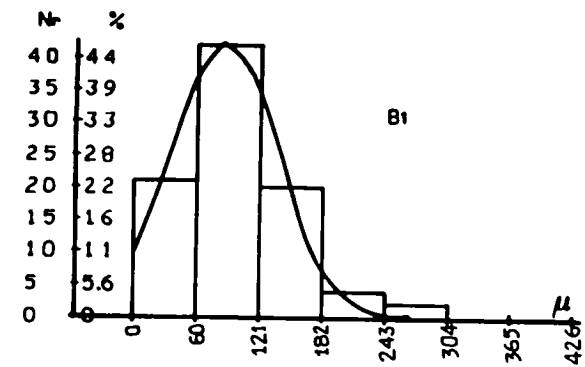
76.51/1 Bottom

Figure 39. Histograms of globule population recorded between 7 positions of the solidification front in the sample 76-51/1-Bottom.
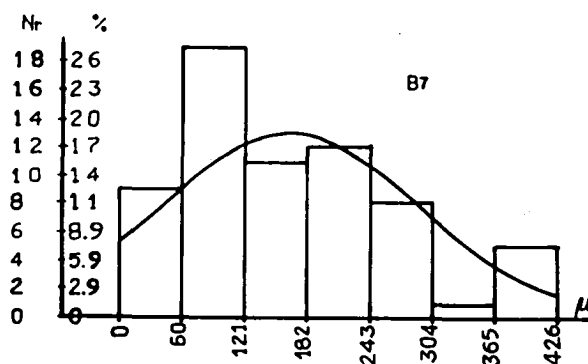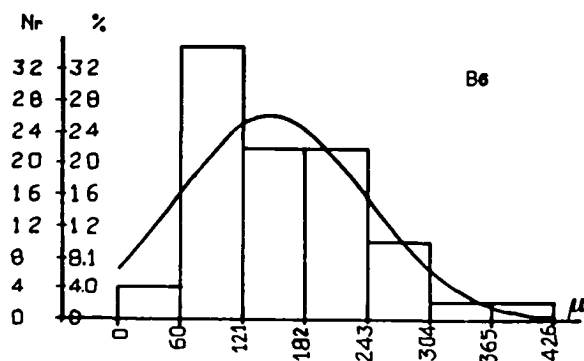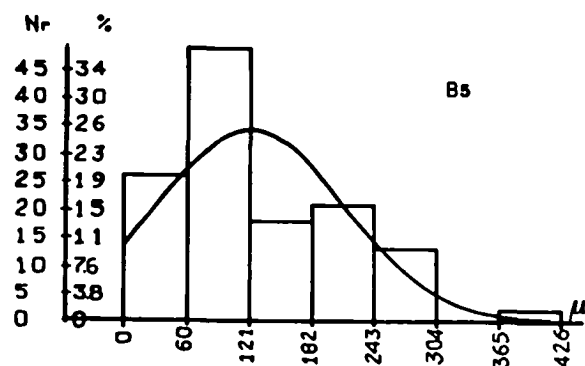
76.51/1 Bottom

Figure 39 (continued)

The following redistributions have a majority of 67μ diameter but again shift towards the 200μ diameter. A shoulder can be remarked for the latter value on the three histograms B5, B6 and B7.

Figure 40 presents the distribution curves of the 40μ and 67 μ diameters as a function of the position of the strip studied with respect to the bottom of the crucible. The frequencies decrease considerably, especially for the 67μ diameter, pass through a minimum value and then tend to stabilize around a not well-defined value.

These frequency curves should be compared with the average speed curve estimated for this sample (fig. 27). A similar variation is observed for this parameter : at the maximum solidification speed (position 0.45 cm) there is a corresponding minimum frequency value of the 67μ diameter and at the following point of inflexion (position 0.6 cm) of the solidification speed a maximum frequency value of this diameter occurs.

Similar observations can be made for the 40μ diameter. The exact correlation existing between these parameters cannot be determined without a stricter investigation. The frequency curves for the 135μ and 200μ diameters (fig. 41) have very comparable and monotonic variations. The frequencies pass through a maximum value situated in the region of the minimum solidification speed, followed by a regularly decreasing value.

The 270μ curve shows a frequency increase rapidly stabilizing as from the 0.25 cm position.
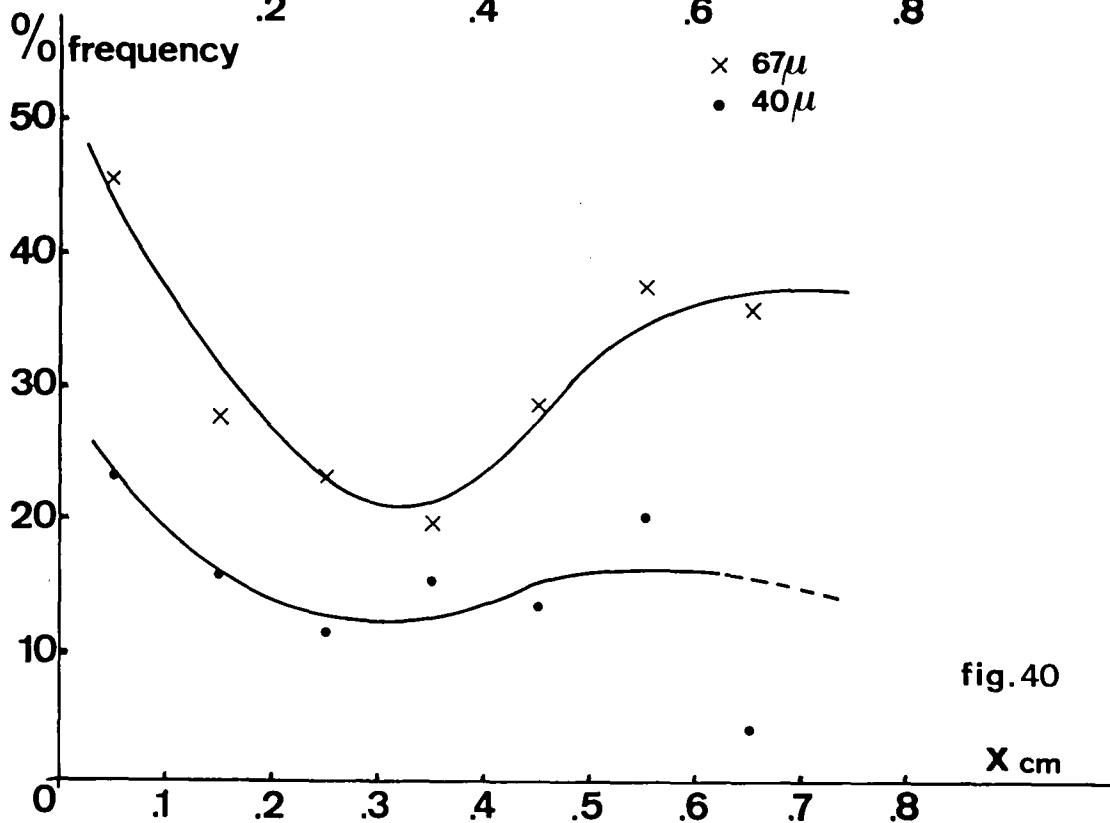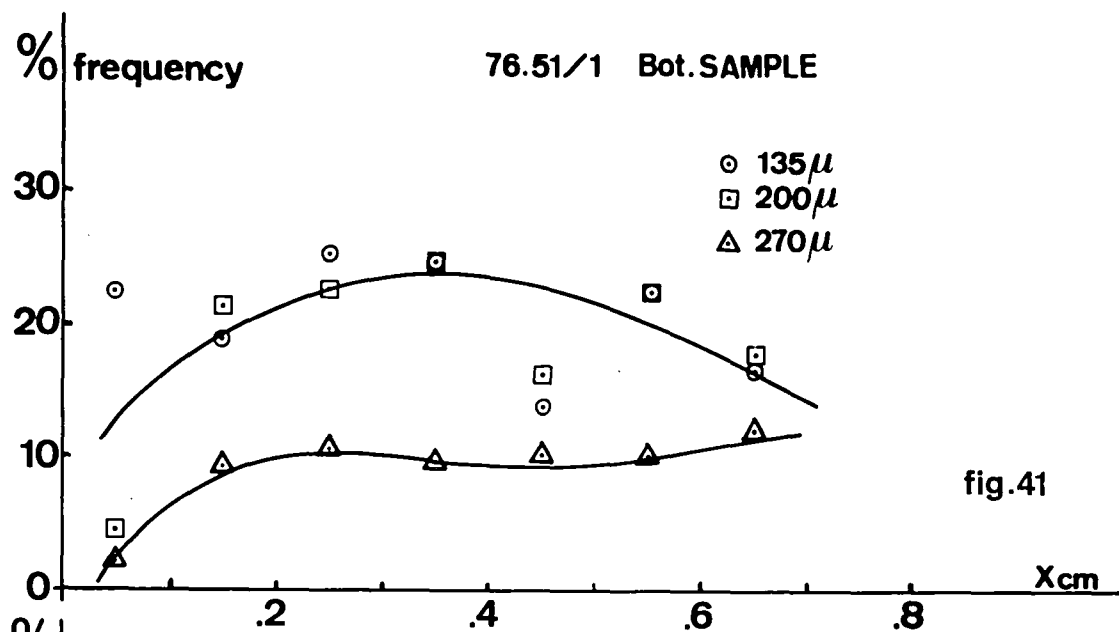
Figure 40.   Diameter distribution curves for 67μ and 40μ in relation to the position of the interface (in sample 76-51/1-Bottom).

Figure 41.   Diameter distribution curve for 135μ to 270μ in relation to the position of the interface (in sample 76-51/1-Bottom).

Note the behavioural difference between the two families of globules.

Radial distribution (76-51/1-Bottom).

Examination of the distribution chart (fig. 31) and the solidification isotherms would suggest an accumulation and enlarging effect of the globules towards the lower point of the isotherm.

This observation has been corroborated by a distribution analysis along lateral verticals (V_2 and V_{13}) and central verticals (V_7 and V_8). Figure 42 presents the curves obtained. Despite the fact that they are very dissymetrical, the VERT 2 and VERT 13 curves indicate a majority of small diameters (40μ, 67μ and 135μ).

The VERT 7 and VERT 8 curves indicate a marked shift towards larger diameters with the disappearance of the 40μ diameter. Very large globules are observed. The hollow shape of the interface can thus have an accumulating and coalescing effect on the globules.

Sample 76-51/2-Bottom.

The thermal conditions governing this sample are as remarked previously, doubtfull as to their accuracy, especially at the beginning of solidification.

In addition, the solidification isotherms are more or less parallel at the bottom of the crucible except near the side walls. On the other hand, it would seem that the end of solidification was more isotropic than the calculation showed.

The distributions were analysed on six strips parallel to the bottom of the crucible (fig. 43). The initial distribution fixed in the solid (B 1) is considerably shifted towards the smaller globule diameters. It is worth noting that the first strip is almost free of globules and the statistical analysis was based on just 7 observations.
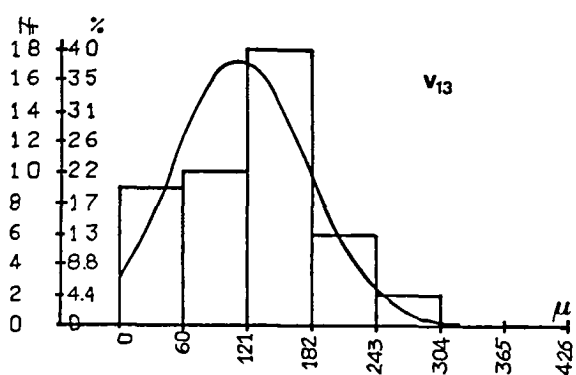
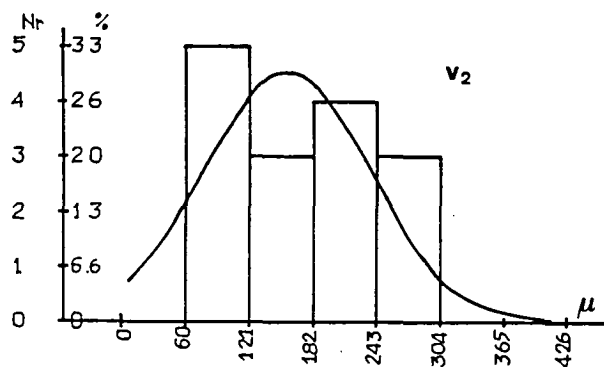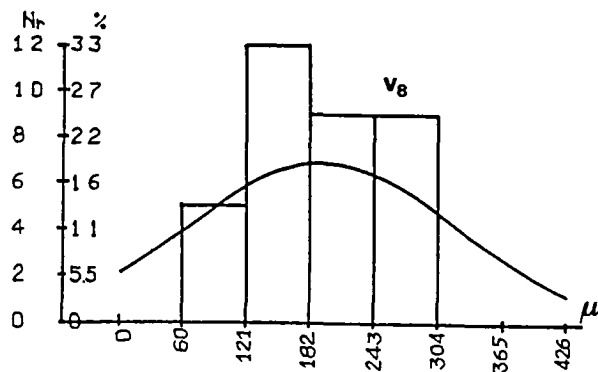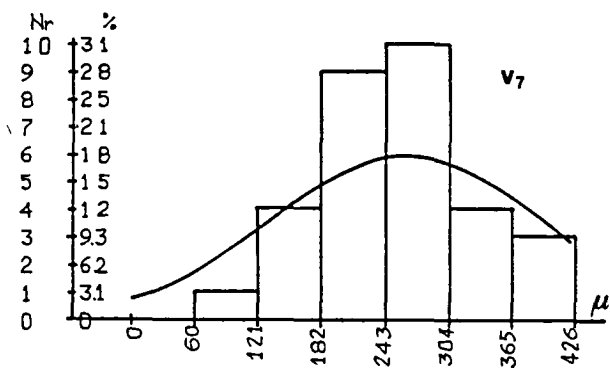Figure 42. Distribution histograms as a function of the position with respect to the axis of the sample 76-51/1-Bottom.
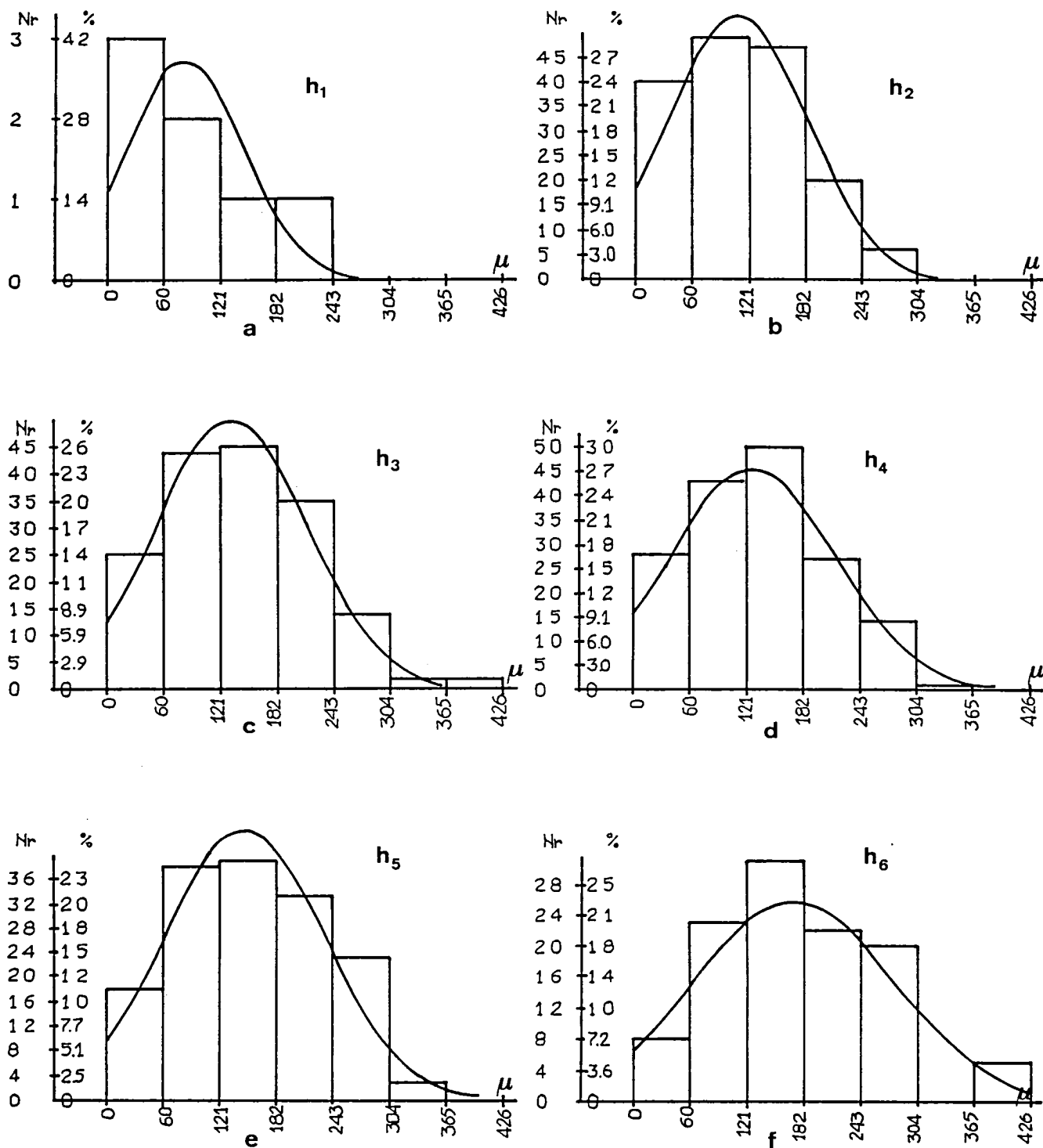
Figure 43 a to f. Histograms of populations recorded between 6 positions of the solidification interface in the sample 76-51/2-Bottom.

These isotherms were considered to be parallel to the bottom of the crucible.

The three following curves show a shift trend towards the 135 μ diameter and the next two curves indicate a stabilization approaching this same diameter.

Figure 44 summarizes these results as a function of the position of the bands with respect to the bottom of the crucible. The tendency of globule diameter size to stabilize around the 135 to 200 μ values is more apparent.

The 40 μ diameters have different behaviour and their frequency is always strongly dependent on the average solidification speed. The point of inflexion of the graph is located in the zone where the solidification front is accelerating (fig. 30).

The radial distribution was not studied. This is because the X-ray examination did not reveal any tendency for globule accumulation towards a particular part of the sample respect to its axis of revolution. This fact is in agreement with the observation of an approximately plane solidification front in this sample.

GENERAL DISCUSSION AND CONCLUSION

The main result of these experiments lies in the preservation of a certain degree of dispersion of the indium primary phase. This result is radically different from those already obtained under microgravity conditions on the same system and compositions [5,6]. The main reasons leading to this result are related to the chosen physico-chemical interactions between the phases present.

Capillarity factors.

First, the strong preferential interaction between aluminium atoms in the liquid alloys and silicon carbide has led to the production of an exclusively monotectic phase as matrix with the indium
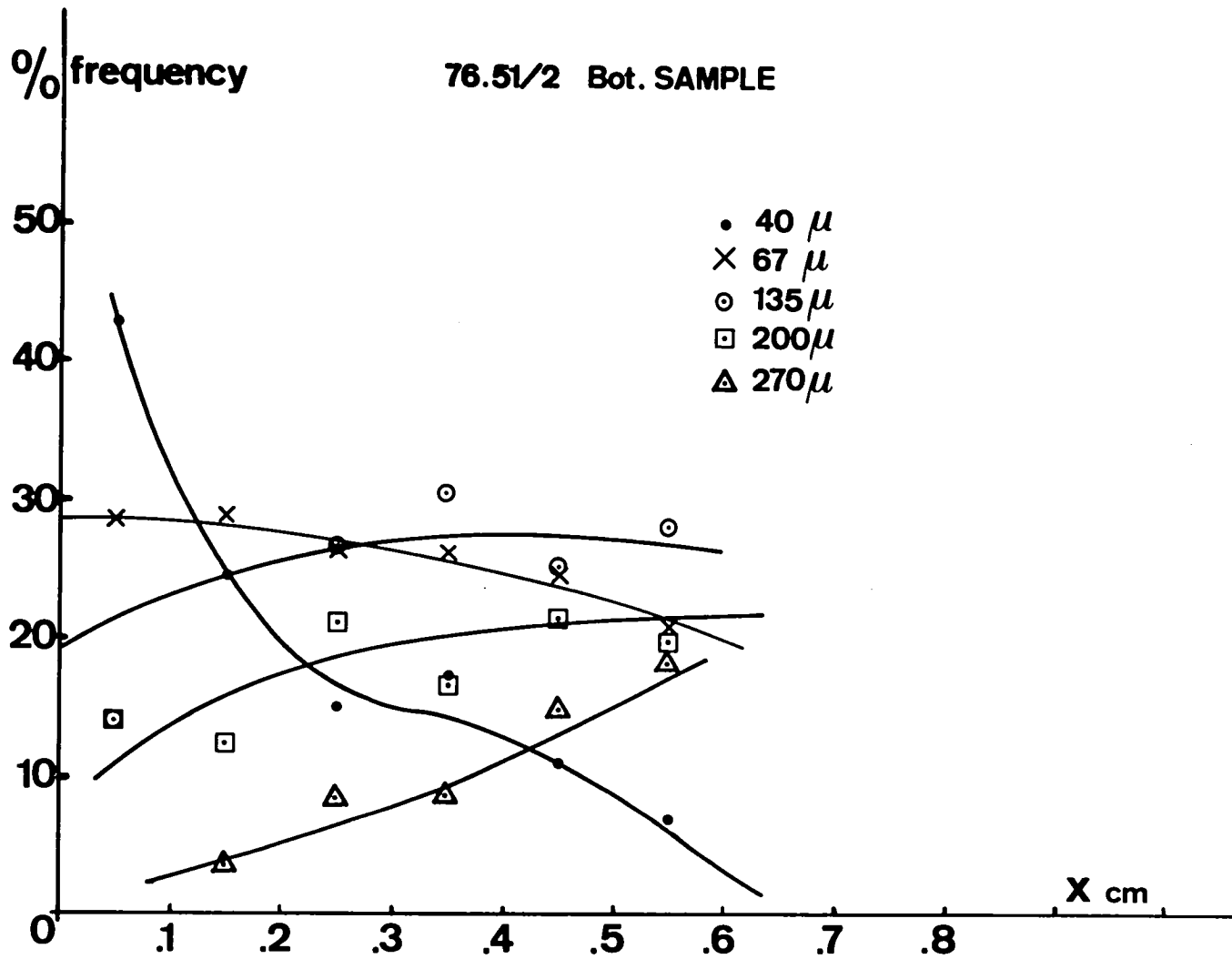
Figure 44. Distribution curve of various globule diameters as a function
of interface position in sample 76-51/2-Bottom.

phase being the distributed medium. This was to be expected, given the inhibiting effect of silicon carbide with regard to the nucleation of the indium phase. The differential wetting of the two liquid phases on the crucible material has also to be accommodated : silicon carbide, with its repulsive effect on the indium atoms, creates perfect non-wetting conditions for the indium phase and completely eliminates any spreading on the crucible walls. This important condition greatly reduces uncontrolled movements of the two liquid alloys and, consequently, the coalescence effects. A second reason is related to the initial state of the sample. Regular structures can be expected from space processing only if uniform fields – concentration, temperature, velocity – in the liquid are first achieved. This condition was certainly closely approached in our experiment for the concentration field. We are consequently in a position to suppose that the nucleations may have appeared at regularly distributed sites in the sample volume which depend only on temperature field variations.

Under thermal gradients obtained in the two-phase liquid, and considering the known physical properties of the alloy, large and generalized migrating effects of the globules throughout the sample volume should be expected according to the classical theory of capillary convection [7]. Such a generalized effect was not observed. Only a localized but severe segregation effect is evident in a narrow zone along the crucible walls. The non-extension of the migrating phenomenon, if caused mainly by capillary convection, must be investigated taking into account the existence of both concentration field and temperature field. Of course, the problem must be solved with consideration also being given to the structure variations of the globule population. Naturally, other reasons could have led to the structures observed. A variable pushing effect of the solidification front must be considered, but we must also suppose the existence of initially globule-free liquid zones along the crucible walls due to the absence of indium nuclei.

Solidification factors.

As previously established on the ground [2] the main inter-action between the solidification front and the indium phase results in a repulsive effect. The excess volume accumulated and coalesced on the free volume limits at the end of the solidification for the bottom samples whereas for the upper samples which solidified differently it accumulated in the shrinkage holes. The degree of dispersion of the incorporated phase demonstrated that coalescence remained limited in the interface zone during pushing. Coalescence of the globules should occur as they are swept by the solid front depending on the mutual forces involved, but the viscosity of the liquid matrix delays the phenomena.

Dispersion behaviour during cooling was studied by using a powerful thermal calculation code. The thermal analysis results were in agreement with what could reasonably be expected from the ill-defined boundary conditions. More precise measurements of these conditions will be necessary in future experiments, with stricter adequation to the conditions required by the experimenter. Conse-quently, the dispersion behaviour analysis was made difficult by the low directionality of the cooling process. The interface curva-ture factor for example, effective on one sample, reduces the effi-ciency of this comparative study.

These uncertainties did not prevent the establishment of coherent observations :

a/ globule populations in the same diameter ranges from 64µ to 200µ,

b/ tendency for a shift in these diameters towards the 135µ to 200µ range during solidification,

c/ variation of 40µ and 67µ diameter frequencies is a sensitive and inverse function of solidification speed,

d/ larger diameters frequencies are less sensitive to solidification speed change,

e/ change in distribution with interface curvature : globule accumulation and enlargement on the hollow interfaces by mutual pressing.

The part played by the thermal gradients in the liquid immediately in front of the solidification interface - the G^L/R ratio - was not clearly estabilished.

The zones solidified under relatively high thermal gradients - bottom of the crucible for bottom samples - are completely free of globules, as are the zones without thermal gradient, adjacent to the side walls of the crucible. These zones are made up of the aluminium-based solid solution - as shown by the chemical analysis - and are thus also free of any monotectic globules. The physicochemical factors would therefore seem to predominate in the SiC-liquid alloy interface zones and create an initial liquid state very different from that occurring in the mass.

Further experiments will be required in order to study this essential factor. The observations made during this phase of the study should serve as a basis for research on a model of globule capture by a solidification front in a metal system.

ACKNOWLEDGEMENTS

advice and assistance during the preparation and implementation of the experiment.

Thanks are due to J. Boissier for this contribution to the technical and experimental parts of this programme and to P. Morgand who performed the computations of the thermal field.

REFERENCES

[1]   C. Potard, 'Review of the mechanisms involved in the directional solidification of Al-In emulsion at zero gravity', Journal of the British Interplanetary Society, Vol. 31 (1978) 275-289.

[2]   C. Potard, 'Etudes de bases préparatoires de l'expérience de solidification dirigée d'alliages immiscibles Al-In en fusée-sonde', in Proceedings of the 3rd European Symp. Mat. Space. Grenoble, France, April 1979, 255-261.

[3]   B. Predel, 'Beitrag zur Konstitution und Thermodynamik von Entmischungssystemen', Zs. Für Metallkunde, vol. 56 791-198.

[4]   M. Gerbaux, 'Condut : ensemble intégré de programmes pour la résolution de l'équation de la chaleur ou de problèmes connexes', Rapport CISI, M 178 (1978).

[5]   S.H. Gelles and A.J. Markworth, 'Agglomeration in immiscible liquids', Final post-flight report on SPAR V experiment nr 74-30, NASA 78275 (1980) 1-105.

[6]   H. Ahlborn and K. Löhberg, 'Aluminium-Indium experiment SOLUOG. Sounding rocket experiment on immiscible alloys'. Proceedings of the 17th Aerospace Science Meeting, New Orleans, La. 1979.

[7]   A. Bewersdorff, 'A mechanism for macroscopic phase separation
        in emulgated liquid systems', COSPAR Meeting, paper VIII,
        2.1., Innsbrück (A) 1978.

SPAR EXPERIMENT 76-36

COMPARATIVE ALLOY SOLIDIFICATION

Principal Investigator: Dr. M. H. Johnston

Co-Investigator: Mr. R. A. Parr

Comparative Alloy Solidification

Background: The tin-3wt% bismuth alloy experiment is one in a succession of casting experiments beginning with the metal-model (NH_4Cl-H_2O) solidification on SPAR I. Three configurations of metal-modes were studied. Publications on these results are given in References 1 and 2. The first metal alloy system, tin-15wt% lead was solidified on SPAR VII. Results from this experiment have been accepted for publication in Metallurgical Transactions.[3]

The tin-3wt% bismuth alloy was chosen as the second in the series of metal systems due to its propensity for dendrite remelting.[4] The physical characteristics of this material are given in Table I.

Ground Based Studies: A series of ground based tests were run at cooling rates of $3^{\circ}C$/Min and $20^{\circ}C$/Min at 4 acceleration levels. A schematic of the centrifuge furnace apparatus is given in Figure 1. This was a duplicate to that used during the SPAR flight. The samples were sectioned for metallographic analysis in a manner shown in Figure 2. They were then polished and etched in a $HCl-FeCl-H_2O$ mixture. Figures 3 and 4 show faces CE and DE of the centrifuge samples.

Additional ground-based samples were run in order to duplicate the unexpected low cooling rates experienced during the SPAR flight. Two samples were processed in the flight unit, one in which the gravity vector was parallel to the cooling isotherms (designated "⊥") and the second in which the gravity vector was perpendicular to the isotherms of these (designated 11"). Figures 5 and 6 show the CA and DB faces of

these samples. In addition, the same low cooling rate was reproduced in the centrifuge furnace and additional samples were run. For this second series the centrifuge furnace was also fixed in the two positions with respect to the gravity vector. Figures 7 and 8 show the polished and etched faces of $CA_\perp$ and $DB_\perp$. Figures 9 and 10 show the polished and etched faces of $CA_{||}$ and $DB_{||}$.

Using quantitative microscopy, the polished surfaces of the samples were examined for porosity. This data has been sent to the Industrial Guest Investigator, Mike Cybulsky, at TRW, Cleveland, for further analysis. Dendrite arm spacing measurements were made on several of the samples to obtain an arm spacing vs. cooling rate relationship. This data is given in Table II. Quantitative analysis of the sample surfaces will be performed at a later date when the metallographic analysis is complete.

Flight Experiment: The tin-3wt% bismuth samples was launched molten at a temperature of 240°C. One hundred and eighty three seconds after launch, power was cut and the quench was initiated. As mentioned earlier, the cooling rate was significantly slower than expected, being on the order of ($10-12^\circ$C/Min).

Figure 11 shows the as-received exterior surfaces of the flight sample. Figures 12 and 13 show the CA and DB faces of the flight, $GB_\perp$ and $GB_{||}$ samples. Figures 14, 15 and 16 show the CE and DE faces of the same specimens.

All of the samples exhibited some degree of centerline porosity as can be seen in Figure 17. This phenomenon is being studied by TRW under the Industrial Guest Investigator program.

Discussion:

Metallographic examination of the flight sample suggests that it began solidification on the 'B' surface with the dendrites proceeding to grow at an angle toward the center and the 'A' face. This is indicated both by the orientation of the dendrites in Figures 12 and 13, and by the occurrence of the large cavity on the 'A' surface. It is not known at this time if unequal acceleration forces drove the molten liquid toward one wall of the crucible, but this seems to be the most probable explanation.

The major question still to be answered is whether the flight sample completed solidification in low-gravity. The expanded temperature curve from the telemetry indicates that the solidification was completed within a few seconds of the end of low-gravity. However, the small grains around the large centerline cavity could be indicative of convection as the sample finished solidifying in a gravity field.

Using the SPAR furnace on board the KC-135 airplane, a tin-3wt% bismuth sample was processed to determine if there is an obvious demarcation in growth structure when a partially molten sample completes its solidification in a different gravity environment. The sample began solidifying in the low-gravity parabola and completed solidification during the high-g pullout. Figure 18 shows the CA and DB surfaces. There is no macroscopically obvious transition. Further studies need to be done in which the quenching rate and time of entry into low-gravity are varied.

It is possible that the small grains near the central cavity of the flight sample are the result of recrystallization rather than convection during solidification. There is extensive recrystallization in the ground-based samples whereas it is localized

in the flight samples. The very fact that the recrystallization itself was influenced by the change in gravity force indicates that there are interesting homogeneity and cold-working differences between low-g and higher-g processed materials.

The major effect seen from low-g processing in the tin-3wt% bismuth alloy was predicted by the earlier metal-model experiments. In contrast to the fine-grained earth-processed samples, the low-g sample solidified with relatively few large grains. The occurrence of small grains due to dendrite remelting was not observed until perhaps the final portion around the cavity.

References

1. M. H. Johnston, C. S. Griner, R. A. Parr & S. J. Robertson, J. of Crystal Growth, Vol. 50, p. 831 (1980).

2. M. H. Johnston & C. S. Griner, Met Trans, Vol 8A, p. 77 (1977).

3. M. H. Johnston & R. A. Parr, accepted for publication, Met Trans.

4. M. E. Glicksman, R. J. Schaefer & J. D. Ayers, Met Trans, Vol. 74, p. 1747 (1976).

TABLE I

LIQUID PHYSICAL PROPERTIES IN CGS UNITS*

	Sn-3 Bi
T_m	283
ρ	7.06
C	0.059
k'	0.076
μ	0.0184
$\beta_T (1/K)$	$1.01 \ 10^{-4}$
$\beta_C (1/w + \%)$	--
D	--
ν	$2.6 \ 10^{-3}$
α	0.18
Pr $(= \nu / \alpha)$	0.014
$\beta_T / \nu \alpha$	0.22
β_T / ν^2	14.9

*cm, gm, sec, C, cal, poise, etc.

SOLID PHYSICAL PROPERTIES IN CGS UNITS*

	Sn-3 Bi
ρ	5.84
C	0.06
λ	14.5
k'	0.08

TABLE II

Secondary Dendrite Arm Spacing	Cooling Rate ($^\circ$C/Min)	Conditions
11.0×10^{-3} cm	3°C/Min	Ground Base
5.44×10^{-3} cm	20°C/Min	Ground Base
8.7×10^{-3} cm	12°C/Min	Flight

FURNACE
PLATES

GAS
QUENCH

GRAPHITE
CRUCIBLE

GLASROCK
INSULATION

TOP VIEW

GAS
QUENCH

TOP

Sn—15Pb

BOTTOM

g-FORCE
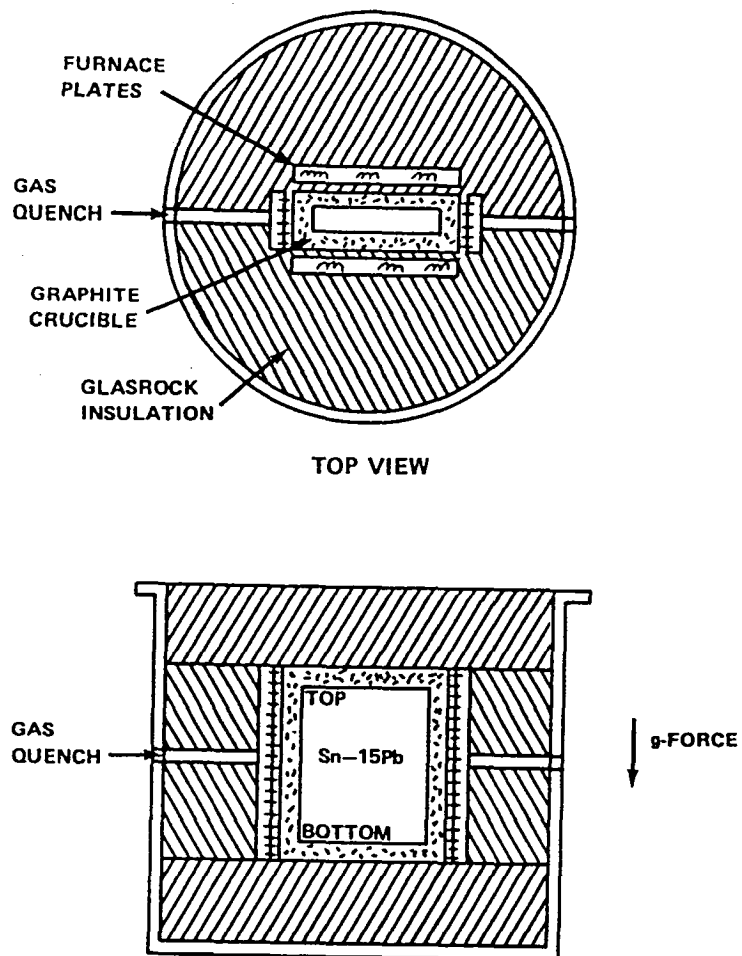
Figure 1. Schematic of Canister Assembly
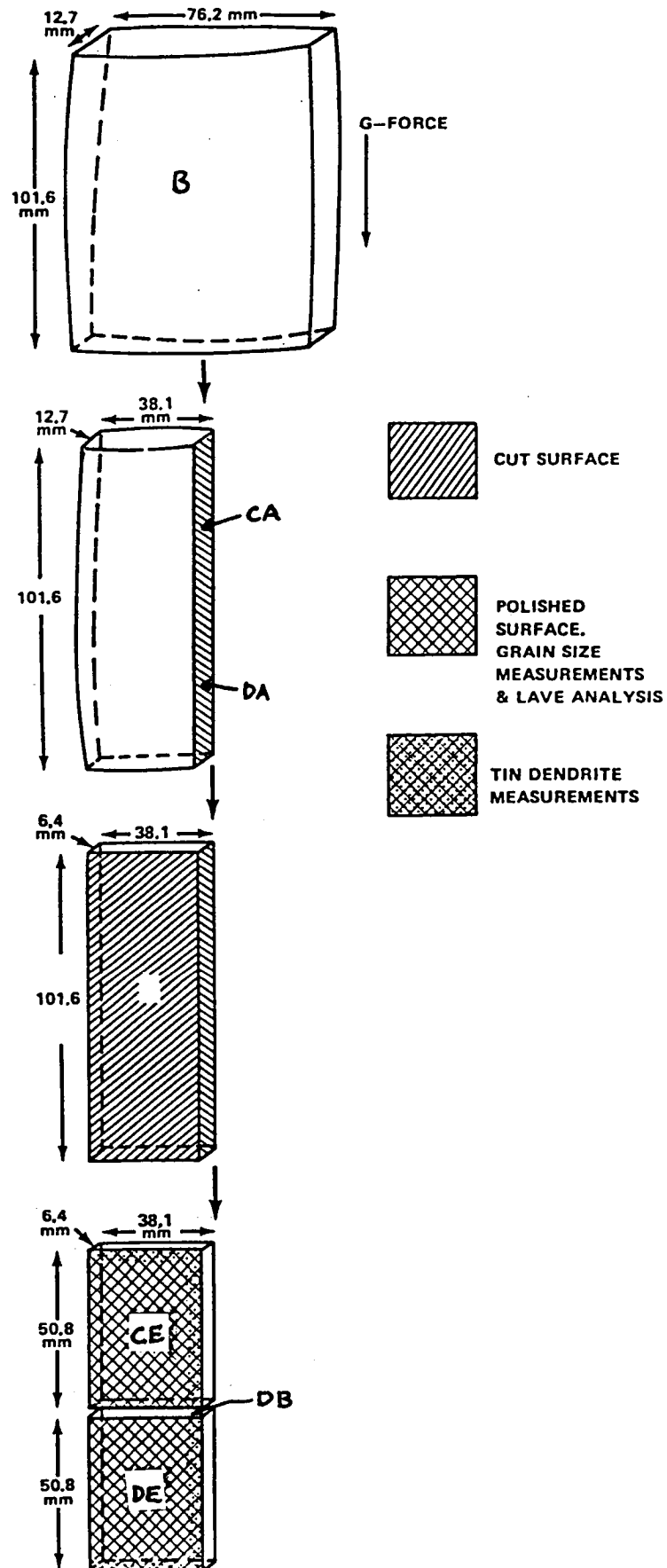
Figure 2. Schematic of Sample Preparation and Analysis

V-8

1 G   1-3/4G   3-1/2G   5 G
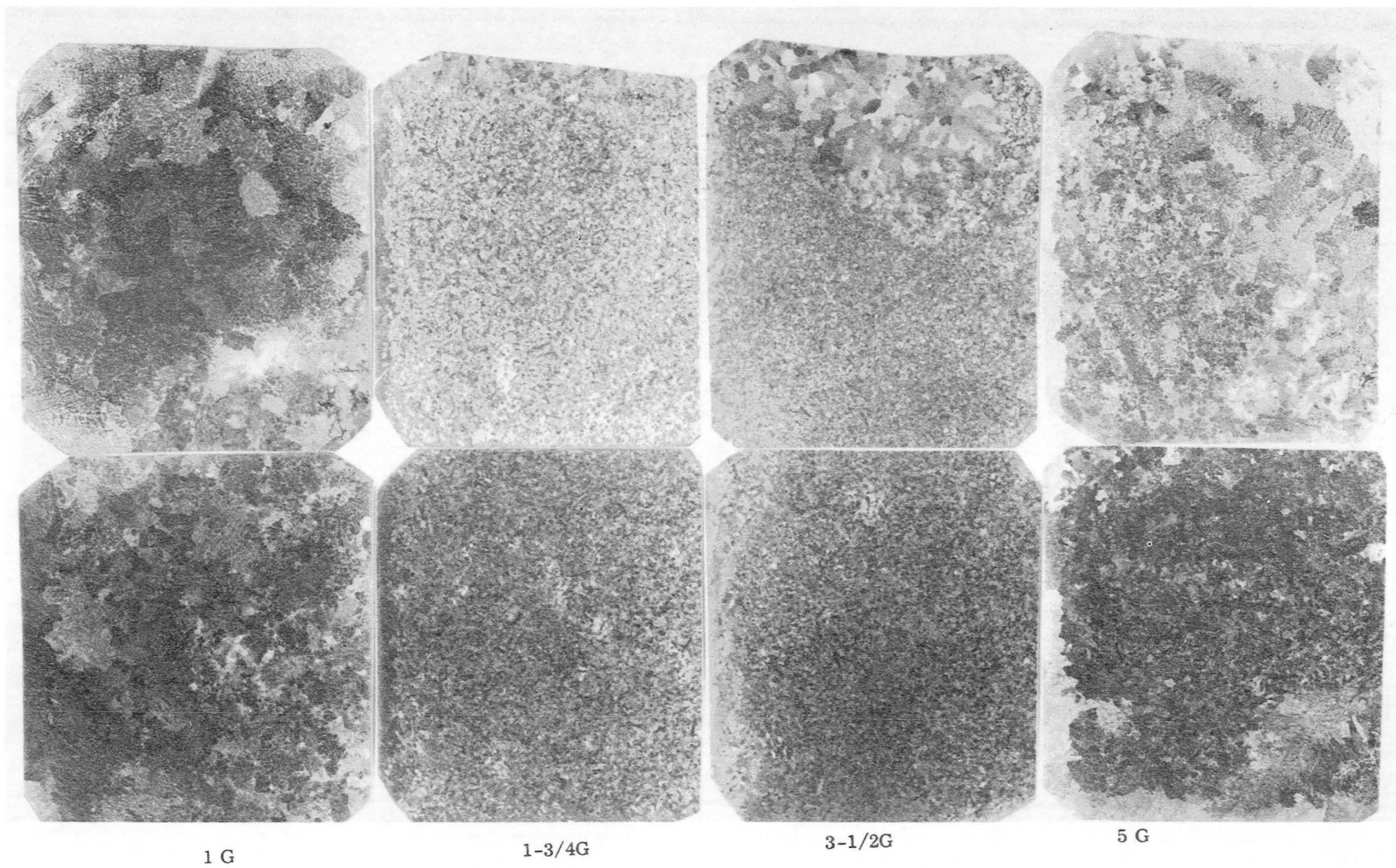
Figure 3.   Tin - 3wt% Bismuth, 20°C/Min Cooling Rate

1 G   1-3/4G   3-1/2G   5 G
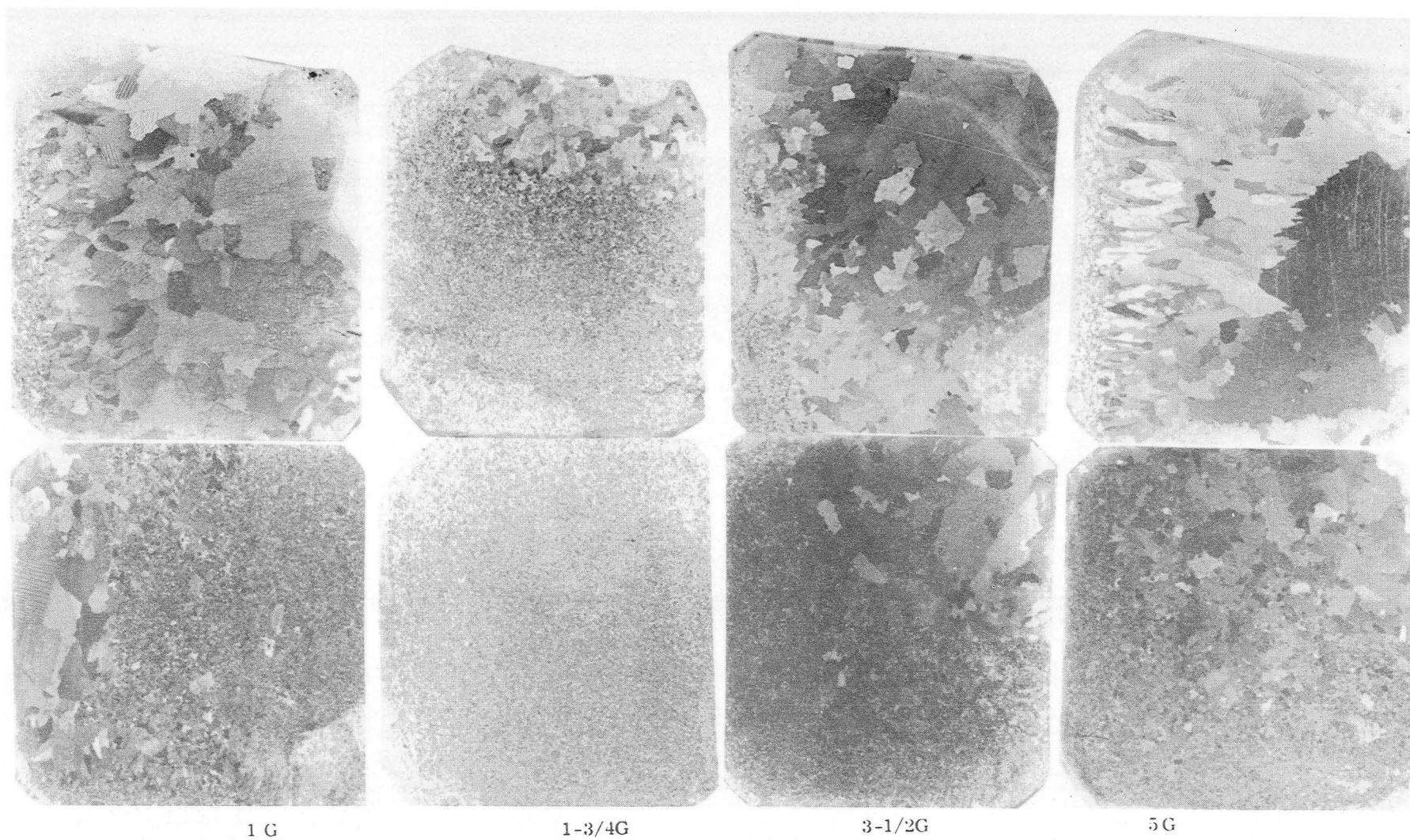
Figure 4. Tin - 3wt% Bismuth, 20°C/Min Cooling Rate
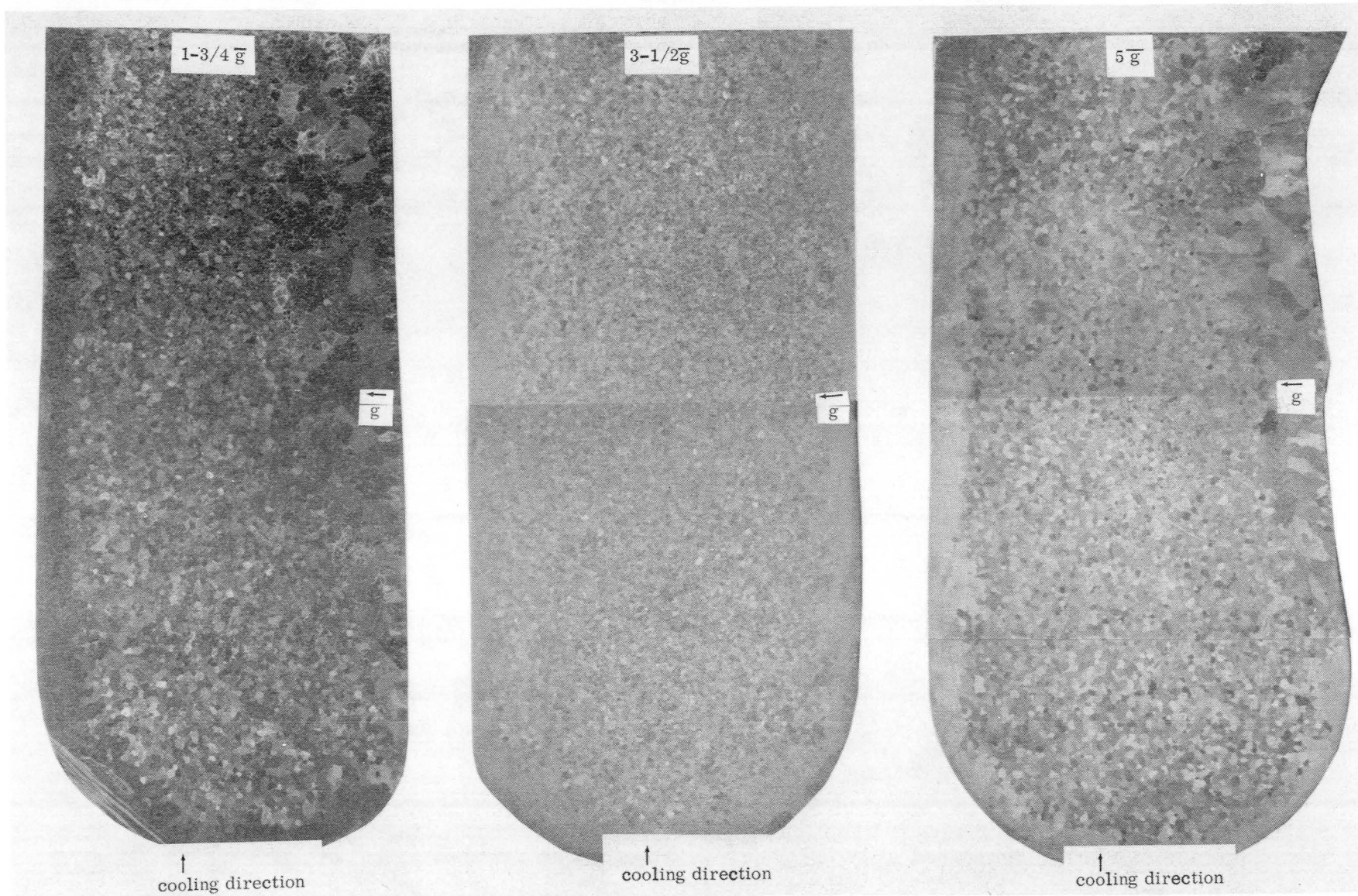
Figure 5. Tin - 3wt% Bismuth Samples, Solidified in Centrifuge with $\overline{g}$ Perpendicular to Sample Axis, 5°C/Min Cooling Rate
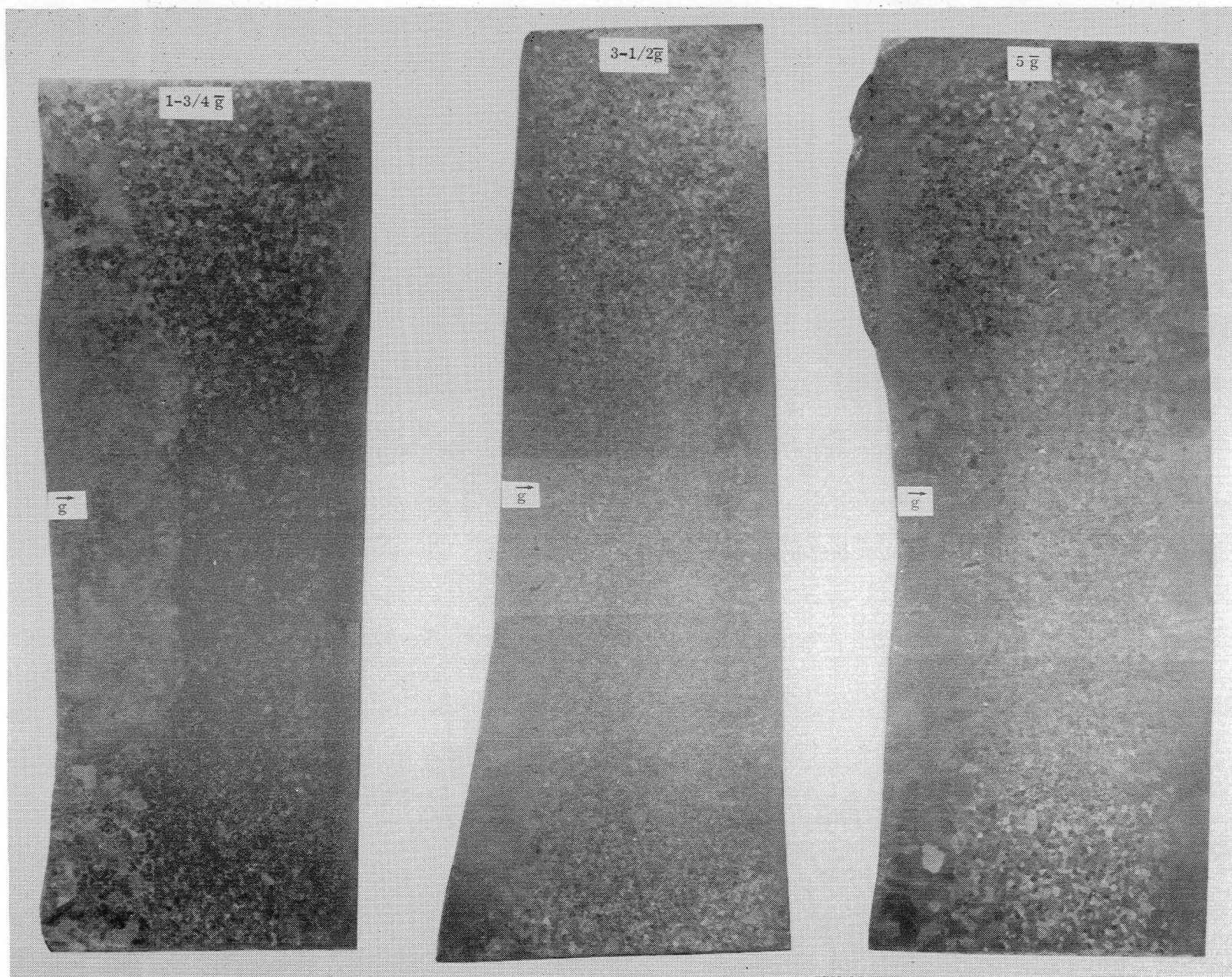
Figure 6. Tin - 3wt% Bismuth Samples, Solidified in Centrifuge with $\bar{g}$ Perpendicular to Sample Axis, 5°C/Min Cooling Rate
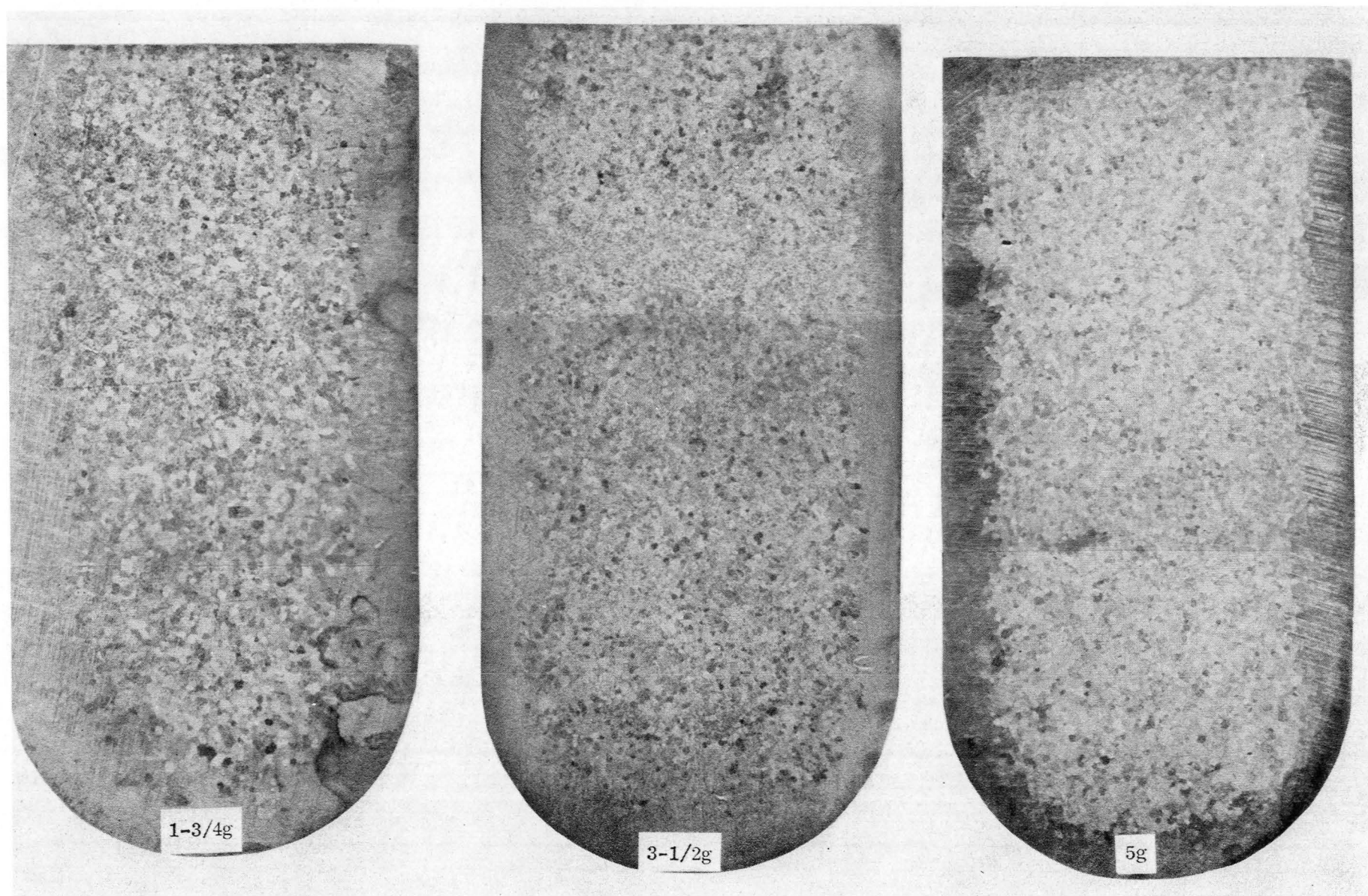
Figure 7. Tin - 3wt%Bi Centrifuge Castings, Center Section Perpendicular to Centerline
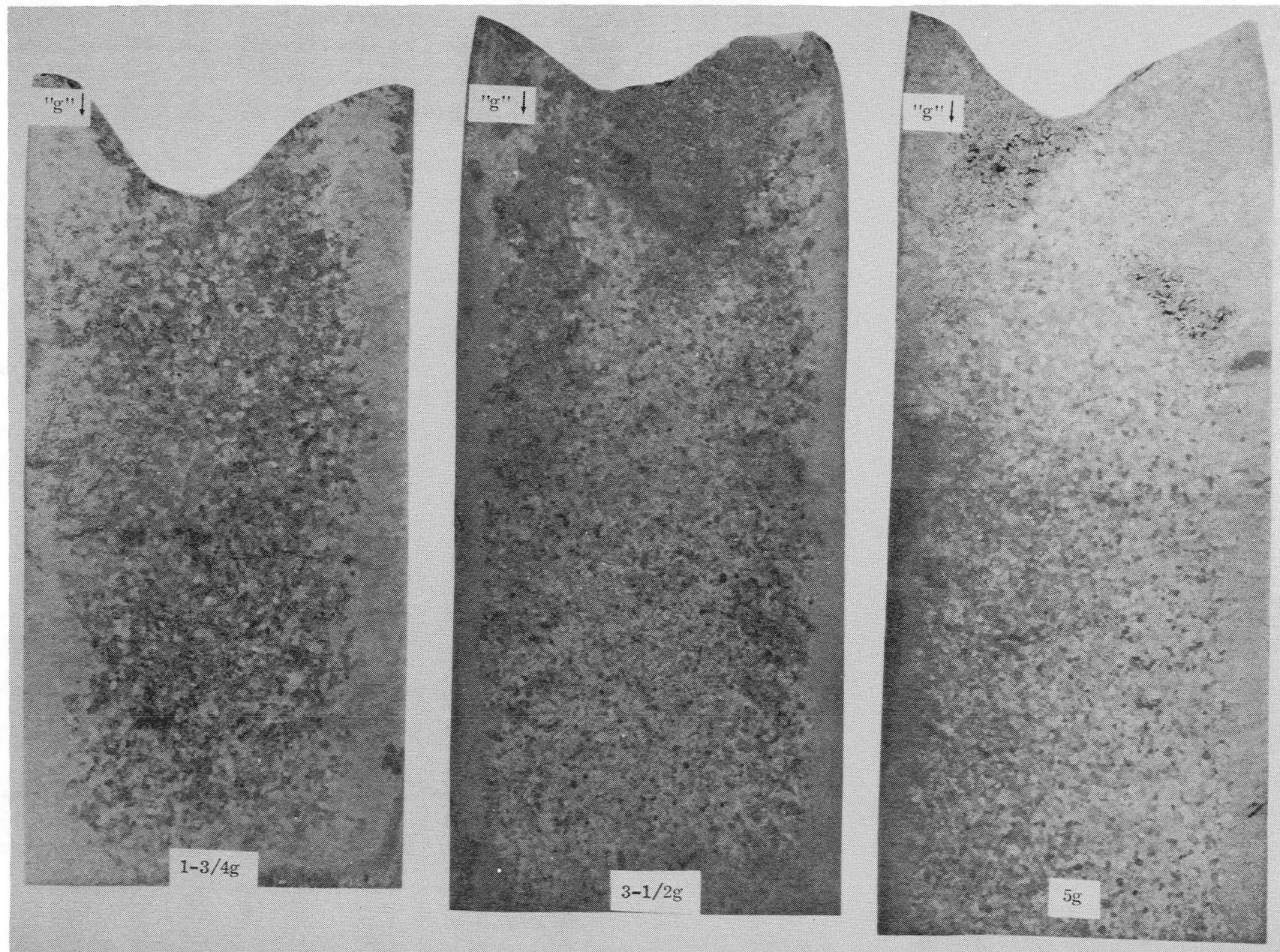
Figure 8. Tin - 3wt% Bi Centrifuge Castings, shown along Centerline
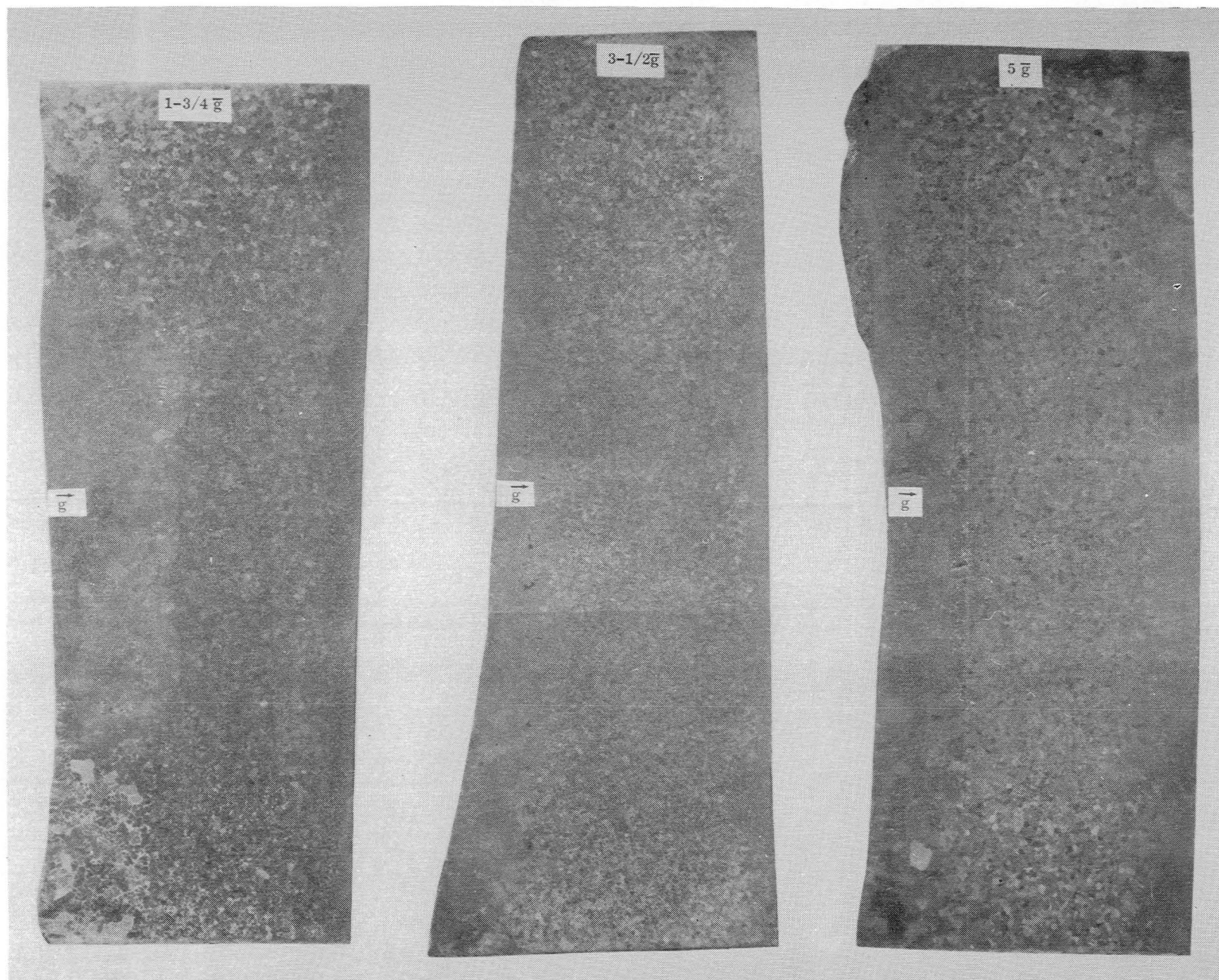
Figure 9. Tin - 3wt%, Bismuth Samples, Solidified in Centrifuge with $\overline{g}$ Perpendicular to Sample Axis, 5°C/Min Cooling Rate
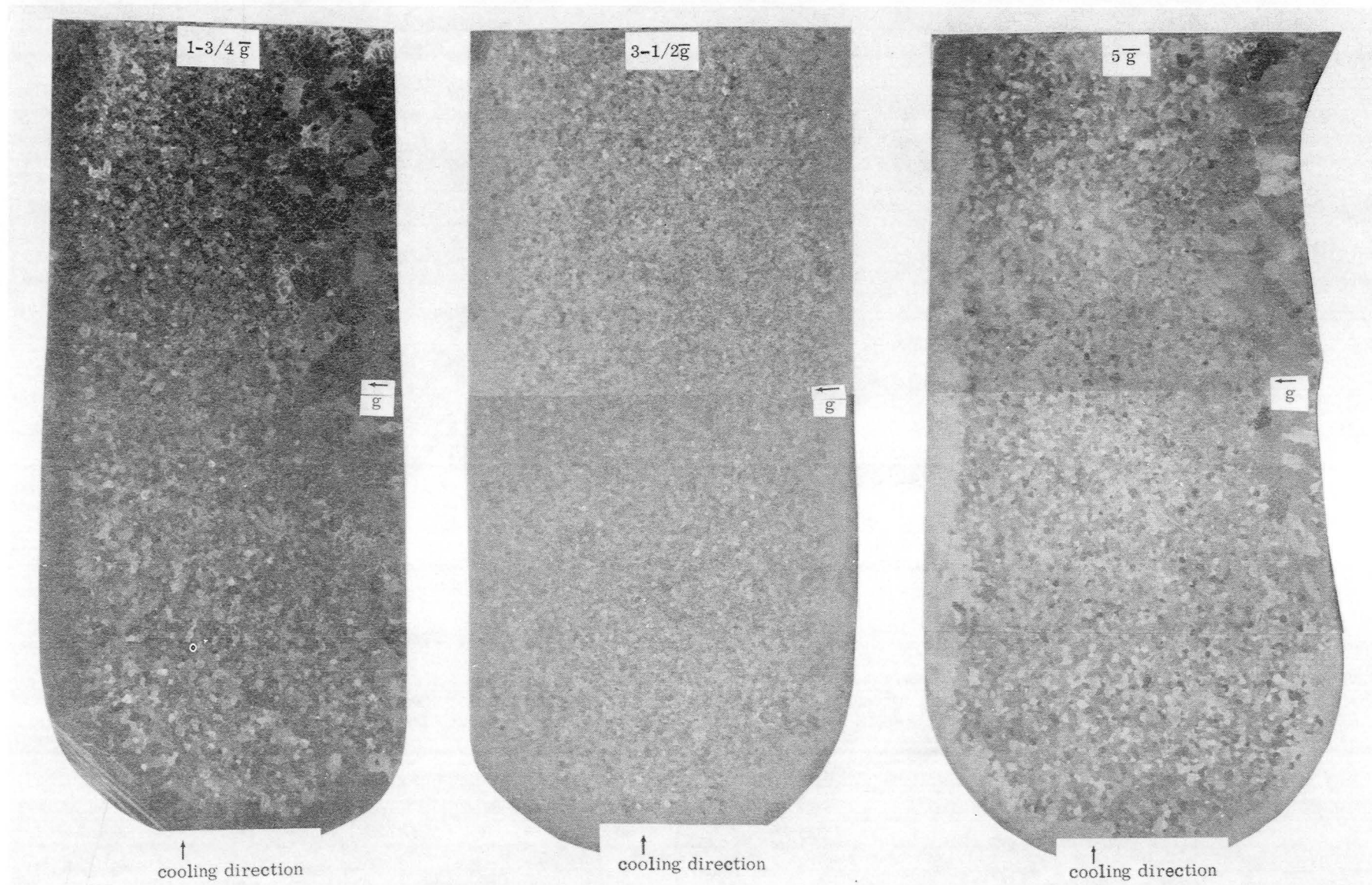
Figure 10. Tin - 3wt% Bismuth Samples, Solidified in Centrifuge with $\overline{g}$ Perpendicular to Sample Axis, 5°C/Min Cooling Rate
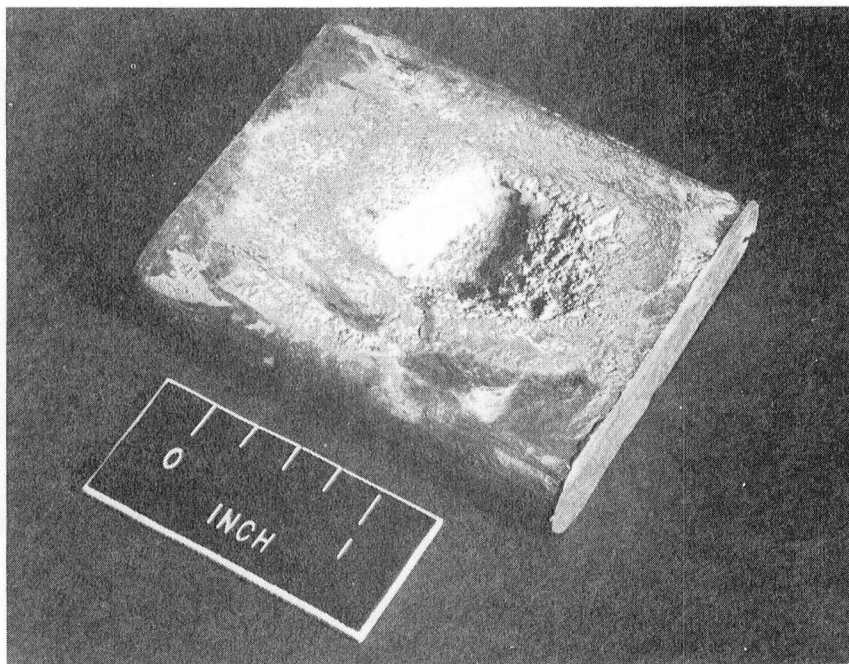
Flight Sample, A Surface
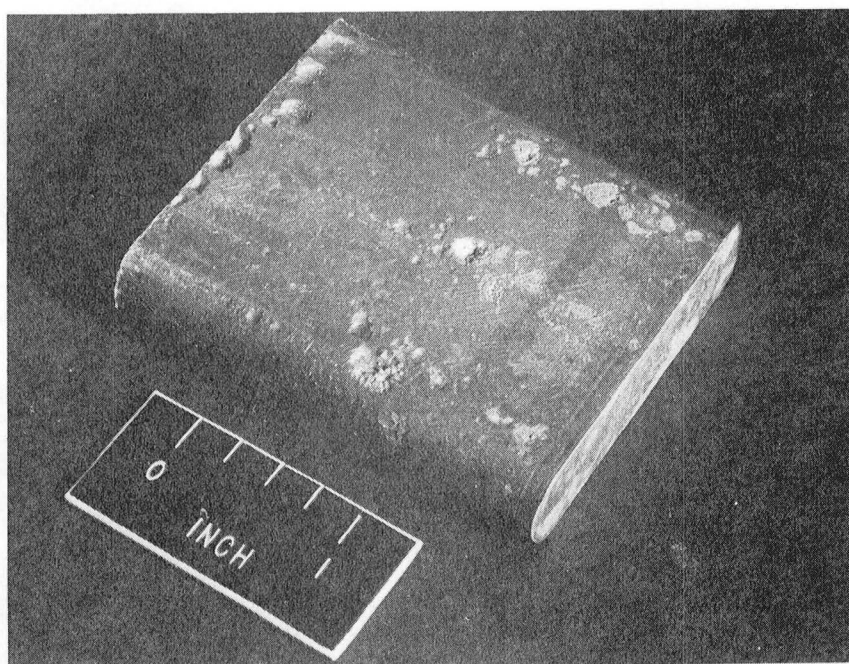
Flight Sample, B Surface

Figure 11. Flight Samples
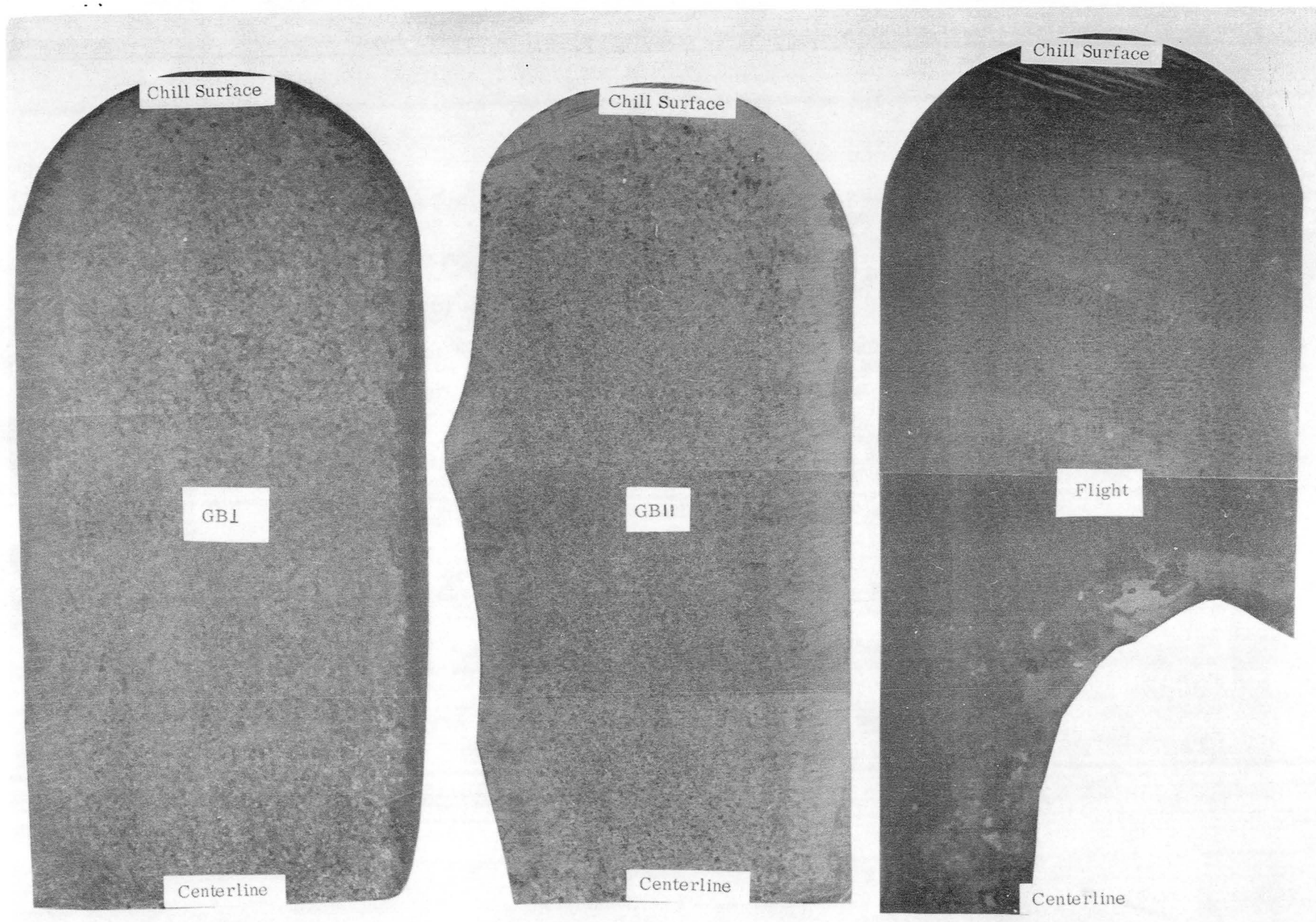
Figure 12. Tin - 3% Bismuth, Flight and Ground-Based Samples
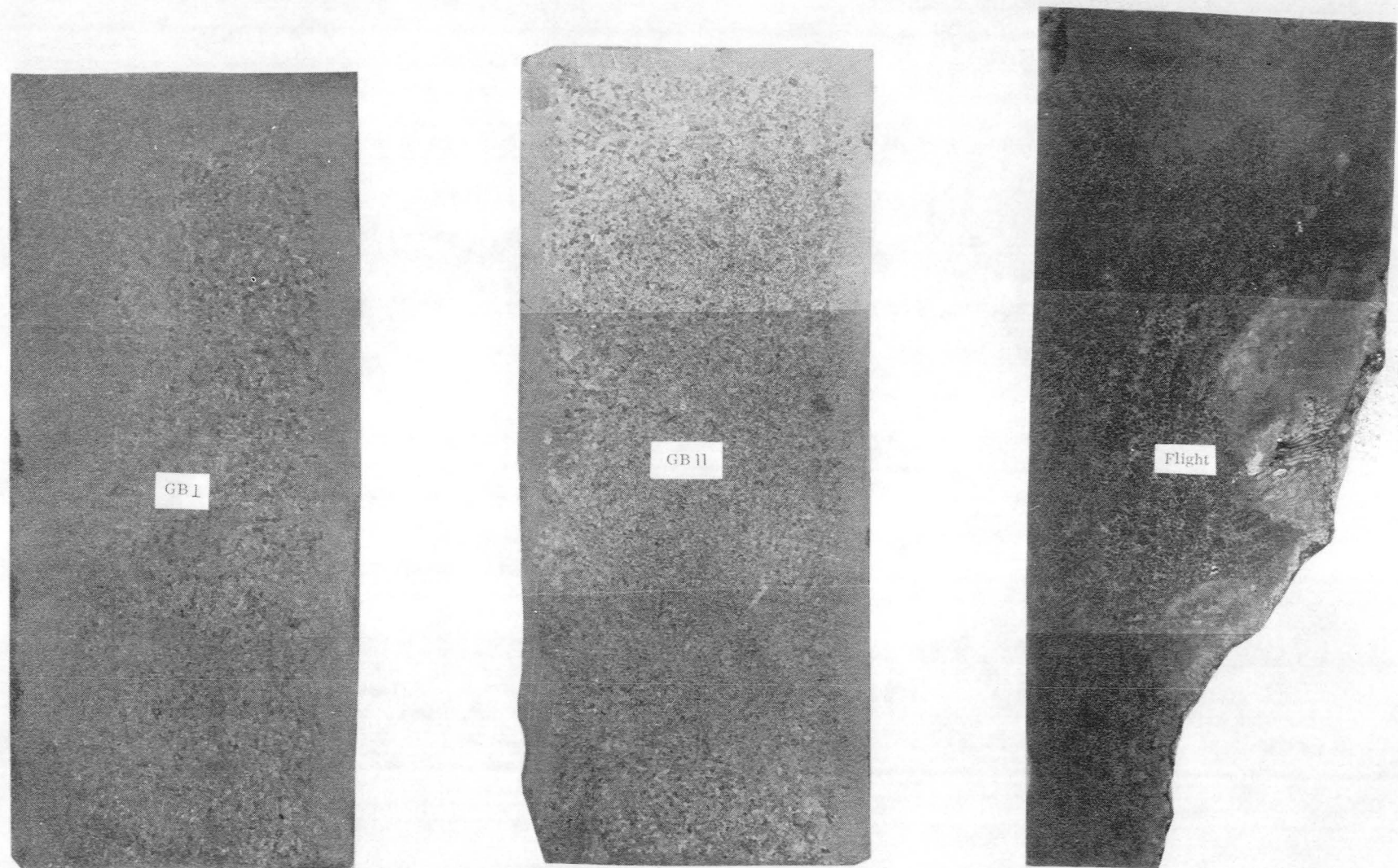
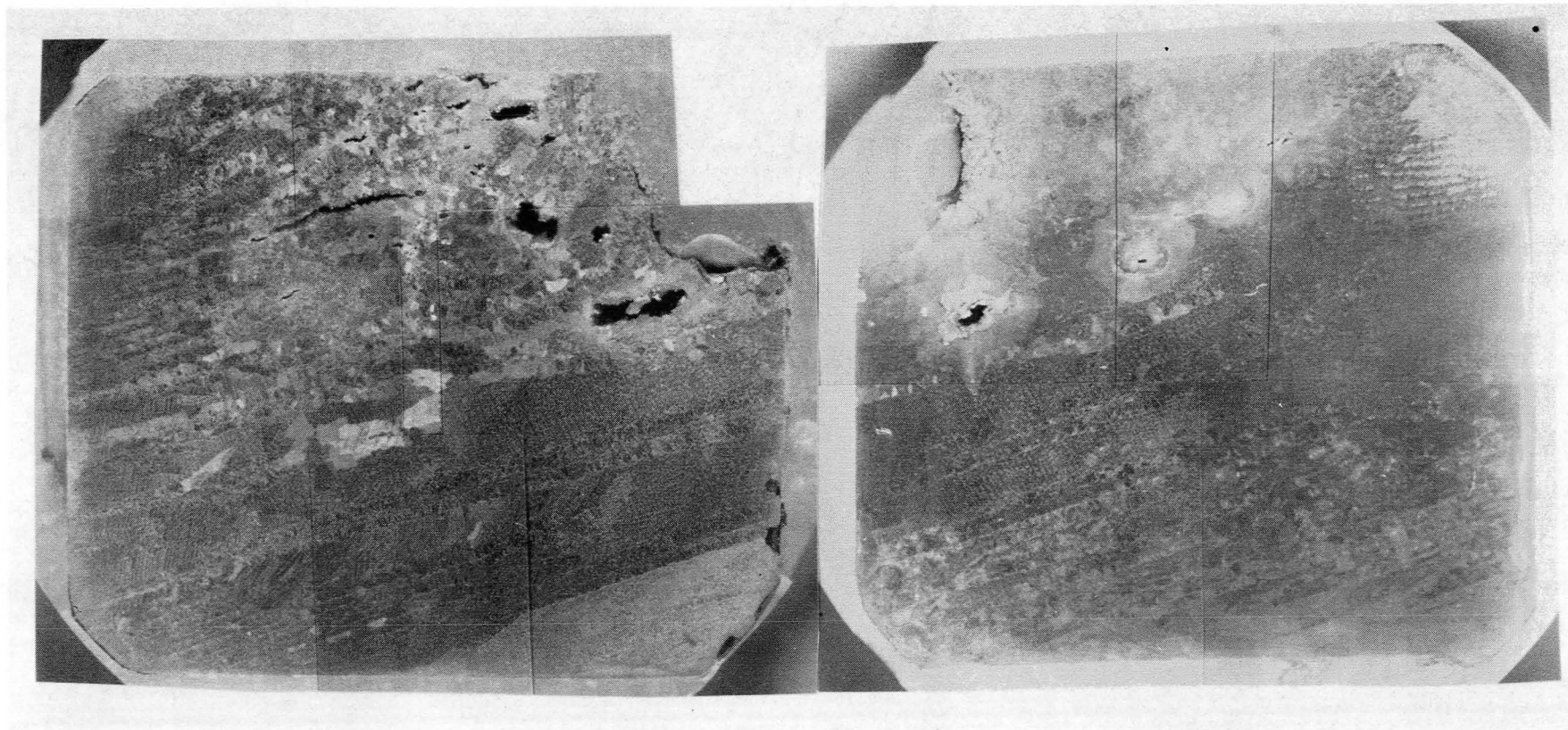Figure 13. Tin - 3% Bismuth, Flight ard Ground-Based Samples, shown along Centerline

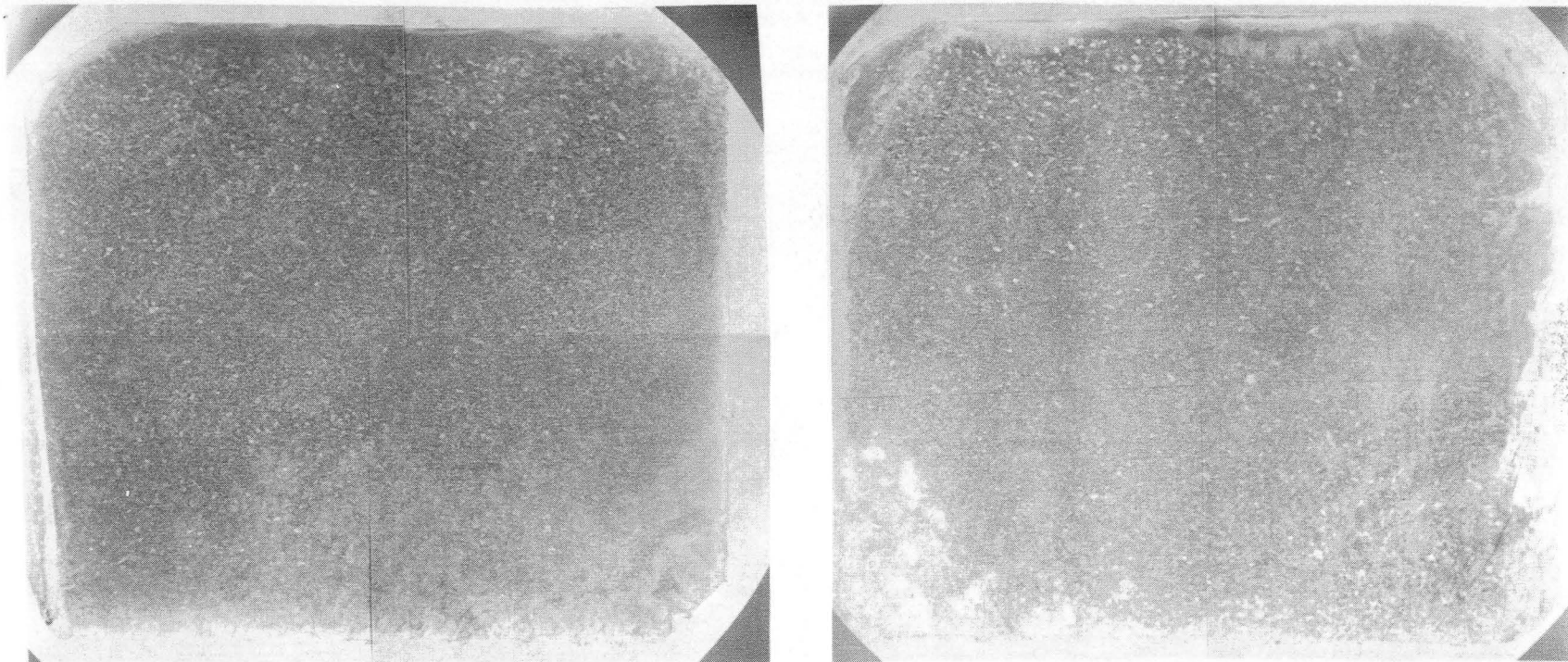Figure 14.   Faces CE and DE of Flight Tin-3wt% Bismuth Sample

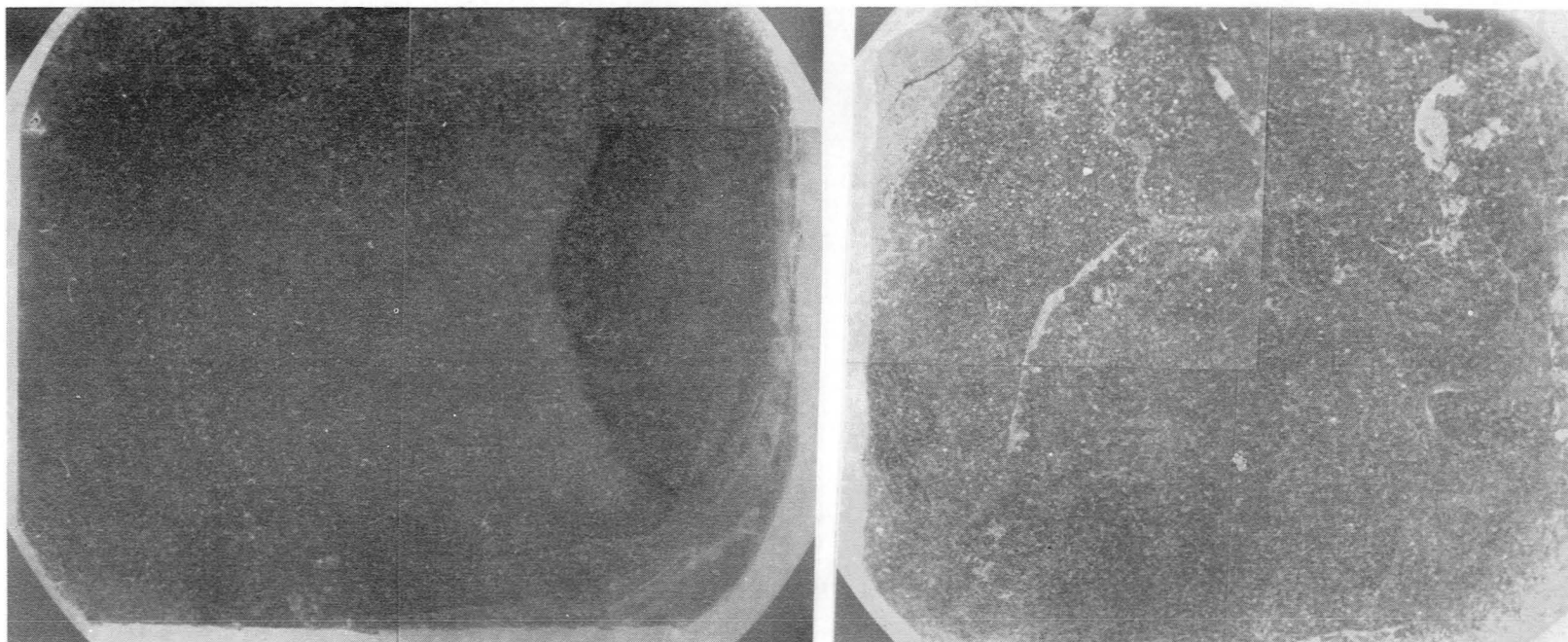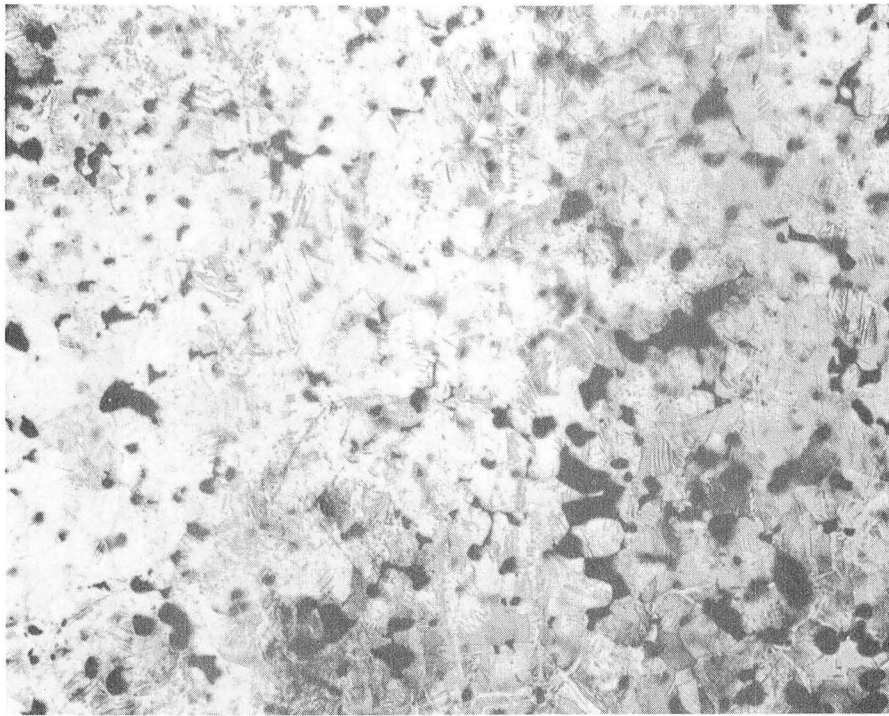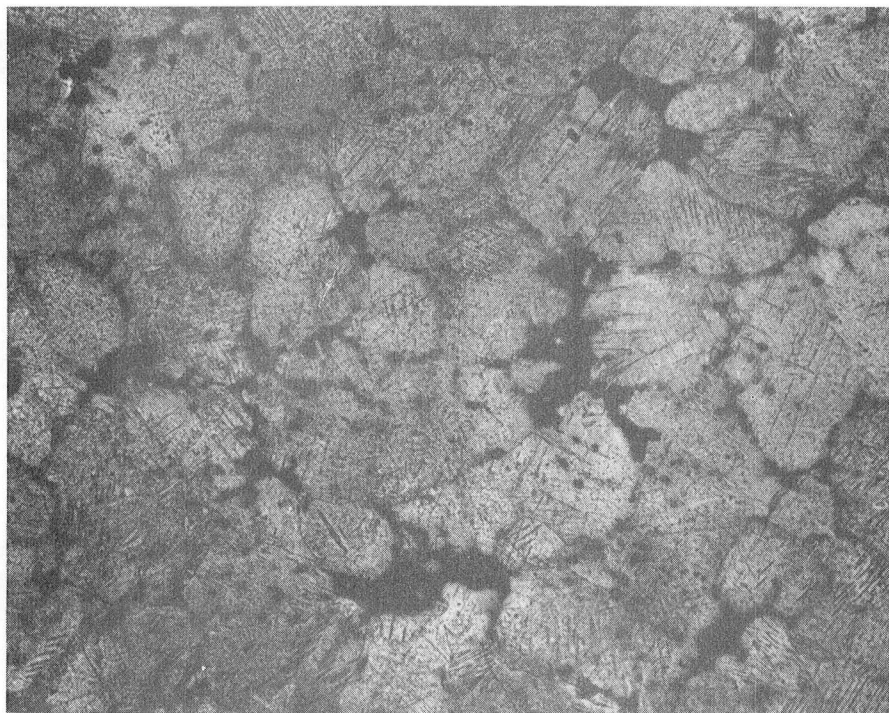Figure 15. Faces CE and DE of Ground-Based ‖ Tin-3wt% Bismuth Sample

Figure 16. Faces CE and De of Ground-Based ⊥ Tin-3wt% Bismuth Sample

Ground-Based   (50X)

Flight (50X)

Figure 17. Porosity in Flight and Ground-Based Samples
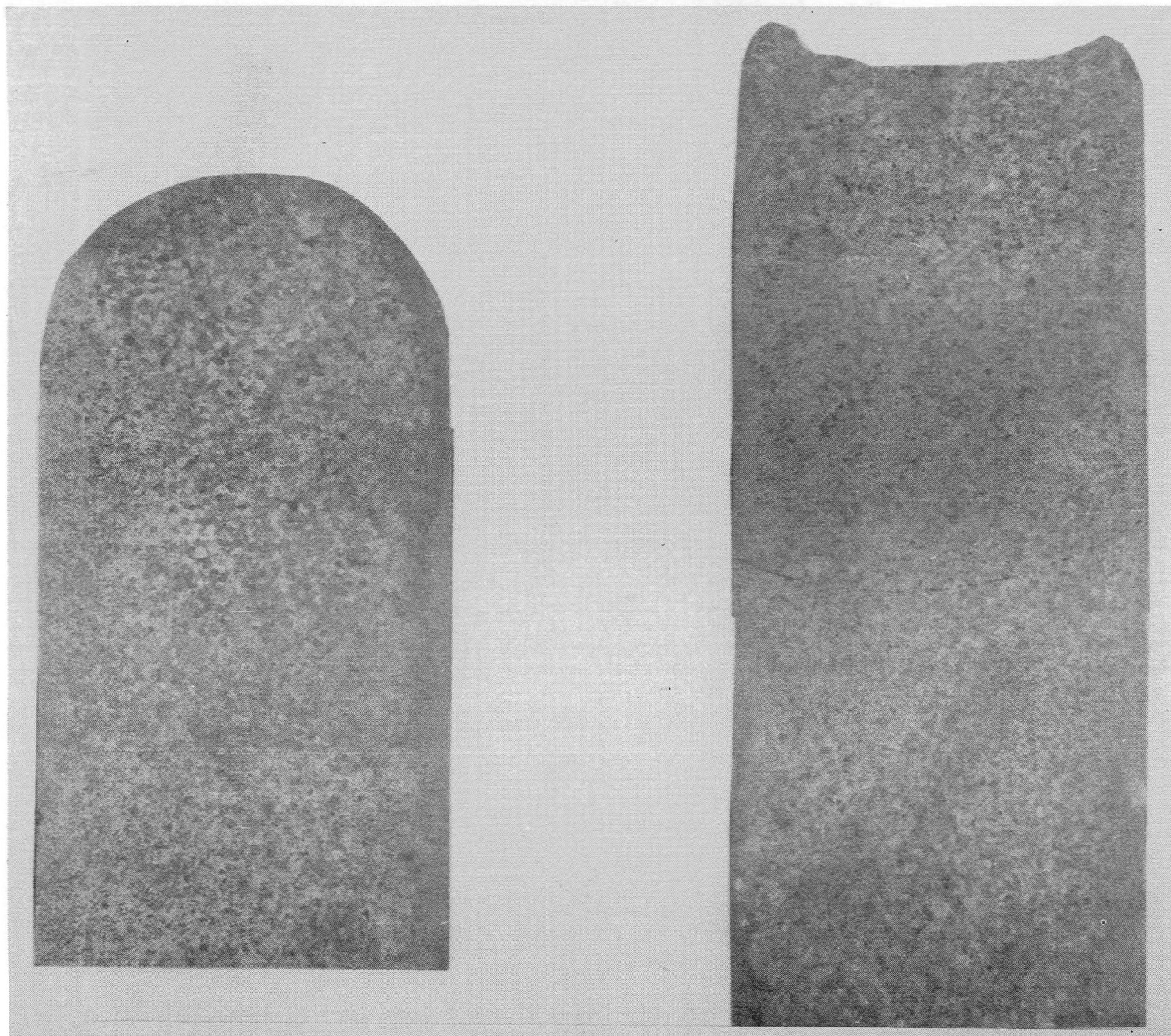
Figure 18.   Tin-3wt% Bismuth Sample Solidified on KC-135 Airplane during
Low-Gravity and Pullout - Faces CA and DB

1. REPORT NO. NASA TM-82549	2. GOVERNMENT ACCESSION NO.	3. RECIPIENT'S CATALOG NO.
4. TITLE AND SUBTITLE Space Processing Applications Rocket (SPAR) Project SPAR IX Final Report		5. REPORT DATE January 1984
		6. PERFORMING ORGANIZATION CODE JA62
7. AUTHOR(S) R. Poorman, Compiler		8. PERFORMING ORGANIZATION REPORT #
9. PERFORMING ORGANIZATION NAME AND ADDRESS George C. Marshall Space Flight Center Marshall Space Flight Center, AL 35812		10. WORK UNIT NO. M-430
		11. CONTRACT OR GRANT NO.
		13. TYPE OF REPORT & PERIOD COVERED
12. SPONSORING AGENCY NAME AND ADDRESS National Aeronautics and Space Administration Washington, D.C. 20546		Technical Memorandum
		14. SPONSORING AGENCY CODE

15. SUPPLEMENTARY NOTES

16. ABSTRACT

The Space Processing Applications Rocket Project (SPAR) IX Final Report contains the compilation of the post-flight reports of each of the Principal Investigators (PIs) of the three selected science payloads, in addition to the engineering report as documented by the Marshall Space Flight Center (MSFC). This combined effort also describes pertinent portions of ground-based research leading to the ultimate selection of the flight sample composition, including design, fabrication and testing, all of which are expected to contribute to an improved comprehension of materials processing in space.

The SPAR project is coordinated and managed by MSFC as part of the Materials Processing in Space (MPS) program of the Office of Space Science and Applications (OSSA) of NASA Headquarters.

This technical memorandum is directed entirely to the payload manifest flown in the ninth of a series of SPAR flights conducted at the White Sands Missile Range (WSMR) and includes the experiments entitled "Directional Solidification of Magnetic Composites" (Experiment No. 76-22/2, "Directional Solidification of Immiscible Aluminum-Indium Alloys" (Experiment Nos. 76-51/1 and 76-51/2), and "Comparative Alloy Solidification" (Experiment No. 76-36/1).

17. KEY WORDS Space processing Solidification Aluminum-Indium Tin-Lead Manganese-Bismuth	18. DISTRIBUTION STATEMENT Unclassified – Unlimited Subject Category: 15

19. SECURITY CLASSIF. (of this report) UNCLASSIFIED	20. SECURITY CLASSIF. (of this page) UNCLASSIFIED	21. NO. OF PAGES 196	22. PRICE A09

MSFC - Form 3292 (May 1969)

National Aeronautics and
Space Administration

Washington, D.C.
20546

Official Business
Penalty for Private Use, $300

SPECIAL FOURTH CLASS MAIL
BOOK

NASA

If Undeliverable (Section 158
Postal Manual) Do Not Return